

博士論文

縞走査干渉法による電子線ホログラフィの高感度化と
それによる微視的磁場の解析

1991年

長谷川 修 司

Thesis

**Sensitivity-Enhanced Electron Holography
with Fringe Scanning Interferometry
and its Application to Analysis of
Microscopic Magnetic Fields**

1991

Shuji Hasegawa

Contents

Chapter 1	Introduction	4
1.1	Historical background	4
1.2	Present work	8
Chapter 2	Electron wave and electron holography	11
2.1	Introduction	11
2.2	Electron coherency and interference	12
2.3	Electron holography microscope	15
2.3.1	Electron gun	
2.3.2	Electron biprism	
2.4	Electron wave propagation in the microscope	21
2.5	Wavefront reconstruction	30
2.5.1	Interference micrographs	
2.5.2	Phase-difference amplification	
2.6	The Aharonov-Bohm effect	38
Chapter 3	Fringe scanning interferometry	46
3.1	Introduction	46
3.2	Principle and experimental set-up	48
3.3	Experimental procedure	52
3.4	Analysis examples	56
3.4.1	Cobalt fine particle	
3.4.2	Ring magnet	
3.5	Conclusions	66
Chapter 4	Stray field from magnetic recording materials	67
4.1	Introduction	67
4.2	Experimental procedures	70
4.2.1	Sample preparation	
4.2.2	Analysis procedures	
4.3	Calculation of magnetic phase caused by magnetic materials	75

4.4	Experimental results and discussions	79
4.4.1	Observation of stray fields	
4.4.2	Analysis of stray fields	
4.5	Conclusions	88
Chapter 5	Phase tomography in electron holography	90
5.1	Introduction	90
5.2	Reconstruction of electromagnetic fields	92
5.3	The use of symmetry	96
Chapter 6	Magnetic flux in superconductors	100
6.1	Introduction	100
6.2	Background	102
6.3	Experimental procedures	109
6.3.1	Sample preparation	
6.3.2	Electron holography microscope	
6.3.3	Optical reconstruction and field analysis	
6.4	Model calculations of fluxon field	118
6.5	Experimental results	125
6.5.1	Observation of magnetic flux structures	
6.5.2	Internal field distributions of quantized fluxes	
6.6	Discussions	138
6.6.1	Detection of a single fluxon	
6.6.2	Magnetic flux structures of lead films	
6.7	Conclusions	144
Chapter 7	Concluding remarks	146
References	148
List of the published papers	157
Acknowledgments	159

Chapter 1

Introduction

1.1 Historical background

Wave nature of electrons, predicted by de Broglie in 1924 [1.1], was experimentally confirmed by Davisson and Germer [1.2] in 1927, and Thomson [1.3], Kikuchi [1.4], Rupp [1.5] in 1928 in the form of electron diffraction phenomena. Combining this fact with the theory of magnetic electron lenses of Busch [1.6], Ruska developed an electron microscope in 1932 [1.7] in order to exceed the resolution limit of optical microscopes. Because of the much shorter wavelength of electron waves, he soon attained the higher resolution compared with the optical microscopes [1.8]. Although, however, the resolution has been now improved up to around 0.1 nm at the cost of elaborate techniques such as electronics and vacuum generation, it is still very poor compared with the wavelength of electrons, $\sim 0.004 \text{ nm}$ at 100 kV acceleration. This is due to the unavoidable aberrations of the electron lenses. As a way to remove the aberrations and break through the resolution limit of electron microscopes, electron holography was devised by Gabor in 1949 [1.9]. Through the electron holography principle, electron wavefronts containing the aberrations are faithfully transformed into light wavefronts, and then the aberrations are compensated through use of versatile optical techniques on an optical bench to obtain the ultra-high resolution. Unfortunately, however, his ingenious idea has not yet realized because of the insufficient coherency and brightness of electron beams. Instead of electron beams, holography technique has come into full bloom as optical holography with the advent of laser beams.

The first experimental trials towards electron holography were carried out in the form of "in-line holography". The hologram in this method is a defocused electron micrograph

in which the Fresnel fringes from specimen edges appear. The scattered wave from a small specimen such as an isolated fine particles, and the transmitted wave through its circumference interfere with each other to form interference fringes, the Fresnel fringes. Although the preliminary results of image reconstruction using this hologram were obtained by Haine and Mulvey (1952) [1.10], and Hibi (1956) [1.11], the reconstructed images were disturbed by their conjugate images. Tonomura *et al.* (1968) [1.12] made in-line holograms on the Fraunhofer diffraction plane instead of the Fresnel diffraction region, so that the image reconstruction almost free from disturbance became possible. The image resolution with this method was improved up to $1nm$ (Much, 1975 [1.13]) or $0.7nm$ (Bonnet *et al.*, 1978 [1.14]) using a field-emission electron beam, which were, however, still lower than that of conventional electron micrographs.

Another approach for electron holography began with the invention of a practical electron interferometer by Möllenstedt and Dücker in 1955 [1.15]. This was an electrostatic biprism which enables one to control the electron interference phenomena, essential for electron holography. Before this invention, the interference with electrons was observed only as diffraction phenomena, and it was hard to intentionally control. Combining the electron biprism with the improvement of the performance of the electron microscope, electron interferometry and electron interference microscopy has been opened up. They were applied for high resolution measurements of inner potentials of fine particles [1.16], investigations of magnetic domain walls [1.17] [1.18][1.19], detection of micro-electric fields of reverse-biased p-n junctions[1.20][1.21], detection of fluxons in superconducting hollow cylinders [1.22][1.23], verification of the Aharonov-Bohm effect [1.24][1.25] and others.

As the analogy of off-axis laser holography developed by Leith and Upatnicks (1962) [1.26], Möllenstedt and Wahl (1968)[1.27] first utilized the electron biprism to produce off-axis Fresnel electron holograms, which can be reconstructed with laser light, free from disturbance from conjugated images. The image resolution was expected to be greatly improved by adopting off-axis image holography [1.28], because the spherical aberrations of an electron lens is compensated by use of optical concave lens on the image reconstruction stage. Using a field-emission electron gun which was developed by Crewe *et al.* in 1968 [1.29], Tonomura *et al.* (1979) [1.30] succeeded to reconstruct the lattice fringes

of 0.24nm-spacing, of which resolution was comparable to that of conventional electron micrographs. Lichte (1985) [1.31] also obtained high-contrast lattice fringes of 0.34nm-spacing. However, the resolution of the reconstructed image has not yet *exceed* that of conventional electron micrographs.

In spite of unsuccessful advance in the resolution improvement of the electron microscope, new applications of electron holography have been spread with practical use of field-emission type electron guns which produce the higher coherent electron waves compared with the conventional thermionic electron guns [1.32]. Both the phase and the amplitude distributions of the electron wavefunction transmitted through a specimen are explicitly measured with angstrom-resolution. This differentiates electron holography from conventional electron microscopy in which only the amplitude of the wavefunction of the electron is recorded.

Electron holography is a two-step imaging method. At its first stage, in an electron holography microscope, the electron wavefront is divided into two parts. One transmits through the sample region and carries the sample information in its phase (object wave). Another passes far from it, acts as a reference wave. By making the two waves overlap and interfere with each other, the phase distribution of the object wave is recorded as an interference fringe pattern on a hologram. At the next step, by illuminating the hologram with a laser beam, the original object wave is optically reconstructed and its phase distribution is visualized as a contour-phase-line pattern. This is as *interference micrograph*.

The electron wave propagation, passed through a material, is delayed in proportion to the thickness of the specimen because of its inner potential. The thickness distribution of a micro-object is, therefore, revealed in the form of a contour map in the interference micrograph. Even a monatomic step on a crystal surface is detectable as a phase shift of $\sim 2\pi/30$ [1.33]. The specimen is in this way observed in three-dimension, which is the most remarkable feature of electron holography as well as laser holography.

Another important application of electron holography is the direct observation of the microscopic distributions of electric and magnetic fields, because the phase of the electron waves is affected by the fields through the electric charge of the waves. This fact differentiates electron holography from laser holography in which no magnetic- and electric-field

information can be deduced for lack of electric charge of photons. The contour phase lines in the interference micrograph of the electron waves, passed through an electric or a magnetic field, directly correspond to the equi-potential lines [1.34] or magnetic lines of force, respectively. In the magnetic case, in particular, since each interference line in the micrograph corresponds to a definite amount of magnetic flux h/ne (h is Plank's constant, e is electric charge of an electron, and n is an integer), irrespective of the electron energy, we can quantitatively analyze the field just by counting the number of the lines. The technique has been successfully applied to the investigation of the detailed magnetic structures of thin films, fine particles, and magnetic recording materials [1.32].

More strictly speaking, it is not the electric and magnetic fields, but the scalar and the vector potentials that act on the electron phase. This is the Aharonov-Bohm effect [1.35], which has been experimentally confirmed using the electron holography technique [1.36]. The relative phase shift is produced between two parts of an electron wavefront which surrounds a magnetic flux, even if they do not intersect the lines of flux. This implies that electromagnetism is underdescribed by field strength only [1.37]. The scalar and vector potentials are more fundamental quantities, and are also observable quantities in the phase factor, not mathematical imaginary, although the potentials are not uniquely determined at any point in space. The relation between the electron phase and the electromagnetic potential will be reviewed in Chapter 2 in order to prepare some mathematical expressions for the field analysis developed in the subsequent chapters.

In this way, we can measure the phase distribution of the electron wave, carrying the electromagnetic information of the investigated sample region, in the form of the contour phase lines drawn at a definite phase interval in the interference micrograph. In the usual case, the phase interval is 2π , because the interference phenomenon is periodic with the phase of 2π . This corresponds to the magnetic flux sensitivity of $h/e (= 4.1 \times 10^{-15} \text{Wb})$. The smallest phase interval we can draw in the interference micrograph is, however, improved up to $\sim 2\pi/30$, corresponding to the $\sim (h/e)/30$ -magnetic flux sensitivity, with use of a "phase-difference amplification" technique [1.33]. The phase sensitivity enhancement by this technique has widened the variety of observation samples such as very weak magnetic fields and biological specimens, which causes the phase shift less than 2π .

1.2 Present work

Owing to the phase-difference amplification technique, the phase resolution of electron holographic observations have been improved up to $\sim \frac{2\pi}{30}$. This phase sensitivity is, however, sometimes insufficient for quantitative analysis of very small amounts of magnetic fluxes such as in superconductors and high-density magnetic recording materials. This is because the phase information between the neighboring contour lines in the interference micrograph is missing and can not be displayed. For this reason I have adopted "fringe scanning interferometry" using digital image processing techniques [1.38][1.39]. This method allowed us to more precisely obtain the subfringe phase information in the interference micrograph. The fringe scanning interferometry has been utilized for testing optical surfaces and lenses in laser interferometry. I have successfully applied this technique to electron holographic interferometry for the first time [1.40]. I constructed a laser interferometer and a software system to analyze the interference micrograph with this method. Special emphasis is placed on its ability of numerical data acquisition which is necessary to the following data processing for magnetic field analysis.

The phase shift of the electron waves passed through the sample region is proportional to the line integral of the electromagnetic potential along the electron path. The phase distribution can be said, therefore, to be a "two-dimensional (2D) projection" of the three dimensional (3D) distribution of the electromagnetic fields. At the next step of the present work, then, from the numerical data of the phase distribution obtained with the fringe scanning interferometry, the 3D distributions of the magnetic field vector components were decomposed. This was carried out through the tomographic technique which was devised by DeRosier and Klug [1.41] for the reconstruction of the 3D structure of a bacteriophage from the conventional electron micrographs. This analysis gave us the much more quantitative and detailed information on the magnetic field distribution compared with the analysis only by interference micrographs.

In chapter 2 I describe the fundamentals of the theoretical and experimental details on electron holography, which are necessary for the magnetic field analysis developed in the subsequent chapters.

In Chapter 3, the fringe scanning interferometry for analyzing the interference micro-

graphs is described. I also show some analysis examples at each analysis step to beguile the tedious mathematical explanations.

Chapter 4 is devoted to describing the observation of the leakage magnetic flux from a very high-density magnetic recording material. It is shown that the phase sensitivity is improved up to $\sim 2\pi/100$ owing to the fringe scanning interferometry [1.40]. This enables quantitative measurement of magnetic flux as small as $\sim (h/e)/100$ ($= 4.1 \times 10^{-17}Wb$), hitherto undetectable, with high spatial resolution. With this technique, I have observed the distribution of stray magnetic field from a thin cross section of a perpendicularly magnetized recording film (Co-Cr) with a recording density as high as 300 *kFCI* (kilo flux change per inch), or 85nm bit length, the highest density ever directly observed.

Chapter 5 is devoted to the discussion on the analysis method to decompose each component of field vectors from the electron phase distributions measured by the fringe scanning interferometry. The algorithm developed in this Chapter is modified from the methods for the reconstruction of the three-dimensional (3D) structure of an objects from its two-dimensional (2D) projections, which is well known as computerized tomography technique. Such field analysis by electron holography has been first made possible owing to the digital data format of electron phase distributions obtained by the fringe scanning interferometry.

In chapter 6, the quantized magnetic flux, fluxon, penetrating through a superconducting lead films, is directly observed. Combining the fringe scanning interferometry with the electron holography technique, I could determine the flux quantum $\frac{h}{2e}$ for individual fluxes with precision of $\sim \frac{h}{100e}$. Using the tomographic algorithm [1.41] developed in Chapter 5, moreover, this method also allows the decomposition of the magnetic field vector components near the fluxon core. The internal field distribution obtained were compared with the one calculated from the Ginzburg-Landau equations using some models, and a whole agreement was found between them. I also observed and analyzed the changes of the magnetic flux structures of lead thin films depending on their thickness. Fluxon pairs were also observed on 0.2 μm -thick film, which may correspond to the ones suggested in the Kosterlitz-Thouless theory [1.42].

I finally summarize the results obtained in the present works, and suggest some future

subjects in electron holographic investigations in Chapter 7. I also show that the availability of electron holography will be widespread by combining the numerical phase data acquisition method described in the present work.

Chapter 2

Electron wave and electron holography

2.1 Introduction

In this chapter I introduce the experimental procedures and their underlying principles of electron holography. I try to give a systematic treatment of wave propagation in the electron holography microscope by the Fresnel diffraction formula, and give some mathematical expressions necessary for the magnetic field analysis developed in the following chapters. Before explaining some hardware components, I would like to review the concept of electron coherency and interference phenomenon in Section 2.2.

In Section 2.3 I give a brief introduction of electron-optical components for the holography electron microscope which are indispensable to the experiments.

Section 2.4 is devoted to describing the electron wave propagation from the specimen to the hologram in the microscope. The wavefront deformation during the propagation is mathematically traced using transmission functions of the optical components and a wave propagation function.

In Section 2.5, I explain how the electron wave is optically reconstructed from the hologram using a laser interferometer, with an introduction of the experimental set-up. The phase-difference amplification techniques are also shown for comparison with the fringe scanning interferometry developed in Chapter 3.

In Section 2.6, I review the physical meanings of the phase of the electron wavefunction which we can explicitly measure by the electron holography technique. Special attention will be focused on the electron phase shift caused by electromagnetic potentials, i.e., the Aharonov-Bohm effect.

2.2 Electron coherency and interference

In an electron gun, each electron is successively emitted from a source, e.g. a tungsten tip, which has finite lateral dimension, not a point source. The energy of the emitted electrons fluctuates within a width. Each electron can be treated as a wave packet with a finite size, laterally and longitudinally. An electron beam in the electron microscope is, therefore, regarded as a system of successive incoherent wave packets of each electron. The wave packets are too sparsely separated to overlap one another, and there is no mutual correlation between them.

The interference phenomenon essentially occurs with a single electron. The interference fringe of the electron interference experiments is built up by individual electrons whose wavefunctions are the same. Each electron arrives at a point on an observation plane, but the location of the point cannot be predicted in advance. However, the distribution of the arriving points of large number of electrons are governed by the wavefunction. The "wave" used so far is the wavefunction, or the probability density wave accompanying with a single electron. Electron interference phenomena are phenomenologically understood by applying the classical interference theory of partial coherent light waves to the wavefunction of a single electron.

The build-up of the electron-interference fringes were experimentally demonstrated by Tonomura *et al.* [2.1] with an electron biprism and a field-emission electron gun mentioned in the next section. The experiment is essentially the same as the Young's double slits experiment with an electron wave packet, shown in Fig. 2.1(a). On the observation screen, individual arriving electrons were detected with a position-sensitive detector, and displayed as bright spots on a monitor. Experimental results are shown in Fig. 2.1(b)~(e). When the number of arriving electrons is not so large, the distribution of the points seems to be random. We can not predict the location of the arriving point of each electron, even though we do know the wavefunction of the electron. But as the number of electrons increases, a fringe pattern becomes recognizable. The fringe distribution, composed of many electrons, can be predicted with the wavefunction. The results clearly show the wave-particle duality of electrons.

Let us consider the size of an electron wave packet in the interference experiment

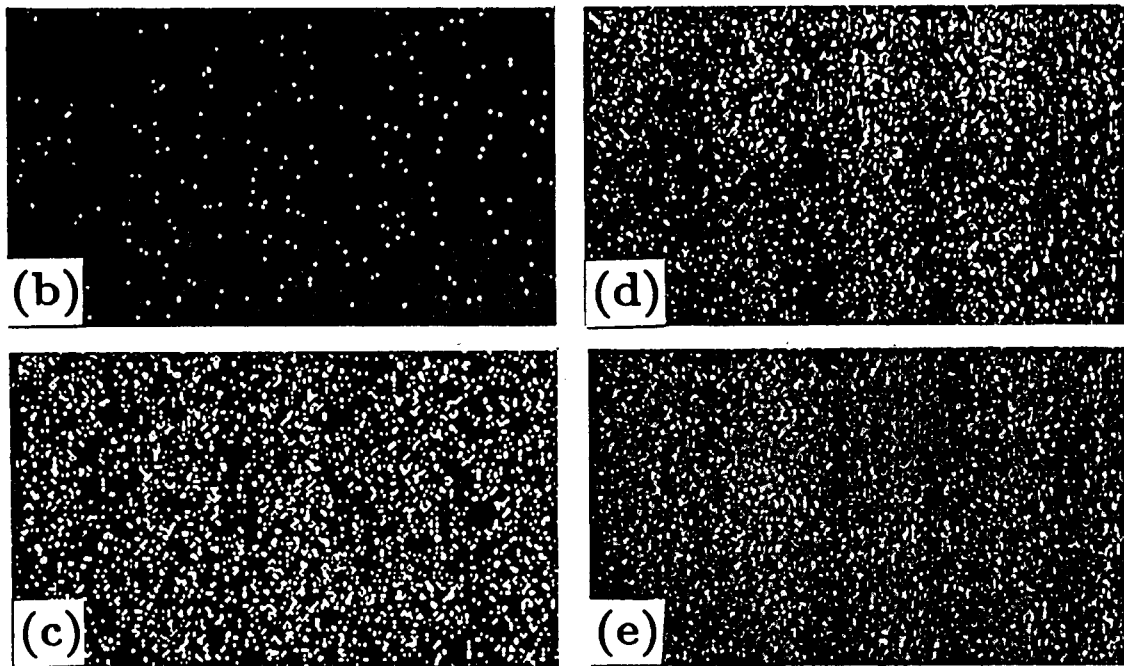
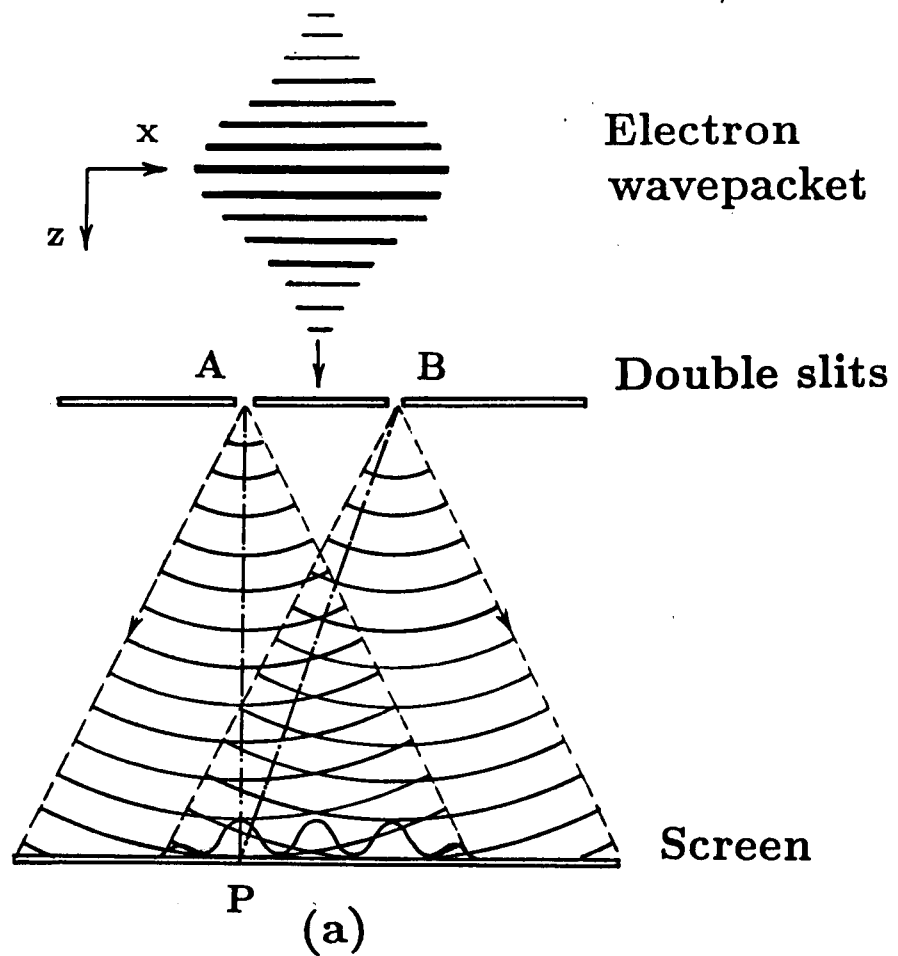


Fig. 2.1. (a) The Young's double-slit-type experiment with electron wave packets. (b)~(e) The interference-fringe build-up in the Young's double-slit-type experiment [2.1]. The experiment were carried out with an electron biprism in an electron holography microscope. The total numbers of electrons on the image are (b) 100, (c) 3000, (d) 20000, and (e) 70000, respectively.

shown in Fig. 2.1(a). For the interference pattern to be observed, first, the *width* of the wave packet of a single incident electron must be large enough to cover the two slits A and B , and second, the phase relation of the partial waves emerging from each slit has to be definite at the screen point P . The second postulate means that the *length* of the wave packet must be longer than the path difference $|\overline{BP} - \overline{AP}|$.

The size of a wave packet is determined from the uncertainty principle;

$$\Delta x \cdot \Delta p_x \sim h, \quad (1)$$

$$\Delta z \cdot \Delta p_z \sim h, \quad (2)$$

where the electron propagates along the z -axis. Δx and Δz are the uncertainty of the electron position, which corresponds to the spread of the wave packet. Δp_x is the uncertainty of its momentum perpendicular to the propagation direction. Δp_z is the uncertainty of the momentum p_z , related to the energy fluctuation.

The width of a wave packet, in exact terms, the transverse coherence length $l_t \sim \Delta x$, is determined from Eq. (1). The de Broglie wavelength is given with its momentum p_z ; $\lambda = h/p_z$. A "divergence angle" β of the propagation direction is defined as $\beta = \Delta p_x/p_z$. Hence, Eq. (1) is rewritten with β as

$$l_t \sim \frac{\lambda}{\beta}. \quad (3)$$

This relation is typically illustrated in Fig. 2.1 (a). When an electron wave packet passes through one of the slits, the width of the wave packet l_t is restricted by the slit width, very narrow. Consequently, the wave packet exiting from the slit fans out with a large divergence angle β . The narrower the slit is, the larger the fan-out angle is.

The length of a wave packet, the longitudinal coherence length $l_l \sim \Delta z$, is determined by uncertainty in wavelength ($\Delta\lambda$) or energy spread (ΔE) of an electron from Eq. (2) as

$$l_l \sim \frac{\lambda^2}{2\Delta\lambda} = \frac{E}{\Delta E} \cdot \lambda. \quad (4)$$

Here, E is the kinetic energy of an electron beam.

The uncertainty principle above mentioned is concerning a single electron. A single electron can go in different directions, and can have different energies at the same time

with some probabilities. In the experiment, however, an individual electron seems to arrive at a definite point on an observation screen with a definite time of flight from the source to the screen. The uncertainty concept, therefore, must be interpreted in a statistical manner. There is no meaning unless we consider the phenomena with a great number of electrons (see Fig. 2.1 (b), meaningless!). That is, in the case of many electrons whose wavefunctions are the same, there is some distributions in their propagation directions and energies, while each electron is assumed to go in a definite direction and have a definite energy. In this interpretation, the uncertainties of the propagation direction β and the energy ΔE of a single electron mean the illumination angle and the energy distribution of a beam consisting of large number of electrons, respectively, which are *experimentally* determined.

An extremely small value of the illumination angle β of the electron beam, an almost parallel beam, is experimentally possible with a very small pinhole, providing a large wavepacket width. However, the intensity of the electron beam in such a case becomes too weak for observation within a reasonable measurement time. The practical value of l_t is, therefore, restricted by the current density per unit solid angle, so called *brightness*. The brightness depends only on the electron beam source, the kind of electron gun employed. The brightness is higher as the emission source size is smaller. The brightness of a field-emission type electron gun is much higher than that of a conventional thermionic electron gun by nearly 3 orders of magnitude. The energy spread of the electron beam is also determined by the electron emitter employed. The coherency of electron beams, consequently, *practically* depends upon the characteristics of the electron beam source.

2.3 Electron holography microscope

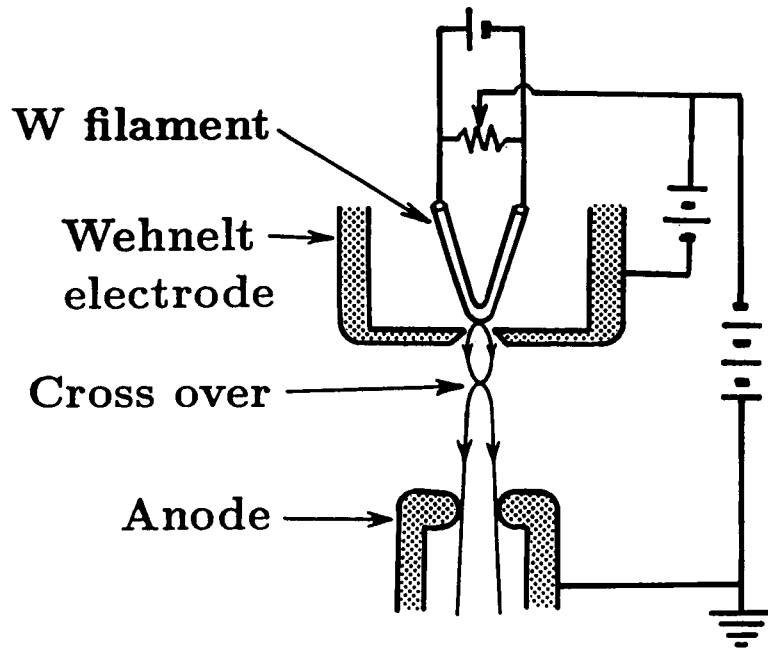
For the holography experiment, we need two special equipments besides the conventional electron microscope. One is an electron beam source with high coherency and brightness, i.e. a field-emission type electron gun. Another is an electron interferometer which coherently divides an electron beam into an object and reference waves, and makes them interfere with each other.

2.3.1 Electron gun

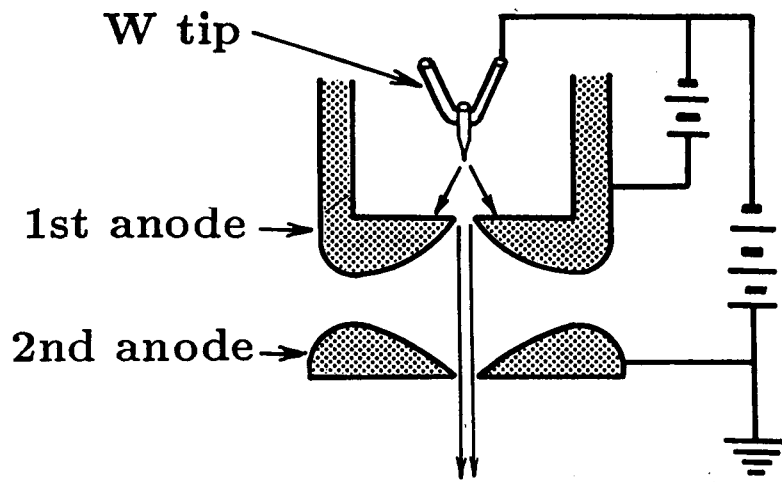
Hairpin-type cathodes (Fig. 2.2(a)) are usually employed in electron microscopy. Thermionic electrons are emitted from a tungsten filament of 0.1mm in diameter heated up to $\sim 2300\text{K}$ by applying an electric current. The emission current is controlled by a negative-bias voltage to the electrode (Wehnelt electrode) surrounding the filament. The emission area is limited only to the tip of the hairpin. The beam has a minimum cross section, crossover, just after the Wehnelt hole. The diameter of the crossover is a few tens of μm , which is the virtual source size. The energy spread of the emitted electron beam is $\sim 2\text{eV}$, which is anomalously larger than the theoretical value ($\sim kT$) by nearly 1 order of magnitude. This is due to electron-electron interactions during acceleration, the Boersch effect [2.2].

Pointed cathodes, developed by Hibi [2.3] in 1956 for the purpose of realizing electron holography, are frequently used for high-resolution electron microscopy. Electrons are emitted only from the tip of a tungsten needle attached to a hairpin filament. The electron source size and the energy spread are reduced to a few μm and 1eV , respectively, since the field-emission effect is added.

The field emission phenomenon was utilized in a field-emission microscope (FEM) for observing a tip surface in an atomic-scale resolution by Müller in 1937 [2.4]. This phenomenon has recently been used also in scanning tunneling microscopy (STM) developed by Binnig and Rohrer [2.5], applying to various fields of science and technology in an enthusiastic manner. Nevertheless, it was Crewe *et al.* [2.6] who utilized the phenomenon for an electron beam source for microscopy for the first time. The structure of a field-emission type electron gun is shown in Fig. 2.2(b). When an electric potential of $3 \sim 6\text{kV}$ is applied between a tungsten tip and the first anode, electrons, $1 \sim 100\mu\text{A}$, are radially emitted from the hemispherical surface of an electrochemically thinned tungsten tip of $\sim 100\text{nm}$ -radius. Only a few ($\sim 1/10000$) of the emitted electrons pass through the first anode hole and are utilized for the microscopy. Their virtual source size is less than 10nm . No space charge effect, due to a strong electric field around the tip, produces high brightness. The energy spread of the beams is as small as 0.3eV at $10\mu\text{A}$ -emission, because of the room-temperature operation and the small total emission current. We need the



(a)



(b)

Fig. 2.2. Schematics for electron guns. (a) An hairpin-type thermionic electron gun. (b) A field-emission electron gun.

ultra-high vacuum (UHV) environment for the stable operation without any high-voltage discharge.

The characteristics of electron guns are compared in Table 1. A field-emission electron gun is a indispensable source for electron holography, which produces much higher coherent and bright electron beams compared with a thermionic electron gun. Even with this high quality of the field-emission beams, however, it is insufficient for the resolution improvement of the electron microscope with use of holography techniques, Gabor's original purpose.

Table 1: Comparison between thermionic and field-emission electron guns.

	Thermionic gun		Field-emission gun
	Hairpin type	Pointed type	
source size (μm)	~ 20	~ 2	~ 0.01
energy spread (eV)	~ 2	~ 1	~ 0.3
brightness at $100keV$ ($A/cm^2/sr$)	$\sim 5 \times 10^5$	$\sim 2 \times 10^6$	$\sim 5 \times 10^8$
longitudinal coherence length (μm)	~ 0.2	~ 0.4	~ 1.3

2.3.2 Electron biprism

I used an electrostatic biprism, developed by Möllenstedt and Dücker [2.7], as an interferometer. It coherently divides the electron wavefront into two partial wavefronts and makes them overlap and interfere with each other. Although an amplitude-division type interferometer was devised by Marton [2.8][2.9] using Bragg reflection in crystals, its operation is too difficult for practical use.

The electrostatic biprism is composed of a thin wire bridged in the center and two plate-shaped electrodes with ground potential on both sides (Fig. 2.3(a)). The distance between the central wire and the grounded plate electrode is $\sim 5 mm$. The diameter of the central wire, $\sim 300nm$, has to be small enough not to obscure the coherent region of an incident electron beam. The wire in our microscope was made by extending a burned rod of quartz, and its surface was completely covered with a gold layer of $\sim 20nm$ thickness using the sputtering technique.

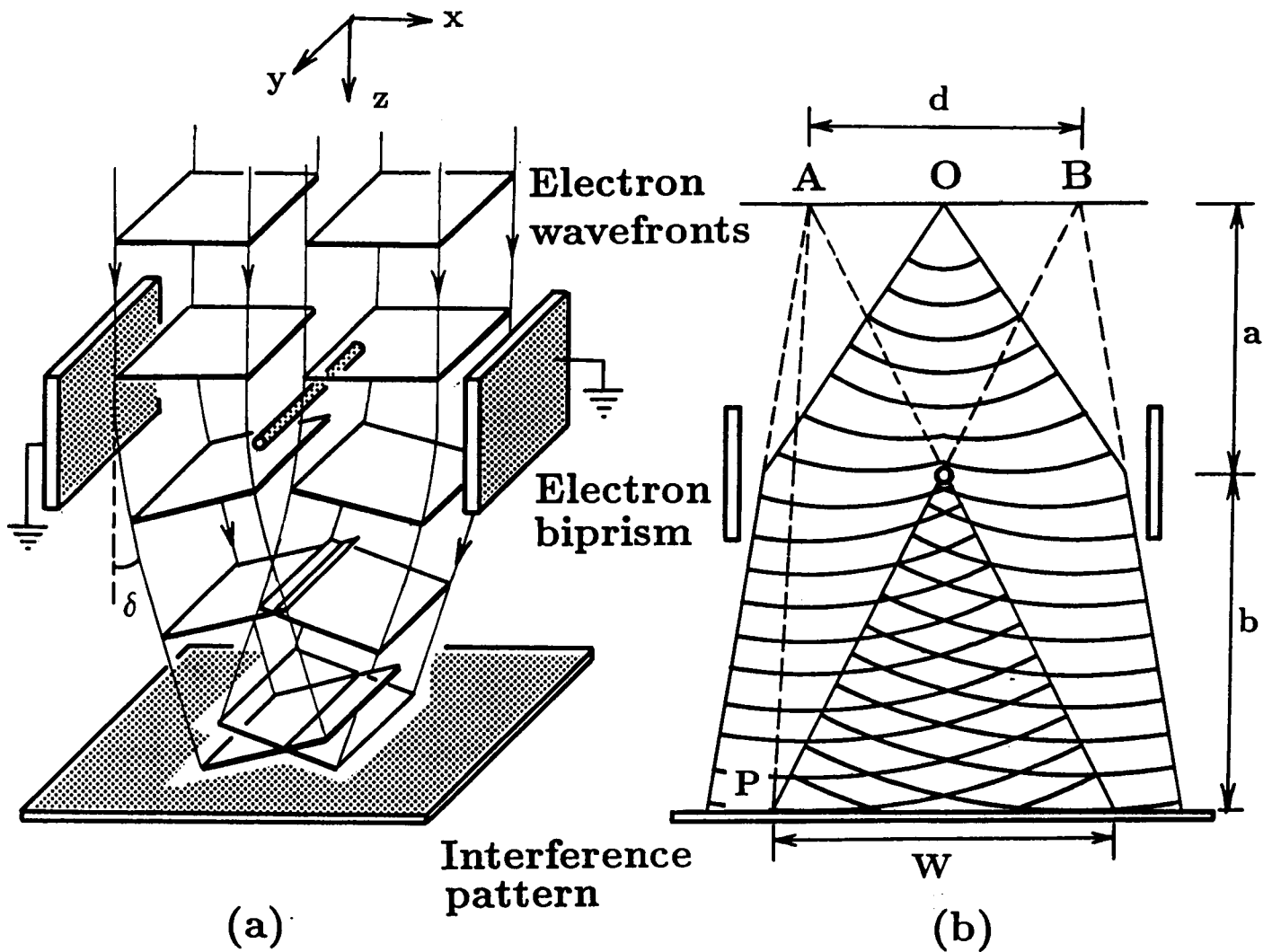


Fig. 2.3. (a) Schematic of the Möllenstedt-Dücker type electron biprism. Two parts of an electron wavefront traveling on both sides of the central wire are attracted towards it by applying a positive voltage to the wire, and overlapped to form an interference pattern on the lower plane. (b) When an electron wave, emitted from a point source O , travels through the both sides of the central wire in the biprism, the wave is divided into two waves and overlapped with each other as if the two waves are coherently emitted from two virtual point sources A and B .

When an positive voltage V_b of $10 \sim 100V$ is applied to the central wire, the electric potential $V(\rho)$ around the wire is axisymmetric depending only on the distance ρ from the center of the wire, and expressed as

$$V(\rho) = V_b \frac{\ln(\rho/\rho_2)}{\ln(\rho_1/\rho_2)}. \quad (5)$$

Here, ρ_1 and ρ_2 are the wire radius and the distance from the wire center to the electrode, respectively ($\rho_1 \sim 150nm$, $\rho_2 \sim 5mm$). Therefore, incident electrons on both sides of the central wire are slightly attracted toward the center (see Fig. 2.3). The deflection angle δ is, then, given when small to be

$$\delta = \frac{\pi e V_b}{2E \ln(\rho_1/\rho_2)}, \quad (6)$$

where E is the kinetic energy of an electron. The deflection angle is constant, irrespective of the incident position ρ of an electron, and simply proportional to the wire voltage V_b . The biprism is a precise electron version of a Fresnel optical biprism.

By this action, when an electron wave, emitted from a point source O (see Fig. 2.3(b)), travels through the biprism, the wave is divided into two waves and overlapped with each other as if the two waves are coherently emitted from two virtual point sources A and B . This is the same situation of the Young's double-slits experiment shown in Fig. 2.1(a). The interference-fringe build-up observation of Fig. 2.1 was done in this way with the biprism [2.1].

Under the usual operating condition, the deflection angle δ is $\sim 10^{-4}rad$, and $a \sim 50mm$, $b \sim 200mm$ (see Fig. 2.3(b)). Then, the distance d between the two virtual sources A and B , the width W of the interference region, and the interference fringe spacing s are respectively given by

$$d = 2\delta a \quad \sim 10\mu m \quad (7)$$

$$W = 2\left(\frac{a+b}{a}\right)\left(\delta\frac{ab}{a+b} - \rho_1\right) \sim 40\mu m \quad (8)$$

$$s = \lambda\left(\frac{a+b}{d}\right) \quad \sim 0.1\mu m. \quad (9)$$

The number of the interference fringes is, therefore, $W/s \sim 400$.

The real electron source O has a finite size with the lateral spread D , not a point

source. Since the sustained angle of the source from the biprism has to be smaller than that of one fringe spacing for the interference fringes observed, D must satisfy that

$$D \leq as/4b \sim 7nm. \quad (10)$$

It is not easy to realize this small source size with a thermionic electron gun. The path difference $|\overline{AP} - \overline{BP}|$ is, on the other hand, $\sim 4nm$. Hence, the maximum number of the observable interference fringes seem to be limited by the source size, or the transverse coherence length.

The biprism action is also described in the wave picture of electrons with a transmission function. The deflection of the angle δ is caused by a phase shift, of which amount is proportional to the distance from the center of the wire, during the passage through the biprism region. When I adopt the coordinate system shown in Fig. 2.3 (a), in which the central wire is parallel to the y -axis, the transmission function of the biprism is given by

$$Q_B(x, y) = \begin{cases} \exp(-\frac{2\pi i \delta |x|}{\lambda}) & (|x| > \rho_1) \\ 0 & (|x| < \rho_1) \end{cases} \quad (11)$$

2.4 Electron wave propagation in the microscope

The microscope employed was a H-800 type Hitachi transmission electron microscope devised for electron holography with a field emission type electron gun and a Möllenstedt-Dücker type biprism. A cutaway illustration of the microscope is shown in Fig. 2.4. Its operating voltage was $150kV$. The pressure in the gun chamber is kept $\leq 10^{-9}$ Torr for the stable operation. The specimen chamber is evacuated by an ion pump to be $\leq 10^{-6}$ Torr. The electron gun and illuminating system are completely covered with Permalloy walls for shielding against electromagnetic disturbance.

The electron optics in the microscope is schematically shown in Fig. 2.5. The electron beam illuminating the specimen can be regarded as a nearly plane-wave, because the divergence angle β of the beam is as small as $1 \times 10^{-8} rad$, which corresponds to the transverse coherence length $l_t \sim 300\mu m$ from Eq. (3). A part of the incident electron wavefront transmits through a specimen region indicated by a small arrow in the figure (object wave), and the remaining part of the wavefront passes without any disturbance

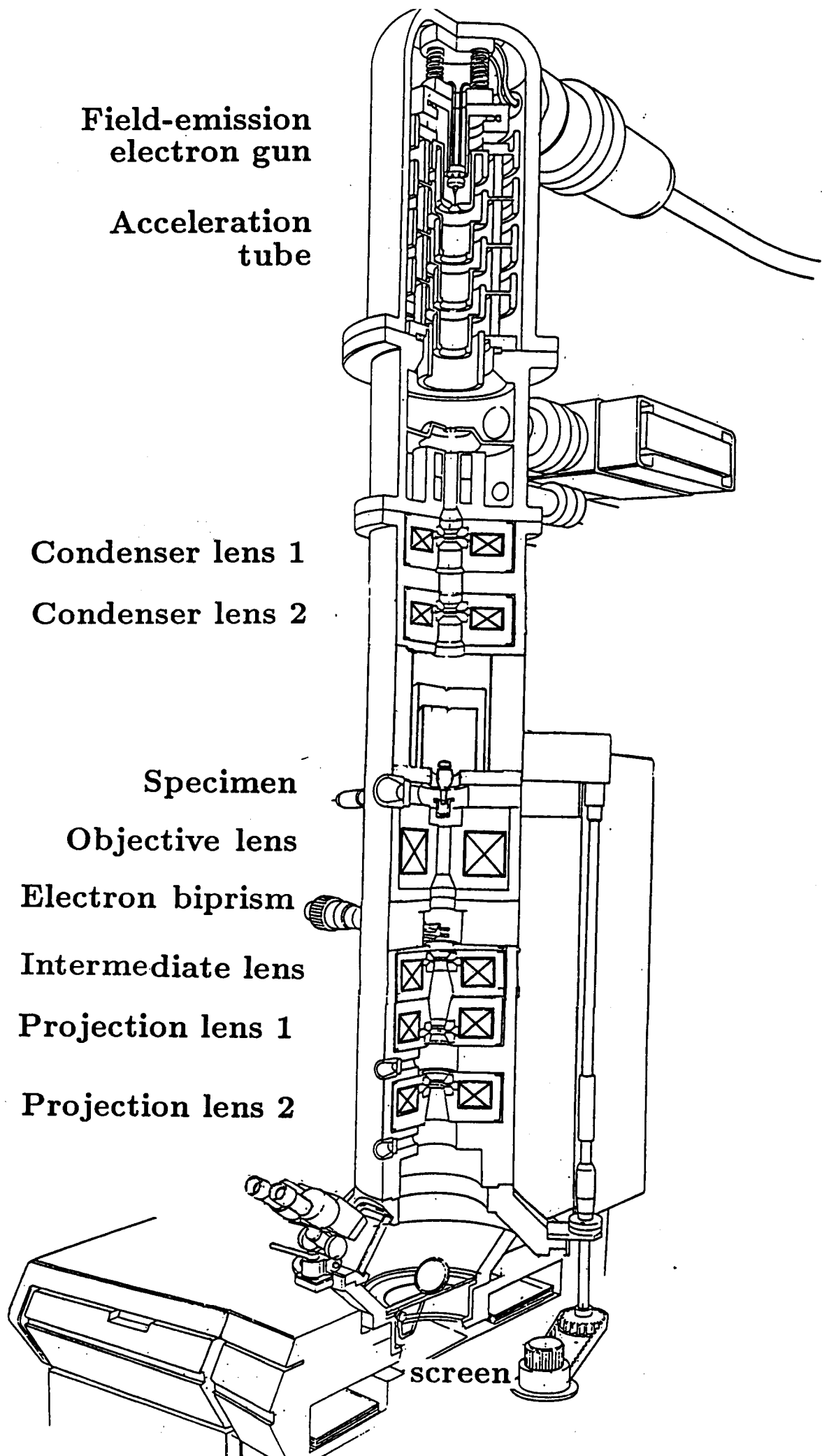


Fig. 2.4. Cutaway illustration of the holography electron microscope. This is a H-800 type Hitachi transmission electron microscope devised with a field emission electron gun and a Möllenstedt-Dücker biprism.

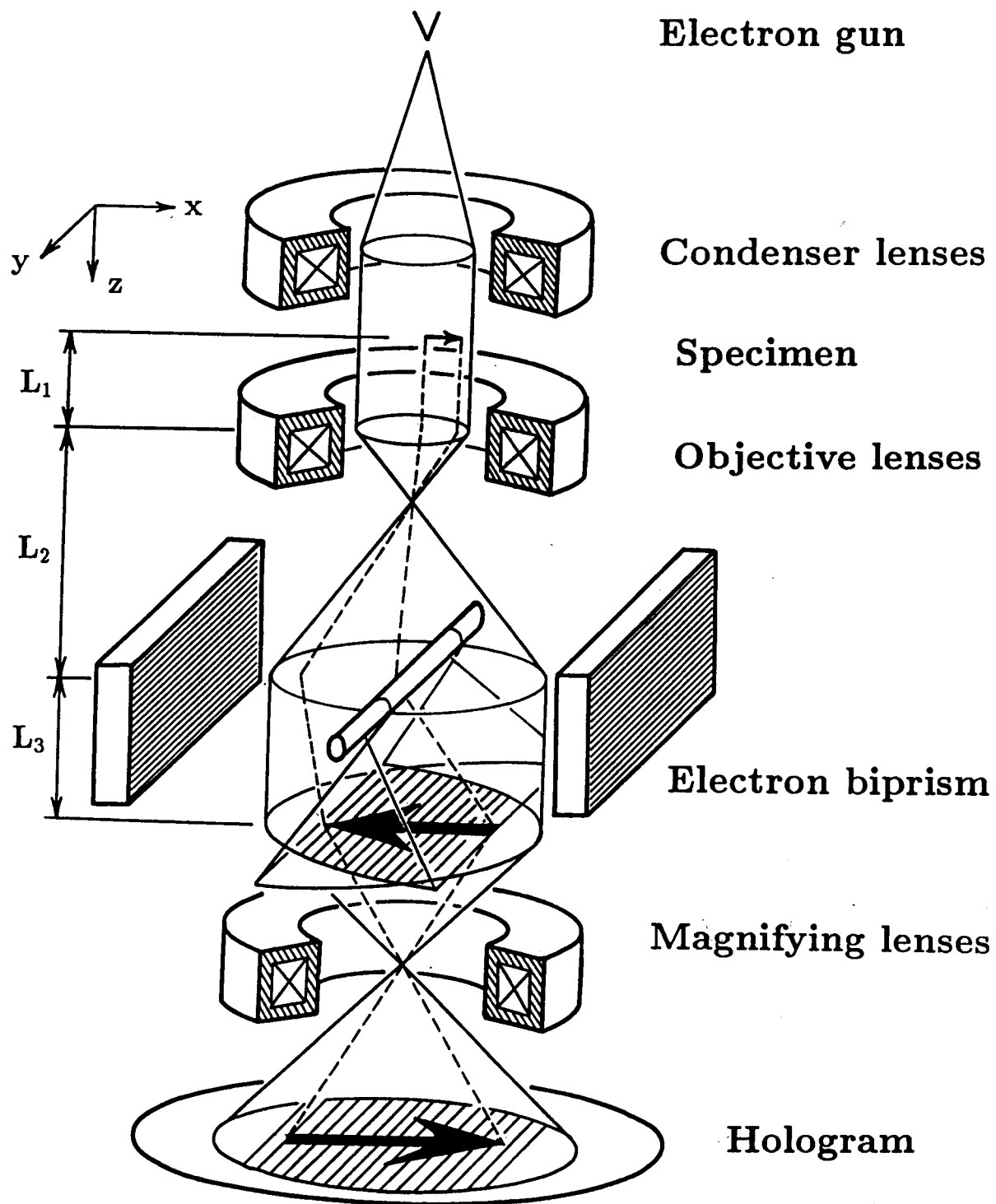


Fig. 2.5. Electron-optical system in the holography electron microscope. Using a coherent electron wave emitted from a cold field-emission type electron gun, an off-axis hologram is made by a Möllenstedt-Dücker type electron biprism.

(reference wave). The electron biprism is installed between the objective lens and its image plane. On the image plane of the lens, the object wave and the reference wave overlap and interfere with each other to get an interference fringe pattern as well as an in-focused image of the sample. This pattern is next magnified by a subsequent lens system to be recorded on a photographic film. This is an off-axis hologram.

Figure 2.6 illustrates the wave propagation from the specimen plane to the image plane of the objective lens in the microscope. The wavefront of the object wave transmitted through the sample is deformed, and carries the information of the sample. The reference wave passes through the specimen plane in the form of a plane wave. Traveling through the objective lens, the wavefronts are reconstructed on the image plane of the lens. The wavefronts of the object and reference waves, however, are slightly inclined with opposite directions, because of the electron biprism action. The intersecting lines between the two wavefronts are recorded as interference fringes on a hologram. In this way, the phase distribution of the object electron wave, or the 3D form of its wavefront is recorded on the hologram.

Let us describe the wave propagation above mentioned by the Fresnel diffraction formula [2.10]. The distances from the specimen plane to the objective lens, from the objective lens to the biprism, and from the biprism to the image plane are designated by L_1 , L_2 , L_3 , respectively (see Fig. 2.5). I set the optical axis along the z -axis, and the biprism filament parallel to the y -axis. I denote the transmission functions of the specimen, the objective lens, and the biprism as $\psi(x, y)$, $Q_L(x, y)$, and $Q_B(x, y)$, respectively. $\psi(x, y)$ contains the information on the specimen. For simplicity, I assume the objective lens as an ideal thin lens with the focal length f , which is a planar object having the transmission function

$$Q_L(x, y) = \exp\{-ik(x^2 + y^2)/2f\}, \quad (12)$$

where k is the wave number of electron waves. The transmission function of the biprism $Q_B(x, y)$ is given by Eq. (11).

The electron wave propagation is, in general, represented by Huygens' Principle, which is expressed by the Kirchhoff formula. From the general Kirchhoff formula, it is possible to derive relatively simple forms, the Fresnel diffraction formula, appropriate to the

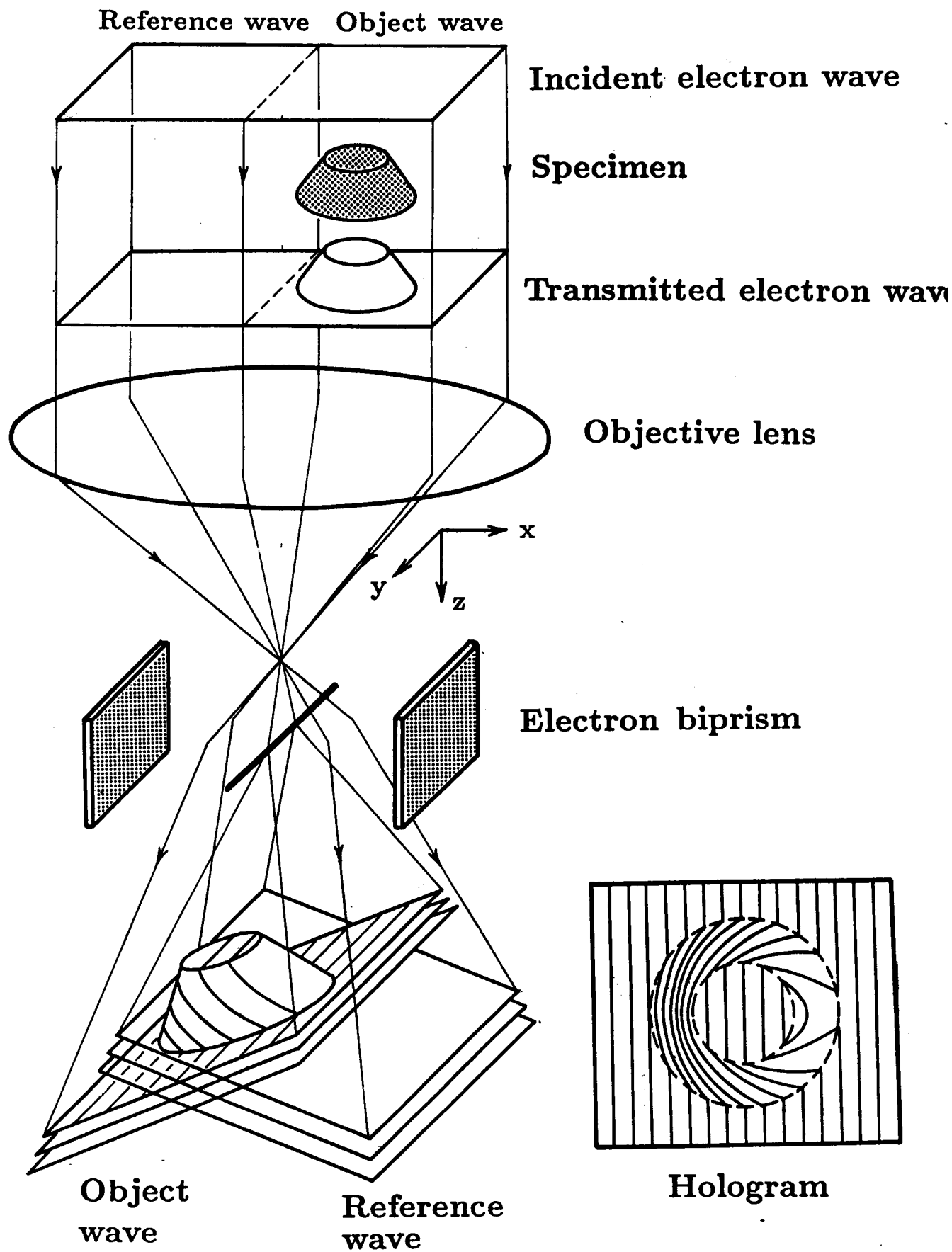


Fig. 2.6. Schematic illustration of the electron wave propagation from the specimen plane to the image plane of the objective lens in the microscope.

conditions which typify electron diffraction, i.e., the angle of deflection is small. In this approximation, wave propagation through the distance R in vacuum is given by convolution with a propagation function $P_R(x, y)$ [2.10],

$$P_R(x, y) = \frac{i}{R\lambda} \exp\{i\vec{k} \cdot \vec{R}\} \cdot \exp\{ik(x^2 + y^2)/2R\}. \quad (13)$$

When an incident plane wave $\Psi_0(x, y, z) = \exp\{ikz\}$ transmits through the specimen, the wavefunction becomes $\psi(x, y)\Psi_0(x, y, z)$. When this transmitted wave reaches the object lens, it is expressed by

$$[\psi(x, y) \Psi_0(x, y, z)] * P_{L_1}(x, y), \quad (14)$$

which is explicitly given by a convolution;

$$\int_{-\infty}^{\infty} dX \int_{-\infty}^{\infty} dY \psi(X, Y) \Psi_0(X, Y, z) P_{L_1}(x - X, y - Y). \quad (15)$$

Next, this wave transmits through the lens, and is modulated to be

$$Q_L(x, y)[[\psi(x, y) \Psi_0(x, y, z)] * P_{L_1}(x, y)]. \quad (16)$$

And then, after propagation through the distance L_2 to the biprism, the wave becomes

$$[Q_L(x, y)[[\psi(x, y) \Psi_0(x, y, z)] * P_{L_1}(x, y)]] * P_{L_2}(x, y). \quad (17)$$

Transmitting through the biprism, moreover, the wave changes to be

$$Q_B(x, y)[[Q_L(x, y)[[\psi(x, y) \Psi_0(x, y, z)] * P_{L_1}(x, y)]] * P_{L_2}(x, y)] \quad (18)$$

Finally, after propagating through the distance L_3 from the biprism, the wave $\Psi(x, y, z)$, reached on the image plane, is given by

$$\Psi(x, y, z) = [Q_B(x, y)[[Q_L(x, y)[[\psi(x, y) \Psi_0(x, y, z)] * P_{L_1}(x, y)]] * P_{L_2}(x, y)]] * P_{L_3}(x, y), \quad (19)$$

which is explicitly written by

$$\begin{aligned} \Psi(x, y, z) = & \iiint \iiint \int_{-\infty}^{\infty} d\xi d\eta d\omega d\zeta d\sigma d\varepsilon Q_B(\sigma, \varepsilon) \cdot Q_L(\omega, \zeta) \cdot \psi(\xi, \eta) \cdot \Psi_0(\xi, \eta, z) \\ & \cdot P_{L_1}(\omega - \xi, \zeta - \eta) \cdot P_{L_2}(\sigma - \omega, \varepsilon - \zeta) \cdot P_{L_3}(x - \sigma, y - \varepsilon). \end{aligned} \quad (20)$$

Inserting each function, Eqs. (11), (12), and (13), I get

$$\Psi(x, y, z) \propto \left\{ \int_{-\infty}^{-\rho_1} d\sigma \exp(ik\delta\sigma) + \int_{\rho_1}^{\infty} d\sigma \exp(-ik\delta\sigma) \right\} \iiint \int_{-\infty}^{\infty} d\xi d\eta d\omega d\zeta d\varepsilon \psi(\xi, \eta) \cdot \Psi_0(\xi, \eta, z) \cdot \exp[-ik \left\{ \frac{(\omega - \xi)^2 + (\zeta - \eta)^2}{2L_1} + \frac{(\sigma - \omega)^2 + (\varepsilon - \zeta)^2}{2L_2} + \frac{(x - \sigma)^2 + (y - \varepsilon)^2}{2L_3} - \frac{\omega^2 + \zeta^2}{2f} \right\}]. \quad (21)$$

After short calculation utilizing the relation $1/f = 1/L_1 + 1/(L_2 + L_3)$, and the image magnification $M = (L_2 + L_3)/L_1$, I finally obtain

$$\Psi(x, y, z) \propto \Psi_l(x, y, z) + \Psi_r(x, y, z) + (\text{diffraction terms from the biprism wire}), \quad (22)$$

where

$$\Psi_l(x, y, z) = \psi\left(-\frac{x}{M} + \frac{L_3\delta}{M}, -\frac{y}{M}\right) \exp\left\{ik\left(\frac{L_2M}{L_1L_3} - \frac{1}{L_1}\right)\frac{L_3\delta}{M^2}x + ikz\right\} \quad (23)$$

comes from the first integral with σ ($-\infty \sim -\rho_1$) in Eq. (21), and

$$\Psi_r(x, y, z) = \psi\left(-\frac{x}{M} - \frac{L_3\delta}{M}, -\frac{y}{M}\right) \exp\left\{-ik\left(\frac{L_2M}{L_1L_3} - \frac{1}{L_1}\right)\frac{L_3\delta}{M^2}x + ikz\right\} \quad (24)$$

comes from the second integral with σ ($\rho_1 \sim \infty$) in Eq. (21). $\Psi_l(x, y, z)$ and $\Psi_r(x, y, z)$ indicate the waves passing through the left and right sides of the biprism wire, respectively.

This result shows, first, that the wavefunction on the image plane is the in-focused image of the specimen magnified by $-M$ times, and second, that Ψ_l and Ψ_r are the original wavefunction $\psi(-\frac{x}{M}, -\frac{y}{M}) e^{ikz}$ displaced in the x -direction with the distance $\frac{L_3\delta}{M}$ in the opposite direction with each other. Third, the phase factors proportional to x -coordinate in Eqs. (23) and (24) indicate the wavefront inclination, of which directions are also opposite between Ψ_l and Ψ_r . These results are sketched in Fig. 2.6.

In the usual experiment to record an off-axis hologram, the specimen is set on a half ($x \geq 0$) of the specimen plane (see Fig. 2.6). So the wave, passed through the region $x \geq 0$, becomes an object wave $\psi(x, y)e^{ikz}$, and the wave in the region $x \leq 0$ becomes a reference wave e^{ikz} . Which side of the biprism wire the object wave passes, depends on the position of the biprism. When the biprism is placed above the backfocal plane of the object lens, i.e., $L_2 < f$ (Fig. 2.7(a)(b)), the object wave passes through the right side of the biprism wire. That is, from Eqs. (23) and (24),

$$\Psi_l(x, y, z) = \exp\left\{ik\left(\frac{L_2M}{L_1L_3} - \frac{1}{L_1}\right)\frac{L_3\delta}{M^2}x + ikz\right\},$$

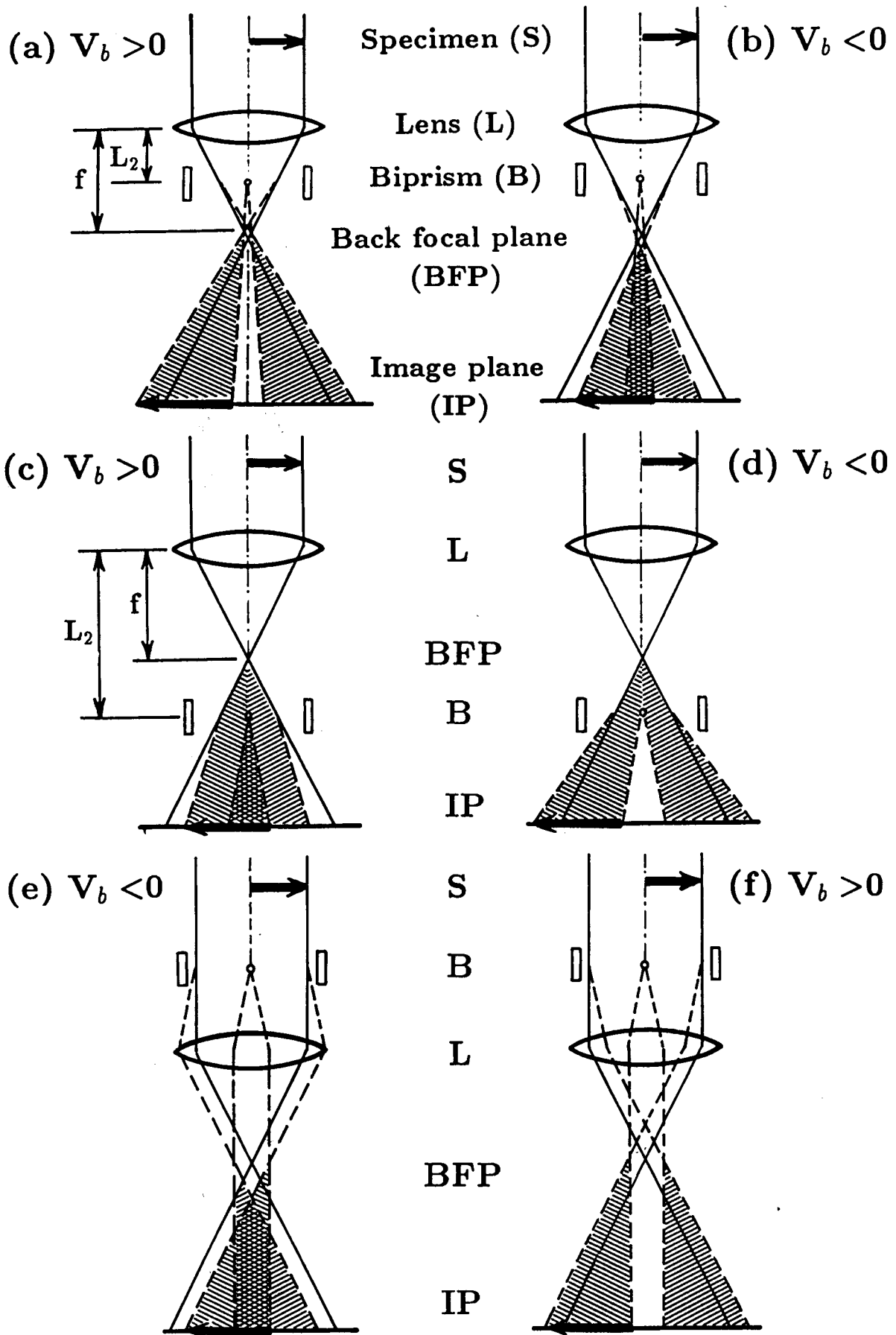


Fig. 2.7. The electron biprism action depends on the position of the biprism. For an electron interferometer, a proper voltage (V_b) must be applied to the central thin wire of the biprism.

$$\Psi_r(x, y, z) = \psi\left(-\frac{x}{M} - \frac{L_3\delta}{M}, -\frac{y}{M}\right) \exp\left\{-ik\left(\frac{L_2M}{L_1L_3} - \frac{1}{L_1}\right)\frac{L_3\delta}{M^2}x + ikz\right\}. \quad (25)$$

Moreover, the phase factor $\left(\frac{L_2M}{L_1L_3} - \frac{1}{L_1}\right)$ in Eq. (25) is negative in this case. Consequently, the object and reference waves are overlapped with each other when $\delta < 0$ (or $V_b < 0$) (Fig. 2.7(b)), and are separated when $\delta > 0$ (or $V_b > 0$) (Fig. 2.7(a)).

In the case that the biprism is set below the backfocal plane of the objective lens, i.e., $L_2 > f$ (Fig. 2.7(c)(d)), Ψ_r and Ψ_l are interchanged. Since the phase factor $\left(\frac{L_2M}{L_1L_3} - \frac{1}{L_1}\right)$ becomes positive in this case, the overlapping between the two waves occurs if $\delta > 0$ ($V_b > 0$). When I place the biprism just on the back focal plane, the biprism does not work as an interferometer. The central thin wire may be broken by an intense electron irradiation in this case.

The diffraction effect from the central wire of the biprism is negligibly small in the region $|x| \gg \rho_1$, and in fact, we use such a region to record a hologram. For realizing such a condition, I have to keep the biprism away from the backfocal plane of the objective lens, and apply a higher voltage to the biprism. From Eqs. (22) and (25), therefore, the intensity distribution $I(x, y)$ of the hologram, which is the only one that we can record on a photographic film, is simply given by

$$\begin{aligned} I_{hol}(x, y) &= |\Psi(x, y, z)|^2 \\ &= |\Psi_l(x, y, z)|^2 + |\Psi_r(x, y, z)|^2 + \Psi_l(x, y, z)\Psi_r^*(x, y, z) + \Psi_l^*(x, y, z)\Psi_r(x, y, z) \\ &= 1 + \left|\psi\left(-\frac{x}{M} - \frac{L_3\delta}{M}, -\frac{y}{M}\right)\right|^2 \\ &\quad + \psi^*\left(-\frac{x}{M} - \frac{L_3\delta}{M}, -\frac{y}{M}\right) \cdot \exp\left\{2ik\left(\frac{L_2M}{L_1L_3} - \frac{1}{L_1}\right)\frac{L_3\delta}{M^2}x\right\} \\ &\quad + \psi\left(-\frac{x}{M} - \frac{L_3\delta}{M}, -\frac{y}{M}\right) \cdot \exp\left\{-2ik\left(\frac{L_2M}{L_1L_3} - \frac{1}{L_1}\right)\frac{L_3\delta}{M^2}x\right\} \end{aligned} \quad (26)$$

The second term indicates the magnified in-focused image of the specimen. A matter of course, the interference terms, the third and fourth terms, in Eq. (26) appear only when Ψ_l and Ψ_r overlap.

When there is no specimen, the transmission function $\psi(x, y) = 1$ and the intensity distribution on the hologram is, from Eq. (26)

$$I_{hol}(x, y) = 2 + 2 \cos\left\{2k\left(\frac{L_2M}{L_1L_3} - \frac{1}{L_1}\right)\frac{L_3\delta}{M^2}x\right\} \quad (27)$$

This is the fundamental fringes (carrier fringes), spacing $\pi/\{k(\frac{L_2M}{L_1L_3} - \frac{1}{L_1})\frac{L_3\delta}{M^2}\}$, on the hologram. This is regarded as an equi-spacing parallel *grating*.

When the specimen is placed only in the region $x \geq 0$, and its transmission function $\psi(x, y)$ is given by its amplitude transmittance $|\psi(x, y)|$ and its phase $\phi(x, y)$;

$$\psi(x, y) = |\psi(x, y)| \exp\{i\phi(x, y)\}, \quad (28)$$

then, the intensity distribution of the hologram Eq. (26) is given by

$$I_{hol}(x, y) = 1 + \left| \psi\left(-\frac{x + L_3\delta}{M}, -\frac{y}{M}\right) \right|^2 + 2 \cdot \left| \psi\left(-\frac{x + L_3\delta}{M}, -\frac{y}{M}\right) \right| \cdot \cos\left\{\phi\left(-\frac{x + L_3\delta}{M}, -\frac{y}{M}\right) + 2k\left(\frac{L_2M}{L_1L_3} - \frac{1}{L_1}\right)\frac{L_3\delta}{M^2}x\right\}. \quad (29)$$

This shows that the spacing of the fundamental fringes Eq. (27) is modulated by $\phi(x, y)$, the phase of the transmission function of the sample, or the phase distribution of the object wave. The hologram, in this way, contains the phase distribution $\phi(x, y)$ in the form of bendings of the interference fringes, as well as the amplitude distribution $|\psi(x, y)|$ of the object wave (see Fig. 2.6).

In the case of the electron optics in which the biprism is installed between the specimen and the objective lens, as shown in Fig. 2.7(e)(f), the similar results can be derived.

When we observe the electromagnetic fields spreading in vacuum, the transmission function Eq. (28) of the investigated sample region has only the phase factor, a pure phase object;

$$\psi(x, y) = \exp\{i\phi(x, y)\}, \quad (30)$$

because the electromagnetic fields modulate only the phase of electron waves. Then, the intensity distribution of the hologram Eq. (29) is given by

$$I_{hol}(x, y) = 2 + 2 \cdot \cos\left\{\phi\left(-\frac{x + L_3\delta}{M}, -\frac{y}{M}\right) + 2k\left(\frac{L_2M}{L_1L_3} - \frac{1}{L_1}\right)\frac{L_3\delta}{M^2}x\right\}. \quad (31)$$

For the purpose of this thesis, analysis of magnetic fields in vacuum, it is enough to treat the hologram Eq. (31) instead of a general expression Eq. (29).

In the case of a sample, of which scattering power for electron beams is weak, i.e., transparent for electrons, such as very thin specimens or biological specimens, its transmission function is also approximated by Eq. (30), and therefore, the contrast is hard to

observe in the conventional electron micrograph. However, phase contrast can be utilized for observation of such a sample using the hologram Eq. (31).

2.5 Wavefront reconstruction

2.5.1 Interference micrographs

Although the phase distribution $\phi(x, y)$ of the electron wave passed through the sample region is recorded on the hologram as Eq. (31), we can not read out the phase information directly from it, because the interference fringes in the hologram are very fine ($\sim 50\mu m$ -spacing) and not the contour phase lines. Therefore, I utilize a laser interferometer to visualize the phase distribution as contour phase lines.

For simplicity, I reset a magnified (x, y) -coordinate system on the hologram and denote the intensity distribution Eq. (31) as

$$I_{hol}(x, y) = 1 + \cos\left\{\phi(x, y) + \frac{2\pi x}{s}\right\}, \quad (32)$$

where $s = \pi\left\{k\left(\frac{L_2 M}{L_1 L_3} - \frac{1}{L_1}\right)\frac{L_3 \delta}{M^2}\right\}^{-1}$ is the carrier fringe spacing. After developing, fixing, and bleaching the hologram, I get a *phase hologram*, of which transmission function Q_H for *visible light* beams is given by

$$Q_H(x, y) = \exp\{iI_{hol}(x, y)\}, \quad (33)$$

where $I_{hol}(x, y)$ is expressed by Eq. (32). Using the identity of the Bessel function;

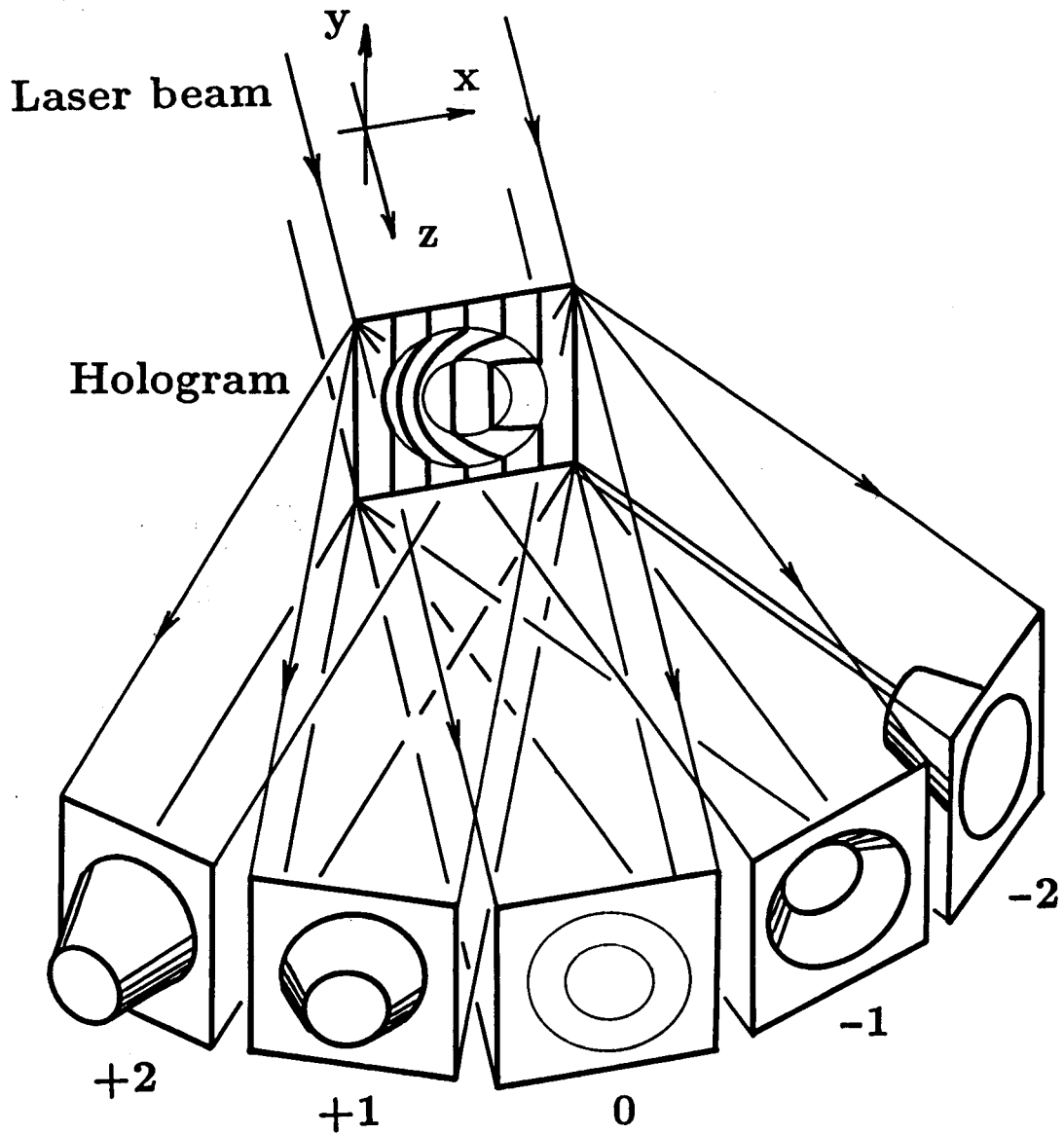
$$e^{ix \cdot \sin\theta} = \sum_{n=-\infty}^{\infty} J_n(z) e^{in\theta}, \quad (34)$$

and

$$J_{-n}(z) = (-1)^n J_n(z), \quad (35)$$

we can rewrite Eq. (33) as

$$\begin{aligned} Q_H(x, y) &= \text{const.} \cdot \sum_{n=-\infty}^{\infty} J_n(1) \exp\left[in\left\{\frac{\pi}{2} - \phi(x, y) - \frac{2\pi x}{s}\right\}\right] \\ &= \text{const.} \cdot [J_0(1) + iJ_1(1) \left[\exp\left\{i\left(\phi(x, y) + \frac{2\pi x}{s}\right)\right\} + \exp\left\{-i\left(\phi(x, y) + \frac{2\pi x}{s}\right)\right\}\right] \\ &\quad - J_2(1) \left[\exp\left\{2i\left(\phi(x, y) + \frac{2\pi x}{s}\right)\right\} + \exp\left\{-2i\left(\phi(x, y) + \frac{2\pi x}{s}\right)\right\}\right] + \dots] \end{aligned} \quad (36)$$



Reconstructed wavefronts

Fig. 2.8. When a laser beam illuminates a hologram, some diffracted waves as well as the transmitted wave emerge, because the carrier fringes on the hologram act as a grating. Although the transmitted wave is a plane wave, the diffracted waves have the same phase distribution, or wavefront as the original electron wave. The phase distribution of the higher-order diffracted waves are amplified by their orders. The conjugate waves also appear with the opposite diffraction angles.

As shown in Fig. 2.8, when a plane light wave $\Psi_{in}(x, y, z) = \exp\{iKz\}$ illuminates the bleached hologram with normal incidence using, say, a He-Ne laser beam (K is the wave number of the laser light), the wave emerging from the hologram is written as

$$Q_H(x, y)\Psi_{in}(x, y, z) \sim \Psi_0(x, y, z) + \Psi_{+1}(x, y, z) + \Psi_{-1}(x, y, z) + \Psi_{+2}(x, y, z) + \Psi_{-2}(x, y, z) + \dots, \quad (37)$$

where

$$\Psi_0(x, y, z) = J_0(1)\exp[iKz], \quad (38)$$

$$\Psi_{+1}(x, y, z) = iJ_1(1)\exp\left[i\left\{\phi(x, y) + \frac{2\pi x}{s} + Kz\right\}\right], \quad (39)$$

$$\Psi_{-1}(x, y, z) = iJ_1(1)\exp\left[i\left\{-\phi(x, y) - \frac{2\pi x}{s} + Kz\right\}\right], \quad (40)$$

$$\Psi_{+2}(x, y, z) = -J_2(1)\exp\left[i\left\{2\phi(x, y) + \frac{4\pi x}{s} + Kz\right\}\right], \quad (41)$$

$$\Psi_{-2}(x, y, z) = -J_2(1)\exp\left[i\left\{-2\phi(x, y) - \frac{4\pi x}{s} + Kz\right\}\right]. \quad (42)$$

This result shows that the phase hologram Eq. (33) acts as a nonlinear grating and produces some diffracted waves $\Psi_{\pm n}$ besides a transmitted wave Ψ_0 as shown in Fig. 2.8. The transmitted wave Eq. (38) is a plane wave, emerging along the z -axis. The 1st-order diffracted wave Eq. (39) propagates in the direction with an off-angle θ from the z -axis, $\theta = \arcsin\left(\frac{2\pi}{Ks}\right)$, and has the phase distribution $\phi(x, y)$. The -1st-order diffracted wave Eq. (40) propagates with a diffraction angle $-\theta$, opposite direction of that of Ψ_{+1} , and has a conjugated phase $-\phi(x, y)$. The diffraction angle and phase shifts of the ± 2 nd-order diffracted waves, Eqs. (41) and (42), are twice of those of the ± 1 st-order diffracted waves.

In this way, the phase distribution $\phi(x, y)$ of the object electron wave is faithfully transferred into the light wave through an intermediate medium, a hologram. Then, various laser interferometric techniques can be utilized for analyzing the phase distribution $\phi(x, y)$ of the diffracted laser wave. This is an ingenious idea of holography by Gabor.

In our experiment, the hologram is set in a Twyman-Green type laser interferometer as shown in Fig. 2.9. A He-Ne laser beam is divided into two waves by a beam splitter. Each wave is reflected by the mirrors A and B , and illuminates the hologram. Two series

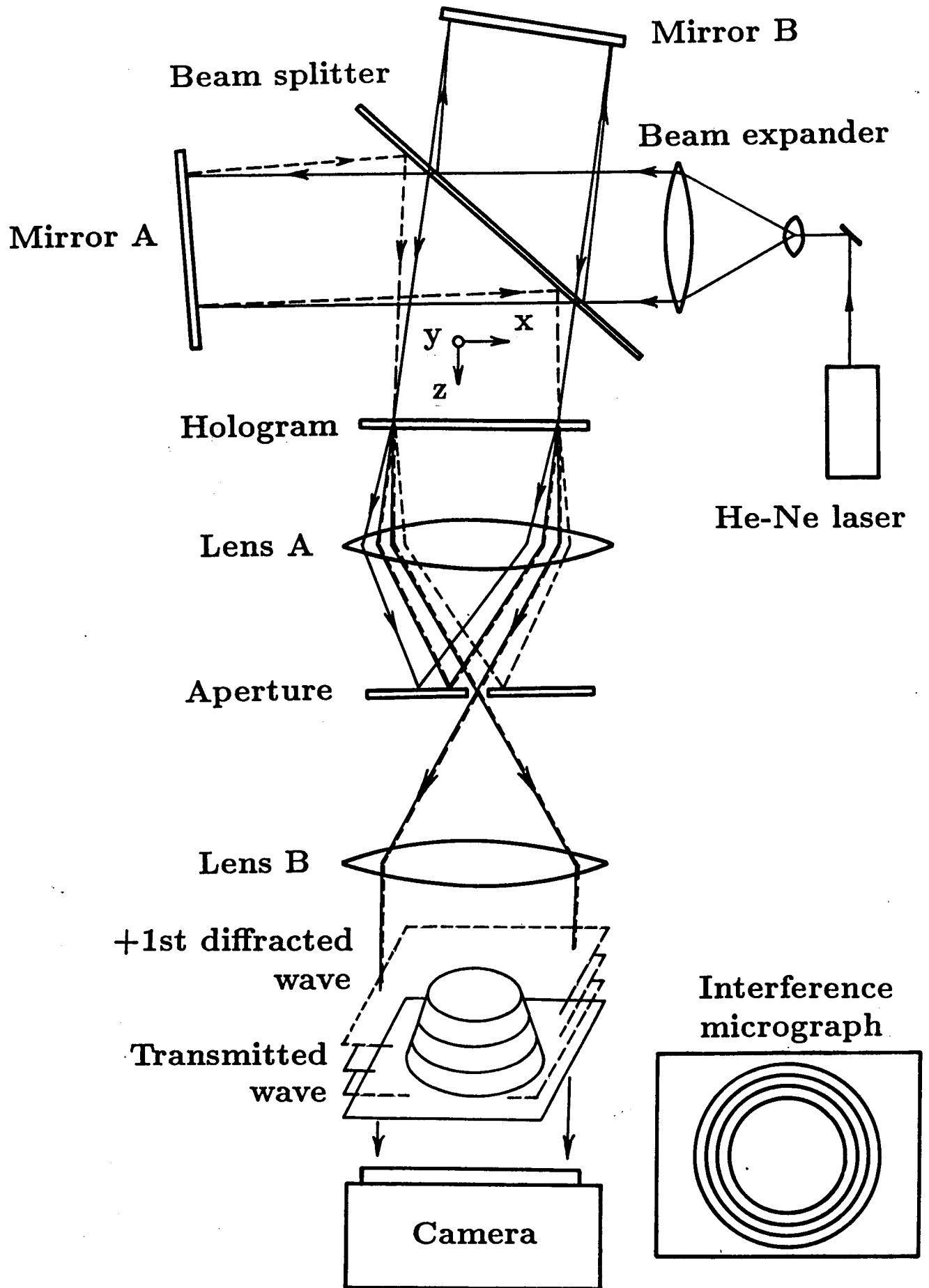


Fig. 2.9. Optical reconstruction setup, a Twyman-Green-type laser interferometer, which enables one to obtain an interference micrograph.

of the emerging waves Eqs. (37)~(42) from the hologram appear for the two illuminating waves. When the illuminating wave A , coming from the mirror A , irradiates the hologram with normal incidence, only the transmitted wave Eq. (38) can pass through the aperture and reach the image plane of the TV camera, which is written as

$$\Psi_A(x, y, z) = J_0(1) \exp\{iKz\}. \quad (43)$$

On the other hand, when, by inclining the mirror B , the illuminating wave B , coming from the mirror B , irradiates the hologram with the off-angle $\theta = \arcsin(\frac{2\pi}{K})$ from the normal incidence, only the 1st diffracted wave Eq. (39) can pass through the aperture and reach the TV camera, which is expressed as

$$\Psi_B(x, y, z) = iJ_1(1) \exp[i\{\phi(x, y) + Kz\}]. \quad (44)$$

The two waves, Ψ_A and Ψ_B interfere with each other, and its interference pattern

$$\begin{aligned} I(x, y) &= |\Psi_A(x, y, z) + \Psi_B(x, y, z)|^2 \\ &= J_0(1)^2 + J_1(1)^2 + J_0(1)J_1(1)\sin\{\phi(x, y)\} \end{aligned} \quad (45)$$

is recorded on the image plane of the TV camera. The interference fringes in this pattern appear with 2π -phase interval, i.e., the carrier fringes are removed and only the contour phase lines of the phase distribution $\phi(x, y)$ appear. The interference pattern Eq. (45) is called "an *interference micrograph*". The phase distribution of the original electron wave transmitted through the sample region is visualized in this way.

2.5.2 Phase-difference amplification

Although the interference micrograph Eq. (45) shows the phase distributions of an electron wave in units of 2π , it is inadequate for observation with higher phase precision. Especially, when the phase modulation is less than 2π in the case of observation of, say, very weak magnetic fields, the interference micrograph shows "zero-fringe pattern", so that the phase distribution can not be accurately displayed. For these reasons, some techniques have been developed to get a "phase-difference amplified" interference micrograph using the unique features of hologram, i.e. the amplification and conjugation of phase. The micrograph is an interference pattern drawn in units of $\frac{2\pi}{n}$ (n is an integer up to ~ 30) in

which finer phase modulations can be visualized. There are two methods for the phase-difference amplification; one employs a higher-order diffracted waves and their conjugates Eqs. (39)~(42) (Fig. 2.10 (a)); another is longitudinally reversed shearing interferometry (Fig. 2.10 (b)).

By utilizing a pair of conjugate waves, ± 1 st waves Eqs. (39) and (40), the phase sensitivity can be made increase twice[2.11][2.12]. When, by inclining the mirror *A* in Fig. 2.9, the illuminating wave *A* is made to irradiate the hologram with the angle of $-\theta$ from the normal incidence, only the -1 st diffracted wave Eq. (40) can pass through the aperture and reach the camera;

$$\Psi_A(x, y, z) = iJ_1(1)\exp[i\{-\phi(x, y) + Kz\}] . \quad (46)$$

In this case, the interference pattern formed with the wave Ψ_B Eq. (44) becomes

$$\begin{aligned} I(x, y) &= |\Psi_A(x, y, z) + \Psi_B(x, y, z)|^2 \\ &= 2J_1(1)^2[1 + \cos\{2\phi(x, y)\}] . \end{aligned} \quad (47)$$

The interference fringes in this pattern are contour phase lines drawn in units of π . This is an interference micrograph with twice "phase-difference amplification".

The phase-difference amplification technique using higher-order diffracted waves from a phase hologram or a nonlinear hologram was developed in the optical interferometry [2.13][2.14]. When, by inclining the mirror *B* in Fig. 2.9, the illuminating wave *B* irradiates the hologram with the angle of 2θ from the normal incidence, only the 2nd diffracted wave Eq. (41) can pass through the aperture and propagates to the camera;

$$\Psi_B(x, y, z) = -J_2(1)\exp[i\{2\phi(x, y) + Kz\}] . \quad (48)$$

Then, the interference pattern formed with the wave Ψ_A Eq. (46) is given by

$$\begin{aligned} I(x, y) &= |\Psi_A(x, y, z) + \Psi_B(x, y, z)|^2 \\ &= J_1(1)^2 + J_2(1)^2 + 2J_1(1)J_2(1)\sin\{3\phi(x, y)\} . \end{aligned} \quad (49)$$

This is an interference micrograph with three-times phase-difference amplification, which shows the contour phase lines in units of $\frac{2\pi}{3}$.

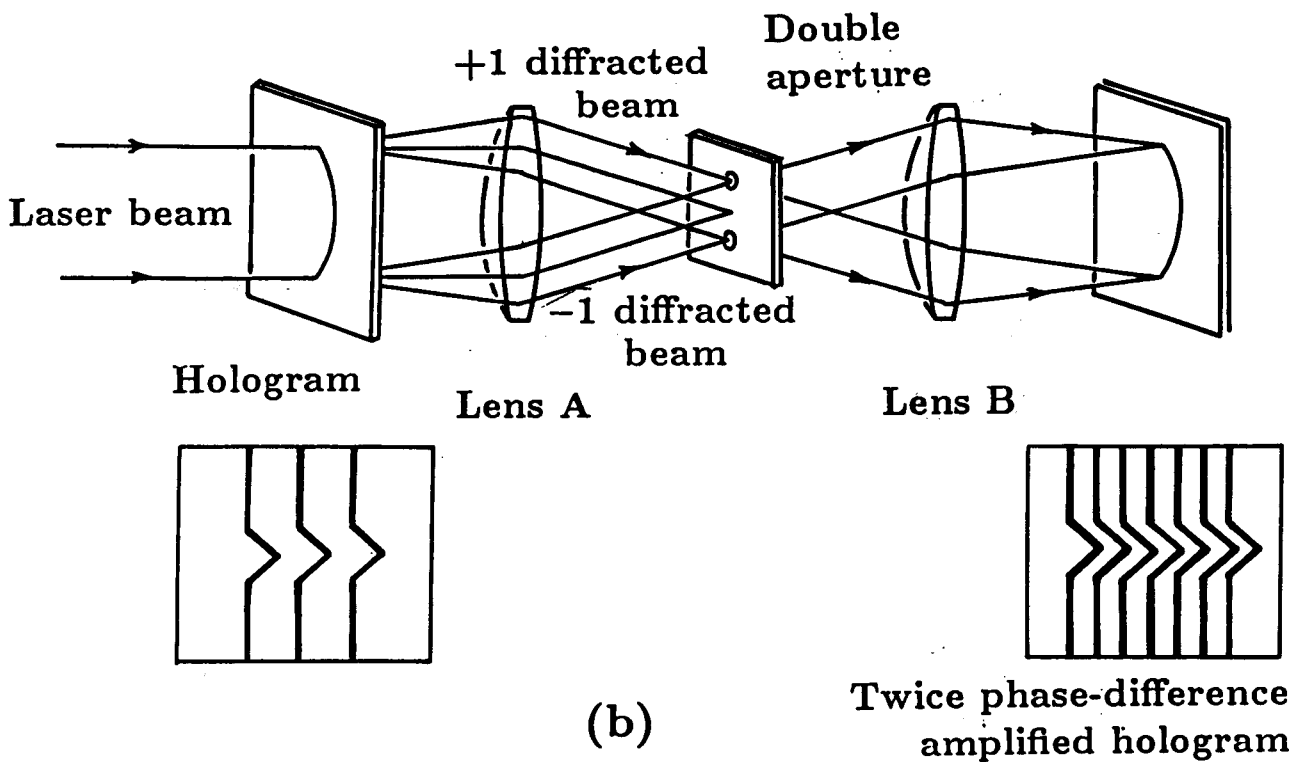
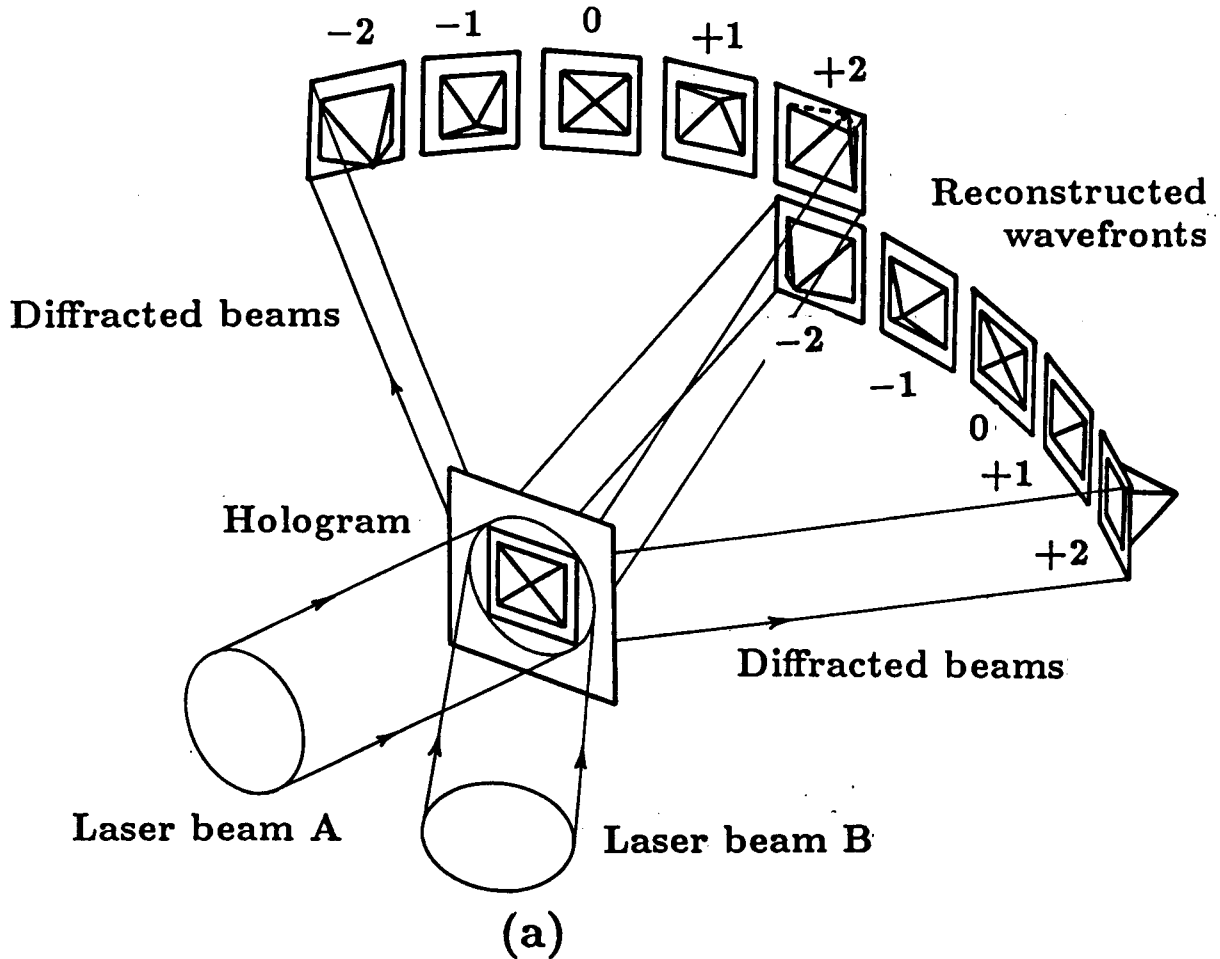


Fig. 2.10. Phase-difference amplification techniques. (a) A phase-difference amplified interference micrograph is obtained by interfering with higher-order diffracted waves and their conjugate waves emerging from a phase hologram. (b) A twice phase-difference amplified hologram is obtained by interfering with the ± 1 st diffracted waves from the original hologram (shearing interferometry).

In this way, using the $+n$ -th order and the $-m$ -th order diffracted waves from the phase hologram, we can obtain $(n + m)$ -times phase-difference amplified interference micrograph in which the contour phase lines in units of $\frac{2\pi}{(n+m)}$ can be drawn, and finer phase changes are visualized. The degree of phase-difference amplification hitherto obtained using this technique ranges up to approximately 30 [2.15]. In other words, contour fringes can be drawn at every $\frac{2\pi}{30}$ phase interval in the interference micrograph. The attainable degree of amplification by this method is primary limited by three factors; (1) diffraction efficiency to get enough intensity of higher-order diffracted waves, (2) distortion of the hologram causing aberrations in diffracted waves, and (3) speckle-pattern noise which is more distinguished in higher-order diffracted waves.

Another technique, longitudinally reversed shearing interferometry was first proposed by Bryngdahl [2.12] and developed by Matsuda *et al.* in the optical interferometry [2.16]. As shown in Fig. 2.10 (b), a collimated laser beam illuminates the hologram and only the ± 1 st diffracted waves are selected with an aperture of double holes situated at the back focal plane of Lens A. Then, a new hologram of twice-phase-difference amplification is formed and recorded on a photographic film.

Next, if, instead of the original hologram, the newly made twice-amplified hologram is set at the position of "Hologram" in the figure, a four-times-phase-difference amplified hologram is made. If this procedure is repeated n times, the degree of amplification increases up to 2^n times. In this method, the diffraction efficiency of the holograms less strictly limits the maximum degree of the phase-difference amplification compared with the higher-order diffraction method above mentioned, although it is much more laborious and time-consuming.

Some examples of phase-difference amplified interference micrographs are shown in Fig. 2.11 [2.17]. The sample is a beryllium fine particle of which three-dimensional shape is shown in Fig. 2.11(a). (b) is its reconstructed image which is equivalent to the conventional electron microscopic image. In the twice phase-difference amplified interference micrograph (d), the number of the fringes becomes doubled compared with the original interference micrograph (c), so that finer phase modulation can be visualized as contour phase lines. Although the 32-times amplified micrograph (e) shows very fine phase

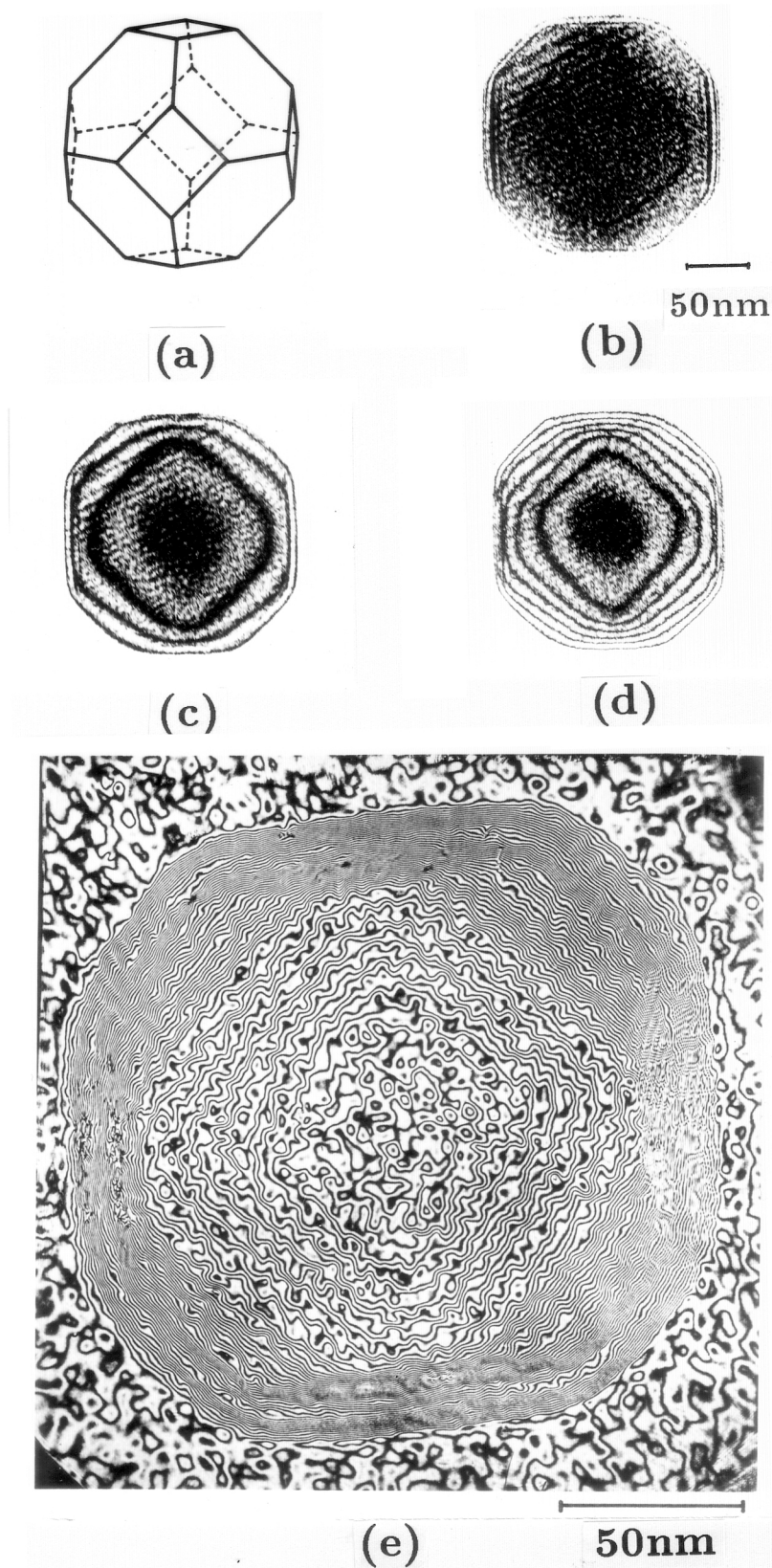


Fig. 2.11. As increasing the degree of the phase-difference amplification, smaller phase modulation, or finer 3D form of the sample, is revealed. The sample is beryllium fine particle. (a) Schematic of the 3D form of the particle. (b) Reconstructed image which is equivalent to the electron microscopic image. (c) Interference micrograph without amplification showing the interference fringes in 2π -phase interval. (d) Twice phase-difference amplified interference micrograph showing the fringes in π -phase interval. (e) 32-times amplified interference micrograph showing the fringes in $\frac{\pi}{16}$ -phase interval [2.17].

variation, speckle-pattern noise is distinguished.

2.6 The Aharonov-Bohm effect

Let us review the physical meaning of the phase factor $\phi(x, y)$ of the transmission function of the specimen Eq. (28), i.e. the phase distribution of the object electron wave. The wavefunction of an electron $\Psi(\vec{r}, t)$, in general, obeys the Schrödinger equation;

$$i\hbar \frac{\partial}{\partial t} \Psi(\vec{r}, t) = \left\{ \frac{1}{2m} \left(\frac{\hbar}{i} \vec{\nabla} + e\vec{A} \right)^2 - eV \right\} \Psi(\vec{r}, t) . \quad (50)$$

In the absence of the electromagnetic potentials \vec{A} and V , the wavefunction $\Psi_0(\vec{r}, t)$ satisfies the free electron's Schrödinger equation;

$$i\hbar \frac{\partial}{\partial t} \Psi_0(\vec{r}, t) = -\frac{\hbar^2}{2m} \vec{\nabla}^2 \Psi_0(\vec{r}, t) , \quad (51)$$

of which solution is a plane wave. The solution of Eq. (50), $\Psi(\vec{r}, t)$, is written as, using the free electron's wavefunction,

$$\Psi(\vec{r}, t) = \Psi_0(\vec{r}, t) \cdot \exp\{i\phi(\vec{r})\} , \quad (52)$$

where the phase factor $\phi(\vec{r})$ is given by

$$\phi(\vec{r}) = -\frac{e}{\hbar} \int (V \cdot dt - \vec{A} \cdot d\vec{r}) , \quad (53)$$

if the variations of the electromagnetic potentials are small enough for the WKB approximation to be valid. The integral goes along the path of the wavefront element of interest in space-time.

This result means that the phase of the illuminating electron wave, a plane wave, is modulated by the electromagnetic potentials during the passage through the sample region. This is the Aharonov-Bohm effect. In principle, therefore, we can derive the distributions of the electromagnetic fields from the phase $\phi(x, y)$ of the object wave recorded on a hologram. The phase we can measure is, in exact terms, the phase difference between the object and reference waves. The phase itself does not uniquely determined due to the arbitrariness in the electromagnetic potentials.

Good examples are shown in Fig. 2.12. Let us consider, at first, a non-magnetic

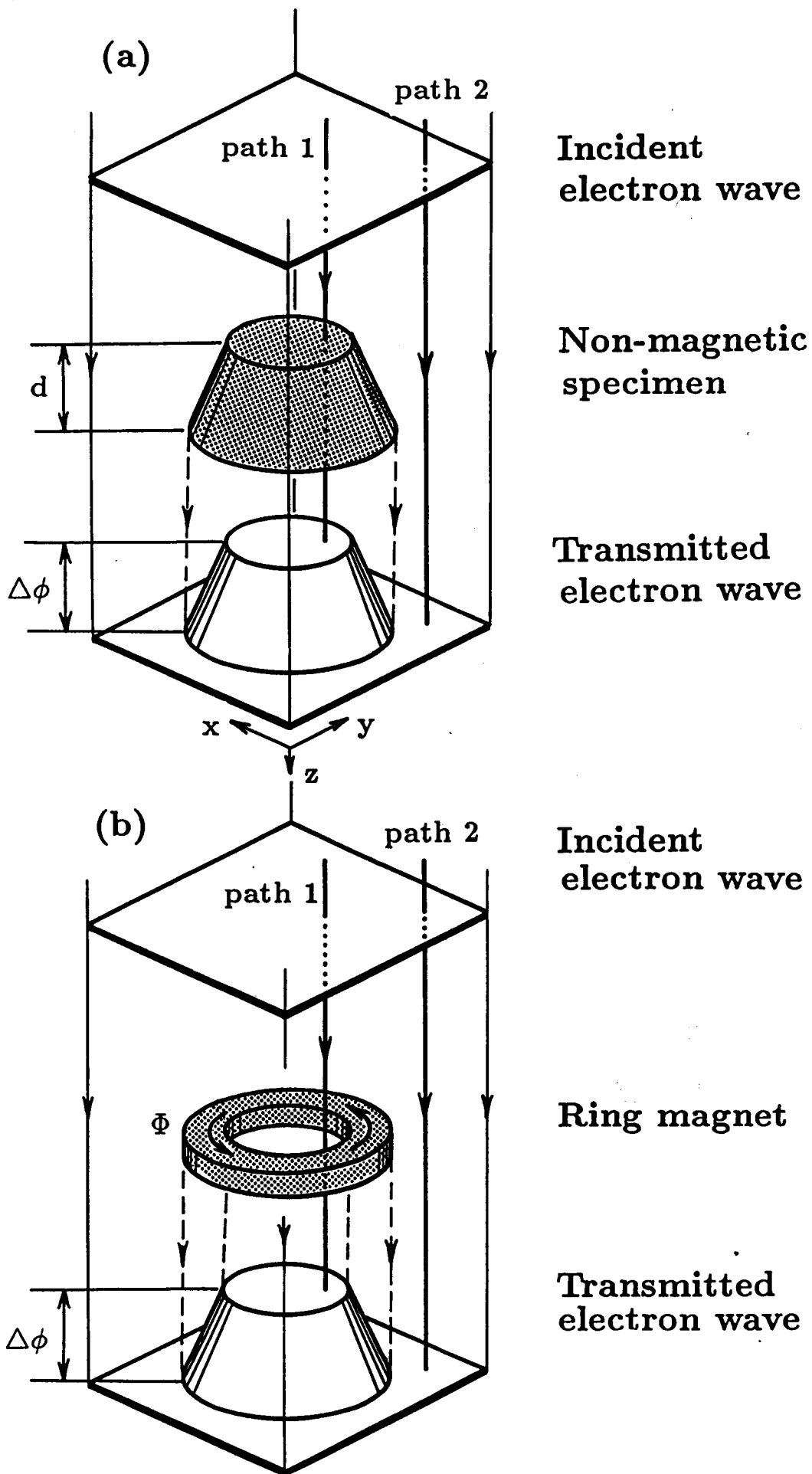


Fig. 2.12. Deformation of electron wavefront by a specimen. (a) In the case of a non-magnetic specimen, the phase shift is proportional to the thickness of the specimen. (b) In magnetic case, the phase shifts in proportion to the amount of the enclosed magnetic flux .

specimen which is truncated-cone-shaped with the height d , as shown in Fig. 2.12 (a). The phase difference $\Delta\phi$ between the transmitted wavefront elements, of which paths are path 1 and path 2 shown in this figure, is given by, from Eq. (53),

$$\Delta\phi = -\frac{e}{\hbar} \left\{ \int_{\text{path 1}} V dt - \int_{\text{path 2}} V dt \right\}. \quad (54)$$

The electrostatic potential V exists only inside the specimen, of which mean inner potential is $-V_0$. Then,

$$\Delta\phi = \frac{e}{\hbar} V_0 \cdot \Delta\tau, \quad (55)$$

where $\Delta\tau$ is the transient time for the electron passing through the specimen, and given with the electron velocity v as $\Delta\tau = d/v$ if we neglect the velocity change. Hence we get

$$\Delta\phi(x, y) = \frac{e}{\hbar} V_0 \frac{d(x, y)}{v}, \quad (56)$$

which implies that the phase shift $\Delta\phi(x, y)$ of the transmitted wave is proportional to the thickness of the specimen $d(x, y)$. When, therefore, we draw the contour phase lines of the transmitted wave, it is equivalent to the contour maps of the thickness distribution of the specimen. In other words, the 3D form of the specimen is revealed as a contour map in its interference micrograph. In the case of 100 kV-electron acceleration and $V_0 \sim 10$ V, the phase shift of 2π occurs for the thickness $d \sim 60$ nm. This sensitivity is not so high in spite of an extremely short wavelength of the electron beam. This is because the inner potential of materials is too small compared with the electron acceleration voltage.

More generally, in the case of observation of an electric field distribution $V(x, y, z)$, the phase distribution of the transmitted electron wave is expressed as

$$\phi(x, y) = -\frac{e}{\hbar} \frac{1}{v} \int_{-\infty}^{\infty} V(x, y, z) dz. \quad (57)$$

Here the electron propagates along the z -axis. For simplicity, $\phi(x, y)$ here denotes the phase difference between the object and the reference waves. Electric field vector \vec{E} can be, therefore, related to the phase distribution through the definition $\vec{E} = -\vec{\nabla} \cdot V$;

$$\frac{\partial\phi(x, y)}{\partial x} = \frac{e}{\hbar} \frac{1}{v} \int_{-\infty}^{\infty} E_x(x, y, z) dz, \quad (58)$$

$$\frac{\partial\phi(x, y)}{\partial y} = \frac{e}{\hbar} \frac{1}{v} \int_{-\infty}^{\infty} E_y(x, y, z) dz. \quad (59)$$

The magnetic case is illustrated in Fig. 2.12 (b). The specimen is a ring magnet, of which total magnetic flux is Φ . The thickness of the ring is ignored for simplicity. I take the path 1 passing through the inner hole of the ring, and the path 2 outside the ring. The phase difference between the wavefront elements traveled along each path is given by, from Eq. (53),

$$\Delta\phi = \frac{e}{\hbar} \left\{ \int_{\text{path 1}} \vec{A} \cdot d\vec{r} - \int_{\text{path 2}} \vec{A} \cdot d\vec{r} \right\}. \quad (60)$$

Since we can regard the starting and ending points of the paths 1 and 2 as the same point at infinite distance,

$$\Delta\phi = \frac{e}{\hbar} \oint \vec{A} \cdot d\vec{r}, \quad (61)$$

where the integral is performed along the closed path determined by the paths 1 and 2. According to the Stokes theorem and $\text{rot } \vec{A} = \vec{B}$ (\vec{B} is the magnetic flux density vector),

$$\Delta\phi = \frac{e}{\hbar} \int \vec{B} \cdot d\vec{S}, \quad (62)$$

where the surface integral is carried out over the surface bordered by the closed path. Consequently we get

$$\Delta\phi = \frac{e}{\hbar} \Phi = 2\pi \frac{\Phi}{(h/e)}. \quad (63)$$

This result is schematically shown in Fig. 2.13 (a). The magnetic flux Φ causes the phase shift $\Delta\phi$ between the electron wavefront elements passing through the either sides of the flux. In other words, this result is interpreted as that the contour phase lines with 2π -interval of the transmitted wavefunction directly show the *magnetic flux lines* in units of $\frac{h}{e}$ ($= 4.1 \times 10^{-15} \text{ Wb}$).

Mathematical expressions generally relating the phase distribution to the magnetic field distribution are given as follows. I set up a coordinate system as shown in Fig. 2.13 (b), in which the z -axis is parallel to the wave propagation. In the case of weak magnetic fields, the paths 1 and 2 can be regarded as straight lines passing through the points $(x, y, 0)$ and $(x + dx, y, 0)$, respectively, and parallel to the z -axis. Hence, $\Delta\phi$ in Eqs. (61)~(63) is written as $\frac{\partial\phi(x, y)}{\partial x} dx$, and the surface element $d\vec{S}$ in Eq. (62) points to the positive direction of the y -axis and $|d\vec{S}| = dx \cdot dz$. Equation (62) is consequently rewritten as

$$\frac{\partial\phi(x, y)}{\partial x} dx = \frac{e}{\hbar} dx \int_{-\infty}^{\infty} B_y(x, y, z) dz. \quad (64)$$

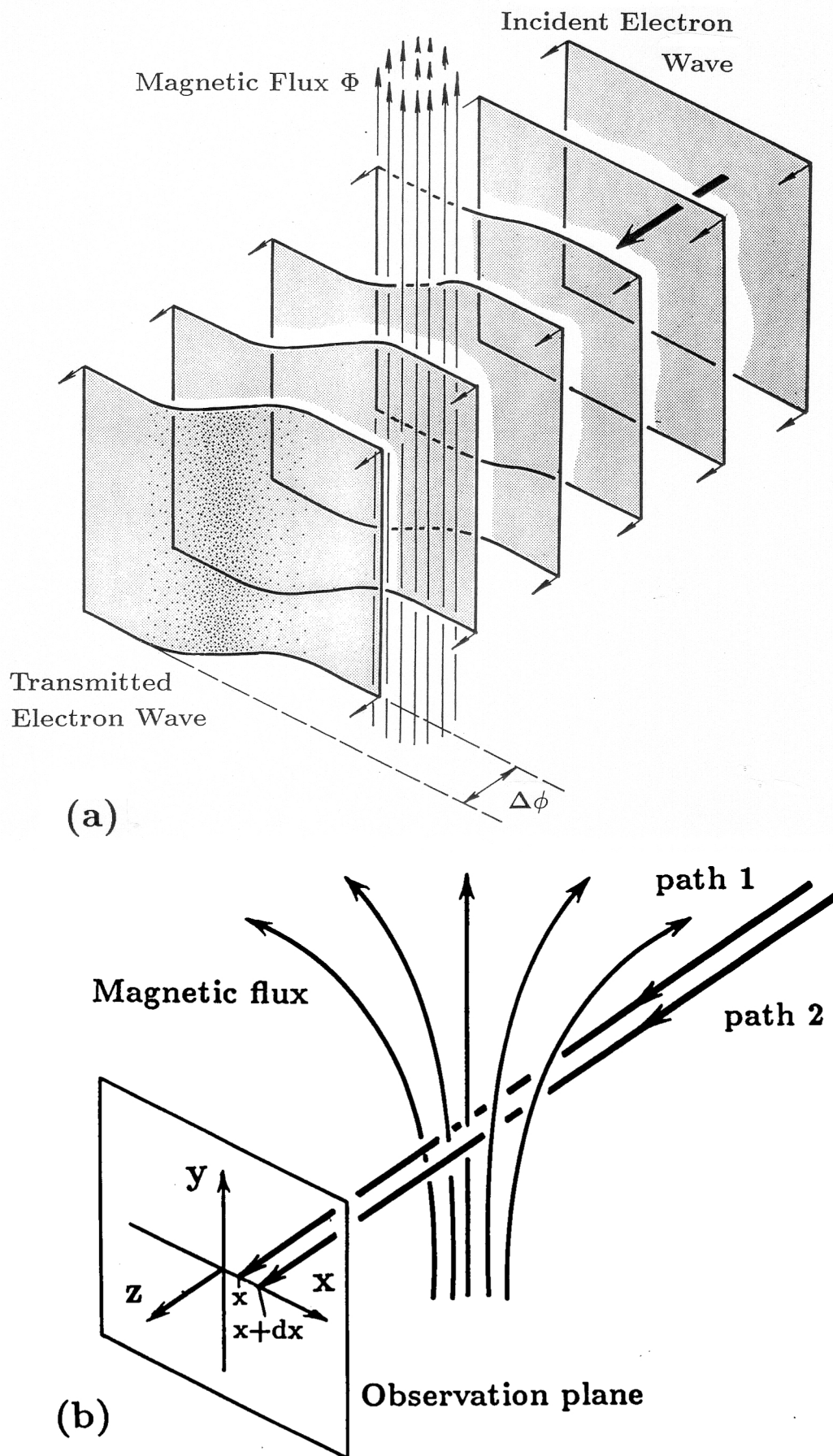


Fig. 2.13. (a) The Aharonov-Bohm effect predicts that the phase shift $\Delta\phi$ of the electron wavefront transmitted through the magnetic flux Φ is related by $\Delta\phi = 2\pi \frac{\Phi}{h/e}$. (b) Coordinate system for the mathematical expressions relating the electron phase and the magnetic field distributions.

We finally get

$$\frac{\partial\phi(x,y)}{\partial x} = \frac{e}{\hbar} \int_{-\infty}^{\infty} B_y(x,y,z)dz . \quad (65)$$

In the same way with the path 2 passing through the point $(x, y + dy, 0)$, we obtain

$$\frac{\partial\phi(x,y)}{\partial y} = -\frac{e}{\hbar} \int_{-\infty}^{\infty} B_x(x,y,z)dz . \quad (66)$$

The direction-of-view (z)-component of the field vector do not affect the phase distribution of the transmitted electron wave.

The phase distribution of the electron wave, in this way, directly related to the electromagnetic field distributions. We can obtain the line integrals of the field vector components along the direction of view from the electron phase information. Equations (58), (59), (65), and (66) will be utilized in Chapter 5 to obtain the field vector components themselves from the derivatives of the electron phase distribution.

Chapter 3

Fringe scanning interferometry

3.1 Introduction

Although the phase-difference amplification technique mentioned in the previous chapter considerably improve the phase sensitivity in the electron holographic observation, up to $\sim 2\pi/30$, so that finer phase shifts can be visualized, it has some disadvantages. (1) The phase sensitivity of the technique is sometimes insufficient for quantitative analysis of very small amounts of magnetic flux or biological specimens which cause only very small changes in electron phase. This inadequate phase sensitivity is due to that the phase information between two neighboring contour phase lines in the interference micrographs are ignored. (2) The technique needs laborious and time-consuming procedures which are far from real-time observation. (3) The interference micrograph for magnetic field observation only shows the flux flow, not distinguishes the direction of the flow. In other words, we can not determine the sign of the phase shift, or can not distinguish the advance or delay in electron wave propagation.

On the other hand, some methods for analyzing optical wavefronts with very high phase accuracy using digital image processing techniques have been recently developed in the field of optical interferometry. They are collectively called "subfringe interferometry" which enables the measurement of the phase variations between two neighboring fringes in interference fringe patterns. They have successfully applied for analyzing the aberrations of optical lenses, fine distortions of macroscopic objects, and others[3.1][3.2]. Since the subfringe interferometry can in principle be applied for the analysis of the optical wavefronts reconstructed from the electron hologram, I constructed a laser interferometer for the method and tried to analyze the electron holograms with it.

The fringe intensity distribution in a real interference micrograph is expressed by

$$I(x, y) = a(x, y) + b(x, y)\sin\{\phi(x, y)\} , \quad (67)$$

instead of Eq. (45), because the average intensity $a(x, y)$ and the fringe contrast $b(x, y)$ are not constant over the image due to the nonuniformity of the illuminating laser beams, nonlinearity of the photographic film, the intensity distribution of the object electron wave, the speckle noise, and others. The phase distribution $\phi(x, y)$ is, then, simply given by

$$\phi(x, y) = \arcsin\left[\frac{I(x, y) - a(x, y)}{b(x, y)}\right] \quad (68)$$

from the measured data of $I(x, y)$, $a(x, y)$, and $b(x, y)$. The high accuracy of the phase measurement, however, is not expected by this analysis method, because the measurement errors of $I(x, y)$, $a(x, y)$, and $b(x, y)$ may be considerable due to the nonlinearity of the TV camera, the speckle noise and others. This fact makes difficult to directly read out the phase distribution from the interference micrograph with high precision.

In the subfringe interferometry, the phase factor of the sine function in Eq. (67) is artificially made changed, so that only the phase $\phi(x, y)$ is separated from the average intensity $a(x, y)$ and fringe contrast $b(x, y)$. There are several kinds of methods in the subfringe interferometry; a) heterodyne interferometry[3.3], b) fringe scanning interferometry[3.4], c) phase-locked interferometry[3.5], d) Fourier transform method [3.6], and e) scanning Moire method [3.7]. In the first three methods, the phase factor of the sine function in Eq. (67) is made changed with time, while in the case of the last two method, the factor is made spatially changed.

Of these techniques, I have adopted the fringe scanning interferometry for the electron hologram analysis because of its high precision in the phase measurement, high spatial resolution, and quickness of the measurement. This method has been found to overcome the difficulties in the phase-difference amplification methods mentioned in the previous chapter. That is, it enables the numerical measurement of the subfringe phase distribution and greatly improve the phase sensitivity up to $\sim 2\pi/100$. The sign of the phase shift is also automatically determined. This method, moreover, remarkably reduced the analysis time compared with the phase-difference amplification method. This availability leads to

new analysis method such as computerized tomography with electron holography, which will be discussed in Chapter 5.

Section 3.2 is devoted to describing the principle and experimental set-up for the fringe scanning interferometry. The analysis procedure is explained in detail in Section 3.3. In Section 3.4, some examples of the electron hologram analysis with this method are shown, and its ability is discussed. The results are summarized in Section 3.5.

3.2 Principle and experimental set-up

Figure 3.1 shows the optical reconstruction system with the fringe scanning interferometry. The laser interferometer is the similar one as that in Fig. 2.9 with the exception that the mirror *A* is movable with a piezoelectric transducer (PZT). As in the case of Fig. 2.9, the illuminating wave *A*, coming from the mirror *A*, irradiates the hologram with normal incidence, and only the transmitted wave pass through the aperture, and finally reach the image plane of the TV camera;

$$\Psi_A(x, y, z) \sim \exp\{iKz\} . \quad (69)$$

If the mirror *A* shifts with the distance *l*, driven by the PZT,

$$\Psi_A(x, y, z; \delta) \sim \exp\{iKz - i\delta\} , \quad (70)$$

where $\delta = 2\pi \frac{2l}{\lambda}$ (λ is the wavelength of the He-Ne laser beam, 632.8 nm). On the other hand, when, by inclining the mirror *B*, the illuminating wave *B*, coming from the mirror *B*, irradiates the hologram with an angle θ from the normal incidence, only the +1st diffracted wave can pass through the aperture and reach the TV camera;

$$\Psi_B(x, y, z) \sim i \cdot \exp\{i\{\phi(x, y) + Kz\}\} . \quad (71)$$

Then, the interference fringe pattern Eq. (67) is modulated to be

$$\begin{aligned} I(x, y; \delta) &= |\Psi_A(x, y, z; \delta) + \Psi_B(x, y, z)|^2 \\ &= a(x, y) + b(x, y) \sin\{\phi(x, y) + \delta\} . \end{aligned} \quad (72)$$

This indicates that the fringes in the interference micrograph shift with the movement of the mirror *A*. The fringe scanning interferometry enables one to extract the phase

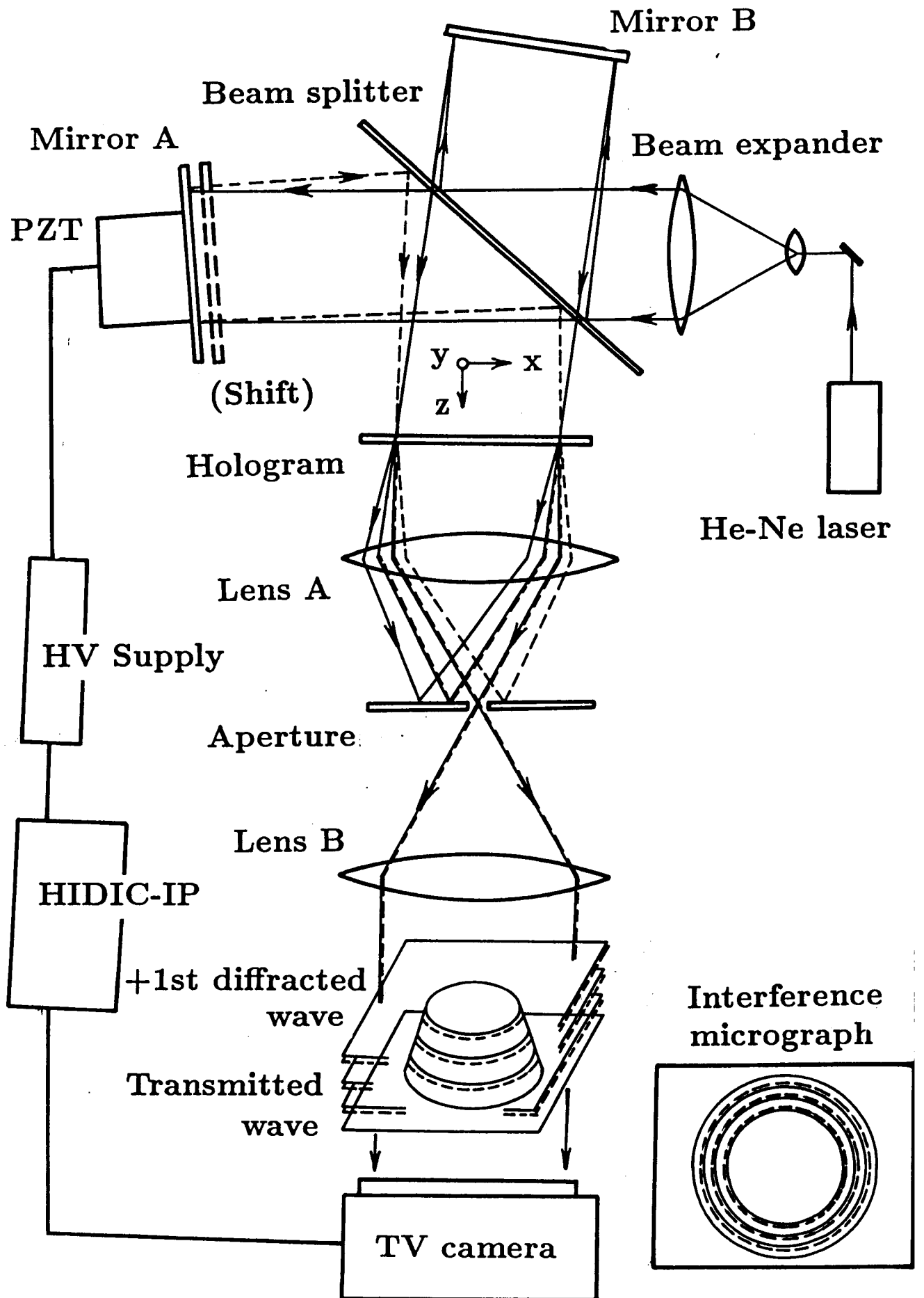


Fig. 3.1. Laser interferometer for the optical reconstruction with the fringe scanning interferometry. The interference micrographs are stored in a Hitachi image processing computer HIDIC-IP which also controls a high voltage (HV) supply to drive a piezoelectric transducer (PZT).

distribution $\phi(x, y)$ from several interference micrographs $I(x, y; \delta)$ with different values of δ 's. The intensity distribution Eq. (72) can be, in general, expressed as a Fourier series with δ ;

$$I(x, y; \delta_j) = \frac{a_0}{2} + \sum_{r=0}^{M-1} a_r \cos\{r\delta_j\} + \sum_{r=0}^{M-1} b_r \sin\{r\delta_j\}, \quad (73)$$

where

$$a_r = \frac{2}{M} \sum_{j=0}^{M-1} I(x, y; \delta_j) \cos\{r\delta_j\}, \quad (74)$$

$$b_r = \frac{2}{M} \sum_{j=0}^{M-1} I(x, y; \delta_j) \sin\{r\delta_j\}, \quad (75)$$

$$\delta_j = \frac{2\pi j}{M}, \quad (j = 0, 1, 2, \dots, M-1). \quad (76)$$

Taking into account Eq. (72), the terms of $r = 1$ are explicitly written by

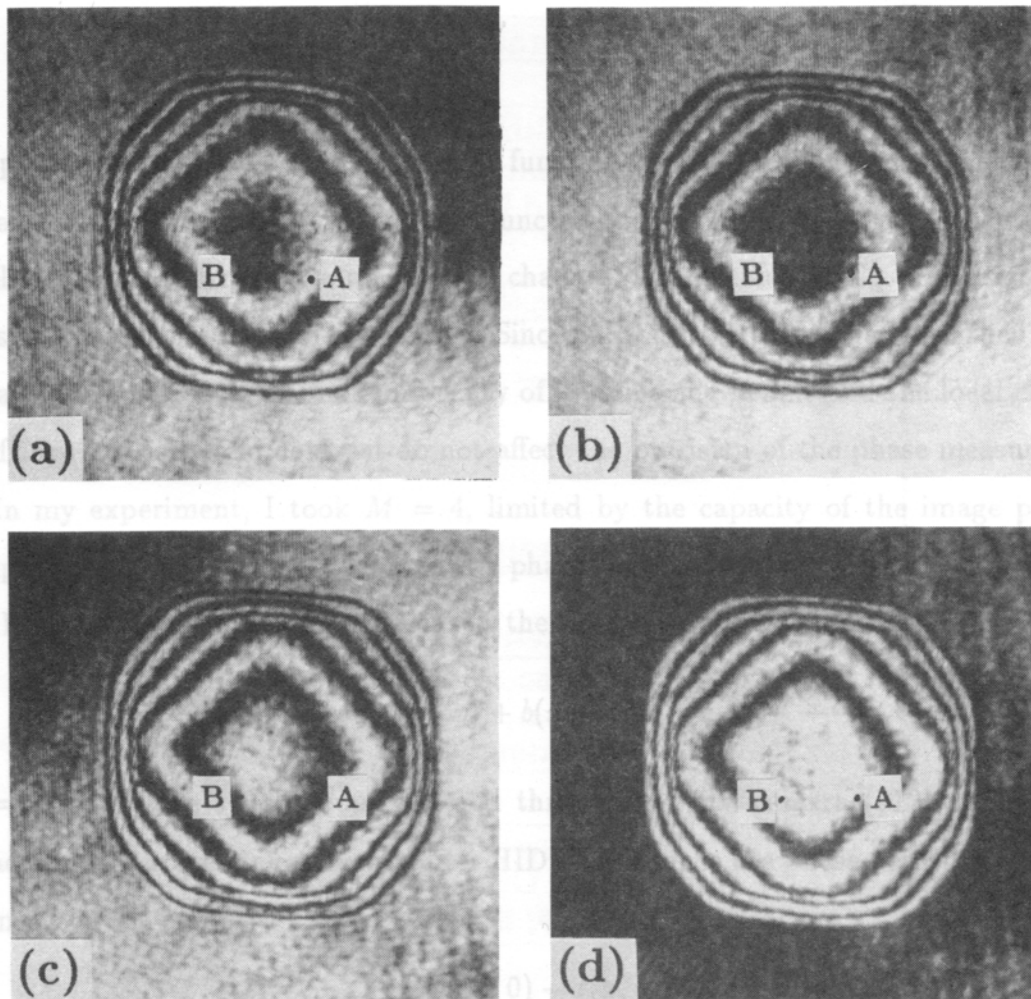
$$\begin{aligned} a_1 &= b(x, y) \sin\{\phi(x, y)\} = \frac{2}{M} \sum_{j=0}^{M-1} I(x, y; \delta_j) \cos(\delta_j), \\ b_1 &= b(x, y) \cos\{\phi(x, y)\} = \frac{2}{M} \sum_{j=0}^{M-1} I(x, y; \delta_j) \sin(\delta_j). \end{aligned} \quad (77)$$

Consequently, we get

$$\begin{aligned} \phi(x, y) &= \arctan \frac{a_1}{b_1} \\ &= \arctan \left\{ \frac{\sum_{j=0}^{M-1} I(x, y; \delta_j) \cos(\delta_j)}{\sum_{j=0}^{M-1} I(x, y; \delta_j) \sin(\delta_j)} \right\}, \quad (\text{mode } 2\pi). \end{aligned} \quad (78)$$

This result implies that, by the stepwise movement of the mirror A with interval of $\frac{\lambda}{2M}$, we obtain M interference micrographs $I(x, y; \delta_j)$, stored in a computer, and finally the phase distribution $\phi(x, y)$ can be calculated according to Eq. (78).

This procedure is physically interpreted as follows with an example in Fig. 3.2. The sample is a similar beryllium fine particle as in Fig. 2.11. Figures 3.2 (a)~(d) are the interference micrographs with the PZT shift of $\frac{\lambda}{8}$ interval. The interference fringes are observed to shift with the movement of the mirror A . In other words, the irradiance at a corresponding pixel A in the interference micrographs (a)~(d) goes through one cycle of periodic variation with the movement of the mirror A , as shown in Fig. 3.2 (e). The irradiance variation at a different pixel B is also sinusoidal with a different phase. The



$$\phi(x, y) = \arctan \frac{I(x, y; 1) - I(x, y; 3)}{I(x, y; 1) + I(x, y; 3)} \quad (\text{mode } 2\pi) \quad (50)$$

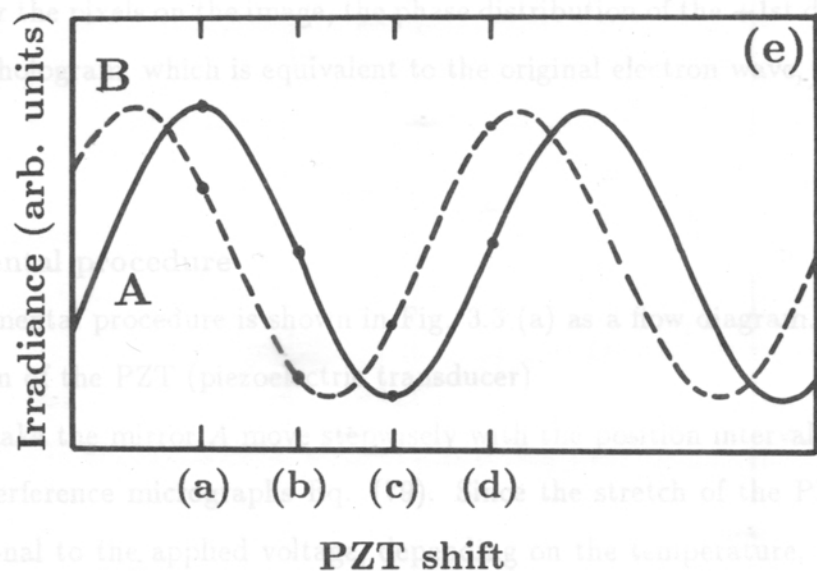


Fig. 3.2. Analysis with the fringe scanning interferometry. The sample is a beryllium fine particle. (a)~(d) Interference micrographs with different positions of the movable mirror A, of which position interval is $\frac{\lambda}{8}$. (e) Schematic graph showing the irradiance variation of a pixel with the mirror shift.

computer determines a best-fit sinusoidal function for the irradiance vs. the phase shift δ ; at each pixel. The phase of the best-fit function is a direct measure of the phase at each pixel. Even if the irradiance nonlinearly changes, the calculation Eq. (78) extracts only the sinusoidal component of the change. Since only the sequential change of the irradiance at each pixel is traced, the nonuniformity of illuminating beams and the local changes of the fringe intensity and contrast do not affect the precision of the phase measurement.

In my experiment, I took $M = 4$, limited by the capacity of the image processing computer, although the precision of the phase measurement increases with the number M . Four images at different positions of the mirror A , of which position interval is $\frac{\lambda}{8}$,

$$I(x, y; n) = a(x, y) + b(x, y) \sin\left\{\phi(x, y) + \frac{2\pi n}{4}\right\} \quad (79)$$

($n = 0 \sim 3$) were synchronously stored through the TV camera (512×512 pixels) in Hitachi image processing minicomputer HIDIC-IP. Hence the phase distribution Eq. (78) is simply given by

$$\phi(x, y) = \text{arc tan} \frac{I(x, y; 0) - I(x, y; 2)}{I(x, y; 1) - I(x, y; 3)}, \quad (\text{mode } 2\pi). \quad (80)$$

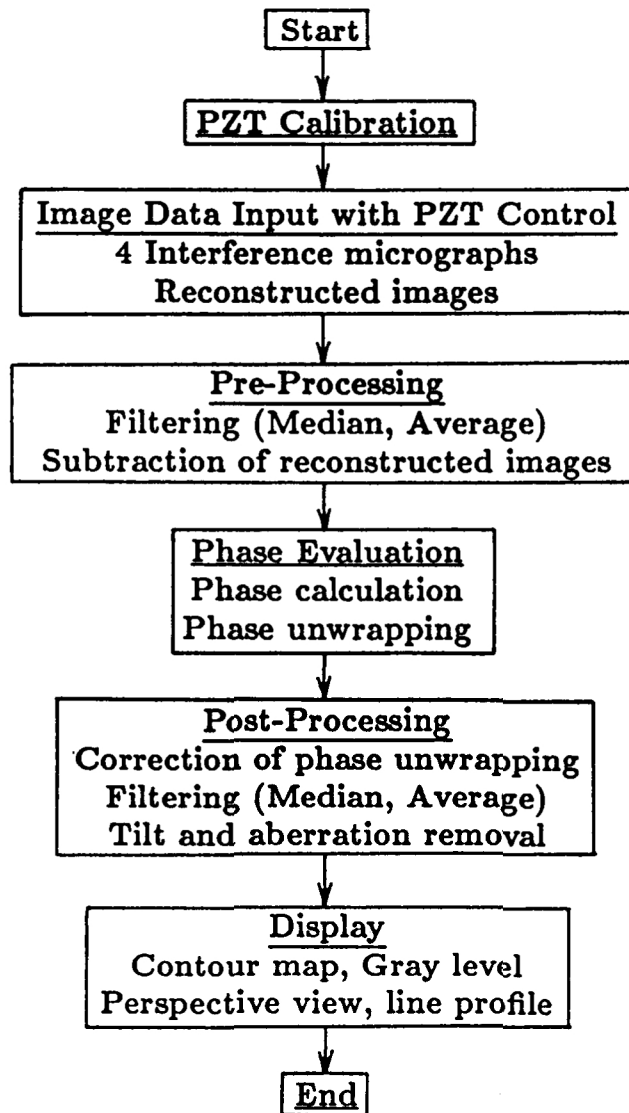
The calculated arctangent values are wrapped between $\pm\pi$. The unwrapped phase value gives the correct shape corresponding to the phase profile. By performing the above calculation all over the pixels on the image, the phase distribution of the +1st diffracted laser wave from the hologram, which is equivalent to the original electron wave, is numerically reconstructed.

3.3 Experimental procedure

The experimental procedure is shown in Fig. 3.3 (a) as a flow diagram.

(1) Calibration of the PZT (piezoelectric transducer)

I have to make the mirror A move stepwisely with the position interval $\frac{\lambda}{8}$ ($= 79.1\text{nm}$) to get four interference micrographs Eq. (79). Since the stretch of the PZT is not linearly proportional to the applied voltage, depending on the temperature, and has some hysteresis, I had to calibrate the movement of the PZT in advance for each measurement with the same interferometer. The control error of the PZT movement directly decreases



(a)

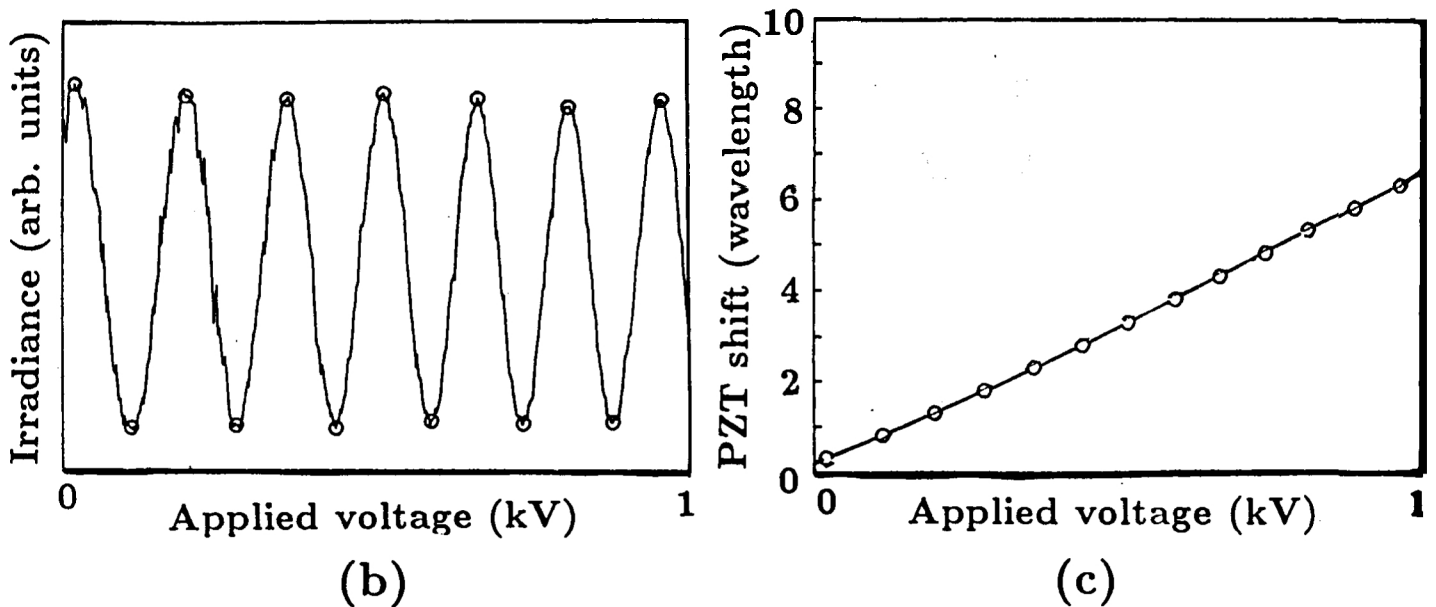


Fig. 3.3. (a) Flow diagram of the software system for image data acquisition and phase analysis. (b) The irradiance of a pixel on a interference micrograph changes with the applied voltage to the PZT. One period in the change corresponds to the mirror shift of $\frac{\lambda}{2}$. (c) Calibration curve of the PZT shift vs. the applied voltage.

the precision of the phase measurement. By increasing the voltage applied to the PZT from 0 V to 1 kV with 2 V interval, the stepwise movement of the mirror A in the interferometer of Fig. 3.1 causes the irradiance change of a marked pixel on the interference micrograph. The irradiance variation is shown in Fig. 3.3 (b) which indicates that several interference fringes pass through the marked pixel with the shift of the mirror A. By counting the number of the passed fringes, I measured the shift distance of the mirror A. By fitting a quadratic curve to the data points of the shift vs. the applied voltage (Fig. 3.3 (c)), the coefficients of the calibration quadratic curve of translation are evaluated. From these evaluated coefficients, a corrected voltage is available for the phase-shifting procedure. That is, the voltages corresponding to the mirror shift of $\frac{\lambda}{8}$ are evaluated at each mirror position.

(2) Image data acquisition

Four interference micrographs Eq. (79) (Fig. 3.2 (a)~(d)) are stored in a computer memory with simultaneously controlling the PZT movement. If necessary, the reconstructed images or the intensity distributions $|\Psi_A(x, y, z)|^2$ and $|\Psi_B(x, y, z)|^2$ of each wave, Eqs. (70) and (71), are also separately stored.

(3) Pre-processing

Unweighted local averaging and median filtering were used to reduce statistical noise in the interference micrographs. If necessary, in order to obtain enhanced fringe contrast and to reduce the background noise, the reconstructed images $|\Psi_A(x, y, z)|^2$ and $|\Psi_B(x, y, z)|^2$, i.e. $a(x, y)$ in Eq. (79), are subtracted from the interference micrographs $I(x, y; n)$.

(4) Phase evaluation

The phase $\phi(x, y)$ is calculated according to Eq. (80) for all pixels (x, y) . The computation of phase by any inverse trigonometric function only provides phase principal values between $\pm\pi$ rad. The line profile (Fig. 3.4 (b)) of the calculated phase distribution along the cross line AB in the interference micrograph Fig. 3.4 (a) shows several phase jumps of $\sim 2\pi$, which correspond to the interference fringes in (a). On the next step, this phase unwrapping was performed to obtain a continuous phase profile (Fig. 3.4 (c)) which corresponds to the shape of the wavefront.

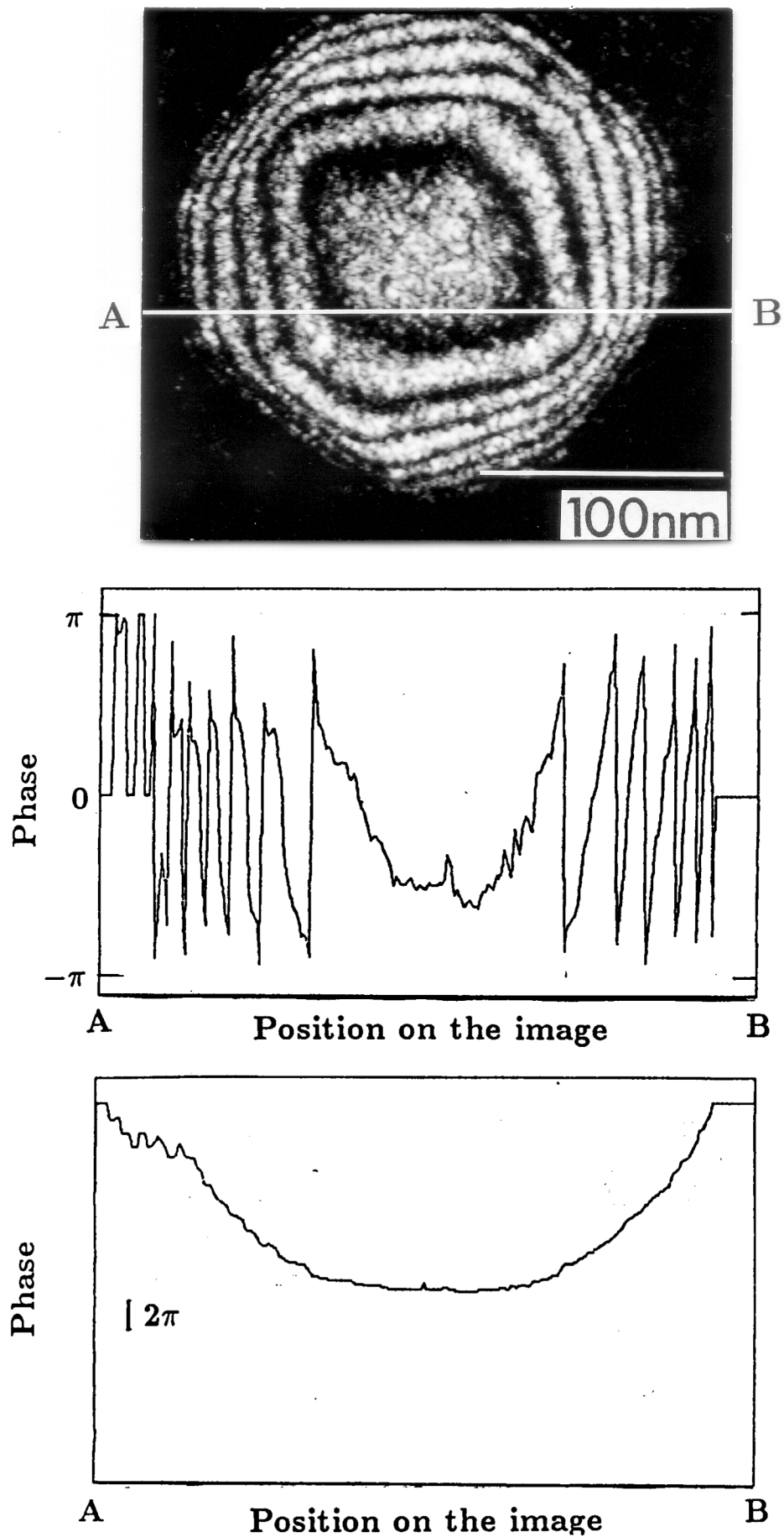


Fig. 3.4. Phase calculation in the fringe scanning interferometry. The sample is a beryllium fine particle. (b) is the line profile of the calculated principal phase distribution along the cross line AB in the interference micrograph (a). After the phase unwrapping, we obtain a continuous phase distribution (c).

(5) Post-processing

The aberration of the optical interferometer and the tilt phase term are subtracted from the unwrapped phase data. Noise reduction processing was carried out also in this stage, if necessary. The phase noise to be considered in electron holographic interferometry are (i) phase irregularity in a carbon film base which supports the specimen (when used) in the electron microscopic observations, (ii) speckle noise caused by dust and such in the optical interferometer, (iii) thickness irregularity and granules of the hologram, and (iv) electronic statistical noise: shot noise and thermal noise in the TV camera.

For the spatial noise due to the first three sources, I use noise reduction techniques by digital image processing including local averaging and median windowing. In particular, median window filtering is powerful in reducing salt-and-pepper spatial noise without reducing spatial resolution. Spatially independent noise such as salt-and-pepper noise in the phase distribution is serious in performing phase unwrapping, resulting in fatal error near the phase discontinuity region. If the phase unwrapping failed at a noise pixel, the unwrapping process had to be carried out afterward by hand using a mouse.

(6) Display

The calculated phase data are displayed in an arbitrary format; contour phase map like interference micrographs, perspective view of the wavefront, gray levels, line profile, and others.

3.4 Analysis examples

3.4.1 Cobalt fine particle

Cobalt fine particles were prepared by gas evaporation technique in 10-Torr inert argon gas atmosphere. The particles grown in the intermediate zone in its smoke were collected on a microgrid at the position 4 cm above the evaporation source [3.8][3.9]. The hologram, which is the same one in ref. [3.10], was re-examined with the fringe scanning interferometry.

Figure 3.5 (b) shows a magnified version of the electron hologram. The holographic carrier fringes are very fine ($\sim 20 \mu\text{m}$), while the Fresnel fringes originated from the

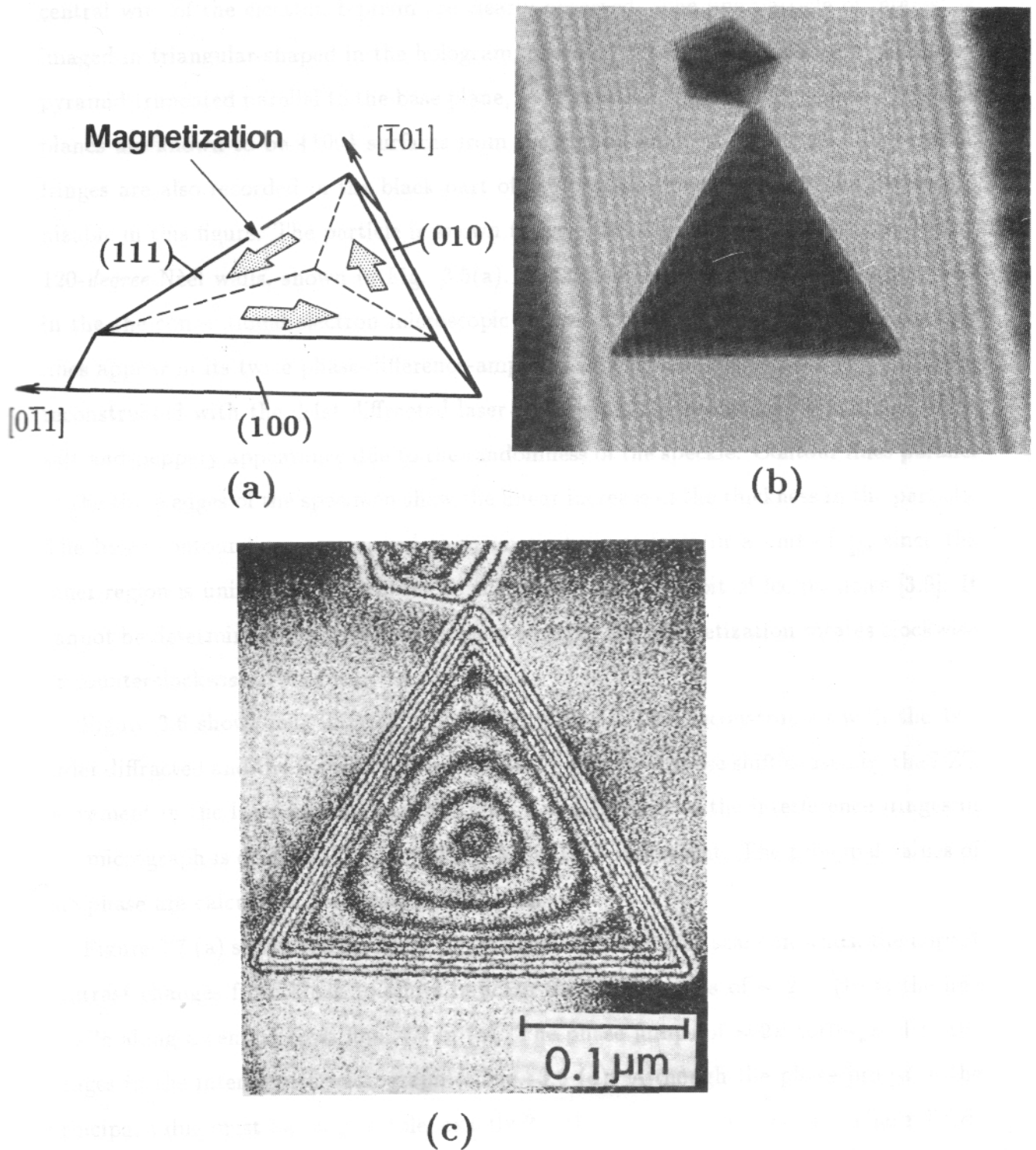


Fig. 3.5. Cobalt fine particle. (a) Schematic showing the 3D shape of the particle and its magnetic structure. (b) Magnified version of an electron hologram. (c) Interference micrograph with twice phase-difference amplification. [3.10]

central wire of the electron biprism are clearly observed. The fine particle of interest is imaged in triangular-shaped in the hologram, of which 3D form is known as a triangular pyramid truncated parallel to the base plane, $\{111\}$ surface, with $\langle 110 \rangle$ edges. The side planes are known to be $\{100\}$ surfaces from the crystal habit of fcc metals. The carrier fringes are also recorded in the black part of the particle image, although hardly recognizable in this figure. The particle is known to have three magnetic domains bounded by 120-degree Néel walls, shown in Fig. 3.5(a). Details of the structure is hardly observed in the the conventional electron microscopic image. On the other hand, several contour lines appear in its twice phase-difference-amplified interference micrograph (c), Eq. (47), reconstructed with the ± 1 st diffracted laser waves from the hologram. The image has a salt-and-peppery appearance due to the randomness of the speckle. Contour lines parallel to the three edges of the specimen show the linear increase of the thickness in the particle. The inner contour lines correspond to magnetic lines of force in a unit of $\frac{h}{2e}$, since the inner region is uniform thickness due to the typical crystal habit of fcc particles [3.9]. It cannot be determined from this contour map whether the magnetization rotates clockwise or counterclockwise.

Figure 3.6 shows four interference micrographs Eq. (79) reconstructed with the 1st-order diffracted and the transmitted waves with $\frac{\pi}{2}$ -reference-phase shift caused by the PZT movement in the laser interferometer of Fig. 3.1. The shift of the interference fringes in the micrograph is observed to be cyclic with the PZT movement. The principal values of the phase are calculated according to Eq. (80).

Figure 3.7 (a) shows the principal phase distribution in gray scale, in which the abrupt contrast changes from black to white indicate the phase jumps of $\sim 2\pi$. (b) is the line profile along a central cross line AB in (a). The phase jumps of $\sim 2\pi$ correspond to the fringes in the interference micrograph of Fig. 3.6 (d). Although the phase jumps in the principal value must be, in principle, exactly 2π , the jumps in the measured phase distributions were often less than 2π as shown Fig. 3.7 (b). This is partly because the steep phase variation is smeared out due to the finite size of the TV pixels. Another reason is the speckle noise of random phase. Anyway, the figure shows that the phase change between the adjacent fringes in the interference micrograph, i.e. the subfringe informa-

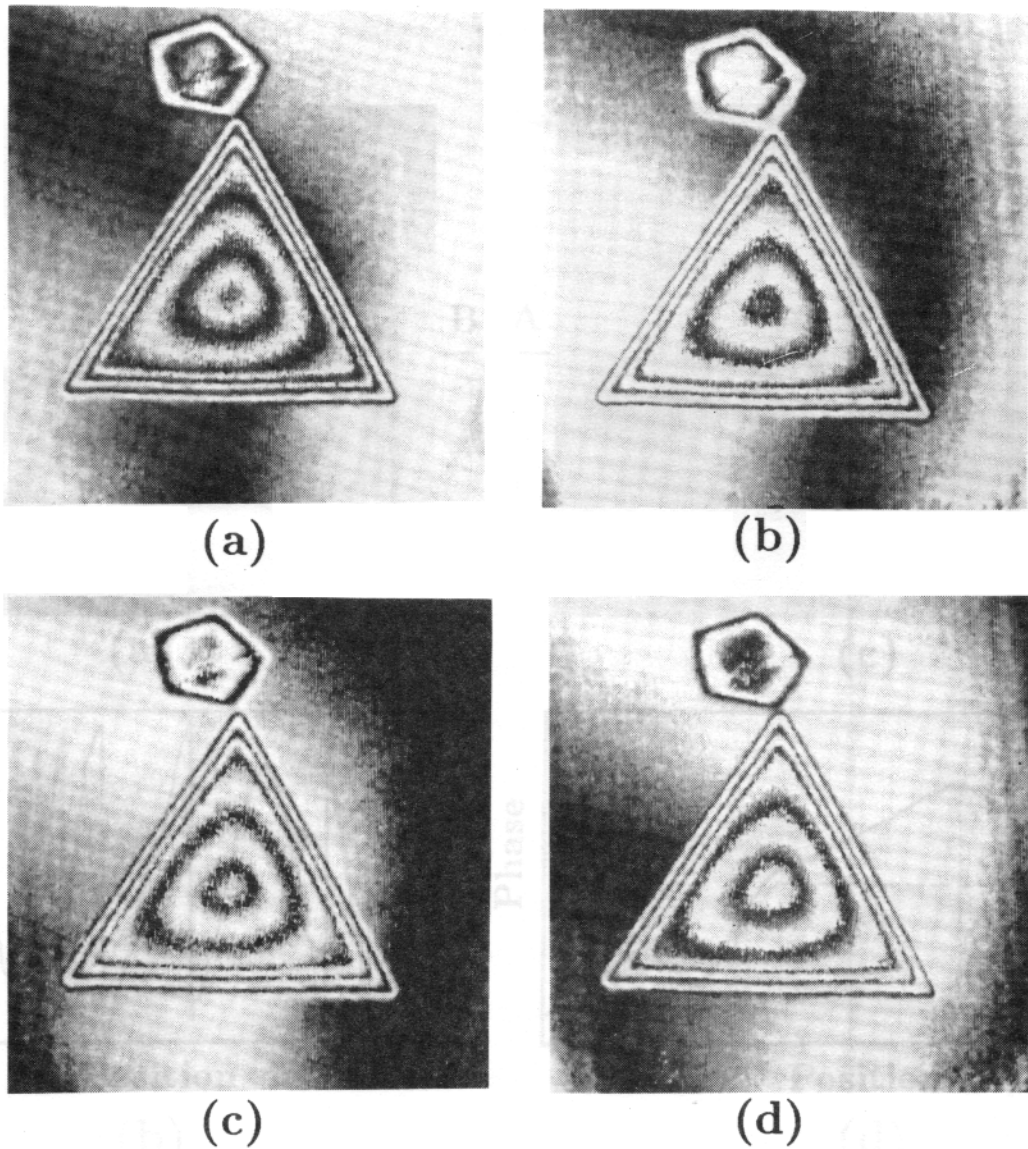


Fig. 3.6. Four interference micrographs Eq. (79) reconstructed with the 1st-order diffracted and the transmitted waves with $\frac{\pi}{2}$ -reference-phase shift caused by the PZT movement in the laser interferometer (Fig. 3.1).

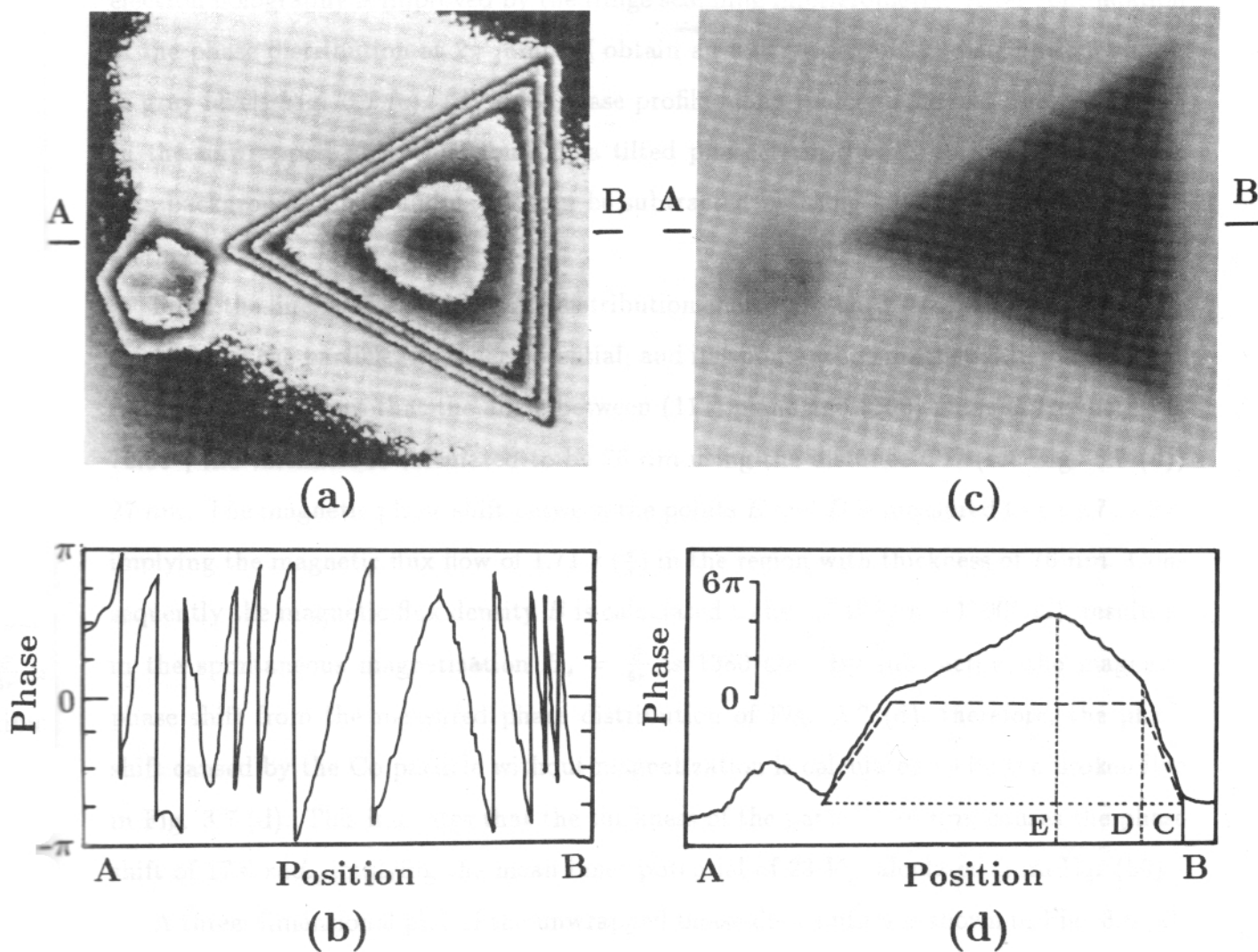


Fig. 3.7. (a) The wrapped phase distribution in gray scale display. (b) Its line profile along a central cross section AB in (a). (c) The unwrapped phase distribution in gray scale display. (d) Its line profile along a central cross section AB in (c).

tion, is numerically measured. This is the reason why the phase measurement precision in electron holography is improved by the fringe scanning interferometry. After continuation of the phase distribution at 2π -jumps, I obtain an unwrapped phase distribution, shown in gray levels Fig. 3.7 (c). (d) is its phase profile along the central cross line AB in (c). In the unwrapped phase distribution, a tilted phase term due to optical misalignment or a background phase undulation can be subtracted by using a least-squares-estimation method.

From the line profile of the phase distribution shown in Fig. 3.7 (d), I can measure the thickness of the particle, its inner potential, and its spontaneous magnetization as follows. According to the fact that the angle between (111) plane and (100) plane of fcc metals is 70.53° , the thickness is calculated to be 76 nm using the distance CD (see Fig. 3.7 (d)) 27 nm . The magnetic phase shift between the points E and D is measured to be $1.71 \times 2\pi$, implying the magnetic flux flow of $1.71 \times (\frac{e}{h})$ in the region with thickness of 76 nm . Consequently the magnetic flux density B is calculated to be 1.7 Wb/m^2 (17000 G), resulting in the spontaneous magnetization $H_s = \frac{B}{4\pi}$ is 1380 Oe . By subtracting the magnetic phase shift from the measured phase distribution of Fig. 3.7 (d), therefore, the phase shift caused by the Co particle without magnetization is calculated to be the broken line in Fig. 3.7 (d). This indicates that the thickness of the particle, 76 nm , causes the phase shift of 17.6 rad. , implying the mean inner potential of 23 V , calculated from Eq. (56).

A three-dimensional plot of the unwrapped phase distribution is shown in Fig. 3.8 (a). This is the electron wavefront just after transmitted through the cobalt fine particle. The wavefront propagation delays due to the particle thickness as well as magnetic field in it, which implies that the rotation of the magnetization in the particle is counterclockwise as shown in Fig. 3.5 (a). The delay or advance in the wave propagation, in general, which corresponds to the direction of magnetic flux flow, is automatically determined in the fringe scanning interferometry. Figure 3.8 (b) and (c) are the contour phase maps with π and $\frac{\pi}{2}$ intervals, respectively. These are equivalent to the interference micrographs with twice and four-times phase-difference amplified interference micrographs, respectively. In this way, once we obtain the numerical data of the phase distribution, it can be transformed in arbitrary display formats.

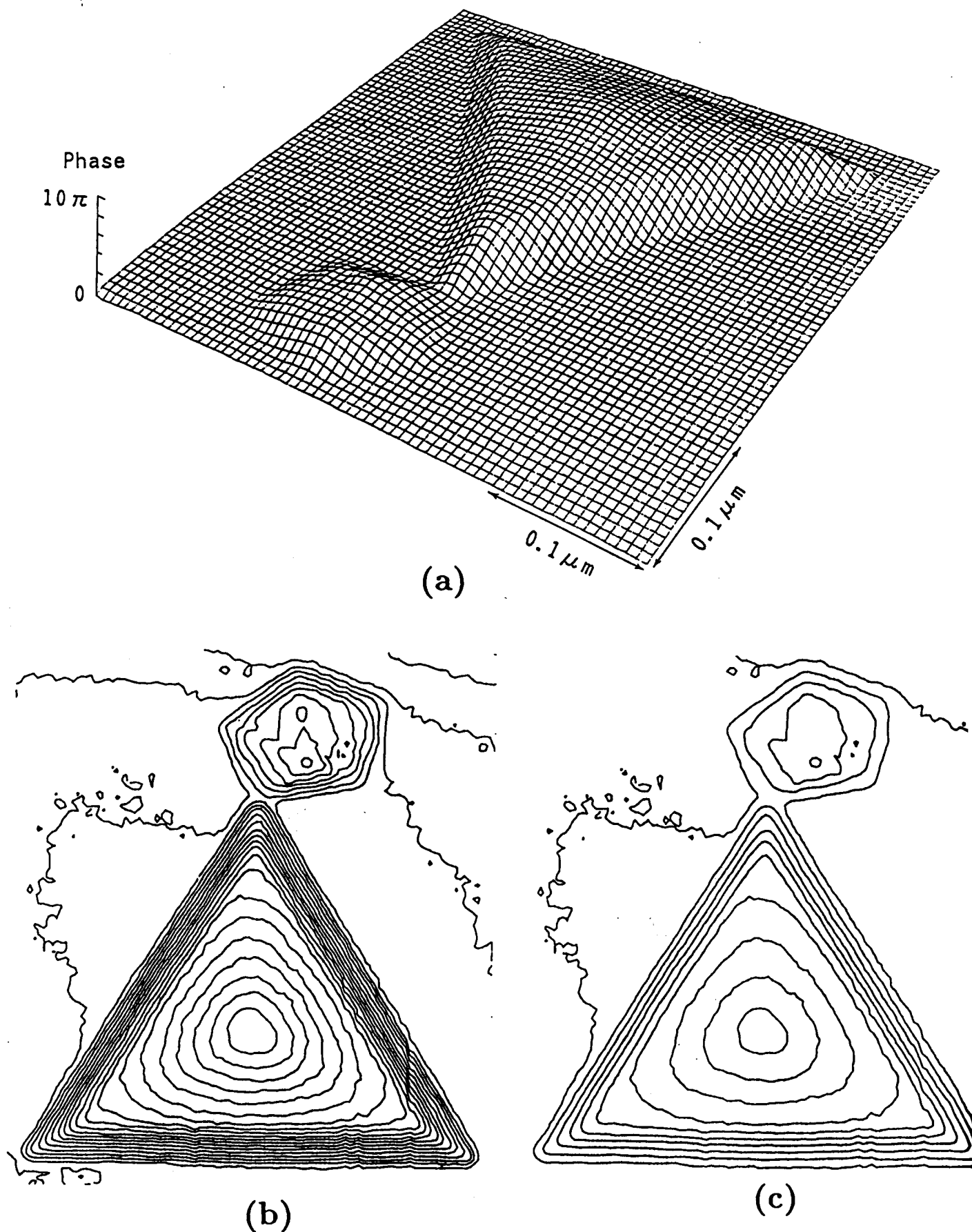


Fig. 3.8 (a) A 3D plot of the unwrapped phase distribution which is equivalent to the electron wavefront just after transmitting through the Co particle. (b) and (c) are the contour phase maps with $\frac{\pi}{2}$ and π intervals, respectively, which were calculated from the numerical data of the phase distribution.

3.4.2 Ring magnet

The second analysis example is with a ring magnet which was used for verifying the Aharonov-Bohm effect [3.11]. The sample (Fig. 3.9 (a)), Permalloy film of ~ 10 nm thickness of toroidal geometry was fabricated with use of photolithography technique. The magnetization in the magnet smoothly rotates with negligible leakage fields. The hologram, which is the same one in ref. [3.12], is re-examined with the fringe scanning interferometry.

Figure 3.9 (b) shows an "interferogram" with twice phase-difference amplification. This was obtained using the 1st diffracted wave Eq. (44) and the -1st one Eq. (46) with somewhat tilted wavefront. The micrograph is not, therefore, a contour phase map. But the fringe shift in the image reveals that phase difference exists between two electron wavefronts that have passed through the inner and outer spaces of the toroidal magnet, while there are no magnetic fields in those spaces.

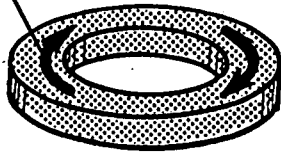
Figure 3.9 (c) shows the numerically reconstructed wavefront with the fringe scanning interferometry. The phase shift in the wavefront between the inner and outer parts of the ring is obvious, which verifies the Aharonov-Bohm effect. The sign of the phase shift is reversed in this figure for clarity. The wavefront passing through the inner hole of the ring was really advanced compared with that outside the ring.

Figure 3.10 (a) is a contour phase map with $\frac{\pi}{2}$ interval which was calculated from the numerical data of the phase distribution. The line profiles of the phase distribution along the cross lines AB and CD in (a) are shown in (b) and (c), respectively. The steep increases of the phase of ~ 1.6 rad. at the inner and outer edges of the ring indicate the phase advance caused by the inner potential and the thickness of the sample.

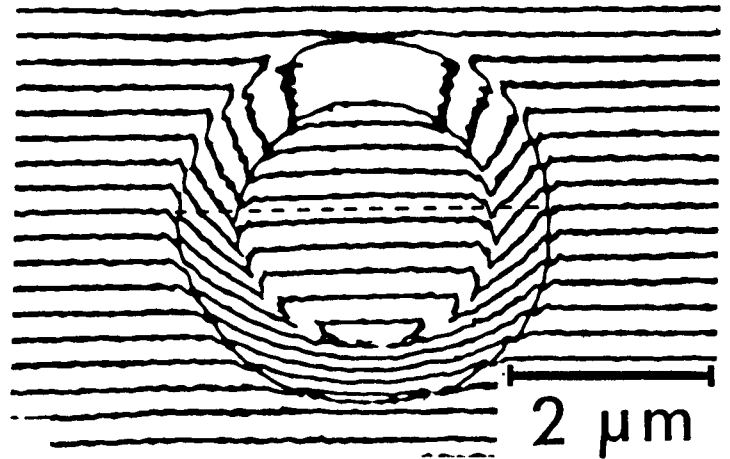
The major phase modulation, the linear increases or decreases of the phase, inside the ring are originated from the rotating magnetic flux, of which direction can be determined to be clockwise from the sign of the phase shift. The phase difference of ~ 7.5 rad between the inner hole and outer area means that the magnetic flux of $\sim 1.2(\frac{h}{e})$ exists in the ring. If the ring had no magnetic flux in it, the phase distribution should be the one indicated by the broken lines in Figs. 3.10 (b) and (c).

Figures 3.10 (d) and (e) are the x -derivatives $\frac{\partial\phi(x,y)}{\partial x}$ of the phase profiles (b) and (c),

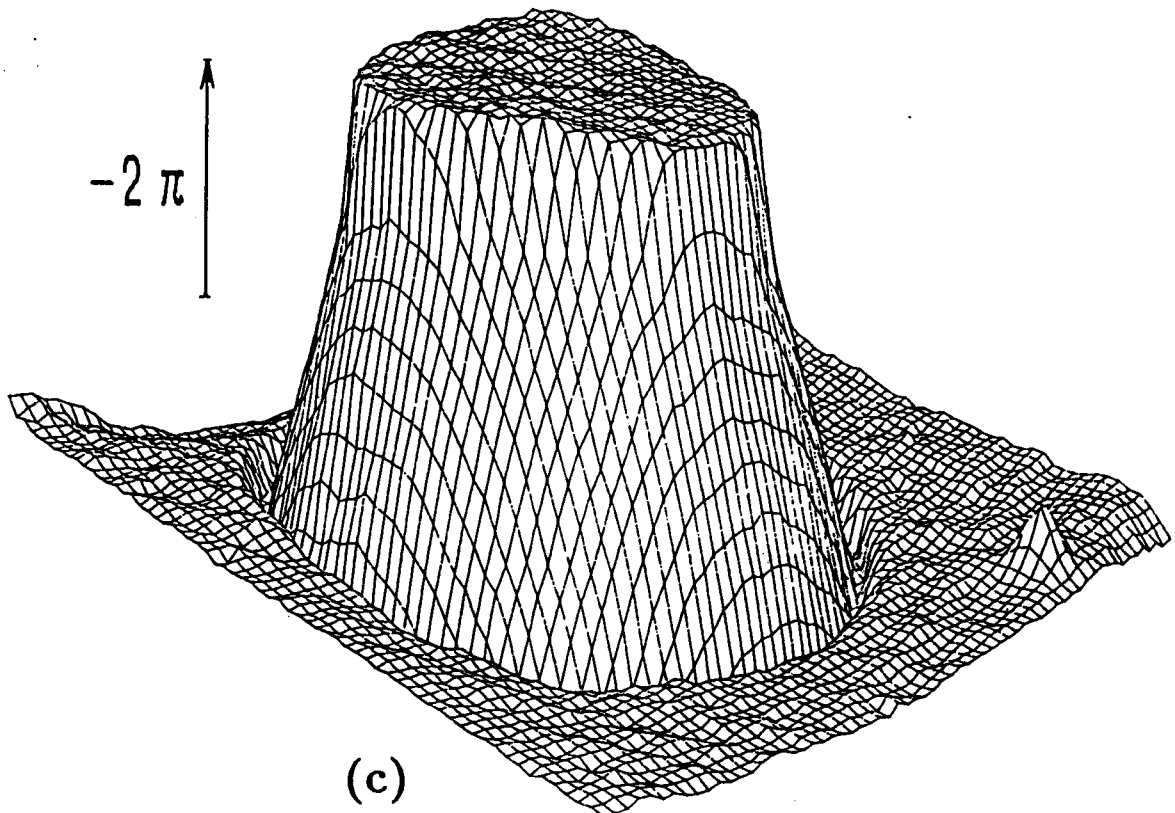
Magnetization



(a)



(b)



(c)

Fig. 3.9 Ring magnet. (a) Schematic showing the 3D shape and the magnetization of the sample. (b) Interferogram with twice phase-difference amplification. (c) The wavefront reconstructed with the fringe scanning interferometry.

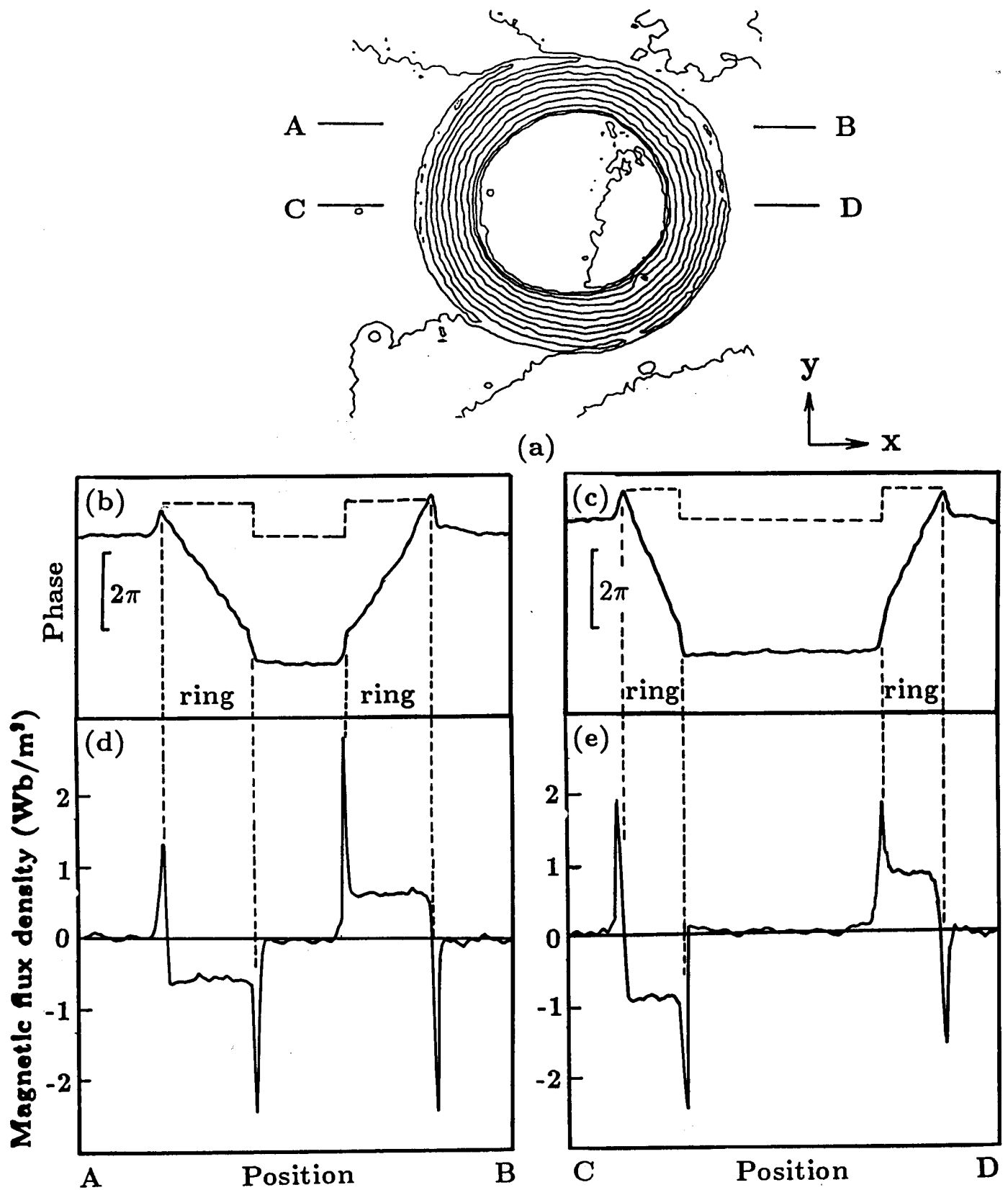


Fig. 3.10 Analysis of the ring magnet. (a) Contour phase map with $\frac{\pi}{2}$ -phase interval. (b) and (c) are the line profiles of the phase distribution along the cross lines AB and CD in (a). (d) and (e) are the derivatives of the phase distributions $\frac{\partial \phi(x,y)}{\partial x}$, which correspond to the distribution of the y -component of the magnetic flux vector, except the sharp peaks of the sample edges.

respectively. According to Eq. (65), these quantities correspond to the line integral of the y -component of the magnetic field vector $B_y(x, y, z)$ along the electron trajectory (z -direction). Since the $B_y(x, y, z)$ is non-zero constant B_{y0} only inside the ring of thickness D , Eq. (65) is reduced to

$$\frac{\partial\phi(x, y)}{\partial x} = \frac{e}{\hbar} B_{y0}(x, y) \cdot D . \quad (81)$$

Hence the curves of Figs. 3.10 (d) and (e) can be regarded as the distribution of B_y -component itself, except the sharp peaks at the sample edges. The spontaneous magnetization of the ring is measured to be 0.85 Wb/m^2 (680 Oe).

3.5 Conclusions

The fringe scanning interferometry allows us to fully read out the phase distribution of the electron wave recorded on the hologram, and to precisely obtain the subfringe information in the interference micrographs. This method, in practice, improves the phase measurement precision of the electron holography. As shown in the next chapter, the phase resolution increases as high as $\sim 2\pi/100$ with suitable samples, which approximately corresponds to the three-times higher phase resolution compared with the previous phase-difference amplification techniques. The analysis time also has become much shorter than in the previous method. Moreover, the numerical data acquisition in the fringe scanning interferometry will lead to the detailed analysis of the 3D shape of the sample and the electromagnetic fields with data-processing by computers. Such availability will be discussed in Chapter 5.

Chapter 4

Stray field from magnetic recording materials

4.1 Introduction

All kinds of information, images, sounds, sentences, numerical data, computer programs, and others, can be nowadays memorized in magnetic recording media such as magnetic tapes and disks in the form of their magnetization patterns. Magnetic recording was pioneered by Poulsen in 1910's using steel wires as a recording medium. As the performance of the data-processing machines such as computers is highly improved, the amount of the treated information has greatly increased, leading to the improvement of the quality of the information. This accordingly postulates high-density data storage in magnetic recording media. Continuous progress in magnetic recording has been made with use of a lot of new concepts and technologies concerning recording methods, magnetic heads, and recording media. Since the invention of magnetic tapes by Pfleumer in 1930's, the recording density has improved by ~ 100 times for ~ 50 years. The mechanism of magnetic recordings and the recorded magnetization patterns have been extensively studied both theoretically and experimentally in order to attain higher recording density and higher reliability.

Two types of recording media have been employed; particulate films and continuous films. The films consisted of ferromagnetic fine particles such as $\gamma\text{-Fe}_2\text{O}_3$ and Fe-Co alloys have been widely adopted for commercial magnetic disks. Continuous films of magnetic materials such as Co-Ni alloys, developed for high-density recordings, have been fabricated by vacuum deposition or sputtering methods.

There are also two types of modes in digital magnetic recording to "write" the magnetization patterns on the media. One is the longitudinal magnetization mode in which

the recorded magnetizations are parallel to the surface of the medium as shown in Fig. 4.1 (a). "1"-bit and "0"-bit correspond to right-directed and left-directed magnetizations, respectively. Another is the perpendicular magnetic recording in which the recorded magnetizations are normal to the film surface as shown in Fig. 4.1 (b). "1"-bit and "0"-bit are distinguished by up- and down-magnetizations, respectively. This mode was first proposed by S. Iwasaki and Y. Nakamura to attain higher-density recording [4.1]. As the recording density increases, or the bit length decreases, the demagnetization field in the longitudinal magnetization mode increases, implying that some practical limit will be reached in higher recording density. The demagnetization field in the perpendicular mode, on the other hand, approaches to zero with decrease of the bit length, so that this mode is more suitable to high-density magnetic recording.

Theoretical studies on the recording mechanism have been carried out using computer simulations [4.2][4.3]. Several reports have also been presented on attempts to experimentally observe recorded magnetization configurations using Lorentz microscopy [4.4]~[4.8], the Bitter method [4.9][4.10], and the colloid scanning electron microscopy (SEM) method [4.11]. Although these methods reveal the magnetization configuration in recorded media, they have insufficient sensitivity and spatial resolution for quantitative analysis of higher recording density.

The electron holographic observations have provided direct and quantitative analysis of the recorded magnetization patterns with very high spatial and magnetic flux resolutions. Complex magnetic structures at bit boundaries in the longitudinal recording mode have been clearly revealed in the interference micrographs [4.12][4.13]. Such observations may provide some guiding principles to develop the methods and materials for higher-density magnetic recording.

As the recording density increases, or the bit length decreases, the amount of magnetic flux emerging in each bit decreases, and accordingly, the higher sensitivity for magnetic flux is required for the analysis methods. Owing to the fringe scanning interferometry described in Chapter 3, the magnetic sensitivity of the electron holography has been greatly improved. This Chapter shows the direct observations of the distributions of stray field from thin cross sections of perpendicularly magnetized recording films (Co-Cr). The

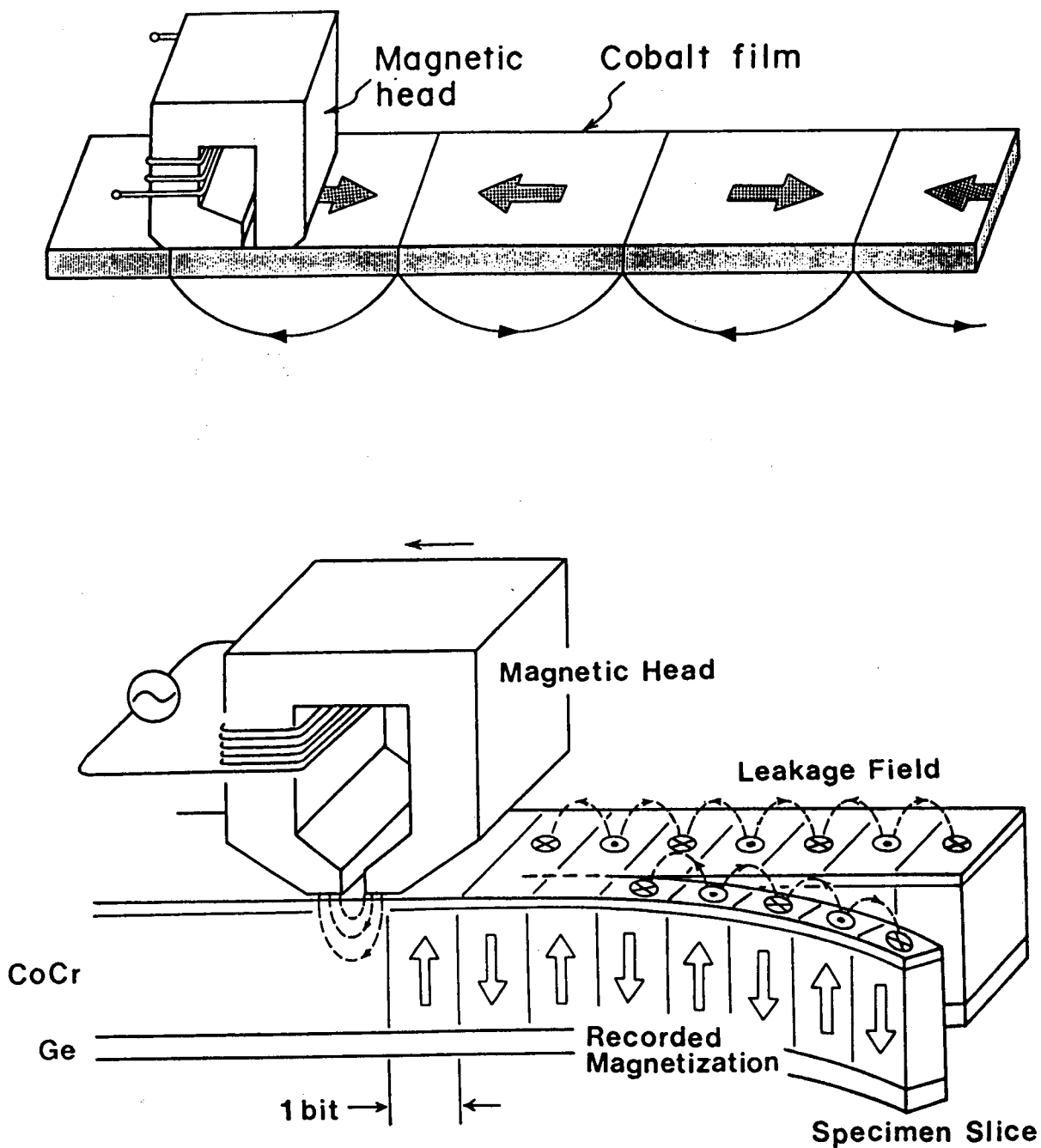


Fig. 4.1 Digital magnetic recordings. (a) Longitudinal magnetization mode. (b) Perpendicular magnetization mode.

magnetic flux as small as $\frac{h}{100e}$ ($= 4.1 \times 10^{-17} Wb$), hitherto undetectable, has successfully observed with high spatial resolution. With this technique, the perpendicular magnetic recording with a recording density as high as 300 *kFCI* (kilo flux change per inch) (85 *nm* bit-length) has been confirmed. This is the highest recording density ever directly observed.

In Section 4.2, I describe the sample preparation and the experimental procedures. Section 4.3 is devoted to calculations of the electron phase modulation by the recorded magnetic film. Experimental results are shown, and analyzed with use of the calculated results in Section 4.4, and finally summarized in Section 4.5. Through the observations described in this Chapter, it can be concluded that the phase detection sensitivity in the electron holography has been improved up to $\sim \frac{2\pi}{100}$ by introducing the fringe scanning interferometry.

4.2 Experimental procedures

4.2.1 Sample preparation

Co-Cr thin films have been intensively investigated as suitable media for perpendicular magnetic recording with high recording density [4.14]~[4.16]. Our observation samples were fabricated by the following procedures. At first, the out-gas from the polyimide film substrate was performed in vacuum by heating the film up to 470 *K* and keeping for 1 *hr*. A Ge film of 30 *nm* thick was deposited on the substrate under the vacuum condition of 6×10^{-4} *Pa*. The substrate temperature was kept at 470 *K* during the deposition, and the deposition rate was ~ 0.8 *nm/sec*. The Co-20 *wt.%* Cr alloy films of 200 *nm* in thickness were next deposited on the Ge layer by electron beam heating in a vacuum of 3×10^{-4} *Pa*. The substrate temperature was 420 *K*, and the deposition rate was ~ 3 *nm/sec*. The Ge layer promotes preferential *c*-axis orientation of columnar growth of the Co-Cr film [4.15]. A protective layer of B in 15 *nm* thickness was finally coated on the Co-Cr film to give durability during read/write processing with a magnetic head. The substrate temperature was 450 *K* during the B-deposition with ~ 0.1 *nm/sec*-rate.

As shown in Fig. 4.1 (b), the magnetizations, which are digitally recorded on the

Co-Cr film in contact with a ring-type magnetic head, are antiparallel bit by bit. The bit length are 85 nm and 127 nm for 300 and 200 *kFCI*-recording densities. The gap length and track width of the magnetic head were 0.25 and 70 μm , respectively. The saturation magnetization of the Co-Cr film was measured 250 *kA/m* (250 *Oe*). The digital recording was performed with all 1's non-return-zero (NRZ) signal. Magnetic fields leak from the surface of the medium as sketched in Fig. 4.1 (b). These stray fields are "read out" by a magnetic head in magnetic recording systems. The film was then sliced with a microtome to approximately 80 nm thick for electron holographic observation. The specimen slice was collected on a microgrid, and installed in the electron holography microscope.

4.2.2 Analysis procedures

The observation and analysis of the magnetic field straying from the Co-Cr film was carried out with the procedures as shown in Fig. 4.2.

The first step in the experiment was to record the hologram in the microscope. An electron wave illuminates the specimen from the direction indicated by the arrow in Fig. 4.3. Although the incident electron wave could not penetrate the film because of the insufficient acceleration voltage (100 *kV*) of the electron microscope used in this experiment, the wave passing through the leakage field in vacuum near the top edge of the sliced film was utilized to form the hologram. The wavefront of the incident wave, which was a plane, is deformed by the leakage field during passage through it, as schematically shown in the figure. Off-axis holograms were formed by making the transmitted electron wave interfere with a reference electron wave. The hologram thus obtained contains the phase distribution of the wave carrying the information on the stray field distribution. The electron optics in the microscope is the same one as shown in Fig. 2.5. The electron wave passing through the far region, ~ 300 nm from the stray field under investigation at the specimen plane, is utilized as a reference wave. The leakage field extends virtually, decaying exponentially from the recorded film edge, into the reference wave area at the specimen plane. But the reference wave is regarded as a plane wave because the phase modulation caused by the fringing field in the reference wave area is estimated to be less than $2\pi/1000$, which is much smaller than the experimental precision. Moreover, since

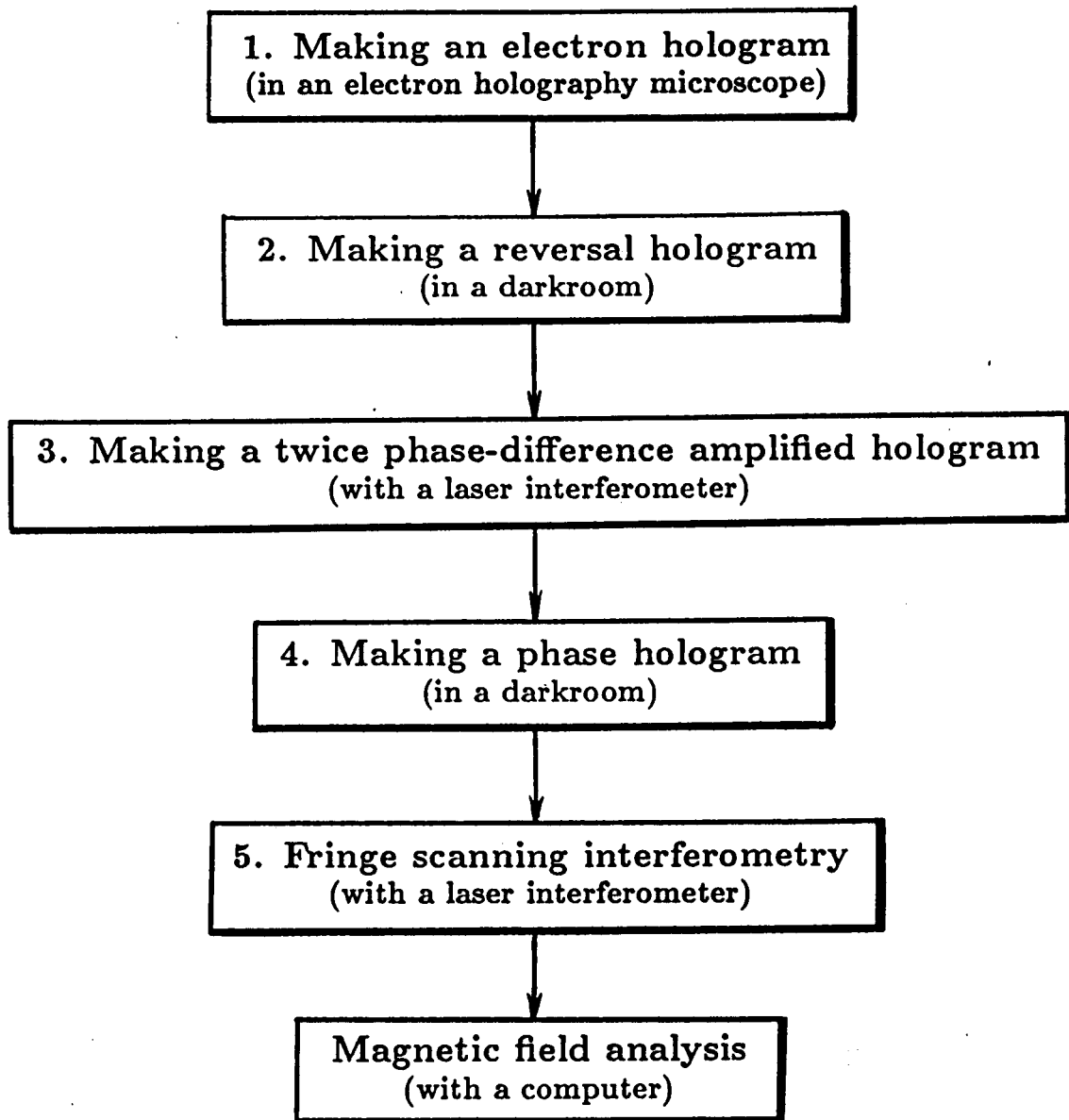


Fig. 4.2 Experimental procedures to analyze the stray field from the perpendicular magnetic recording film.

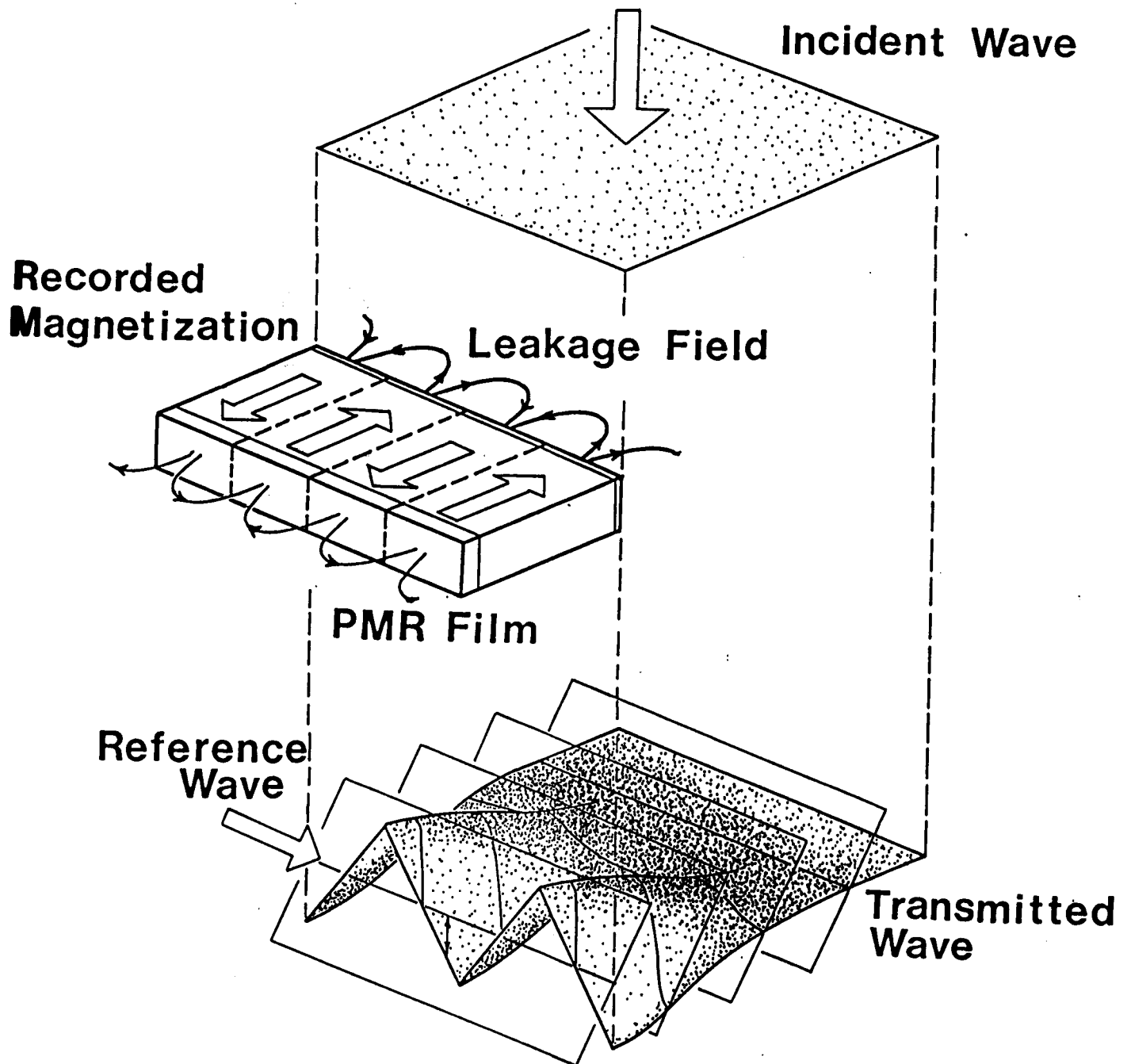


Fig. 4.3 The electron wavefront is deformed by the leakage magnetic field from the top edge of the recorded Co-Cr sliced film. The three-dimensional form of the transmitted wavefront is recorded on an electron hologram by overlapping a reference wave in an electron holography microscope.

the divergence angle of the illuminating electron beam is $\sim 1 \times 10^{-8}$ rad, the incident wave is also regarded as a plane wave with $2\pi/1000$ accuracy. An image hologram with magnification of 6000 is obtained by applying a positive voltage (~ 20 V) to the central thin wire of the electron biprism. The holograms were recorded on FG electron microscope films. The hologram width and its carrier fringe spacing were set to be 4 mm and $70 \sim 150$ μm on the film or 600 nm and $10 \sim 20$ nm at the specimen plane, respectively.

Next the hologram processing techniques previously developed for the phase-difference amplification described in Chapter 2 were adopted. At the second step, a reversal hologram was made on a Sakura high-resolution plate from the original one by contact printing to enhance the contrast of the interference fringes recorded on the hologram.

At the third step, a twice phase-difference amplified hologram was made from the reversal hologram on an optical bench as shown in Fig. 2.10 (b). He-Ne laser beams irradiated onto the reversal hologram are diffracted by its interference fringes, and some diffracted waves emerge as well as the transmitted wave. Only the ± 1 st diffracted waves were selected with a diffraction lens *A* and a double aperture, and made interfere with each other to form a twice phase-difference amplified hologram. This hologram was recorded on Kodak High-Speed Holographic Plate 131. Spatially high-frequency noises are cut off by a filtering with the aperture.

At the 4th step, the twice amplified hologram was bleached to obtain a phase hologram and enhance the diffraction efficiency.

At the final step, the fringe scanning interferometry was carried out with the phase hologram in the laser interferometer of Fig. 3.1. The ± 4 th diffracted laser waves from the phase hologram were made interfere with each other to form a 16-times phase-difference amplified interference micrograph. The interference fringes in this image are contour phase lines of $2\pi/16$ interval. Acquisition of the four different interference images formed by the PZT shift, the wavefront was numerically reconstructed. A single pixel on the image in this experiment corresponds to a 0.9 nm square at the specimen plane. From this phase data, magnetic flux lines in arbitrary units and field vector components were analyzed.

4.3 Calculation of magnetic phase caused by magnetic materials

Following the formulas derived by Fukuhara *et al.* [4.17], I show the relation between the magnetization within a magnetic specimen and the resulting electron phase modulation in order to simulate the holographic observations of perpendicular magnetic recording materials. As described by Eq. (53) in Section 2.5, the magnetic phase change in electron waves is given by

$$\begin{aligned}\phi(x, y) &= \frac{e}{\hbar} \int \vec{A}(x, y, z) \cdot d\vec{s} \\ &= \frac{e}{\hbar} \int_{-\infty}^{\infty} A_z(x, y, z) dz ,\end{aligned}\quad (82)$$

where the integral is taken along a straight line corresponding to the classical electron trajectory, parallel to the z -axis. This is because the deflection of an electron beam is so small in experiments with a thin magnetic specimen in an electron holography microscope. \vec{A} is the vector potential originating from the magnetic specimen. Arbitrariness in \vec{A} within the Coulomb gauge is assumed to be eliminated as

$$\text{div } \vec{A}(x, y, z) = 0 ,\quad (83)$$

and $\vec{A}(x, y, z) = 0$ at infinity from the specimen. Although the observable quantity is the phase difference between the object and the reference waves, Eq. (82) can be regarded to be the observed phase distribution provided that the value of \vec{A} vanishes, in effect, along the pass of the reference wave.

In general, the vector potential $\vec{A}(P)$ at a point P is expressed in terms of the magnetization $\vec{M}(Q)$ at a point Q in the specimen and the vacuum permeability μ_0 ,

$$\vec{A}(P) = \frac{\mu_0}{4\pi} \int_{\text{specimen}} dV_Q \frac{\vec{M}(Q) \times \vec{R}_{PQ}}{R_{PQ}^2},\quad (84)$$

provided that the specimen, in which \vec{M} is not zero, does not extend to infinity. \vec{R}_{PQ} is a distance vector from the points P to Q (Fig. 4.4). After integration along the z -axis in Eq. (82), therefore, we get

$$\phi(p) = \frac{e}{\hbar} \mu_0 \int_{\text{specimen}} dV_Q \frac{[\vec{M}(Q) \times \vec{r}_{pq}]_z}{r_{pq}^2},\quad (85)$$

where the point $p = (x, y)$ and q are projections of the points P and Q onto a plane perpendicular to the z -axis, respectively. \vec{r}_{pq} is the distance vector from the point p to q

on the plane.

A magnetic specimen may be composed of several magnetic domains in such a way that the magnetization is not continuous across domain boundaries but is differentiable within each domain. In such a case, by performing the partial integration of Eq. (85), we obtain

$$\phi(p) = \frac{e}{h} \mu_0 \sum_{\text{domains}} \left\{ \int_{\text{surface}} dS_Q [\vec{n} \times \vec{M}(Q)]_z \cdot \log r_{pq} - \int_{\text{domain}} dV_Q [\vec{\nabla} \times \vec{M}(Q)]_z \cdot \log r_{pq} \right\}, \quad (86)$$

where the summation is taken over all domains in the specimen, and \vec{n} is the outward unit vector normal to each domain surface.

To simulate the perpendicular magnetic recording films, I adopt a model of simple alternating step-magnetizations in which the magnetization \vec{M} in each bit is uniform as shown in Fig. 4.4. Then the second term in Eq. (86) vanishes, and

$$\phi(p) = \frac{e}{h} \mu_0 D \sum_{\text{bits}} \oint ds_q [\vec{v} \times \vec{M}(q)]_z \cdot \log r_{pq}, \quad (87)$$

where the integral is performed along the outline of each projected bit with the outward normal vector \vec{v} , and D is the thickness of the specimen along the z -direction. Then,

$$\phi(p) = \frac{e}{h} \mu_0 D \cdot \Delta M \sum_{\text{bit boundaries}} \int_0^d dy \cdot \log r_{pq}. \quad (88)$$

Here, $\Delta M = 2M$, and the summation is taken over all bit boundaries. The contribution from a single bit boundary $A_n - B_n$ (see Fig. 4.4) is calculated to be

$$\Delta\phi_n(p) = \frac{e}{h} \mu_0 D \cdot \Delta M \cdot \begin{cases} y \cdot \log |y| - (y-d) \cdot \log |y-d| - d & (x = x_n) \\ \frac{1}{2} y \cdot \log \{(x-x_n)^2 + y^2\} - \frac{1}{2} (y-d) \cdot \log \{(x-x_n)^2 + (y-d)^2\} - d \\ \quad + (x-x_n) \{ \arctan(\frac{x-x_n}{y-d}) - \arctan(\frac{x-x_n}{y}) \} & (\text{otherwise}) \end{cases} \quad (89)$$

Here the phase value at a point $p = (x, y)$ is calculated by summing $\Delta\phi_n$ over all bit boundaries

$$\phi(x, y) = \frac{e}{h} \mu_0 D \cdot \Delta M \sum_n \Delta\phi_n(x, y). \quad (90)$$

The calculated result is shown in three-dimensional form in Fig. 4.5 (a). The magnetization $|\vec{M}|$ is assumed to be the saturation magnetization of the Co-Cr film 250 kA/m,

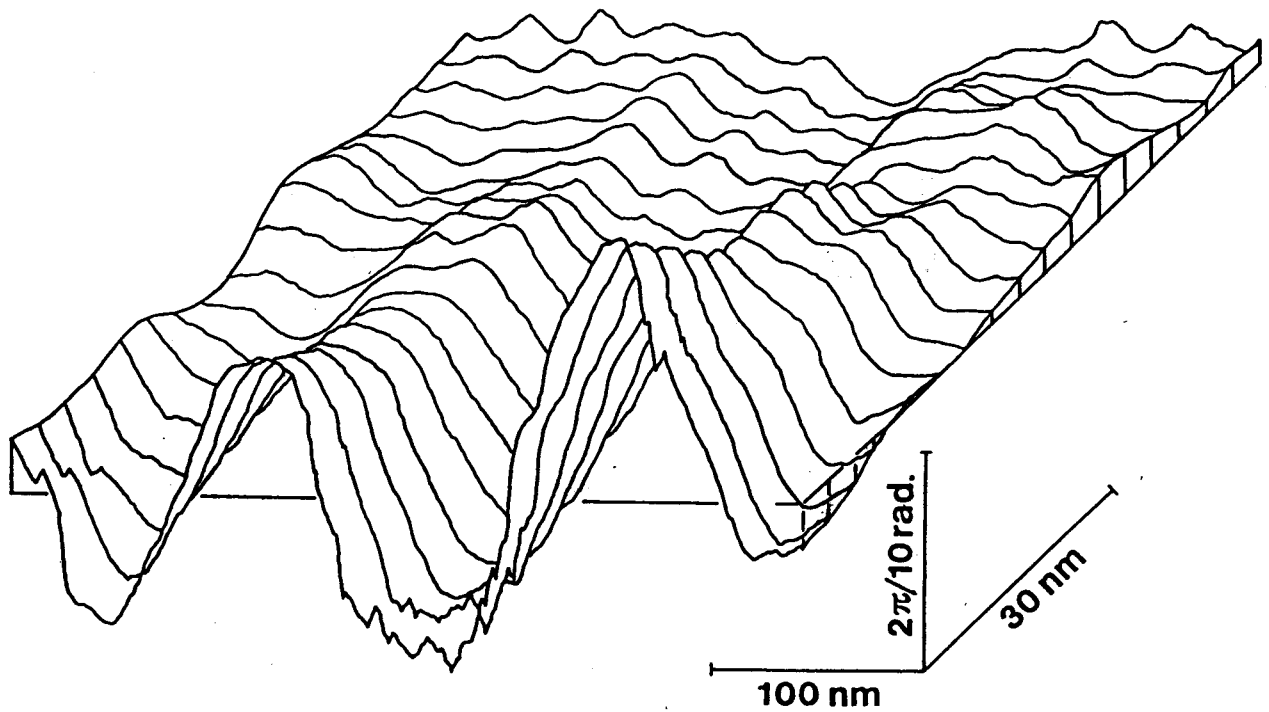
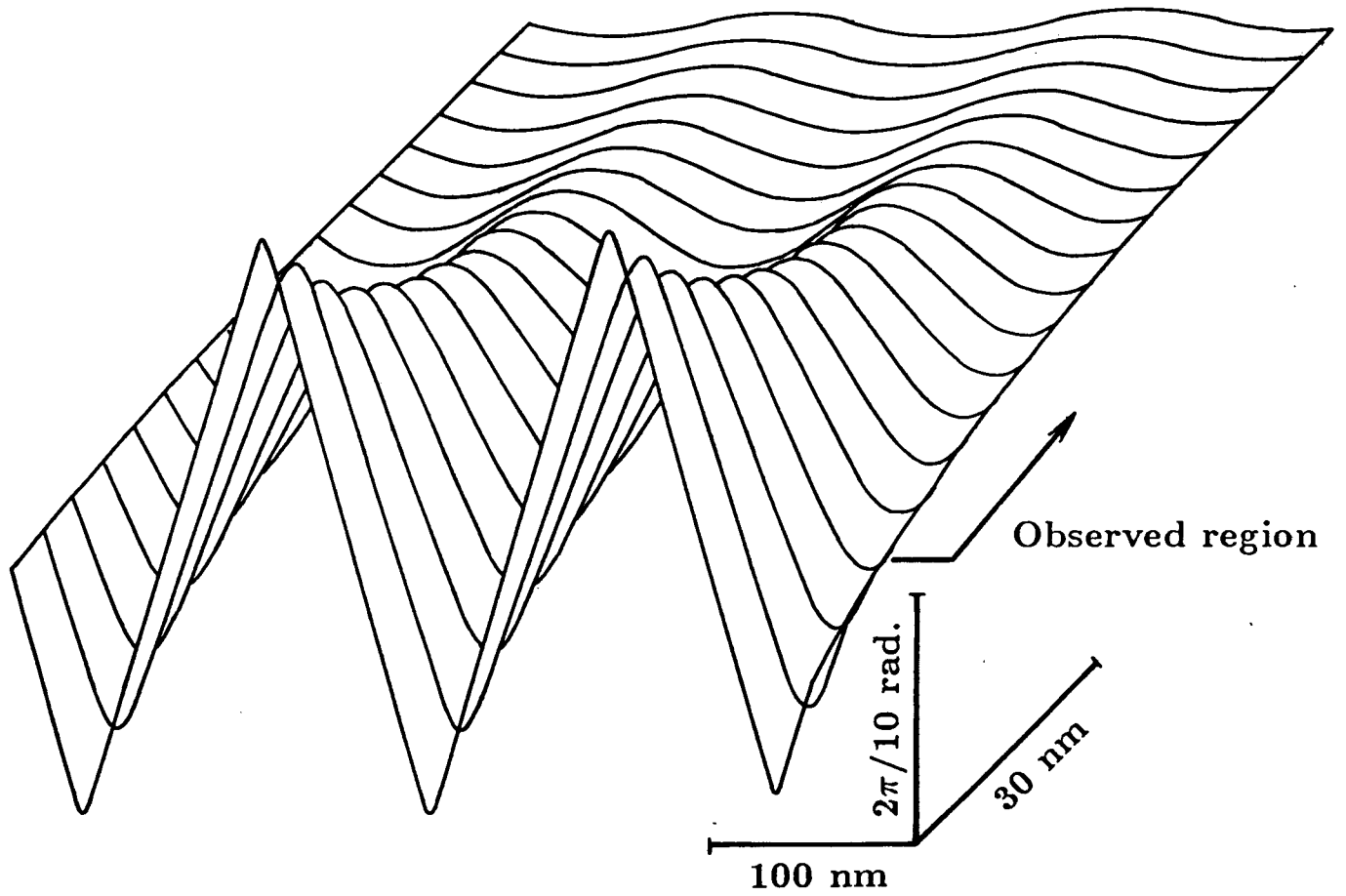


Fig. 4.5 Wavefront of the electron just passed through the leakage magnetic field from the Co-Cr film. (a) Simulated result using Eqs. (89) and (90). (b) Experimentally reconstructed result using the fringe scanning interferometry.

and $D = 80\text{nm}$, $d = 200\text{nm}$, and the bit length 85 nm . This result corresponds to the electron wavefront just passed through the stray field. The near side of the wavefront is adjacent to the top edge of the Co-Cr film. With increased distance from the film surface, the phase modulation of the electron wave decays.

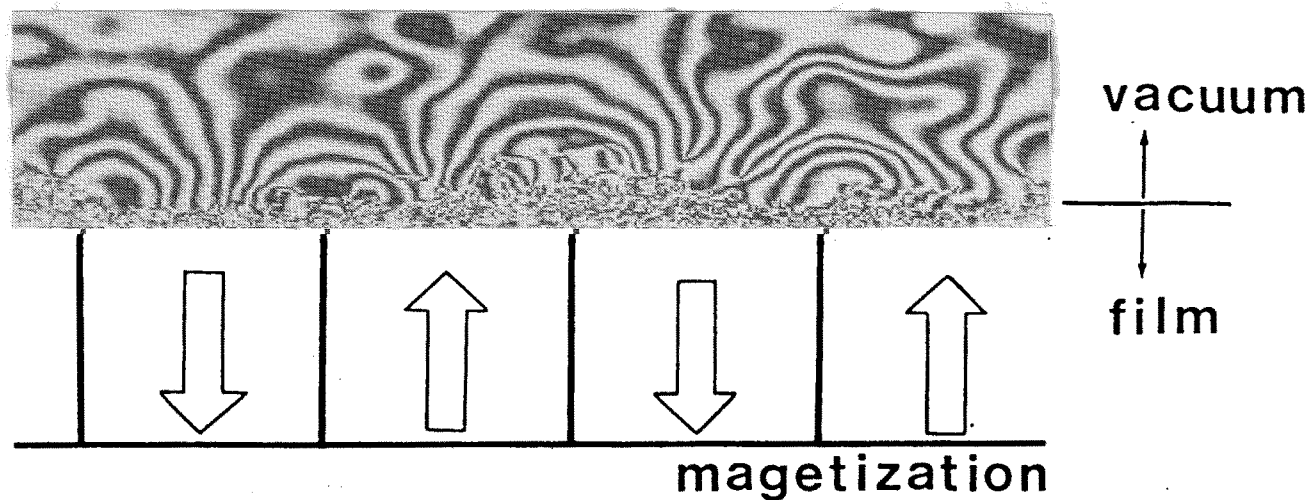
4.4 Experimental results and discussions

4.4.1 Observations of stray fields

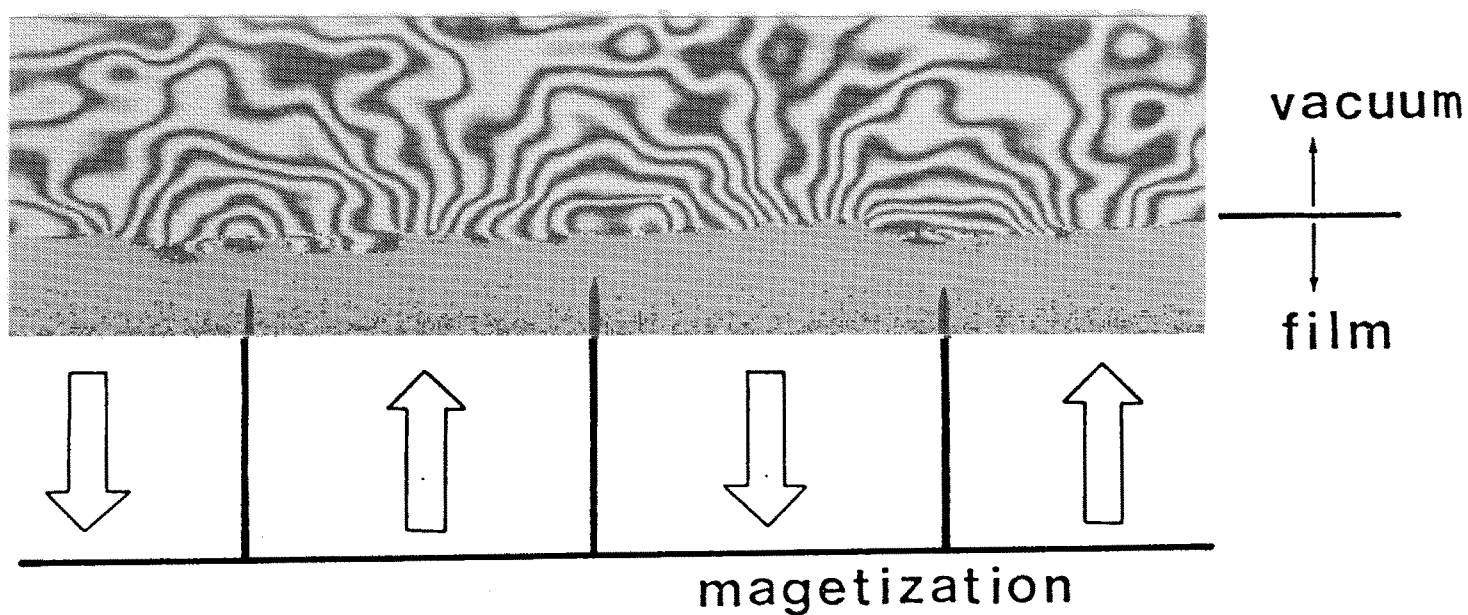
The numerically reconstructed wavefront of the electron wave passing near the top edge of the slice of the Co-Cr recording film is shown in Fig. 4.5 (b). The specimen was a 300 kFCI perpendicularly magnetized Co-Cr film in 80 nm thickness. Since the sign of the phase shift, i.e. retardation or advance in wave propagation, is automatically determined in the fringe scanning interferometry, the 3D form of the wavefront can be completely reconstructed. The deformation of the wavefront decreases with increase of the distance from the film edge. A phase shift of smaller than $2\pi/10\text{ rad.}$ is successfully detected at a high signal-to-noise ratio. The near side of the wavefront is not adjacent to the top edge of the Co-Cr film, because the B-protective layer of 15 nm thickness covers the film surface. Comparing with the calculated wavefront of Fig. 4.5 (a), therefore, the steep phase change just near the Co-Cr film surface was not observed.

If the magnetic field generated by the recording head reached the bottom of the Co-Cr layer at the recording process and the layer was wholly magnetized to the bottom as shown in Fig. 4.3, the straying field from the bottom edge as well as from the front edge of the sliced Co-Cr film had been expected to be detected. However, the wavefront deformation by the field straying from the bottom edge of the sliced film was not observed within the present experimental precision, implying that the recorded magnetization in the film does not penetrate to the bottom. This suggests the complex magnetic-domain structures to terminate the magnetic flux flow inside the specimen.

The contour phase lines of the wavefront was next calculated from the numerical data of the phase distribution to obtain an interference micrograph. Figure 4.6 (a) shows the result in a contour phase map of $2\pi/60$ interval. In the figure, the area of the recording



(a)



(b)

Fig. 4.6 Interference micrographs showing the stray magnetic fluxes from the Co-Cr films. The recording densities are (a) 300 *kFCI* (85 *nm*-bit length) and (b) 200 *kFCI* (127 *nm*-bit length), respectively. The degrees of the phase-difference amplifications are (a) 60 and (b) 72, respectively, showing that one interference fringe corresponds to magnetic flux of $\frac{h}{60e}$ and $\frac{h}{72e}$, respectively.

film is shown as random contrast because the electron wave could not penetrate the film and no phase information from the area was obtained. The roughness of the film edge seems to have been caused partly by slicing the sample. The lines are also magnetic flux lines in units of $h/60e (= 6.8 \times 10^{-17} Wb)$. The magnetic flux is clearly observed to flow out from a bit region and flow into the neighboring both sides of the 85-nm-length bit. A flux of $(0.14 \pm 0.02)(h/e)$ per bit emerges. The leakage field spreads approximately 70 nm from the B film surface (or 85 nm from the Co-Cr surface), indicating that the magnetic head must be taken down to 70 nm close to the surface of the recording medium in order to read out the recorded information in a magnetic recording system. Figure 4.6 (b) shows the interference micrograph with 72 times phase-difference amplification, taken from a specimen of 200 kFCI recording (127 nm bit length). Similar results are also observed in this case.

Figure 4.7 shows the interference micrographs with phase-difference amplifications of (a) 2, (b) 10, (c) 30, (d) 60, (e) 100 times, respectively. These were calculated from the same phase data numerically obtained as shown in Fig. 4.5 (b). Once the phase value at every point on the image is obtained by the fringe scanning interferometry, magnetic flux lines can be drawn in arbitrary units. More detailed information on magnetic flux distributions can be visualized with higher phase-difference amplifications. In Fig. 4.7 (e), a magnetic flux as small as $h/100e (= 4.1 \times 10^{-17} Wb)$ is successfully visualized with high spatial resolution. Phase sensitivity, hitherto obtained only using the previous techniques with photographic processing, was as low as that of Fig. 4.7 (c). The fringe scanning interferometry has improved the detection sensitivity for magnetic flux by approximately three times.

Fringe fluctuations in the micrographs seem to be due to granular noise in the hologram, speckle noise, and the Fresnel diffraction effect from the central thin wire of the electron biprism. Such noises are also faithfully visualized with higher phase-difference amplifications. Phase measurement error in the fringe scanning interferometry is caused mainly from control error in the PZT movement [4.18], which was suppressed to less than $2\pi/400$ in this experiment.

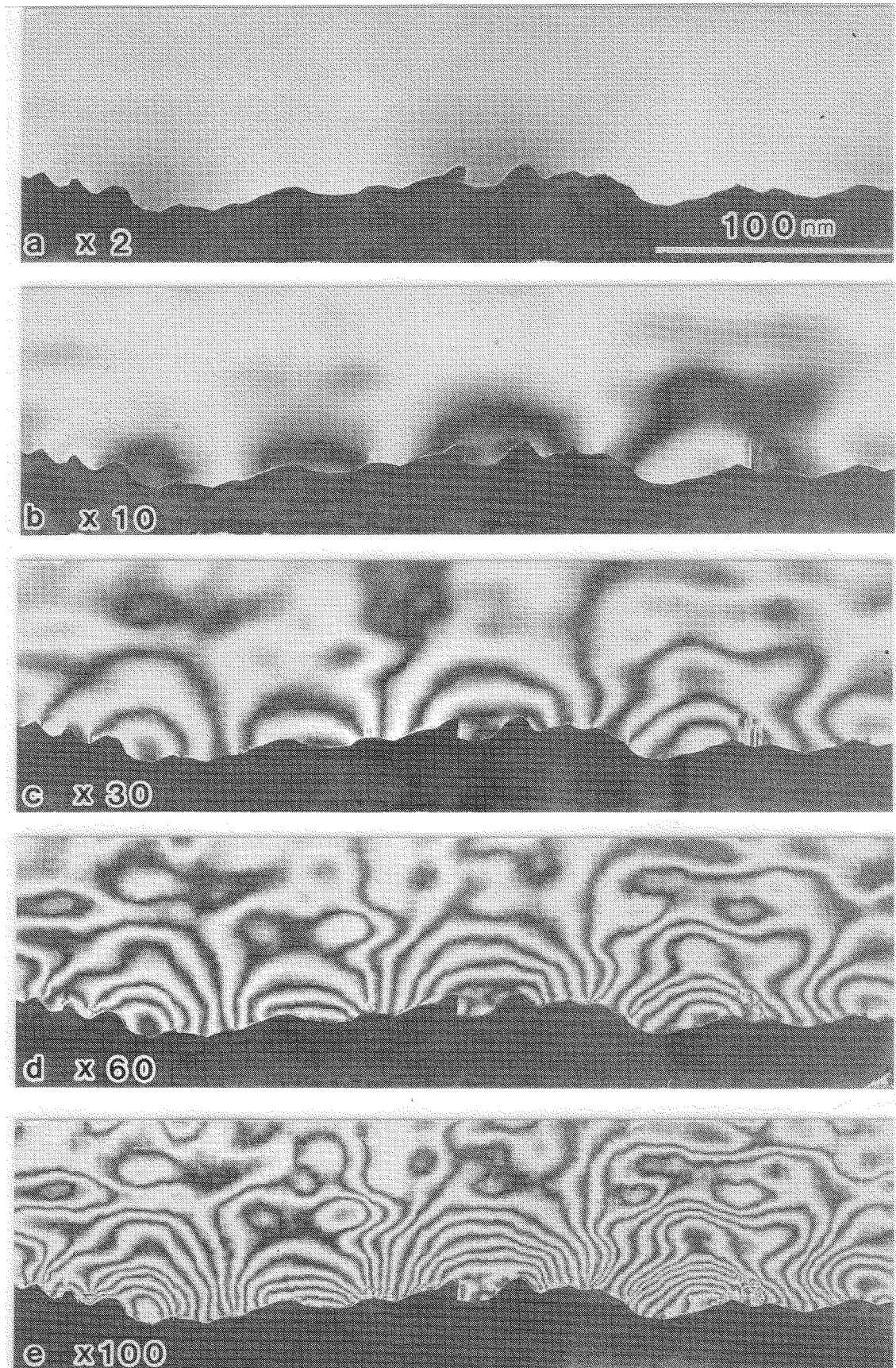


Fig. 4.7 Interference micrographs with phase-difference amplifications of (a) 2, (b) 10, (c) 30, (d) 60, and (e) 100 times, respectively, calculated from the same phase data measured by the fringe scanning interferometry. One interference fringe corresponds to a magnetic flux of (a) $\frac{1}{2}$, (b) $\frac{1}{10}$, (c) $\frac{1}{30}$, (d) $\frac{1}{60}$, and (e) $\frac{1}{100}$ of $\frac{h}{e}$, respectively.

4.4.2 Analysis of stray fields

Although the interference micrographs shows the magnetic flux flow with a definite flux unit, the direction of the flow cannot be determined. On the other hand, from the gradients of the reconstructed wavefront of Fig. 4.5 (b), we can distinguish the direction of the magnetic flux flow. From the numerical data of the phase distribution $\phi(x, y)$, I calculated its derivatives, $\frac{\partial\phi(x, y)}{\partial x}$ and $\frac{\partial\phi(x, y)}{\partial y}$. As indicated by Eqs. (65) and (66), the derivatives correspond to the quantities of the field vector components, B_y and B_x , integrated along the electron trajectory. The results are shown in Fig. 4.8 (b) and (c) in which the quantities are presented in gray scale. White means positive values (upward vector) and black, negative (downward vector). The figures clearly show that the stray field turns over bit by bit. The direction of the field vector is in this way automatically determined by the numerical data acquisition with the fringe scanning interferometry. Although Fig. 4.8 (b) and (c) do not directly show the distribution of the field vector components themselves, we can obtain the qualitative information on their distribution from the figures. Contrast variation parallel to the specimen surface in Fig. 4.8 (c) is caused by the Fresnel diffraction effect from the electron biprism.

The solid lines in Fig. 4.9 shows the line profiles of the phase distribution along the lines indicated in the interference micrograph shown in the lower. The profiling lines are (b) 10 nm, (c) 20 nm, (d) 30 nm, (e) 40 nm, and (f) 50 nm apart from the surface of the recording material, or above the B-protective layer. The phase changes sinusoidally and its variation amplitude decays with the distance from the specimen surface. The phase variation along the line f-f approximately corresponds to the detection limit of the phase change, $\sim \frac{2\pi}{100}$.

The solid lines in Fig. 4.10 are the line profiles of the phase derivative $\frac{\partial\phi(x, y)}{\partial x}$ along the lines indicated in the lower gray-scale image. The profiling lines are (b) 10 nm, (c) 20 nm, (d) 30 nm, (e) 40 nm, and (f) 50 nm apart from the specimen surface.

It is not straightforward to derive the vector component $B_y(x, y, z)$ from $\frac{\partial\phi(x, y)}{\partial x}$, (see Eq. (65)), because the distribution of the $B_y(x, y, z)$ along the z -direction is unknown. In fact, the field variations along the z -direction near the edge of the specimen surface are calculated as shown in Fig. 4.11. These results were obtained by summing up the

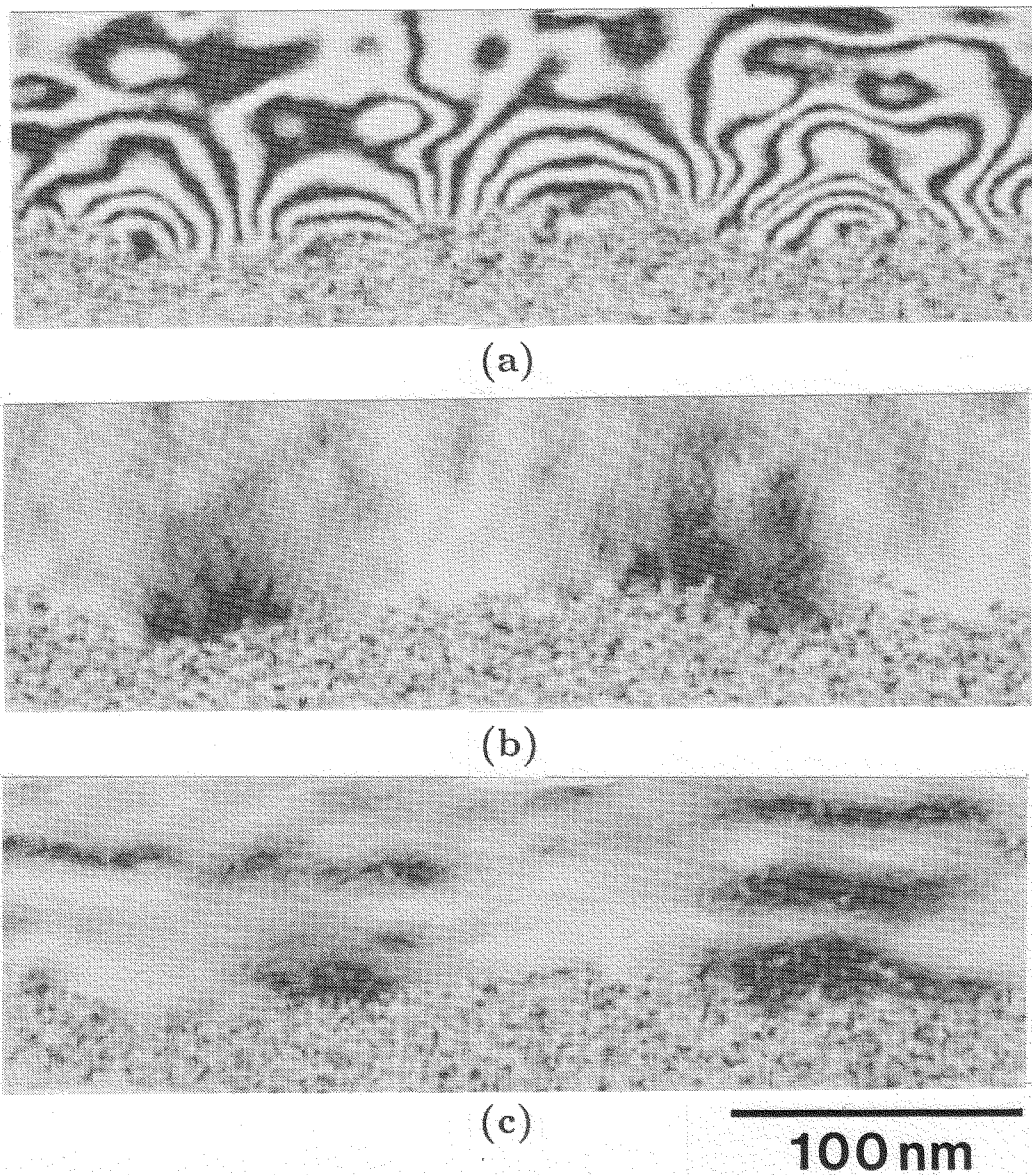


Fig. 4.8 Analysis of leakage magnetic field from the 300 *kFCI*-perpendicular magnetic recording film. (a) Interference micrograph showing magnetic flux distribution in units of $\frac{h}{60e}$ flux. (b) The phase derivative $\frac{\partial\phi(x,y)}{\partial x}$, which approximately corresponds to the perpendicular component of the leakage magnetic field vector, is displayed in a gray scale image. White means positive values (upward vector) and black means negative (downward vector). The degree of brightness indicates the absolute value of the components. (c) The phase derivative $\frac{\partial\phi(x,y)}{\partial y}$, which approximately corresponds to the parallel component of the leakage magnetic field vector, is displayed in a gray scale image.

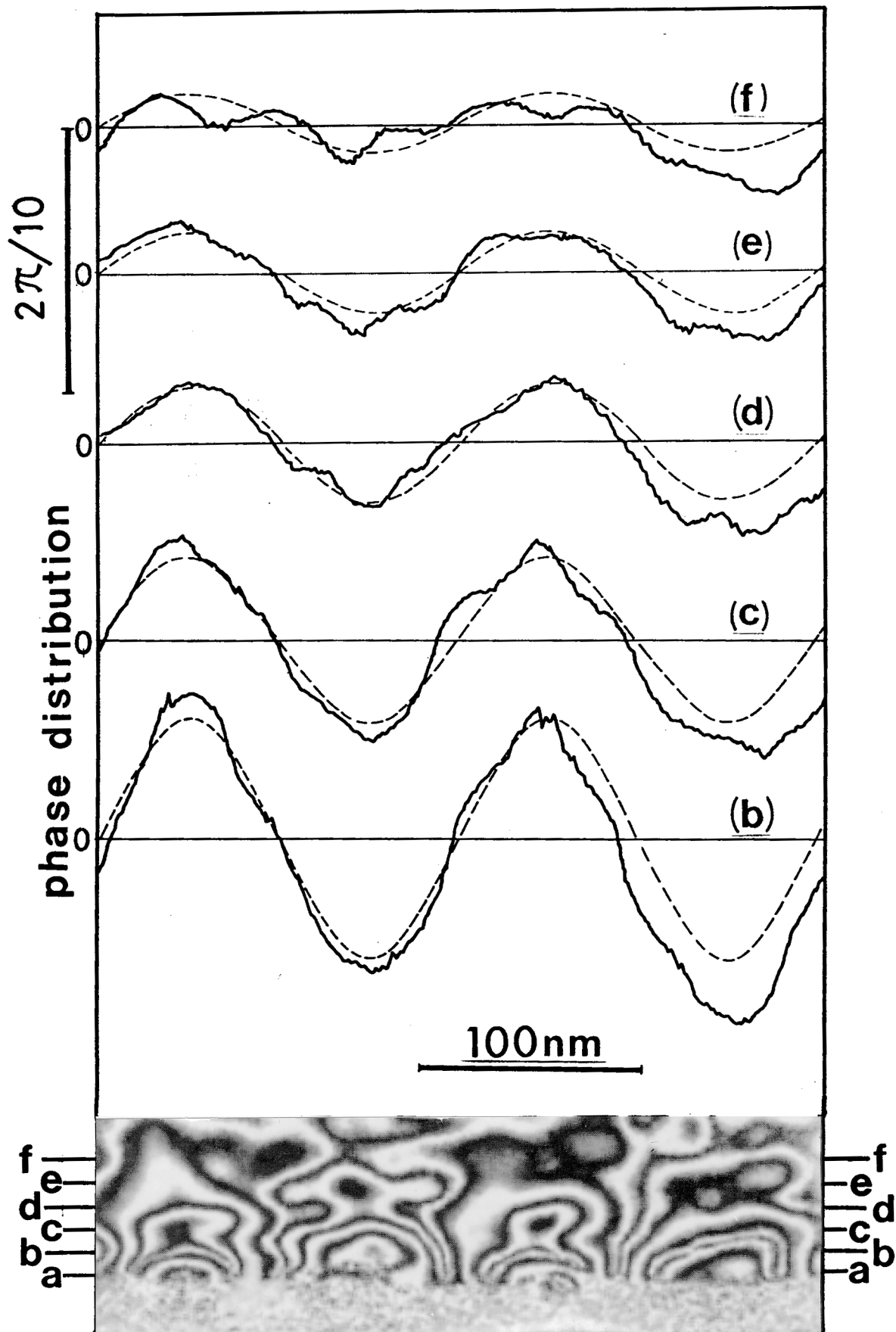


Fig. 4.9 Line profiles of the phase distribution along the cross lines in the lower interference micrograph. The lines are (b) 10 nm, (c) 20 nm, (d) 30 nm, (e) 40 nm, (f) 50 nm, respectively, apart from the film surface.

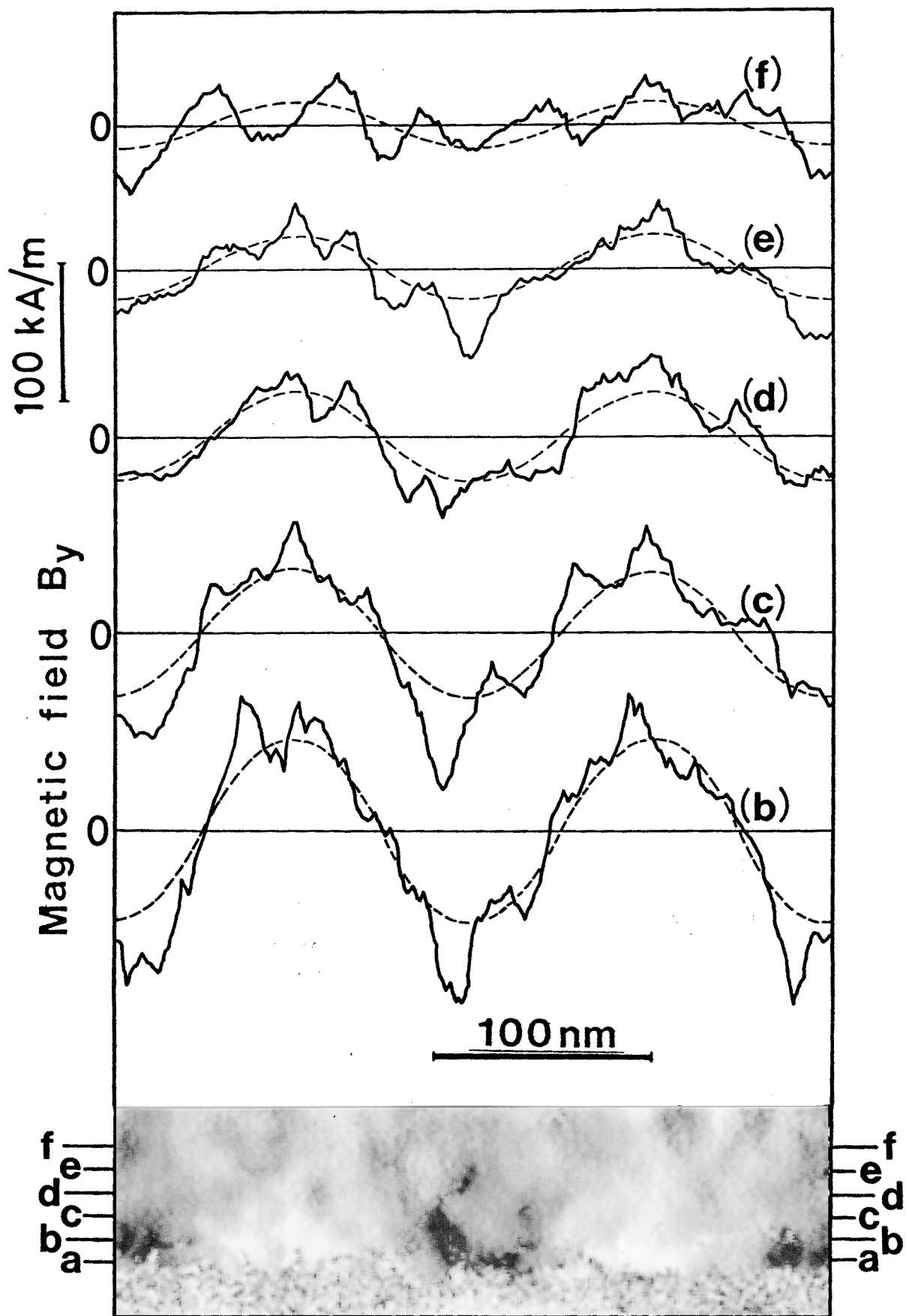


Fig. 4.10 Line profiles of the phase derivative $\frac{\partial\phi(x,y)}{\partial z}$ along the cross lines in the lower gray-scale image. The lines are (b) 10 nm, (c) 20 nm, (d) 30 nm, (e) 40 nm, (f) 50 nm, respectively, apart from the film surface. The phase derivative approximately corresponds to the perpendicular component of the stray field.

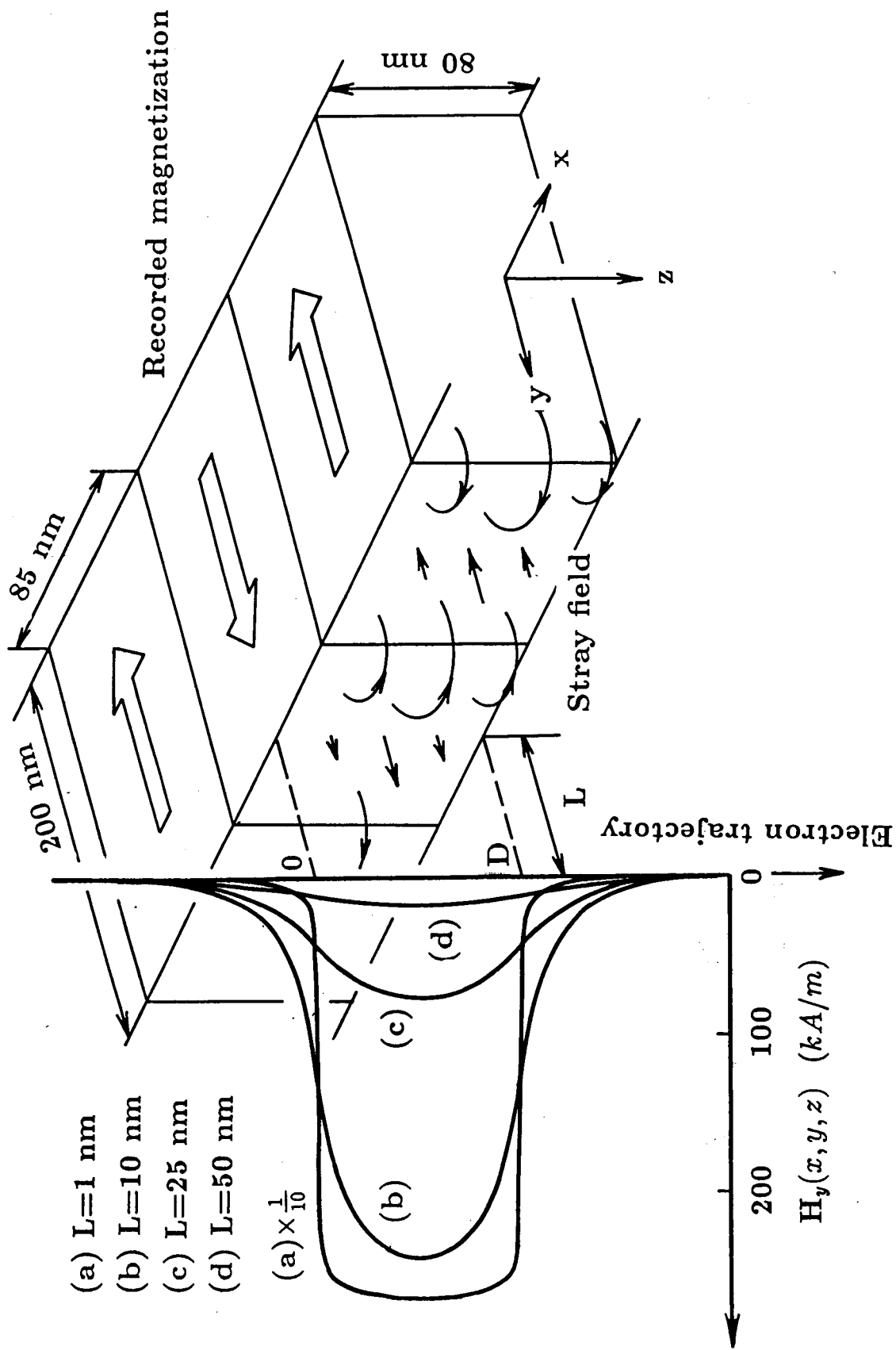


Fig. 4.11 Perpendicular component of the stray field $H_y(x, y, z)$. Its line profiles along the electron trajectories (z -direction) apart from the recorded material by the distance L . These were calculated with the simple step-magnetization model for the perpendicularly magnetized pattern.

fields originating from a lot of small magnetic dipoles composing each bit of the recording material. As a matter of course, the field is restricted only at the space above the film surface just near the film edge ($L = 1nm$), while the field spreads broader with increased distance L from the film edge. Because of the field distribution along the z -direction like this, it is impossible, in general, to decompose the field vector from the phase distribution. Such a problem, the decomposition of the three-dimensional field distribution from its two-dimensional projections along the direction of view, will be discussed in Chapter 5. In this Chapter, I simply assume the field distribution along the z -direction such that the stray field strength is non-zero constant B_{y0} only in front of the film edge ($0 < z < D$) and zero elsewhere, in order to estimate the leakage field strength. Obviously the validity of this assumption becomes worse with increased distance L in the y -direction from the specimen surface as shown in Fig. 4.11. The phase derivative $\frac{\partial\phi(x,y)}{\partial x}$, then, can be directly connected to B_{y0} as described in Eq. (81). The line profiles shown in Fig. 4.10, therefore, approximately correspond to the distributions of $H_y(x, y, z)$ itself with the amplitude indicated at the ordinate. That is, the perpendicular component of the leakage field varies sinusoidally with approximately 100 kA/m peak height on the profiling line (b). The error caused by the assumption above mentioned is estimated to be $\sim 15\%$ by comparing the calculated field distribution of Fig. 4.11.

The broken lines in Figs. 4.9 and 4.10 show the calculated results of the phase distributions and its derivatives, respectively, using the simple step-magnetization model Eq. (90) (Fig. 4.4). The calculate and experimental curves qualitatively agree well in spite of noise fluctuation. The line profiles in Fig. 4.10 indicate that the field direction does not seem to turn over so abruptly at the bit boundaries. This is because the profiling lines are apart from the specimen so that the abrupt change in the field direction is smeared out. If I can observe the closer space above the Co-Cr film surface, I obtain more detailed information on the magnetizations inside the Co-Cr film. Especially, the magnetization at the bit center is expected to be reduced due to demagnetization effect [4.19]. A finite transition width at the bit boundary, moreover, may exists. Such detailed magnetization will be revealed by the electron holographic observation of the stray field just above the Co-Cr film surface.

4.5 Conclusions

Phase sensitivity in electron holography has been improved up to $\sim 2\pi/100$ by introducing the fringe scanning interferometry at the optical reconstruction stage, combined with the phase-difference amplification techniques. This sensitivity allows the detection of magnetic flux as small as $h/100e (= 4.1 \times 10^{-17} \text{Wb})$ with high spatial resolution. With this technique, the magnetic recording in perpendicular magnetization mode with 300 *kFCI* recording density in a Co-Cr film has been confirmed for the first time by direct observation of the stray field.

Chapter 5

Phase Tomography in Electron Holography

5.1 Introduction

As described in Chapter 3, the fringe scanning interferometry has made possible to fully read out the phase information recorded on an electron hologram, and to numerically map the phase distribution of an electron wave. Then, the method may provide more detailed analysis on physical quantities such as electromagnetic fields. As mentioned in Section 2.5, the derivatives of the phase distribution $\phi(x, y)$ of an electron wave correspond to the line integrals of the components of electromagnetic field vectors, \vec{E} and \vec{B} , along the direction of view, z -axis;

$$\frac{\partial\phi(x, y)}{\partial x} = -\frac{e}{\hbar v} \int_{-\infty}^{\infty} dz E_x(x, y, z), \quad (91)$$

$$\frac{\partial\phi(x, y)}{\partial y} = -\frac{e}{\hbar v} \int_{-\infty}^{\infty} dz E_y(x, y, z) \quad (92)$$

for electric fields, and

$$\frac{\partial\phi(x, y)}{\partial x} = \frac{e}{\hbar} \int_{-\infty}^{\infty} dz B_y(x, y, z), \quad (93)$$

$$\frac{\partial\phi(x, y)}{\partial y} = -\frac{e}{\hbar} \int_{-\infty}^{\infty} dz B_x(x, y, z) \quad (94)$$

for magnetic fields. We cannot obtain any information on the line-of-sight (z -) components of the fields from the electron phase data. These equations implies that the three-dimensional (3D) fields are two-dimensionally (2D) projected along the direction of view. In magnetic case, for example, $\frac{\partial\phi(x, y)}{\partial x}$ and $\frac{\partial\phi(x, y)}{\partial y}$ are regarded as the 2D projections of $B_y(x, y, z)$ and $B_x(x, y, z)$ along the z -direction, respectively. This is because of the relatively large depth of focus of the electron microscope. This Chapter is devoted to describing the technique for the deconvolution of the line-of-sight integrals to get each

competent of the field vectors from their projections, $\frac{\partial\phi(x,y)}{\partial x}$ and $\frac{\partial\phi(x,y)}{\partial y}$. In Chapter 6, I actually utilize the method for analyzing the internal magnetic field distributions of a quantized magnetic flux in superconductor. This is one of new attempts to spread the availability of electron holography.

The problems of reconstruction of 3D field distributions or 3D structure of an object from their 2D projections have intensively investigated in various fields of science and technology including computerized tomography [5.1][5.2][5.3]. With light beams, X-rays, electron beams, ions, neutrons, sound waves, and others, 2D images of 3D fields or objects, projected from different directions, can be used to reconstruct the original 3D structures. Rowly [5.4] showed the reconstruction of the refractive index field of an 3D phase object from multidirectional interferometric data with light waves, which enabled the analysis of density and temperature distributions in plasma, gas, and others [5.5]~[5.7]. Bracewell [5.8] has applied the method to radio astronomy, reconstruction of 2D radio sky with a strip-scan radio antenna. Since some electron microscopic images may be interpreted as projections of the specimen, DeRosier and Klug [5.9]~[5.11] have developed to synthesize the 3D structure of the specimen from a number of its electron micrographs. Oldendorf [5.12], Kuhl and Edwards [5.13], and Cormack [5.14] independently applied the method to medical diagnostic purpose, well known as X-ray computerized tomography, the most significant application to date of image reconstruction from projections. The technique has now been widely applied to microscopy, defectoscopy of industrial goods, solid state physics, geophysics, Earth and planetary atmospheric physics, aero- and hydrodynamics, plasma physics, analytic chemistry, medical diagnostics, and others.

The first important contribution to the general theory of 3D reconstruction appears to be that of Radon [5.15]. His inversion formulas are the basis of many modern developments, both theoretical and practical. A number of different algorithms for the reconstruction from projections have been known, which may be roughly classified into four groups; 1) back projection, 2) analytic method including the direct inversion and the Fourier synthesis, 3) series expansion method, and 4) iterative method. An appropriate algorithm is chosen, taking into account the structure of the object under investigation, angle range of direction of view, noise, measurement time, and others. They are compared

and discussed in several reviews [5.3][5.6][5.15]~[5.17].

While the physical quantities measured in most of 3D reconstruction experiments have been scalar ones such as refractive index, absorption coefficients for X-rays and electron beams, and so on, the present work treats the reconstruction of the 3D distributions of vector fields, magnetic (and electric) fields from their 2D projections. The projections are measured in the form of the phase distributions of the electron waves transmitted through the fields. In principle, all known algorithms for the reconstruction of scalar quantities can be utilized for each component of the field vectors.

A general consideration on the algorithms is given in Section 5.2 in which no symmetry of the investigated fields is assumed. A simplified version of the theory are presented in Section 5.3 by introducing axisymmetry of the test field, in which a single projection data is enough for the reconstruction of the field. The algorithm derived here will be utilized in the analysis of the internal magnetic field distribution of quantized magnetic fluxes in superconductors in Chapter 6. The tomographic analysis has been made possible owing to the digital format of the electron phase distributions obtained by the fringe scanning interferometry.

5.2 Reconstruction of electromagnetic fields

I restrict myself only to the reconstruction of magnetic fields, since the same discussion developed here can be also applied to the electric field. In order to obtain the inverse relations between the field vectors and the phase distributions in Eqs. (93) and (94), we must collect the phase distribution data of the electron waves that traverse the test field in a variety of directions. The phase data obtained by such multi-directional interferometry can be used to reconstruct the 3D field distributions.

Although the electron path passing through the field under investigation are, in general, curved by the field, I assume the field to be weak enough that the path curvature is minor and the line integral in Eqs. (93) and (94) can be evaluated along a straight line parallel to the z -axis.

Consider the rotation of the sample, which carries the test field, around the y -axis by an angle α as shown in Fig. 5.1 (a). The coordinate system (ξ, y, ζ) is fixed on the

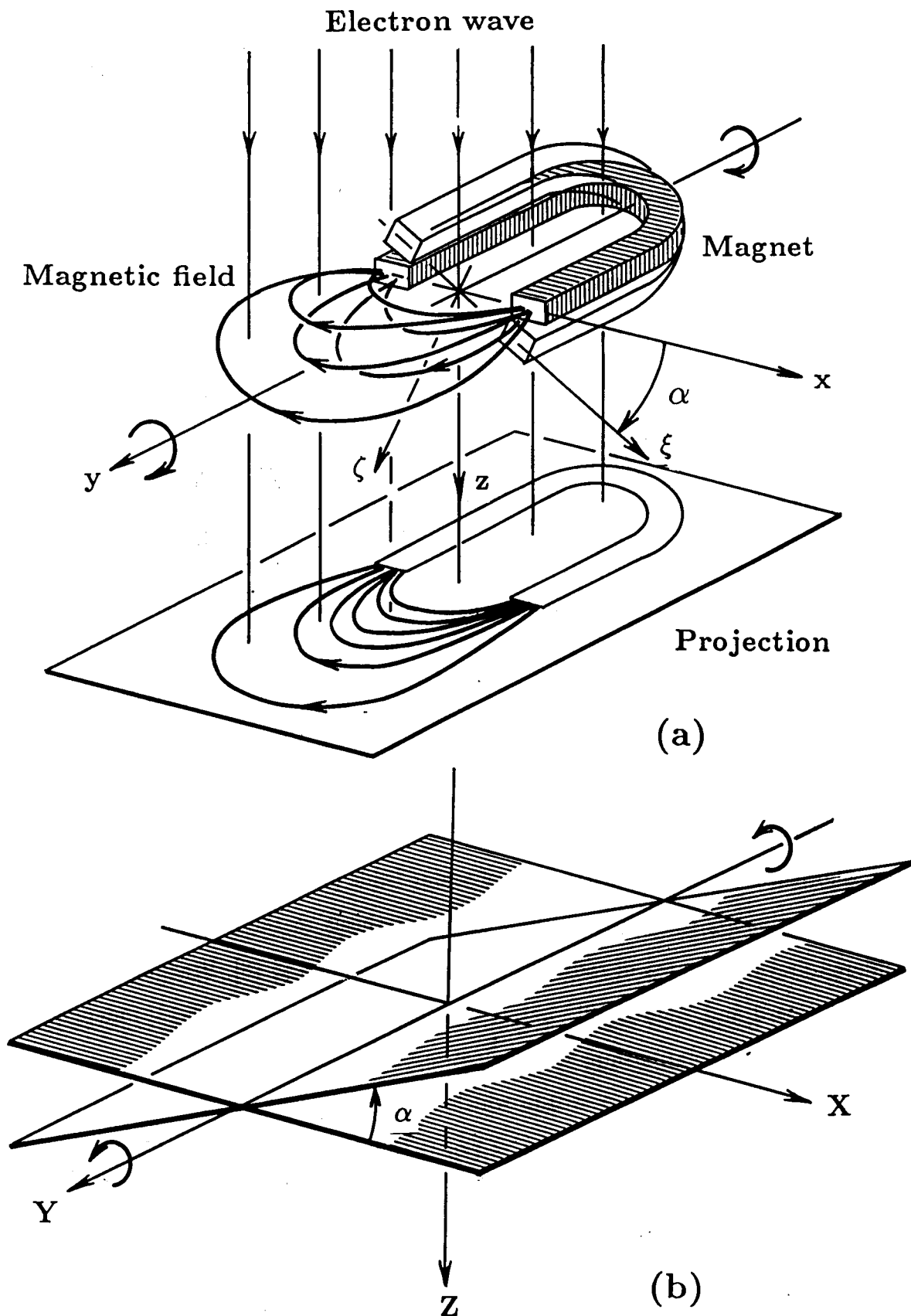


Fig. 5.1 Notation for the Fourier analysis of the 3D distribution of magnetic field. (a) At each rotation angle α around the y -axis, an electron hologram is taken to record the phase distribution of the electron wave transmitted through the field. (b) The phase distribution at the sample rotation angle α determines the values of the Fourier transform on a plane through the y -axis with rotation angle α in the reciprocal space with respect to x and z .

sample, and the system (x, y, z) on the electron microscope;

$$\xi = x \cos\alpha + z \sin\alpha, \quad (95)$$

$$\zeta = -x \sin\alpha + z \cos\alpha. \quad (96)$$

If the phase distribution of the electron wave transmitted through the rotated test field is expressed as $\phi(x, y; \alpha)$, Eqs. (93) and (94) are rewritten as

$$\frac{\partial\phi(x, y; \alpha)}{\partial x} = \frac{e}{\hbar} \int_{-\infty}^{\infty} dz B_y(\xi, y, \zeta), \quad (97)$$

$$\frac{\partial\phi(x, y; \alpha)}{\partial y} = -\frac{e}{\hbar} \left\{ \sin\alpha \cdot \int_{-\infty}^{\infty} dz B_\xi(\xi, y, \zeta) - \cos\alpha \cdot \int_{-\infty}^{\infty} dz B_\zeta(\xi, y, \zeta) \right\}. \quad (98)$$

In the absence of any symmetry in the test field, we must, in principle, collect the phase data $\phi(x, y; \alpha)$ over a π -range-of-viewing angle $(-\frac{\pi}{2} \leq \alpha \leq \frac{\pi}{2})$ to reconstruct the investigated field $\vec{B}(\xi, y, \zeta)$.

From Eq. (97), the y -component $B_y(\xi, y, \zeta)$ of the test field can be derived from the collected data $\frac{\partial\phi(x, y; \alpha)}{\partial x}$ by following the usual algorithms developed for scalar field reconstruction. I present an example of reconstruction algorithm using the Fourier transform which will be specialized in Section 5.3 for the analysis of axisymmetric magnetic field. Other algorithms for the reconstruction of scalar fields [5.3][5.7][5.15]~[5.17] can also be applied to derive B_y component. The Fourier synthesis method appears to have been considered first in the area of radioastronomy by Bracewell [5.18], Bracewell and Riddle [5.8], and Smerd and Wild [5.19]. Later, DeRosier and Klug [5.9]~[5.11] independently developed the same relationships for applications in electron microscopy.

Consider a single view of $\alpha = 0$ in which Eq. (97) turns again to Eq. (93). Taking the 2D Fourier transform of both sides of Eq. (97) with respect to x and y , we get

$$\begin{aligned} \mathfrak{F}_{xy}\left[\frac{\partial\phi(x, y; 0)}{\partial x}\right] &= \int_{-\infty}^{\infty} dx \int_{-\infty}^{\infty} dy \frac{\partial\phi(x, y; 0)}{\partial x} e^{2\pi i(Xx + Yy)} \\ &= \frac{e}{\hbar} \int_{-\infty}^{\infty} dx \int_{-\infty}^{\infty} dy \int_{-\infty}^{\infty} dz B_y(x, y, z) e^{2\pi i(Xx + Yy + Zz)} \Big|_{z=0} \\ &= W(X, Y, Z) \Big|_{z=0}, \end{aligned} \quad (99)$$

where $W(X, Y, Z)$ denotes the 3D Fourier transform of $B_y(x, y, z)$. The last expression in Eq. (99) indicates that the 2D Fourier transform of the phase derivative data $\frac{\partial\phi(x, y)}{\partial x}$ for a view normal to the (xy) -plane is equal to the 3D Fourier transform of $B_y(x, y, z)$ evaluated

on the (XY) -plane in the reciprocal space. This is known as the central-slice theorem. The theorem generally tells us that the Fourier transform of a 2D projection of a 3D object is identical with the corresponding central section of the 3D Fourier transform of the object. The result Eq. (99) can be generalized to include all values of α between $\pm\frac{\pi}{2}$. In other words, $\mathfrak{S}_{xy}[\frac{\partial\phi(x,y;\alpha)}{\partial x}]$ gives the values on a plane which contains the Y -axis and rotates by an angle α around the Y -axis (Fig. 5.1 (b)) in the reciprocal space. The Fourier transform of data $\frac{\partial\phi(x,y;\alpha)}{\partial x}$ at each α can then build up a plane in the reciprocal space at a time until the entire reciprocal space is filled by rotating the sample. The projected views from various directions may be collected either by using a number of identical objects in different but identifiable orientations, or by examining a single object using a sample-tilting stage, or by a combination of these methods. The necessary information is accumulated in the computer memory. Then, $B_y(x, y, z)$ can be obtained by taking the inverse Fourier transform of collected data of $W(X, Y, Z)$;

$$B_y(x, y, z) = \int_{-\infty}^{\infty} dX \int_{-\infty}^{\infty} dY \int_{-\infty}^{\infty} dZW(X, Y, Z)e^{-2\pi i(Xx+Yy+Zz)}. \quad (100)$$

Since, in practice, the data can be collected for only finite number of views and positions, the algorithm mentioned above must be modified to accept discrete data by utilizing discrete Fourier transforms.

In the case of reconstruction of B_x (and B_z), the phase derivative $\frac{\partial\phi(x,y;\alpha)}{\partial y}$ (Eq. (98)) can not be utilized in a straightforward manner as in the case of B_y above mentioned, because Eq. (98) indicates that B_t and B_l components are intermixed by the specimen rotation around the y -axis, and their contributions to the phase distribution can not be separated.

There are two methods to obtain the distributions of B_x - and B_z - components. One is a general technique which is applicable to any field distributions. If the test field can be made rotate by angles between $-\frac{\pi}{2}$ and $\frac{\pi}{2}$ around the x -axis, instead of the y -axis, the same algorithm above mentioned for the B_y -component can be utilized for the decomposition of the B_x -component. The same analysis can be performed by rotating the sample by an angle $\frac{\pi}{2}$ around the z -axis, and by successive rotation around the y -axis between $\pm\frac{\pi}{2}$ to obtain the B_x -component. In order to derive the B_x -component, moreover, the rotation of the sample around the x -axis by an angle $\frac{\pi}{2}$ should be carried out before the multi-

directional interferometric measurement around the y -axis. This method in either case requires a specimen stage to rotate the specimen around three axes.

Another method to derive the distributions of the B_x - and B_z -components is by solving the Maxwell equations with use of the decomposed data of $B_y(x, y, z)$ as the boundary conditions on the boundary planes parallel to the (xz) -plane. This method is applicable only to the magnetic fields such that appropriate boundary conditions on other boundaries are *a priori* given. It is adequate for this method to rotate the specimen around a single axis, the y -axis, for the decomposition of the B_y -components. A similar, but not same, technique has been employed for global-scale 3D reconstruction of the magnetic field of the solar corona [5.20].

The analysis method must be chosen, taking into account the field structure under investigation as well as the apparatus performance.

5.3 The use of symmetry

I here develop a simplified algorithm for the reconstruction of axisymmetric magnetic fields for preparing the field analysis of quantized magnetic fluxes in superconductors in Chapter 6. The field is inhomogeneous only in the radial and axial directions, and can be three-dimensionally reconstructed from a single projection. I introduce the cylindrical polar coordinate (ρ, φ, y) with its axis on the y -axis to describe the field distribution (see Fig. 5.2). Because of φ -independence, $\vec{B}(x, y, z) = \vec{B}(\rho, y)$, and \vec{B} has only the ρ and y components.

I now employ the same algorithm as the reconstruction of the 3D structure from the electron microscopic images using the Fourier transform [5.9]~[5.11]. I at first calculate the Fourier transform $F(X, y)$ of Eq.(93) with respect to x ;

$$\begin{aligned} F(X, y) &\equiv \int_{-\infty}^{\infty} dx \cdot \frac{\partial \phi(x, y)}{\partial x} e^{2\pi i x X} \\ &= \frac{e}{\hbar} \int_{-\infty}^{\infty} dx \int_{-\infty}^{\infty} dz \cdot B_y(x, y, z) e^{2\pi i x X}. \end{aligned} \quad (101)$$

Transforming into the cylindrical coordinate, $B_y(x, y, z) = B_y(\rho, y)$;

$$F(X, y) = \frac{e}{\hbar} \int_0^{2\pi} d\varphi \int_0^{\infty} d\rho \cdot \rho \cdot B_y(\rho, y) e^{2\pi i \rho X \cos \varphi}. \quad (102)$$

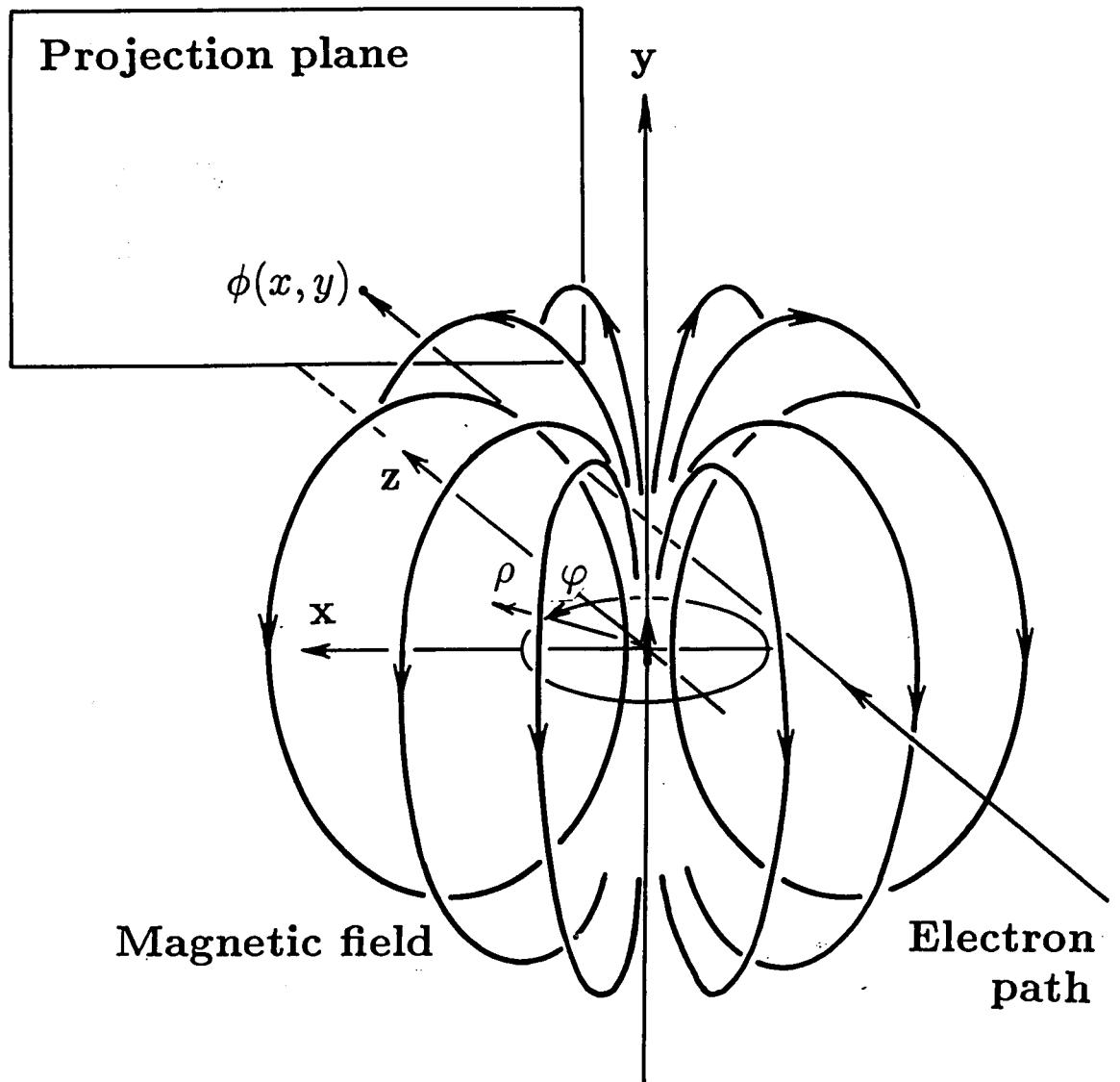


Fig. 5.2 Coordinate system to analyze an axisymmetric magnetic field, e.g. from a magnetic dipole.

Taking into account the definition of the n -th order Bessel function

$$J_n(x) = \frac{1}{2\pi i^n} \int_0^{2\pi} d\varphi \cdot e^{i(x \cos\varphi + n\varphi)}, \quad (103)$$

Equation (102) is rewritten as

$$F(X, y) = \frac{2\pi e}{\hbar} \int_0^\infty d\rho \cdot \rho \cdot B_y(\rho, y) \cdot J_0(2\pi\rho X). \quad (104)$$

After multiplying $X \cdot J_0(2\pi t X)$ to the both sides of Eq.(104), and integrating with X , we get

$$\int_0^\infty dX \cdot X \cdot F(X, y) \cdot J_0(2\pi t X) = \frac{2\pi e}{\hbar} \int_0^\infty d\rho \int_0^\infty dX \cdot \rho \cdot X \cdot B_y(\rho, y) \cdot J_0(2\pi\rho X) \cdot J_0(2\pi t X). \quad (105)$$

By replacing $\eta = 2\pi X$, the right hand side of Eq. (105) is

$$\frac{e}{2\pi\hbar} \int_0^\infty d\rho \int_0^\infty d\eta \cdot \rho \cdot \eta \cdot B_y(\rho, y) \cdot J_0(\rho\eta) \cdot J_0(t\eta). \quad (106)$$

Using the identity for the Fourier-Bessel transform for an arbitrary function $f(t)$,

$$f(t) = \int_0^\infty d\rho \int_0^\infty d\eta \cdot \rho \cdot \eta \cdot f(\rho) \cdot J_n(\rho\eta) \cdot J_n(t\eta), \quad (107)$$

Equation (106) is equivalent to $\frac{e}{2\pi\hbar} B_y(t, y)$. Consequently Eq.(105) is reduced to

$$B_y(\rho, y) = \frac{2\pi\hbar}{e} \int_0^\infty dX \cdot X \cdot F(X, y) \cdot J_0(2\pi\rho X). \quad (108)$$

Next the ρ -component of the field vector is derived from Eq. (94). Transforming into the cylindrical coordinate, Eq. (94) is rewritten as

$$\frac{\partial\phi(x, y)}{\partial y} = -\frac{e}{\hbar} \int_{-\infty}^\infty dz \cdot B_\rho(\rho, y) \cdot \cos\varphi. \quad (109)$$

Taking the Fourier transform with respect to x ,

$$\begin{aligned} S(X, y) &\equiv \int_{-\infty}^\infty dx \cdot \frac{\partial\phi(x, y)}{\partial y} \cdot e^{2\pi i x X} \\ &= -\frac{e}{\hbar} \int_{-\infty}^\infty dx \int_{-\infty}^\infty dz \cdot B_\rho(\rho, y) \cdot \cos\varphi \cdot e^{2\pi i x X} \\ &= -\frac{e}{\hbar} \int_0^{2\pi} d\varphi \int_0^\infty d\rho \cdot \rho \cdot B_\rho(\rho, y) \cdot \cos\varphi \cdot e^{2\pi i \rho X \cos\varphi} \end{aligned} \quad (110)$$

The φ -integral can be performed by taking into account the definition of the Bessel function Eq. (103);

$$S(X, y) = -\frac{2\pi i e}{\hbar} \int_0^\infty d\rho \cdot \rho \cdot B_\rho(\rho, y) J_1(2\pi\rho X). \quad (111)$$

After multiplying $X \cdot J_1(2\pi tX)$ to the both sides of Eq. (111), and integrating with X , we get

$$\int_0^\infty dX \cdot X \cdot S(X, z) \cdot J_1(2\pi tX) = -\frac{2\pi ie}{\hbar} \int_0^\infty d\rho \int_0^\infty dX \cdot \rho \cdot X \cdot B_\rho(\rho, y) \cdot J_1(2\pi\rho X) \cdot J_1(2\pi tX). \quad (112)$$

By replacing $\eta = 2\pi X$, the right hand side of Eq. (112) is

$$-\frac{ie}{2\pi\hbar} \int_0^\infty d\rho \int_0^\infty d\eta \cdot \rho \cdot \eta \cdot B_\rho(\rho, y) \cdot J_1(\rho\eta) \cdot J_1(t\eta). \quad (113)$$

Using the identity Eq. (107), Eq. (113) is equivalent to $-\frac{ie}{2\pi\hbar} B_\rho(t, y)$. Consequently Eq. (112) is reduced to

$$B_\rho(\rho, y) = -\frac{2\pi\hbar}{ie} \int_0^\infty dX \cdot X \cdot S(X, y) \cdot J_1(2\pi\rho X). \quad (114)$$

In this way, by differentiating the measured phase distribution of the electron wave and taking their Fourier transforms Eqs. (101) and (110), each component of the field vector \vec{B} can be directly calculated from a single "projection" $\phi(x, y)$ as Eqs. (108) and (114). In Chapter 6, I actually calculated the field components from the phase data measured by the fringe scanning interferometry.

Chapter 6

Magnetic flux in superconductors

6.1 Introduction

The essential character of superconductivity has manifested itself in macroscopic quantum state, showing its properties in various interesting phenomena, especially the magnetic flux quantization in units of $\Phi_0 = \frac{h}{2e}$, fluxon, expressed only by universal constants. Exact evaluation of the quantity Φ_0 and analysis of the internal structure of a fluxon, therefore, have great importance for basic research on superconductivity [6.1][6.2]. Fluxons form a flux line lattice in type-II superconductor under external magnetic fields, and they are forced to move by transport currents. When its electromagnetic driving force exceeds the fluxon pinning force, the fluxon starts to move into viscous flow with energy dissipation, resulting in the ohmic resistance and limiting the superconducting critical current. Investigation of the static and dynamic behaviors of the fluxons play an important role for basic research as well as for industrial applications of superconductors.

As reviewed in Section 6.2, various kinds of experimental techniques have been employed for the observation of fluxons since the prediction of Abrikosov. Although, especially, the methods using electron waves such as Lorentz microscopy were considered powerful, they have not yet attained enough results, because the observation had to be carried out near the measurement limitation from the uncertainty principle, as suggested by Suzuki and Seeger [6.3]. Only some special techniques of electron wave interferometry by Boersch *et al.* [6.4] has succeeded in detection of the fluxon existence in a superconducting hollow cylinder without microscopic cite determination.

By introducing the holographic technique, on the other hand, We have recently succeeded to overcome the measurement limitation for simultaneously obtaining high spatial

resolution and magnetic flux sensitivity [6.5]. Singly-quantized fluxes emerging on the surface of superconducting lead film has been directly imaged in the form of magnetic flux lines. The present chapter shows the detailed analysis on the internal field distributions around the fluxon center by combining the fringe scanning interferometry [6.6] described in Chapter 3 with the electron holography. This method enables the numerical measurement of the phase distribution of electron waves by the digital data processing [6.7]. The decomposition of the magnetic field vector components from the electron phase distribution has become possible by utilizing the axisymmetry of the fluxon field distributions. The tomographic technique developed in Chapter 5 has been used for this analysis. Then direct comparison between the experimental analysis and the theoretical calculation is available. I have numerically calculated the internal field distribution around the fluxon center in terms of the Ginzburg-Landau (GL) equations using some models such as the Clem model [6.8]. In consequence, a whole agreement was found between the experimental and calculated results.

I also observed structure changes in the magnetic flux distributions of thin lead films, depending on their thickness. Our results on the structural transition from the type-I- to the type-II-state behaviors of lead films were consistent with earlier works [6.9]~[6.14]. Fluxon pairs consisting of two anti-parallel fluxons were also observed in $0.2\mu\text{m}$ -thick lead films, which may corresponds to the ones suggested in the Kosterlitz-Thouless theory [6.15].

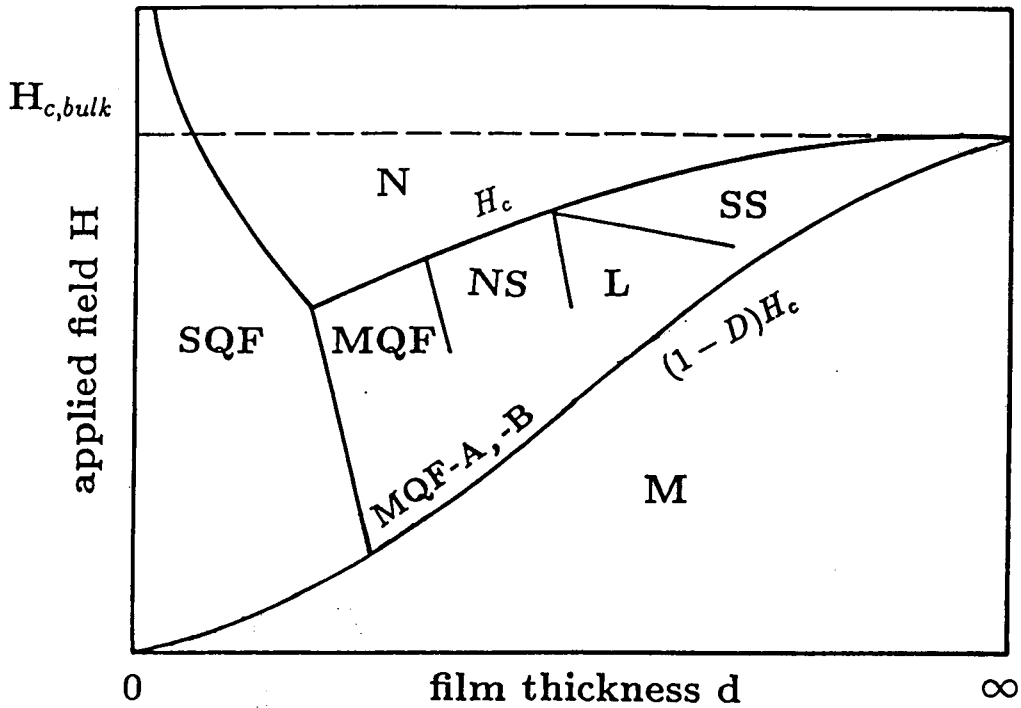
In Section 6.2, I briefly review the earlier works on the magnetic flux structures of thin films of type-I superconducting materials, and the experimental techniques for their investigations. Section 6.3 is devoted to describing our experimental details and analysis methods. In Section 6.4, I calculate the internal field distributions of quantized fluxes penetrating through a superconductor by numerically solving the GL equations using some models. Especially, the flux spread near the surface of the superconductor is evaluated for comparison with the experimental results. Experimental results are shown in Section 6.5, and compared with the calculated results in Section 6.6, and finally summarized in Section 6.7.

6.2. Backgrounds

It is appropriate for the electron holographic observation to choose a superconducting material of the low GL parameter κ value, because the fluxons in such a material are so fine that the flux density is well high to be detectable. From this point of view, I adopted lead material, of which pure thin films could be simply prepared. The type-I superconductors such as lead enter the intermediate state under the magnetic field between $(1 - D)H_c$ and H_c (H_c is the critical field, D is the demagnetization factor). In this state the macroscopic normal regions (N), through which magnetic fluxes penetrate, appear in the superconducting phase (S). When the thickness of the specimen along the external field becomes thinner, the N/S distribution changes in the way that the N region is divided into smaller dimension of normal spots. The variation is based on the change of the thermodynamical free energy which is composed of the N/S interface energy and the non-uniform magnetic field energy. Both are in counter-proportional relation with the N/S structure size, whence its equilibrium size is determined from the minimum energy condition for given thickness of the superconductor.

The N/S interface energy can be expressed in terms of the effective GL parameter κ . When the specimen thickness becomes as thin as a critical thickness, the κ value goes near to $\frac{1}{\sqrt{2}}$ and the normal spot size is in microscopic scale of the penetration depth λ , containing the magnetic flux quantized in units of Φ_0 . This means that sufficiently thin films of any superconducting materials can go into type-II superconducting state with the mixed state. At the intermediate region of the thickness, the N/S structures and its corresponding magnetic flux distributions show various kinds of patterns; normal spots (NS) containing macroscopic amounts of fluxes, multiply-quantized fluxes (MQF), and singly-quantized fluxes (SQF). Various kinds of magnetic flux structures in a film of type-I superconducting materials under the magnetic field perpendicular to the film surface are schematically shown in Fig. 6.1 (b)~(f)

Tinkham [6.16] was the first to point out the possibility of the N/S structure changes even for the type-I superconducting materials. After his prediction, the magnetic flux structures in superconducting films have been theoretically studied from the GL theory in more detail by Guyon *et al.*[6.17], Pearl [6.18], Maki [6.19], Lasher [6.20], and Fetter



(a)

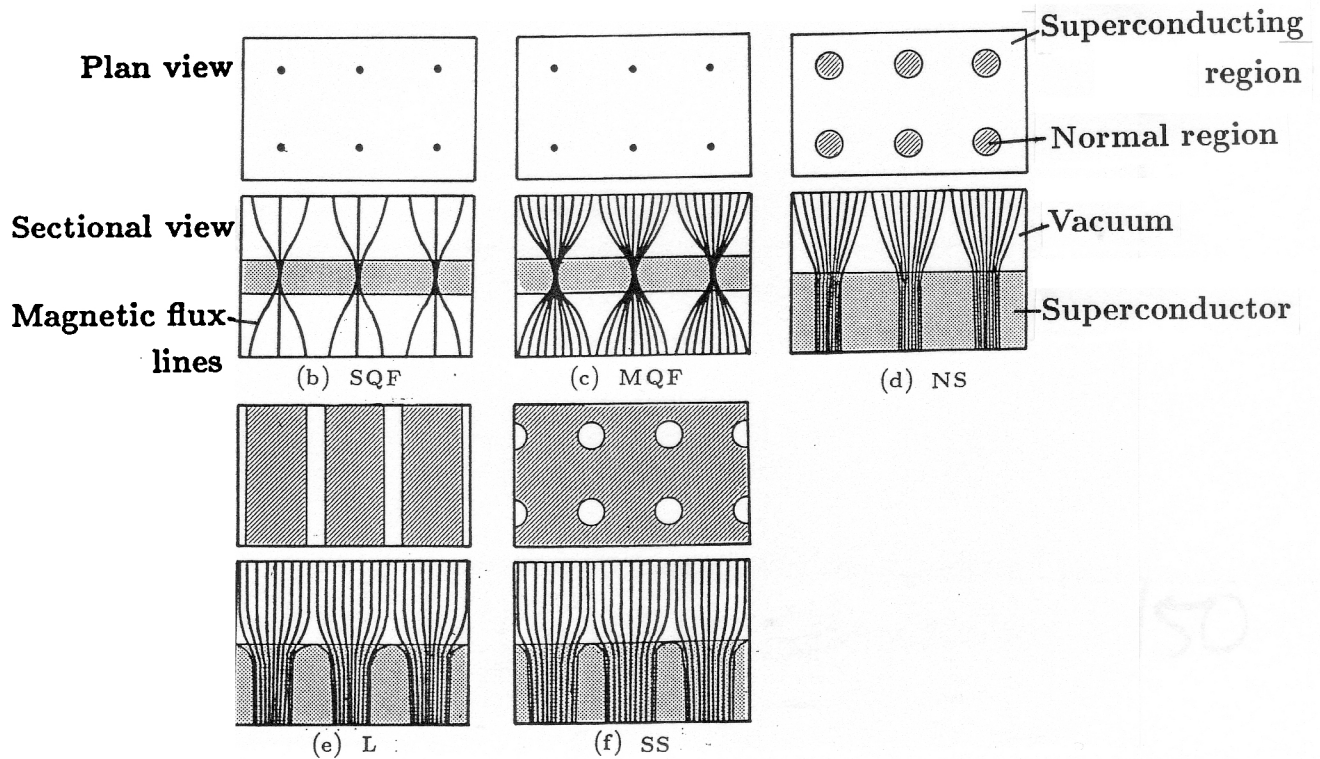


Fig. 6.1 (a) Schematic phase diagram showing various magnetic flux structures in a film of a type-I superconducting materials under the magnetic field perpendicular to the film surface. The structures depend on the film thickness and the applied magnetic field. M: Meissner state, N: normal state, SQF: singly-quantized flux line structure, MQF: multiply-quantized flux line structure, NS: normal spot structure, L: laminar structure, SS: superconducting spot structure. $H_{c,bulk}$ indicates the thermodynamical critical field of a bulk superconductor. D denotes the demagnetization factor. Two types of multiply-quantized flux line structures, MQF-A and MQF-B, are found in the present study. (b) SQF. (c) MQF. (d) NS. (e) L. (f) SS.

and Hohenberg [6.21]. They mainly discussed the stability of each magnetic flux structure and the critical thickness of the film. According to Lasher [6.20], as the film thickness increases, the MQF line structures are more energetically favorable than the SQF structures in the high field region. In the MQF structure, individual flux bundle with several flux quanta can arrange in the lattice form like the Abrikosov's. With further increase of the film thickness, normal-state spots with finite diameters appear in the superconducting phase and semi-macroscopic multi-quanta fluxes penetrate therein. This is the Goren's normal spot (NS) model [6.22]. And finally, the Landau's laminar structure is most favorable at the sufficiently thick superconductors.

These magnetic flux structures in thin films of superconducting materials have been experimentally observed in various ways. Direct observations of the SQF static distributions on lead alloy films were performed by Essman and Träuble [6.23][6.24], and also by Sarma [6.25] with use of the modified Bitter method which had been applied for imaging the domain boundaries in ferromagnetic materials [6.26]. This powerful method has been intensively applied for the investigations of magnetic flux distributions in type-I and -II superconductors of various thicknesses by Barbee [6.9], Rodewald *et al.* [6.10]~[6.12], and Dolan and Silcox [6.13][6.14], and many other investigators [6.27]~[6.30]. This method has recently applied also to high- T_c oxide superconductors to investigate the flux line lattice, its melting, and the pinning effects [6.31]~[6.34]. The transition from the type-I- to type-II-state behavior was also detected by electrical and magnetic measurements [6.35]~[6.38]. Since the reports on this subject is too many to cite thoroughly, the reader should consult the monograph [6.1] to find the further literatures. The earlier results on the magnetic flux structures in films of type-I superconductors, e.g. lead, may be summarized in a phase diagram at a relatively high temperature T ($T < T_c$) as sketched in Fig. 6.1(a). Although the figure is only qualitative and should not be taken strictly, it has the virtue to explain the conditions under which each investigation is performed, involving the present work. Although most of the earlier works, theoretically and experimentally, were carried out in relatively high field regions, the present observation covers only very low field regions, just above the Meissner phase, due to the apparatus limitation.

In addition to the Bitter method, various kinds of experimental techniques have been

employed to observe the magnetic flux structures in superconductors [6.1][6.39]. They are summarized in Fig. 6.2 based on their spatial resolution and the sensitivity for magnetic flux. It shows rough estimations of availability of typical experimental methods. The shadowed area covers the resolution and sensitivity necessary for observing the mixed state in type-II superconductors.

In the Bitter method, the exit points of the flux lines on the superconductor surface are decorated with ferromagnetic fine particles. As shown in Fig. 6.3 (a), the fine particles are produced in helium gas during a condensation process of the evaporated ferromagnetic materials such as cobalt. The superconductor is half immersed in a bath of liquid helium. As the particle size crucially depends on the helium gas pressure, the most favorable conditions have to be adjusted to produce single-magnetic-domain particles of which diameters are around 20 nm. Some of the arriving particles are attracted to the points where the flux lines meet the top surface of the superconductor, and form a picture of the flux line lattice. Once the particles are attached to the surface, they do not move any more. After the decoration process like this, the decorated pattern is next observed in an electron microscope. Figure 6.3 (b) shows an example of the Bitter pattern showing the triangular flux line lattice on the surface of a lead-at4% indium rod at 1.1 K[6.2]. The black dots consist of small cobalt particles. Although this method is very useful to observe the details of various kinds of magnetic flux structures in superconductors, it is difficult to quantitatively estimate the amount of the flux and the flux spread. Since, moreover, the decoration process takes considerable time of orders of several seconds, it is also difficult to observe the dynamical behaviors of the fluxes in superconductors.

The neutron diffraction method [6.40] allows very quantitative analysis on the flux structures, only when the flux is well periodically distributed. This method cannot be applied to the analysis of the magnetic flux structures without periodicity such as the state of the flux line lattice melting and the intermediate state of the type-I superconductors.

Electron microscopic observations such as shadow electron microscopy [6.41], electron interferometry [6.4], and out-of-focus electron microscopy [6.42], have not yet obtained enough spatial resolution and flux sensitivity at the same time. As suggested by Suzuki and Seeger [6.3], in particular, it is almost impossible to observe the internal field distri-

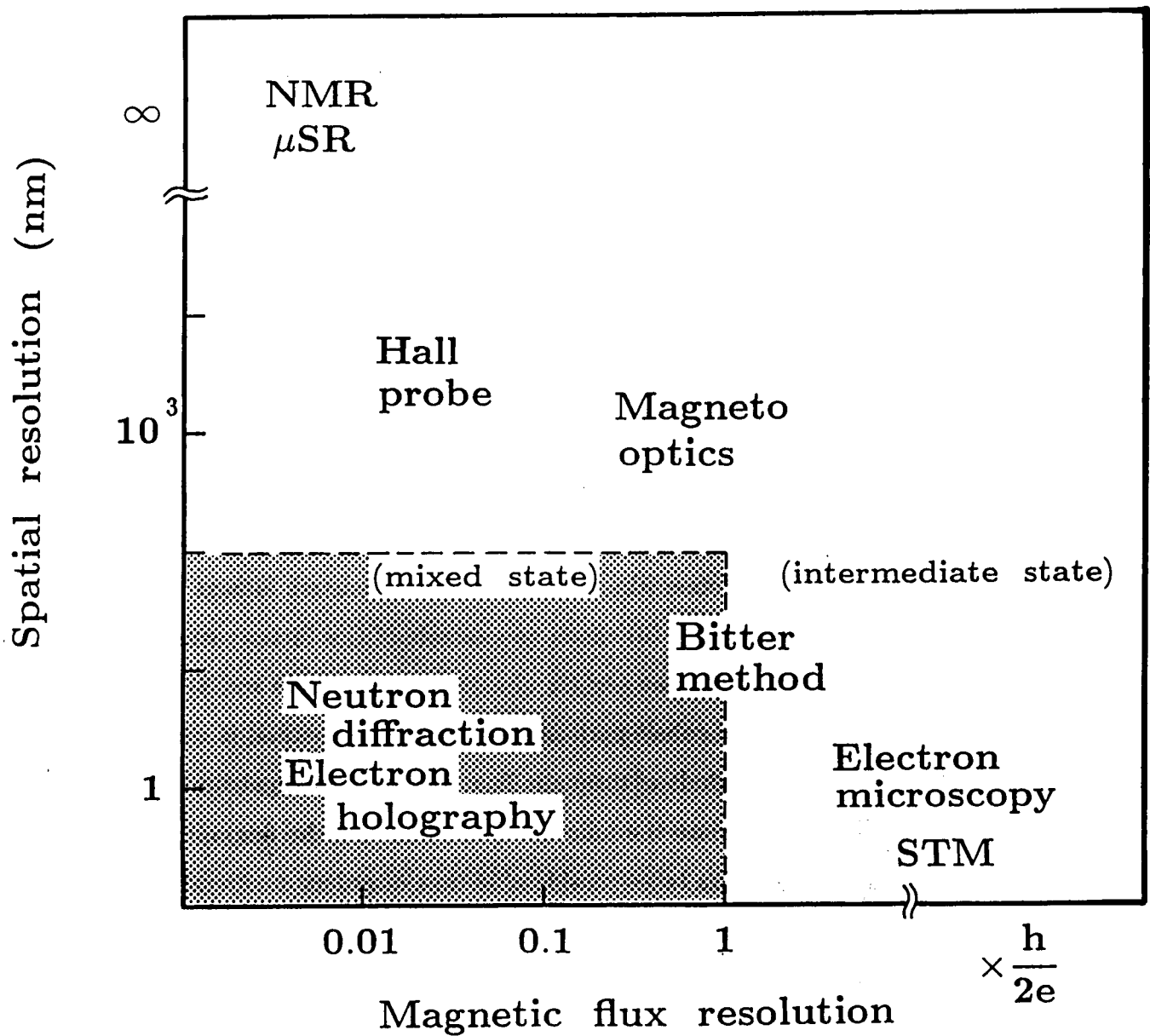
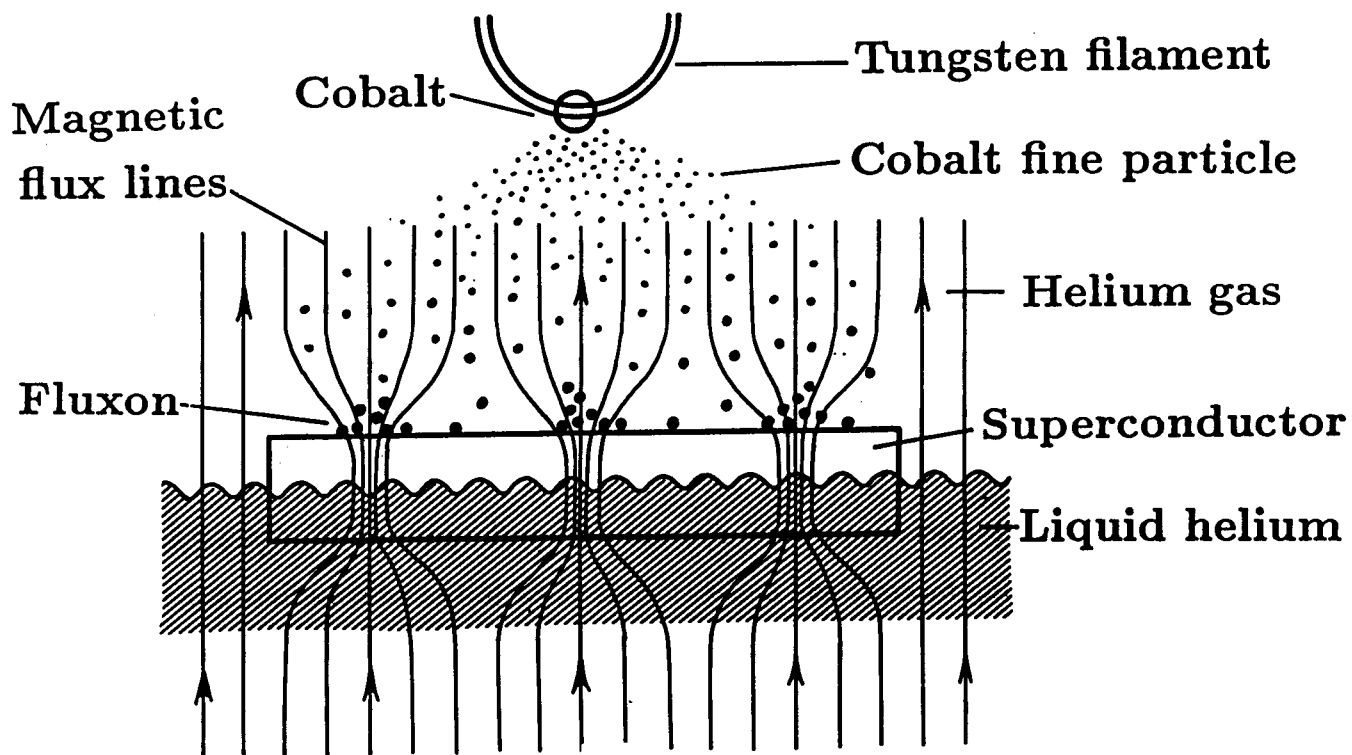
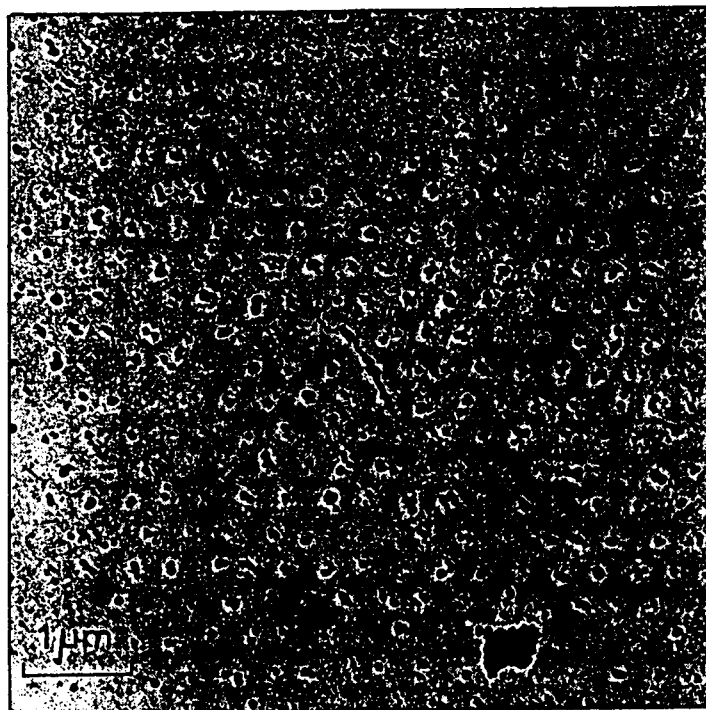


Fig. 6.2 Typical experimental methods to observe the flux structures in superconductors. They are roughly classified in terms of their spatial resolutions and magnetic flux resolutions.



(a)



(b)

Fig. 6.3 The Bitter method. (a) Experimental procedure. (b) The Bitter pattern showing a triangular lattice of flux lines on the surface of a lead-4at% indium rod at 1.1 K. The black dots consist of small cobalt particles [6.23].

bution of a single fluxon by out-of-focus electron microscopy because of the uncertainty principle.

Recent observation using scanning tunneling microscopy (STM) [6.43] reveals a flux line lattice, which, however, does not probe the magnetic flux itself, but the electronic state changes near the fluxon center at the surface. The NMR (nuclear magnetic resonance) [6.44] and the μ SR (muon spin rotation) [6.45] also provide some information on the magnetic flux distribution, although they have no spatial resolution. The obtained data with these methods are some averages over macroscopic regions, as in the case of the neutron diffraction experiment, assuming the periodicity of the flux distribution. The magneto-optical observation [6.46] and the Hall probe method [6.47][6.22] can be useful only for observing macroscopic fluxes such as those in the intermediate state.

Electron holography, on the other hand, enables the direct observation of very weak magnetic fields with angstrom-resolution as mentioned so far. As shown in the previous chapters, we have analyzed the detailed magnetic structures of thin films, fine particles, and magnetic recording materials [6.48]. The magnetic field distributions are revealed in the form of magnetic flux lines in the interference micrographs. Since each line in the micrograph corresponds to a definite amount of magnetic flux $\frac{h}{ne}$ (h is Plank's constant, e is electric charge of an electron, and n is an integer up to about 100), we can quantitatively analyze the field just by counting the number of the lines. Furthermore, a more quantitative field analysis is shown by introducing the fringe scanning interferometry. The present chapter shows the direct observations of *individual* fluxons with high spatial resolution and the quantitative analysis of the internal field distribution of an *individual* fluxon. Such analysis is possible even though the fluxes are not periodically distributed.

The electron holography has another advantage in dynamical observation of fluxons. Several investigators tried to observe the movement of the magnetic fluxes in, for instance, lead foils with transport current by means of the Bitter method [6.24], the shadow electron microscopy [6.49], and the neutron diffraction method [6.50]. They have not, however, yet attained satisfactory results for lack of enough time and spatial resolutions. In contrast to those techniques, the electron holography has high resolution in time and space enough to observe the SQF movement with real time. In the present work, though, I focus my

attention only on static observations of fluxons.

6.3 Experimental procedures and analysis method

6.3.1 Sample preparation

Superconducting lead film of thickness ranging from $0.1\mu m$ to several μm were fabricated by vacuum deposition on one side of a tungsten wire of $30\mu m$ diameter at room temperature. I have chosen the film thicknesses according to the earlier works which report that the transition of the magnetic flux structures from the type-I- to the type-II-state takes place in this range of the thickness [6.14][6.35]. The tungsten wire surface was made clean and smooth in advance by direct current heating up to $2300K$ in vacuum. The sample is shown in Fig. 6.4. The lead film was made up with grains of single crystals, so that special attention was paid to preparing films almost free from surface roughness, pinholes, and cracks at grain boundaries. The critical temperature of the lead films was measured to be $7.2 K$, and the residual resistance ratio (RRR) $\frac{\rho_{300K}}{\rho_{7.5K}} = 50 \sim 80$ for the $0.2\mu m$ -thick films and better for thicker films. The quality of the prepared films were recognized in same grade with the specimens in other studies [6.14][6.35] because of the similar RRR values.

The RRR value, a measure of the disorder in the film structure, always corresponds to the effective mean free path [6.51],

$$l = (RRR - 1) \frac{\rho l}{\rho_{300K}}, \quad (115)$$

where the values of ρl and ρ_{300K} are obtained from the literature [6.52]; $\rho l = 1.5 \times 10^{-11} \Omega cm^2$, $\rho_{300K} = 21 \mu \Omega cm$. From the values of RRR for our lead films; $RRR = 50 \sim 80$ for the $0.2\mu m$ -thick films, we obtain $l = 360 \sim 560 nm$.

In the case of sufficiently thin films, on the other hand, the effective mean free path is limited primarily from diffuse reflection of the electrons at the sample surfaces. According to the Fuchs' classical theory of the size effect [6.53],

$$\frac{1}{l} = \frac{1}{l_{\infty}} + \frac{3}{8d}, \quad \frac{l}{l_{\infty}} > 0.1, \quad (116)$$

where l_{∞} is the mean free path of a bulk specimen of the same purity and defect content,

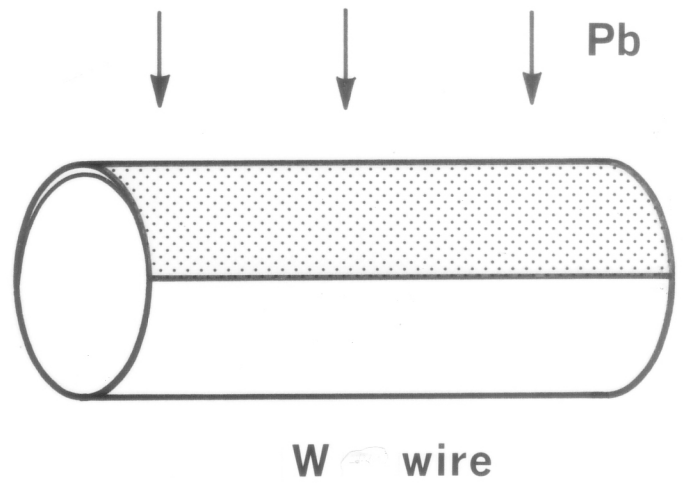
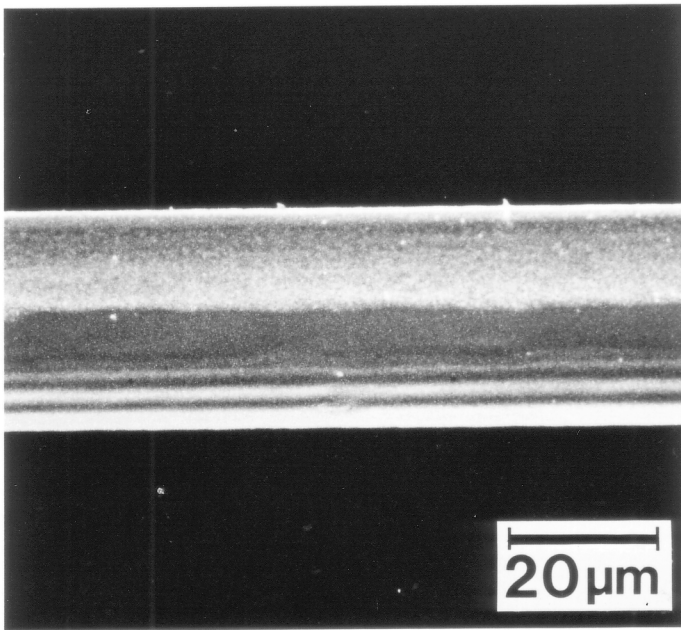


Fig. 6.4 Scanning electron micrograph of the observation sample. The lead film was deposited on one side of a tungsten wire of $30\mu m$ diameter.

and d is the film thickness. For the film of $d = 0.2\mu m$, using the value of l above obtained, l_∞ should be longer than $1.1\mu m$ estimated from Eq. (116). This implies that our lead films had enough high quality and purity so that the mean free path is not limited by the impurity and defect scatterings, but primarily by the film thickness.

The wire was fixed on a sample holder with indium-layer thermal contact. In our electron holography microscope (Fig. 6.5), the lead film was cooled down to be superconducting with fluxons under the magnetic field perpendicular to the film surface. Because the electron beam could not transmit through the film, we could only observe the fluxons spreading out into vacuum outside the film surface, not the fluxons in the film. So I had to catch the root of the fluxon just above the film surface in order to investigate the internal field distribution of the fluxon inside the film. For this reason the film was curved to insure the fluxons exit at the extreme edge of the sample shadow.

But the observed fluxons did not necessarily stand on the extreme edge of the sample shadow. In fact, fluxons with different root diameters were observed even on the same sample. Therefore, I cannot measure the intrinsic fluxon diameters with fluxons of broader roots which do not stand on the extreme edge and are probably shadowed by the edge. Since, however, it is considered that the fluxons with the finest roots among the large number of observed fluxons really exit at the extreme edge of the sample shadow, they were used for the analysis of the inner field distribution around the fluxon center.

6.3.2 Electron holography microscope

Our microscope was an H-800 type Hitachi transmission electron microscope devised for electron holography with a cold field-emission type electron gun and a Möllenstedt-type electron biprism as illustrated in Fig. 2.5. Its operating voltage was 150 kV. The sample chamber of the microscope column was devised for a sample cooling stage and electromagnet pairs to cool down the sample under the applied magnetic field perpendicular to the lead film.

The sample cooling stage depicted in Fig. 6.6 was set in the sample chamber of the column, and thermally connected to a liquid helium and nitrogen container which was set outside the column. The sample holder (SH) was introduced from the sample ex-

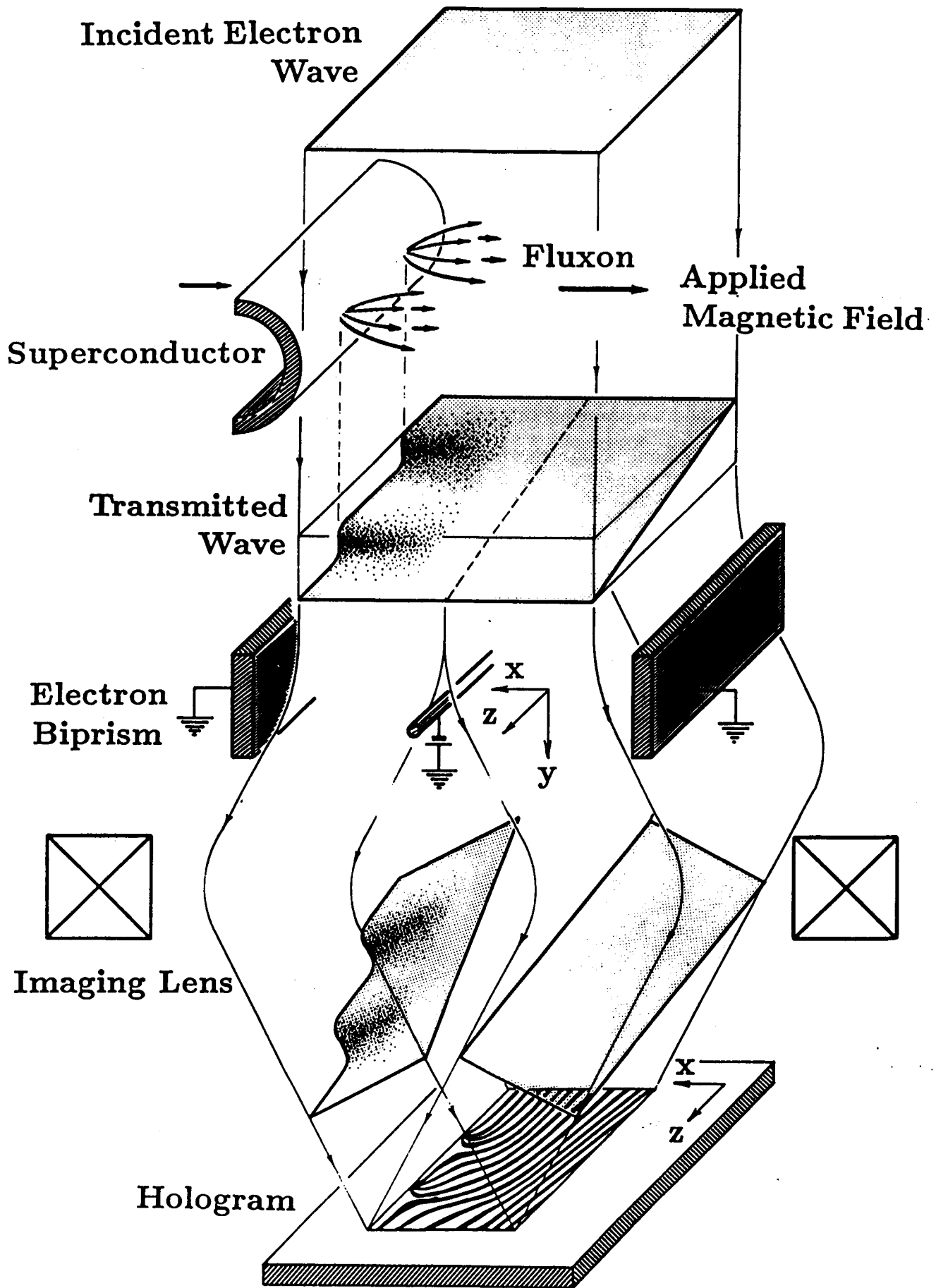


Fig. 6.5 The electron wave propagation in the electron holography microscope. The wavefront is deformed by the fluxons and divided into two parts, an object wave and a reference wave, by an electron biprism to form a hologram.

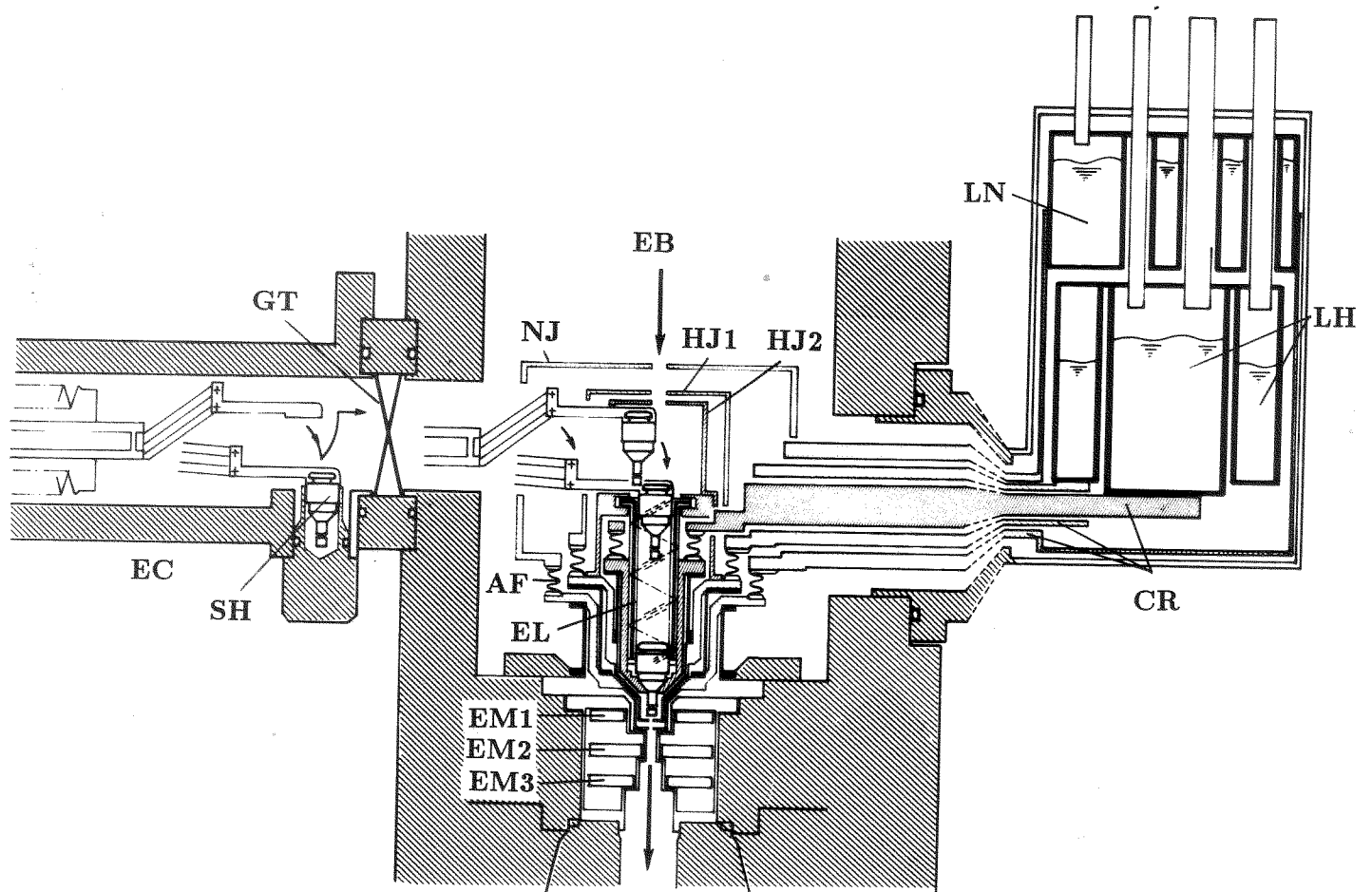


Fig. 6.6 The sample cooling stage and the electromagnet pairs equipped in the sample chamber of the electron microscope column. The sample holder (SH) is introduced from the exchange chamber (EC) through the gate valve (GT) into the column. The holder is set at the observation position by the elevator (EL) and thermally connected to the cooling stage. The stage is connected through a Cu rods (CR) to a liquid helium (LH) and nitrogen (LN) containers set outside the column. The stage and container are composed of three shells; the outer shell (NJ) is cooled down to 100K by the liquid nitrogen, the intermediate shells (HJ1) is 5K by the liquid helium, and the inner shell (HJ2), which contacts to the sample holder, is 2.5K by pumping the inner liquid helium container. Thin flexible Ag foils (AF) thermally connect the sample and the refrigerant container, and at the same time, absorb mechanical vibrations. The first electromagnet pair (EM1) apply the magnetic field perpendicular to the sample lead film. The second (EM2) and the third (EM3) electromagnet pairs correct the electron beam (EB) path deflected by EM1 for microscopic observation.

change chamber (EC) through the gate valve (GT) and rapidly cooled down from room temperature by thermal connection with the stage. The sample holder, which can be cooled down to $2.5K$ by pumping out the liquid helium container, is surrounded with two shells for thermal radiation shielding. The intermediate shell (HJ1) was cooled down to $5K$ with liquid helium and the outer (NJ) was $100K$ with liquid nitrogen. The sample temperature could be reversibly set at any points between $2.5K$ and $20K$ with a heater attached to the stage. Annealed silver flexible foils of $30\mu m$ thickness (AF) were used for the thermal connection of the sample to the refrigerant container, and at the same time, for the absorption of the external mechanical vibrations.

The first electromagnet pair (EM1) produces the transverse magnetic field up to $35Oe$ to create the fluxons in the lead film. Since the field, however, deflects the electron beam (EB), I need the second (EM2) and third electromagnet pairs (EM3) to correct the beam path for microscopic observation. The excitation of the latter two electromagnets are adjusted according to the first magnetic field strength. In this way it became possible to carry out the in-field cooling and the in-field observation, of which temperature and magnetic field ranges were $2.5K \sim 20K$ and $-35Oe \sim 35Oe$, respectively.

The propagation of electron waves in the microscope is illustrated in Fig. 6.5. The illuminating electron wave, emitted from the field emission tip, is regarded as a plane wave. Transmitting through the sample region, the wavefront is deformed by the magnetic field; the localized field of a fluxon causes steep phase change, although the wavefront passing far from the lead film is only inclined smoothly because of a uniform field. By electron biprism action, the transmitted wave is divided into two parts, superimposed, and interfere with each other. Interference fringes were recorded on a hologram. One of the divided waves, passed near the lead film surface, becomes an object wave which contains the information on the fluxons. Another wave, passed through the far distant region, $\sim 6\mu m$ from the investigated lead film surface at the specimen plane, acts as a reference wave. The phase distribution of the object wave is thus recorded in the form of interference fringe distributions, an off-axis hologram.

Strictly speaking, the reference wave is not a plane wave because the magnetic field modulation by the fluxons virtually extends, decaying exponentially from the film sur-

face, into the reference wave area at the specimen plane. Since, however, the phase change caused by the modulation in the reference wave area is estimated to be less than $\frac{\pi}{200}$ which is smaller than the experimental precision, the reference wave can be regarded as plane and the phase distribution recorded on the hologram is only the object wave's. Moreover the divergence angle of the illuminating electron beam is $\sim 1 \times 10^{-8} \text{rad}$ so that the incident wave is also regarded as a plane wave with $\frac{\pi}{500}$ accuracy.

The sample image was focused by the intermediate lens, because the objective lens was switched off to prevent the extra field applying the sample. An image hologram with magnification of $1500 \sim 2000$ was obtained by applying a negative voltage ($\sim -20V$) to the central thin wire of the electron biprism. The holograms were recorded on KODAK 4489 electron microscope films. The carrier fringes were set to be parallel to the lead film edge shadow, or perpendicular to the fluxons, in the hologram. The hologram width and its carrier fringe spacing were set to be $4 \sim 10 \text{mm}$ and $60 \sim 100 \mu\text{m}$ on the film, or $4 \sim 6 \mu\text{m}$ and $30 \sim 60 \text{nm}$ at the specimen plane, respectively.

6.3.3 Optical reconstruction and field analysis

I utilized the laser interferometer for the optical reconstruction as shown in Fig. 3.1 with the fringe scanning interferometry mentioned in Chapter 3. This method allows the numerical measurement of the phase distribution of the wave reconstructed from the hologram, and improve the phase measurement precision up to $\sim \frac{2\pi}{100}$. A single pixel on the TV image (512×512 pixels) corresponds to a $\sim 8 \text{nm}$ -square on the specimen plane.

As reviewed in Chapter 2, the phase distribution of the electron wave is directly related to the magnetic field distribution. The internal field distribution of the flux can be measured from the curvature of the transmitted wavefront. I set up a coordinate system as shown in Fig. 6.7 to give some mathematical expressions. The y -axis is the core axis of an isolated fluxon, and the region of $y \leq 0$ is occupied by a semi-infinite superconductor. The region of $y \geq 0$ is vacuum and the surface of the superconductor is the plane $y = 0$. The incident electron wave comes from $z = -\infty$ along the z -axis. Its wavefront is parallel with the (xy) plane and infinitely spreads in the vacuum $y \geq 0$.

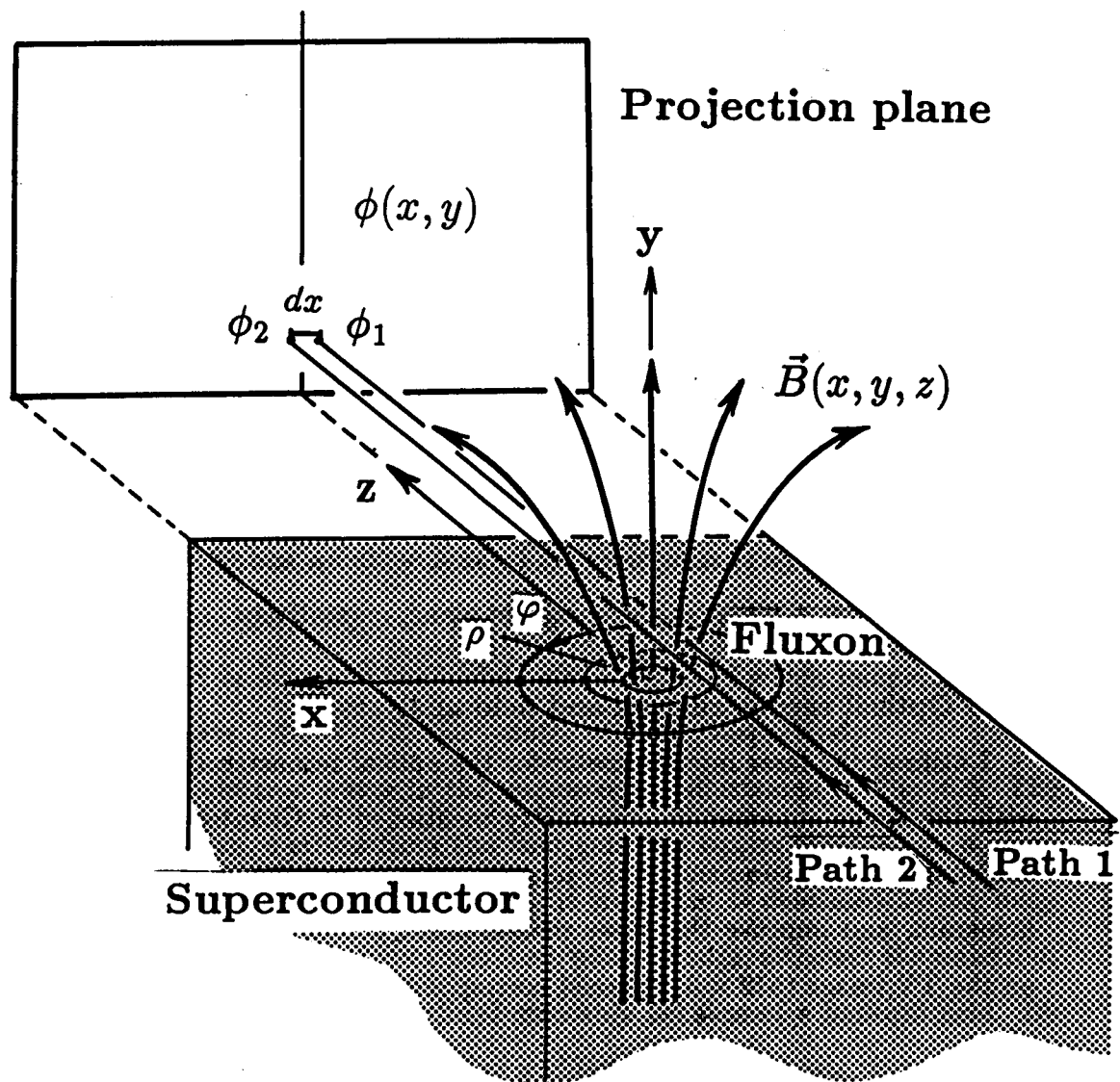


Fig. 6.7 Coordinate system for analyzing the internal field distribution around a fluxon center from the measured phase distribution of the passed electron wave.

Transmitting through the fluxon, the wave gets the phase shift $\phi(x, y)$ which is expressed by a line integral of the vector potential \vec{A} along the path of the wavefront element of interest;

$$\phi(x, y) = -\frac{e}{\hbar} \int_{\text{path1}} \vec{A} \cdot d\vec{s}. \quad (117)$$

Taking into account the spatial resolution of our observation, we can neglect the deflection of the path by the fluxon field. In fact, its deflection angle is $\sim 10^{-5} \text{rad}$ and the decrease of the spatial resolution by this effect in an in-focused hologram is estimated 0.001nm . So the path 1 is regarded as a straight line passing through the point $(x, y, 0)$ and parallel to the z -axis. Then, the phase distribution of the transmitted electron wave $\phi(x, y)$ and the field vector $\vec{B}(x, y, z)$ are related through Eqs. (65) and (66);

$$\frac{\partial \phi(x, y)}{\partial x} = \frac{e}{\hbar} \int_{-\infty}^{\infty} dz \cdot B_y(x, y, z), \quad (118)$$

$$\frac{\partial \phi(x, y)}{\partial y} = -\frac{e}{\hbar} \int_{-\infty}^{\infty} dz \cdot B_x(x, y, z). \quad (119)$$

In this way, by differentiating the measured phase distribution of the electron wave, we obtain a two-dimensional "projection" of the three dimensional magnetic field distribution along the direction of view. Data processing of the numerically measured phase is possible with an image processing computer.

On the next step I calculate the field vector components B_y, B_x (or B_ρ) themselves from their projections Eqs. (118) and (119) using the analysis method developed in Chapter 5. Since the magnetic field distribution \vec{B} of the fluxon and the persistent current \vec{j} circulating around the fluxon are axisymmetric with respect to the y -axis, I introduce the cylindrical polar coordinate (ρ, φ, y) with its axis on the fluxon core axis. \vec{j} has only the φ component only in the superconductor. But \vec{B} has the y and ρ components near the superconductor surface and in vacuum, although it has only the y component in the sufficiently inner bulk region of the superconductor (see Fig. 6.7). Each component of the field vector is directly obtained through Eqs. (108), (114), (101), and (110);

$$B_y(\rho, y) = \frac{2\pi\hbar}{e} \int_0^\infty dX \cdot X \cdot F(X, y) \cdot J_0(2\pi\rho X), \quad (120)$$

$$B_\rho(\rho, y) = -\frac{2\pi\hbar}{ie} \int_0^\infty dX \cdot X \cdot S(X, y) \cdot J_1(2\pi\rho X), \quad (121)$$

where

$$F(X, y) \equiv \int_{-\infty}^{\infty} dx \cdot \frac{\partial \phi(x, y)}{\partial x} e^{2\pi i x X}, \quad (122)$$

$$S(X, y) \equiv \int_{-\infty}^{\infty} dx \cdot \frac{\partial \phi(x, y)}{\partial y} \cdot e^{2\pi i x X}. \quad (123)$$

In this way, by differentiating the measured phase distribution of the electron wave and taking their Fourier transforms, each component of the field vector \vec{B} can be calculated from a single "projection" $\phi(x, y)$. In Section 6.5, I actually calculated the field components from the phase data measured by the fringe scanning interferometry, and then the results are compared with the field distribution calculated from the Ginzburg-Landau equations.

6.4 Model calculations of fluxon field

In this section, I numerically calculate the internal field distributions of quantized magnetic fluxes near the surface of a superconductor. The magnetic flux distribution around the fluxon center in the superconductor has been qualitatively described by the London model [6.54] and semi-quantitatively by the Clem model [6.8]. For quantitative discussions for the field distribution, the GL equations, or more strictly speaking, the Eilenberger equations [6.55] derived from the Gor'kov equation, should be solved. But it needs a huge numerical calculation with a high-speed computer.

Since I could not observe the fluxons *in* the superconductors, but only the fluxons appearing *on* the superconductor surface as mentioned so far, the comparison with theories is not straightforward. For the flux begins to spread even below the superconductor surface, so that the field distribution around the core axis differs from that in the inner bulk. Then I numerically solved the GL equations in the superconductor and the Maxwell equations in vacuum in order to correctly evaluate the flux spreading near the surface. Although our experiments were carried out in the range of low magnetic fields and low temperatures, in which the GL theory is not applicable, I start from the equations often used for phenomenological understandings. Since, however, the GL equations,

$$-\frac{\hbar^2}{2m}(\vec{\nabla} - \frac{2ie}{\hbar}\vec{A})^2\Psi = \alpha\Psi - \beta|\Psi|^2\Psi \quad (124)$$

$$\frac{1}{\mu_0} \text{rot rot } \vec{A} = n_s \left\{ \frac{\hbar e}{2mi} (\Psi^* \vec{\nabla} \Psi - \vec{\nabla} \Psi^* \Psi) - \frac{2e^2}{m} |\Psi|^2 \vec{A} \right\}, \quad (125)$$

where $\Psi(\vec{r})$ is the order parameter, $\vec{A}(\vec{r})$, the vector potential, μ_0 , the permeability of the vacuum, n_s , the number density of the Cooper pairs, α and β are the coefficients calculated from the BCS theory, are nonlinear for the unknown functions $\Psi(\vec{r})$ and $\vec{A}(\vec{r})$, we can not easily solve them. So I assumed some functions for $\Psi(\vec{r})$ and solved Eq. (125) only for $\vec{A}(\vec{r})$. Once the vector potential is obtained, we can calculate the flux density $\vec{B}(\vec{r})$ and the persistent current density $\vec{j}(\vec{r})$ circulating around the flux;

$$\vec{B}(\vec{r}) = \text{rot } \vec{A}(\vec{r}), \quad (126)$$

$$\vec{j}(\vec{r}) = \frac{1}{\mu_0} \text{rot rot } \vec{A}(\vec{r}). \quad (127)$$

Using the coordinate system shown in Fig. 6.7, the fluxon near the surface is described by

$$\begin{aligned} \Psi(\rho, \varphi, y) &= |\Psi(\rho, y)| e^{-i\varphi}, \\ \vec{A}(\rho, \varphi, y) &= A_\varphi(\rho, y) \hat{\varphi}, \\ \vec{B}(\rho, \varphi, y) &= B_\rho(\rho, y) \hat{\rho} + B_y(\rho, y) \hat{y}, \\ \vec{j}(\rho, \varphi, y) &= j_\varphi(\rho, y) \hat{\varphi}, \end{aligned} \quad (128)$$

where $\hat{\rho}$, $\hat{\varphi}$, and \hat{y} are the unit vectors for the respective directions. Equation (125) then has only the φ -component;

$$\frac{\partial^2 A_\varphi(\rho, y)}{\partial y^2} + \frac{\partial}{\partial \rho} \left\{ \frac{1}{\rho} \frac{\partial}{\partial \rho} (\rho A_\varphi(\rho, y)) \right\} - \frac{1}{\lambda^2} \left\{ A_\varphi(\rho, y) - \frac{\Phi_0}{2\pi\rho} \right\} |\Psi(\rho, \varphi, y)|^2 = 0, \quad (129)$$

where the magnetic flux penetration depth $\lambda = \left(\frac{m}{2e^2 \mu_0 n_s} \right)^{\frac{1}{2}}$ and the magnetic flux quantum $\Phi_0 = \frac{h}{2e}$. And then, from Eqs. (126) and (127),

$$B_\rho(\rho, y) = -\frac{\partial A_\varphi(\rho, y)}{\partial y}, \quad (130)$$

$$B_y(\rho, y) = \frac{1}{\rho} \frac{\partial}{\partial \rho} \{ \rho A_\varphi(\rho, y) \}, \quad (131)$$

$$\begin{aligned} j_\varphi(\rho, y) &= \frac{1}{\mu_0} \left\{ \frac{\partial B_\rho(\rho, y)}{\partial y} - \frac{\partial B_y(\rho, y)}{\partial \rho} \right\} \\ &= -\frac{1}{\lambda^2} \left\{ A_\varphi(\rho, y) - \frac{\Phi_0}{2\pi\rho} \right\} |\Psi(\rho, \varphi, y)|^2. \end{aligned} \quad (132)$$

For the SQF line, I adopted the Clem model [6.8] for the order parameter;

$$\Psi_1(\rho, \varphi, y) = \begin{cases} \frac{\rho}{(\rho^2 + \xi^2)^{\frac{1}{2}}} e^{-i\varphi} & (y \leq 0) \\ 0 & (y > 0) \end{cases} \quad (133)$$

where ξ is the coherence length which approximately corresponds to the radius of the fluxon. I assume the y -independence of the order parameter near the superconductor surface. Equation (129) then becomes the Maxwell equation in vacuum $y > 0$. Equation (129) with Eq. (133) was numerically solved by the finite difference method using the DEQSOL (differential equation solver) program [6.56] with a Hitachi computer HITAC M680H. The area for solving the equation was a square of $\rho = 0 \sim 1 \mu\text{m}$, $y = -0.5 \sim 0.5 \mu\text{m}$ with 200×200 square meshes (Fig. 6.8), and the boundary conditions were

$$\begin{aligned} A_\varphi &= 0 && , \text{because of the symmetry on } \rho = 0, \\ A_\varphi &= \frac{\Phi_0}{2\pi\rho} && , \text{implying } B_\rho = 0, \text{ on } \rho = 1\mu\text{m}, \\ A_\varphi &= \frac{\Phi_0}{2\pi\lambda^2} \frac{\rho}{400} && , \text{implying } B_y = \text{constant}, \text{ on } y = 0.5\mu\text{m}, \\ \frac{\partial A_\varphi}{\partial y} &= 0 && , \text{implying } B_\rho = 0, \text{ on } y = -0.5\mu\text{m}. \end{aligned} \quad (134)$$

The boundary conditions Eq. (134) should be different between an isolated fluxon and a fluxon in a flux line lattice. But the calculated internal field distribution around the fluxon center near the superconductor surface were almost independent of the boundary conditions and the calculation area size. Our main interest in the analysis of the experimental results lies in the internal field distribution at the flux root just above the superconductor surface.

For numerically solving the GL equation Eq. (129) with the Clem model Eq. (133), I must estimate the characteristic parameters of our lead films, λ and ξ . In the case of superconductors characterized by the local field theory, the weak-field penetration depth $\lambda(T, d)$, which depends on the temperature T and possibly on the film thickness d , is given by [6.57];

$$\lambda(T, d) = \lambda_L(T) \left(1 + \frac{\xi_0}{l}\right)^{\frac{1}{2}}. \quad (135)$$

Here, $\lambda_L(T)$ is the London penetration depth, ξ_0 is the Pippard coherence distance, and l is an effective mean free path arising from either scattering by impurities or the surfaces of

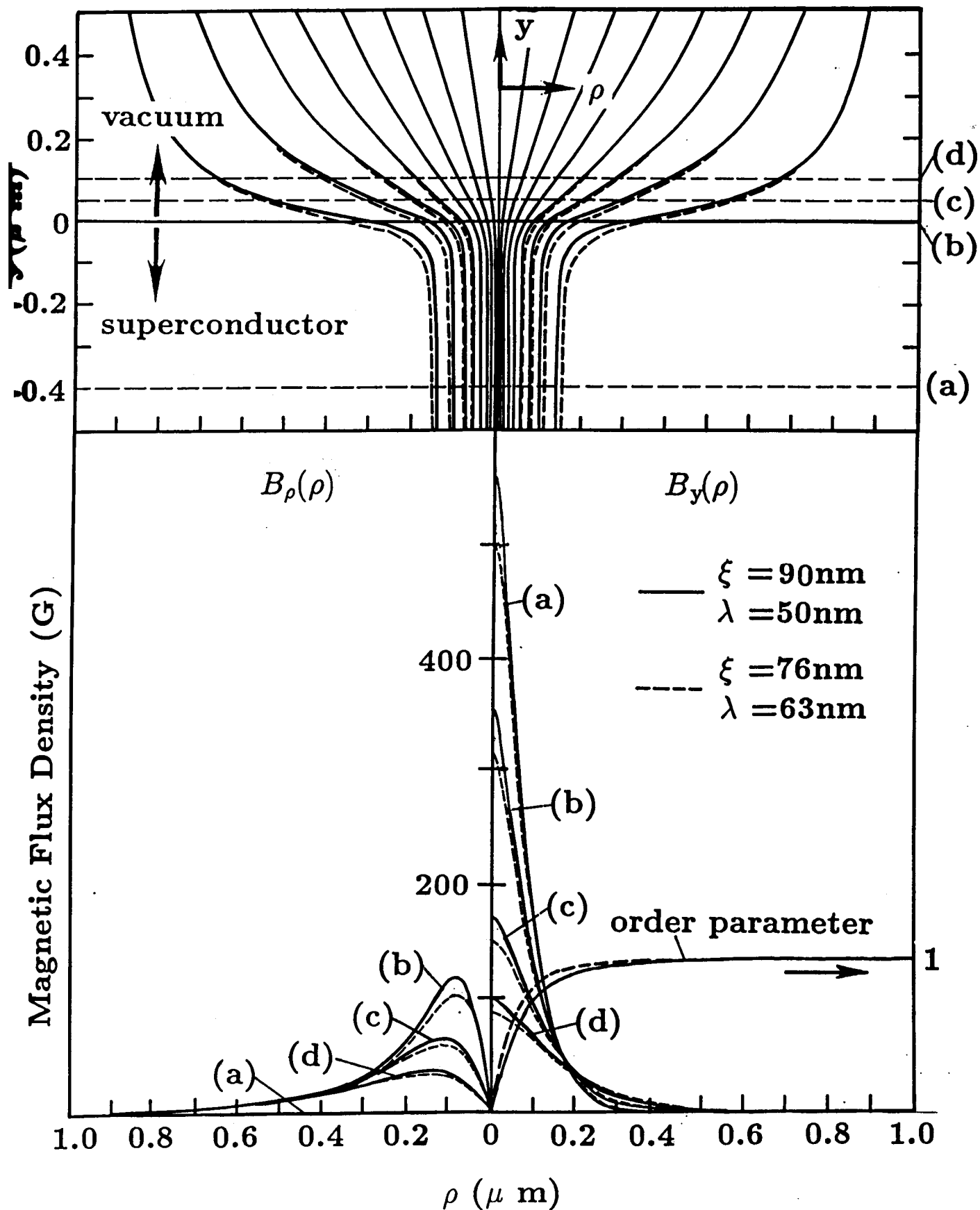


Fig. 6.8 The magnetic flux distributions of a fluxon near the superconductor surface, calculated with the DEQSOL program using the Ginzburg-Landau equation Eq. (129) combined with the Clem model Eq. (133). The curved solid lines are calculated with the parameters, $\xi = 90\text{nm}$, $\lambda = 50\text{nm}$, and the curved dash-lines are with $\xi = 76$, $\lambda = 63\text{nm}$. The upper figure shows the flux line distributions. The lower figure shows the profiles of the field distribution along the lines indicated in the upper figure. The field vector components are separately shown.

the film. Since a real sample, lead, is not, however, recognized to be quite local, Tinkham [6.35] has suggested the following modification of Eq. (135) as a suitable extrapolation form for $\lambda(T, d)$;

$$\lambda(T, d) = \lambda(T, \infty) \left(1 + \frac{\lambda_L(T)^2 \xi_0}{\lambda(T, \infty)^2 l}\right)^{\frac{1}{2}}, \quad (22)$$

where $\lambda(T, \infty)$ is the bulk weak-field penetration depth. I assume the temperature dependence of λ 's by the usual Gorter-Casimir ones, namely $\lambda(t) = \frac{\lambda(0)}{(1-t^4)^{\frac{1}{2}}}$, where $t = \frac{T}{T_c}$.

Then, Eq, (136) becomes

$$\lambda(T, d) = \frac{\lambda(0, \infty)}{(1-t^4)^{\frac{1}{2}}} \left(1 + \frac{\lambda_L(T)^2 \xi_0}{\lambda(T, \infty)^2 l}\right)^{\frac{1}{2}}. \quad (23)$$

Using the values of the effective mean free path l obtained in Section 6.3, and $\frac{\lambda_L(T)^2}{\lambda(T, \infty)^2} \xi_0 = 69nm$ at $T = 4, 2K$, $\lambda(0, \infty) = 44nm$ [6.35], we get $\lambda(4.2K, 200nm) = 50 \sim 52nm$.

In the same way, the GL parameter $\kappa(T, d)$ is given by [6.35]

$$\kappa(T, d) = \kappa(T, \infty) \left(1 + \frac{\lambda_L(T)^2 \xi_0}{\lambda(T, \infty)^2 l}\right), \quad (24)$$

where

$$\begin{aligned} \kappa(T, \infty) &= \frac{2\sqrt{2}\pi H_c(T) \lambda(T, \infty)^2}{(h/2e)} \\ &= \frac{2\sqrt{2}\pi H_c(0) \lambda(0, \infty)^2}{(1+t^2)(h/2e)}. \end{aligned} \quad (25)$$

Here, H_c is the thermodynamical critical field, $H_c(0) = 803G$, and $\frac{h}{2e} = 2.07 \times 10^{-15} Wb$, the flux quantum. We obtain, therefore, $\kappa(4.2K, 200nm) = 0.56 \sim 0.59$, and consequently, from the relation $\xi(T, d) = \lambda(T, d)/\kappa(T, d)$, we get $\xi(4.2K, 200nm) = 88 \sim 90nm$. These values of the parameters, λ and ξ , for our lead films are not dissimilar to other reports [6.12][6.14], in spite of our unusual substrate for the lead deposition. I adopt these values hereafter.

The curved solid lines in Fig. 6.8 shows the magnetic flux distributions around the fluxon center, calculated from Eqs. (129) and (133) using the parameters $\xi = 90 nm$, $\lambda = 50 nm$. It shows that the flux begins to spread even below the superconductor surface. The field distribution in the inner bulk region of the superconductor coincides with the original Clem model;

$$B_y(\rho) = \frac{\Phi_0}{2\pi\lambda\xi} \frac{K_0\left(\frac{\rho^2 + \xi^2}{\lambda}\right)^{\frac{1}{2}}}{K_1\left(\frac{\xi}{\lambda}\right)}, \quad (26)$$

where K_0 and K_1 are the modified Bessel functions. The result with a wider calculation area ($\rho = 0 \sim 2.5\mu m$, $y = -0.5 \sim 2\mu m$) is utilized for the comparisons with experimental results in Section 6.4.

The same calculation was performed for comparison using the literature values for the parameters of a polycrystalline thin film of lead [6.58], $\xi = 76 \text{ nm}$, $\lambda = 63 \text{ nm}$. The calculated results are shown with curved dash-lines in Fig. 6.8. Although the difference between the curved solid lines ($\xi = 90 \text{ nm}$, $\lambda = 50 \text{ nm}$) and the curved dash-lines are distinguished in the superconductor, it is vanishing in vacuum with the distance from the superconductor surface. As a matter of course, the flux distribution in vacuum less reflects the internal field distribution in the superconductor. Since our experiments could catch the flux distribution only above the superconductor surface, it is difficult to quantitatively determine the values of the GL parameters. The calculated results with the both pairs of parameters are utilized for the comparison with the experimental results.

For comparison, moreover, the magnetic flux distribution is also calculated with an order parameter;

$$\Psi_1(\rho, \varphi, y) = \begin{cases} \{1 - \exp(-\frac{\rho^2}{\xi^2})\}e^{-i\varphi} & (y \leq 0) \\ 0 & (y > 0) \end{cases} \quad (141)$$

instead of the Clem's one Eq. (133), using $\xi = 90 \text{ nm}$, $\lambda = 50 \text{ nm}$. The calculated results are shown with the curved dash-lines in Fig. 6.9, indicating that the difference of the flux distribution between the Clem model and the model Eq. (141) is clear only near the fluxon center, and is vanishing in vacuum.

According to Lasher [6.20], the order parameter $\Psi_n(\rho)$ of a state consisting of MQF (n -flux quanta) is given in terms of that of the state of SQF $\Psi_1(\rho)$ as

$$\Psi_n(\rho) = \{\Psi_1(\frac{\rho}{\sqrt{n}})\}^n. \quad (142)$$

Then, using the Clem model Eq. (133), the order parameter of the MQF structure is given by

$$\Psi_n(\rho, \varphi, y) = \begin{cases} \left\{ \frac{\frac{\rho}{\sqrt{n}}}{(\frac{\rho^2}{n} + \xi^2)^{\frac{1}{2}}} \right\}^n e^{-in\varphi} & (y \leq 0) \\ 0 & (y > 0) \end{cases} \quad (143)$$

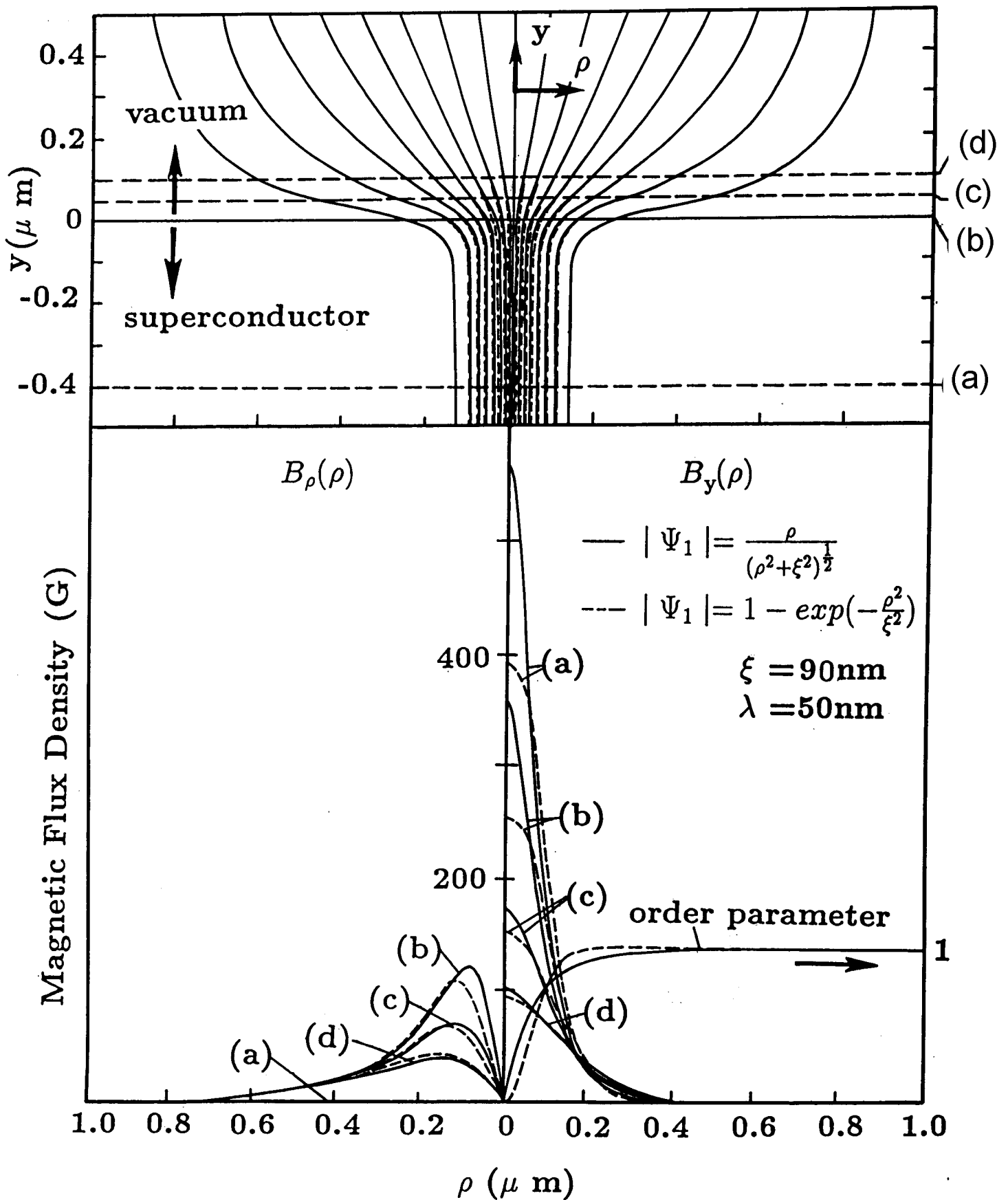


Fig. 6.9 The magnetic flux distributions of a fluxon near the superconductor surface, calculated with the DEQSOL program using the GL equation Eq. (129). The curved solid lines are calculated with the Clem model Eq. (133), and the curved dash-lines are with a model Eq. (141). Both are calculated with the parameters, $\xi = 90\text{nm}$, $\lambda = 50\text{nm}$. The upper figure shows the flux line distributions. The lower figure shows the profiles of the field distribution along the lines indicated in the upper figure. The field vector components are separately shown.

Figure 6.10 shows the calculated results from Eqs. (129) and (143) for $n = 1$ and 4 using $\xi = 90nm$ and $\lambda = 50nm$. The ordinate, flux density, in the lower figure is normalized for the flux density of a SQF. The difference of the flux distributions between the two models can be distinguished even in the vacuum above the superconductor surface.

For the SQF line in a film of thickness d , the flux distribution was calculated by utilizing the Clem's order parameter;

$$\Psi_1(\rho, \varphi, y) = \begin{cases} 0 & (y > 0) \\ \frac{\rho}{(\rho^2 + \xi^2)^{\frac{1}{2}}} e^{-i\varphi} & (-d < y \leq 0) \\ 0 & (y \leq -d) \end{cases} \quad (144)$$

The calculated results using $\xi = 90 \text{ nm}$, $\lambda = 50 \text{ nm}$, from Eq. (129) with Eq. (144) for various values of d are shown in Figs. 6.11(b)~(d). Figure 6.11 (b) shows that the flux distribution just above the surface of the film is almost the same as that of the semi-infinite superconductor Fig. 6.11(a). I therefore utilize the results calculated for the semi-infinite superconductor for the comparison with the experimental results in Section 6.6. Figures 6.11 (c) and (d) indicate that the flux distribution becomes broader with decrease of the film thickness.

6.5 Experimental results

6.5.1 Observations of magnetic flux structures

After the in-field cooling in which the film was cooled down from $15K$ to $4.2K$ under the magnetic field of the fixed strengths, the holograms were taken during applying the field (in-field observation). I observed three kinds of magnetic flux structures in superconducting lead films, depending on the film thickness and the applied magnetic field. Figure 6.12 shows the interference micrographs with π -phase interval, in which a single interference fringe exactly corresponds to a magnetic flux line of a single flux quantum $\frac{h}{2e}$. The shadowed areas are the curved lead films and I can only observe the flux spreading out into vacuum after penetrating through the films. The observation areas for a lead film are not necessarily the same under the different applied magnetic fields.

Although the fluxons were observed in the $0.2\mu m$ -thick film under the 1.0 Oe field, the

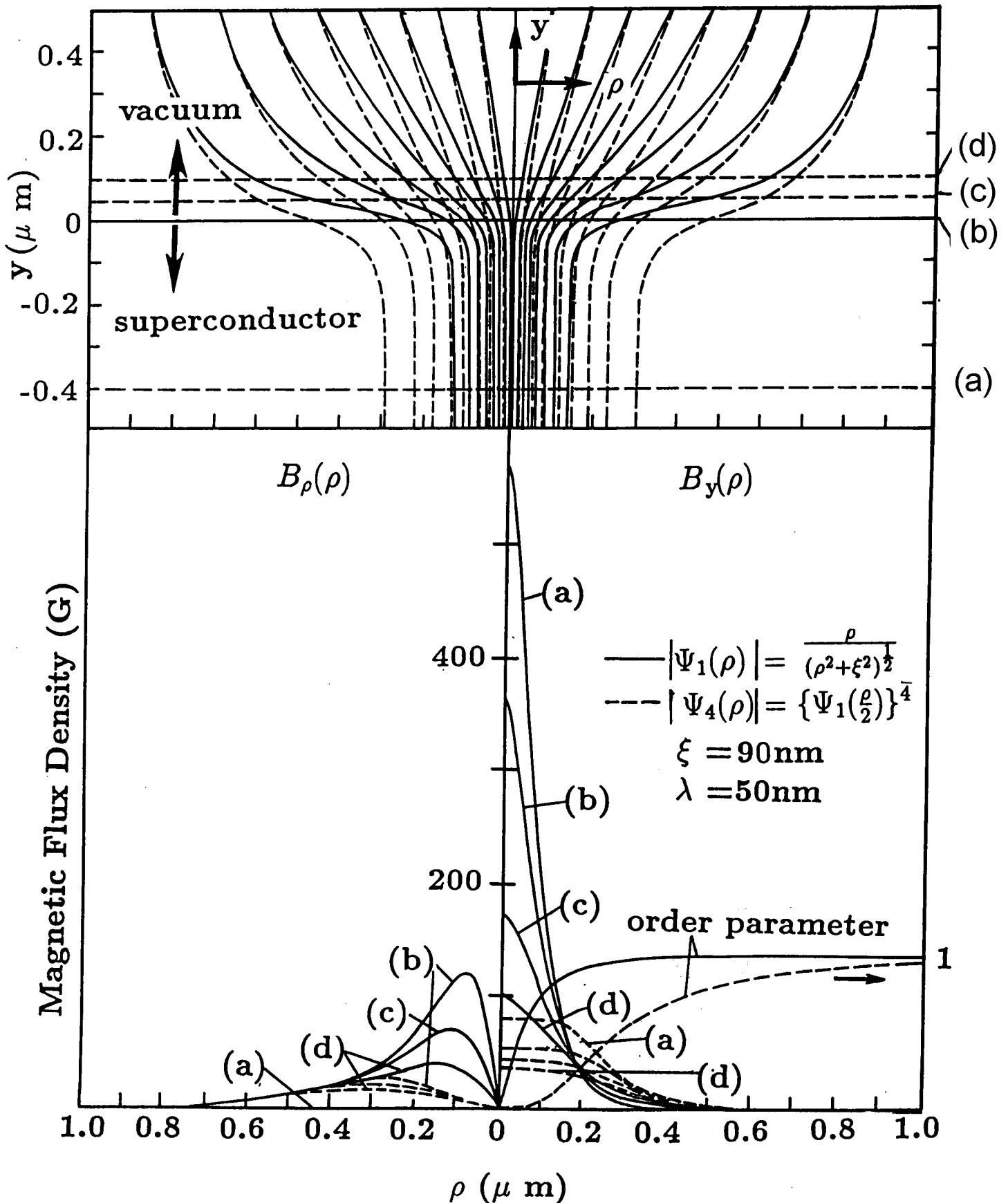


Fig. 6.10 The magnetic flux distributions of a fluxon near the superconductor surface, calculated with the DEQSOL program using the GL equation Eq. (129). The curved solid lines are calculated with the Clem model Eq. (133), and the curved dash-lines are with the Laser model Eq. (143). Both are calculated with the parameters $\xi = 90\text{nm}$, $\lambda = 50\text{nm}$. The upper figure shows the flux line distributions. The lower figure shows the profiles of the field distribution along the lines indicated in the upper figure. The field vector components are separately shown.

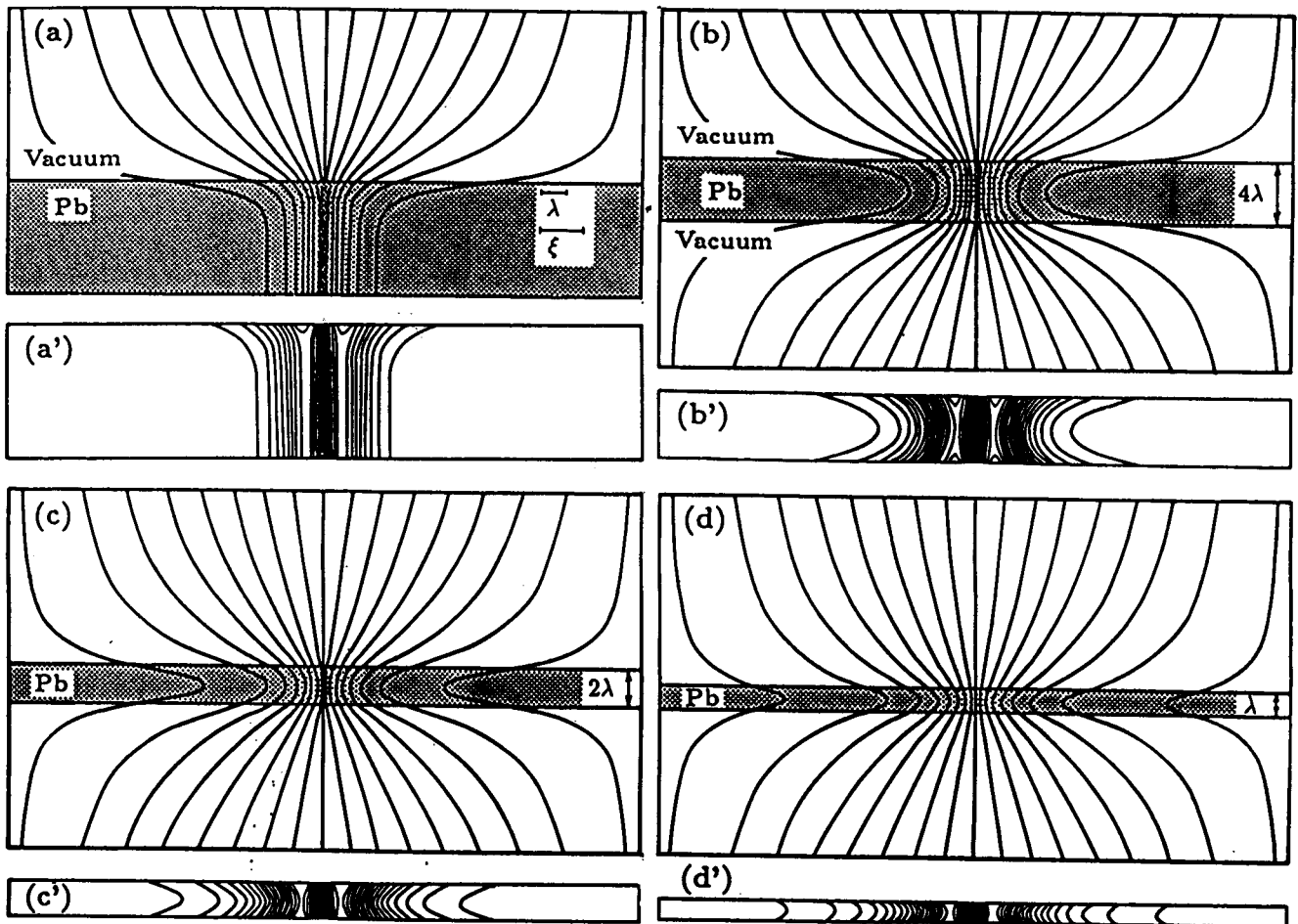


Fig. 6.11 The flux (upper figures) and circulating current (lower figures) distributions of a fluxon penetrating through (a) a semi-infinite, and thin films of thickness $d =$ (b) 4λ , (c) 2λ , and (d) λ of superconductors are calculated with the DEQSOL program using the GL equation Eq. (129) combined with the Clem models, Eq. (133) and (144), respectively.

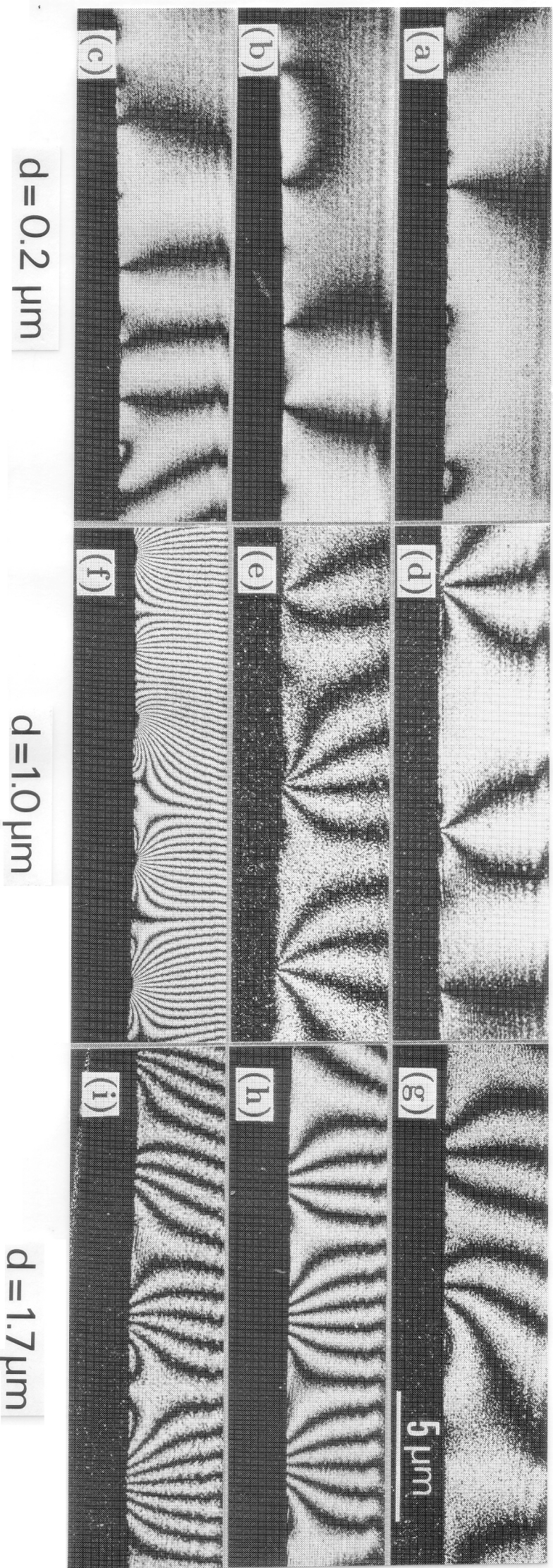


Fig. 6.12 Interference micrographs with phase interval of π showing the quantized magnetic fluxes appearing on the surfaces of the superconducting lead films. A single interference fringe exactly corresponds to a single flux quantum $\frac{h}{2e}$. The magnetic flux structures vary depending on the film thickness d and the applied field H . (a) $H = 1.60\text{Oe}$, (b) $H = 3.70\text{Oe}$, (c) $H = 5.00\text{Oe}$ for $d = 0.2\mu\text{m}$. (d) $H = 3.70\text{Oe}$, (e) $H = 5.00\text{Oe}$, (f) $H = 18.30\text{Oe}$ for $d = 1.0\mu\text{m}$. (g) $H = 7.50\text{Oe}$, (b) $H = 12.20\text{Oe}$, (c) $H = 18.30\text{Oe}$ for $d = 1.7\mu\text{m}$.

fluxons did not appear under the fields below 2.0 Oe for the $1.0\mu m$ -thick film, and below 5.0 Oe for the $1.7\mu m$ -thick film. This fact indicates that the Meissner phase extends into the higher field region with increase of the film thickness (see Fig. 6.1).

In the case of the films of $0.2\mu m$ thickness (Fig. 6.12 (a)(b)(c)), the fluxes penetrate in the form of the SQF lines, independent of the applied fields. They are the SQF structures of Tinkham [6.16]. With increase of the film thickness to $1.0\mu m$ (Fig. 6.12 (d)(e)(f)), flux bundles with several flux quanta penetrate in the form of thin filaments, and their exits on the surface are point-like. This is a MQF structure, which I call "MQF-A type" hereafter. In this structure, with the applied magnetic field, the amount of the flux contained in a single MQF line increases and the number of the MQF lines also increases. In the case of $1.7\mu m$ (Fig. 6.12 (g)(h)(i)), moreover, the flux penetrate in the form of flux bundles, as in the case of the $1.0\mu m$ -thick film. But the diameters of the flux bundles are much larger than those of the MQF-A lines. I call this structure "MQF-B type" from now on. In this case, with increase of the field strength, the diameters of the flux exits on the film surface seem to increase, although the diameters seems to remain unaltered in the MQF-A structure in the $1.0\mu m$ -thick film. Figure 6.12 clearly shows three kinds of structures, SQF, MQF-A, and MQF-B, in the form of the distribution of magnetic flux lines. The differences between these structures will be more clearly shown in the detailed analysis of the internal field distributions around the fluxon center in the next subsection.

Although the SQF lines tend to arrange in the lattice form according to Tinkham [6.16], the observed SQF lines in the film of $0.2\mu m$ seem to arrange at random. This is thought to be originated from the strong pinning force caused by the inhomogeneity of the film, the most prominent of which are grain boundaries [6.14]. The arrangement can also be made random by the creation and annihilation of the vortex-antivortex pairs in the Kosterlitz-Thouless (KT) region [6.15] just below the superconducting transition temperature. The KT theory has been extensively discussed concerning the melting of the flux line lattices in two-dimensional superconductors [6.59][6.60]. The fluxon pairs observed in Fig. 6.12 (a),(b) may correspond to the ones predicted in the KT theory. The pairs may have been created when the film was cooled down through the KT regime, and "frozen" by pinning so that the opposite fluxons would have not met to annihilate each other. The

polarity of each fluxon is easily distinguished in the interference micrograph. Unless the polarities of the two fluxons are opposite, the fluxons individually stand up and fan out, not make a pair. This is one of the unique features to the electron holographic observation compared with other experimental methods. The pairs were not observed in the films of $1.0\mu\text{m}$ and $1.7\mu\text{m}$ -thicknesses. This is naturally understood because the KT theory is applicable only for the two-dimensional system, and on the contrary, for this reason, it is suggested that the observed flux pairs are the ones predicted by the KT theory.

Figure 6.13 (a) shows the interference micrograph of the SQF line appearing in the $0.2\mu\text{m}$ -thick film under the 3.7 Oe field, in which a single fringe exactly corresponds to a single flux quantum. Figure 6.13 (b) is a phase-difference-amplified interference micrograph analyzed from the same hologram as Fig. 6.13(a). This micrograph was obtained not by the techniques using the conjugate and higher-order diffracted waves from the hologram mentioned in Chapter 2, but by drawing the contour phase lines at $\frac{\pi}{4}$ phase intervals, instead of π interval in Fig. 6.13 (a), from the phase data numerically measured by the fringe scanning interferometry. This is an eight-times phase-difference amplified interference micrograph in which a single fringe corresponds to a magnetic flux line of $\frac{h}{8e}$. The total amount of flux and the detailed flux distribution can be estimated with higher accuracy.

The MQF-A line with four flux quanta emerging in the $1.0\mu\text{m}$ -thick film under the 5.0Oe field is shown in Fig. 6.14 (a), and (b) is its eight-times phase-difference-amplified interference micrograph in which a single fringe corresponds to a magnetic flux line of $\frac{h}{8e}$. The flux penetrating through the superconductor looks as fine as that of the SQF in Fig. 6.13.

Figure 6.15 shows the MQF-B line with four flux quanta appearing on the $1.7\mu\text{m}$ -thick film under the field of 12.2 Oe . The root of the flux is much broader than that of the MQF-A line in Fig. 6.14, while the amounts of the flux are the same.

In this way, the structural changes from the SQF to the MQF-A and the MQF-B structures are clearly and directly shown in the form of magnetic flux distributions in interference micrographs. The changes seem to originate only from the increase of the film thickness, because, from the RRR measurement, the quality of the films is estimated

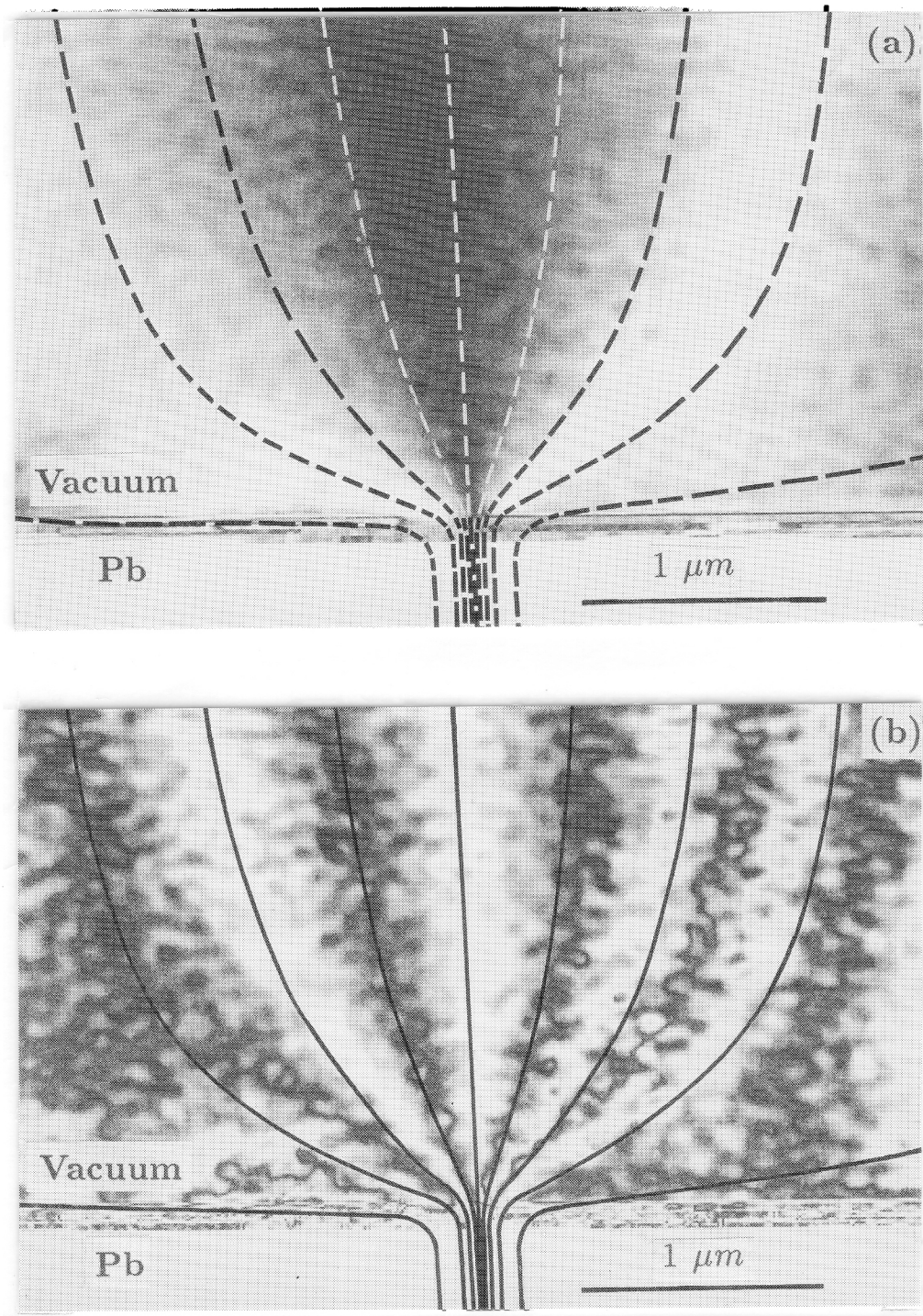


Fig. 6.13 A singly quantized flux (SQF) line appearing in the $0.2 \mu m$ -thick lead film under the $3.7 Oe$ -field. (a) Interference micrograph showing the flux lines in units of $\frac{h}{2e}$, and (b) in units of $\frac{h}{8e}$ (an 8-times phase-difference amplified interference micrograph). The curved dash-lines in (a) and the curved solid lines in (b) are the flux distribution calculated from the GL equation with the Clem model using the parameters $\xi = 90 nm$, $\lambda = 50 nm$.

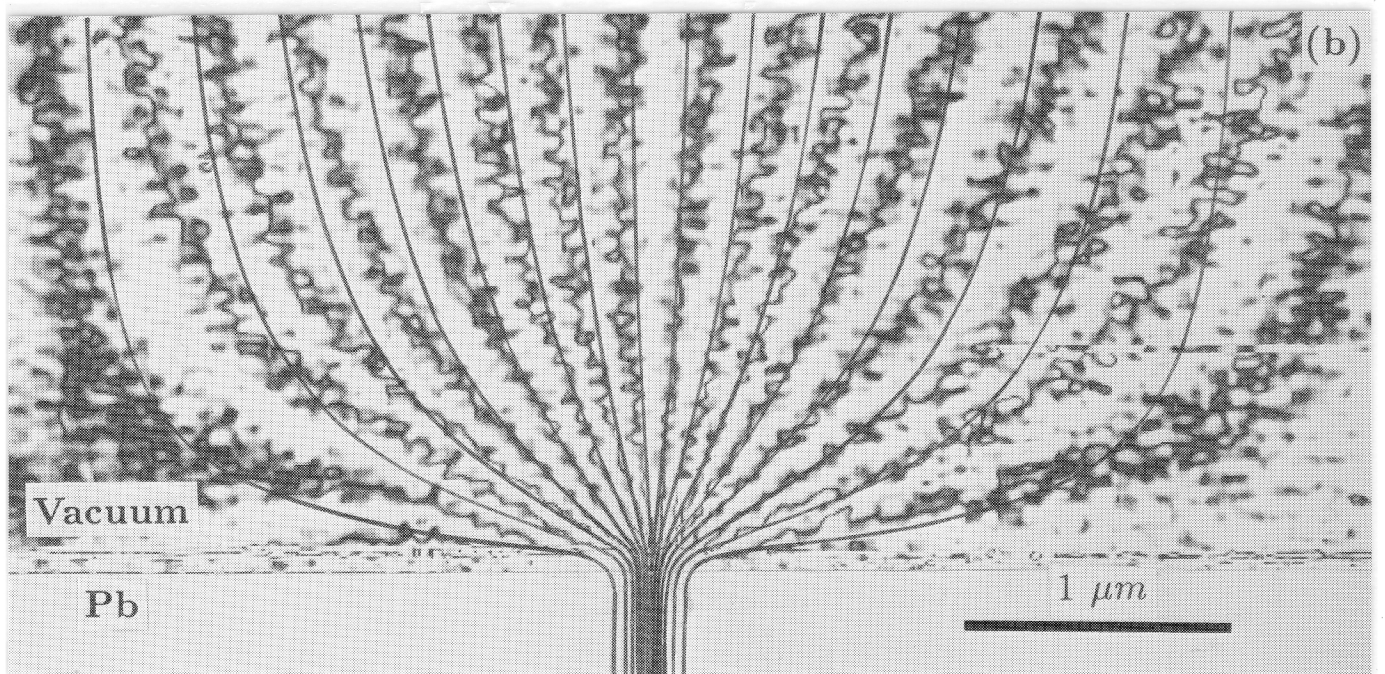
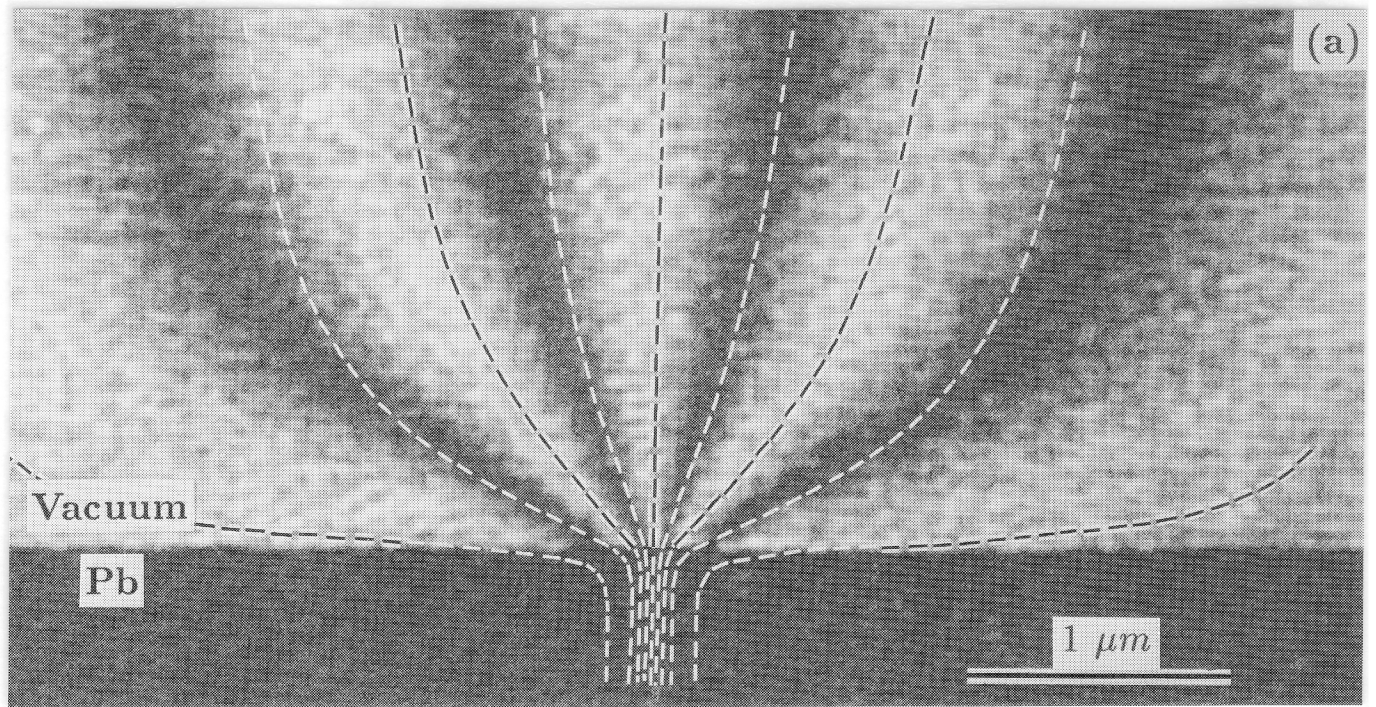


Fig. 6.14 A multiply quantized flux (MQF-A) line appearing on the $1.0\mu\text{m}$ -thick lead film under the $5.00e$ -field. (a) Interference micrograph showing the flux lines in units of $\frac{h}{2e}$, and (b) in units of $\frac{h}{8e}$ (an 8-times phase-difference amplified interference micrograph). The curved dash-lines in (a) and the curved solid lines in (b) are the flux distribution calculated from the GL equation with the Clem model using the parameters $\xi = 90\text{nm}$, $\lambda = 50\text{nm}$.

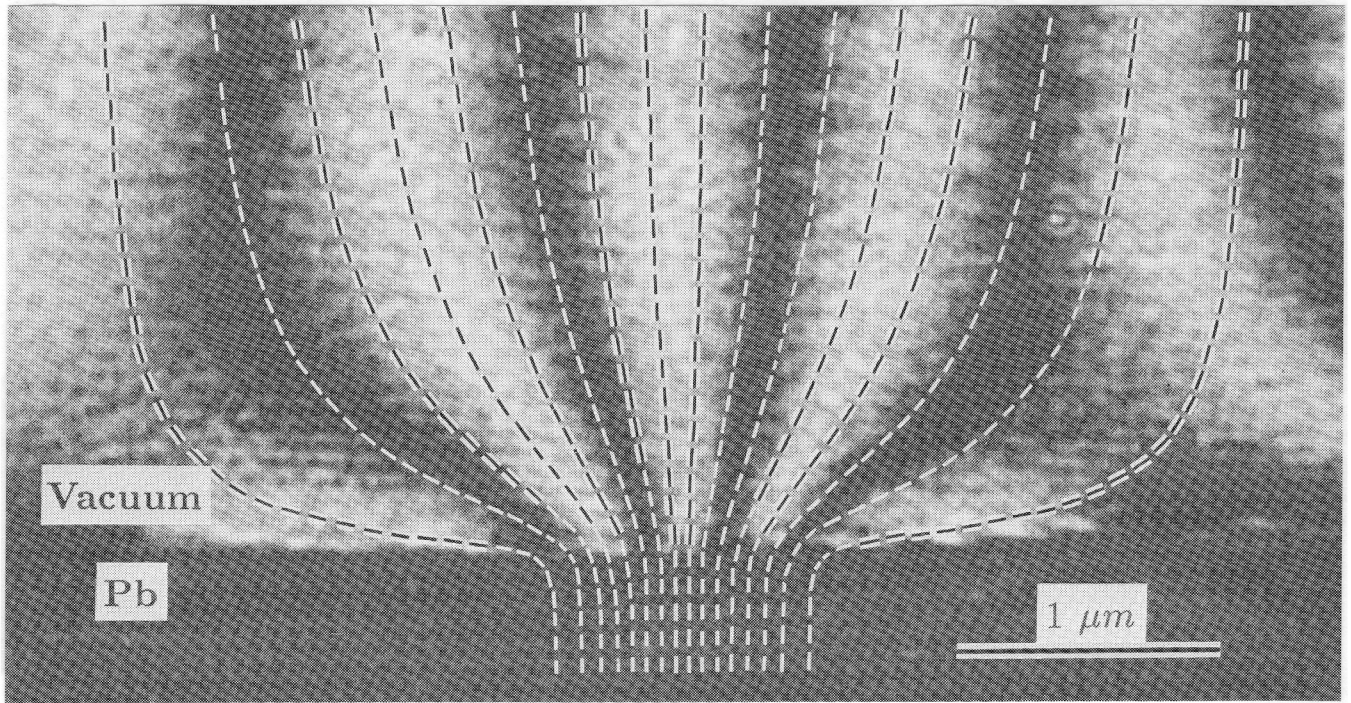


Fig. 6.15 A multiply quantized flux (MQF-B) line appearing on the $1.7\mu\text{m}$ -thick lead film under the 12.2Oe -field. An interference fringe corresponds to the flux quantum $\frac{h}{2e}$. The curved dash-lines shows the flux distribution calculated from the GL equation with a model Eq. (148) with $R = 0.4\mu\text{m}$, $\xi = 90\text{nm}$, $\lambda = 50\text{nm}$.

to remain unaltered with the thickness change.

6.5.2 Internal field distributions of quantized magnetic fluxes

The phase distributions of the electron waves transmitted through the fluxons were numerically measured, and then the field vector components around the fluxon centers were decomposed using the digital phase analysis method as described in Chapter 5.

At first, I analyzed the hologram taken from the $1.0\mu\text{m}$ -thick lead film under the $5.0Oe$ field (MQF-A). Figure 6.16 (b) shows the line profile of the phase distribution along the line AA just above the superconductor surface in the interference micrograph Fig. 6.16 (a). It shows that the phase steeply shifts at the flux exits and does not shift between them. This shows the Aharonov-Bohm effect.

The wavefront numerically reconstructed in this way is three-dimensionally displayed in Fig. 6.17. The near side of the wavefront ($y = 0$) is adjacent to the lead film surface. This wavefront is an expected one shown in Fig. 6.5. The sudden phase shifts at the flux exits are multiples of π , and their multiples are the number of fringes in Fig. 6.16 (a). This fact precisely means the flux quantization in units of $\frac{h}{2e}$. The phase measurement precision in the fringe scanning interferometry corresponds to the flux resolution of $\sim \frac{h}{100e}$ [6.7] as described in Chapter 4.

On the next step, the field vector components were derived from the numerically measured phase distributions by the data processing method mentioned in Chapter 5. The derivative $\frac{\partial\phi(x,y)}{\partial x}$ is calculated from the phase profile Fig. 6.16(b) and presented in Fig. 6.16 (c). It has peaks at the flux exits because it is the line integral of the field vector component B_y , normal to the surface along the electron path as expressed by Eq. (118). In the same way Fig. 6.16 (d) is the derivative $\frac{\partial\phi(x,y)}{\partial y}$ which corresponds to Eq. (119). Using these data, then, the field vector components were calculated according to Eqs. (120)~(123). The solid broken lines in Fig. 6.18 show the result obtained from the flux bundle with four- flux quanta appearing at the left end of Fig. 6.16 (a) or Fig. 6.14. The ordinate is normalized for the flux density of a SQF. Electron holography combined with the fringe scanning interferometry in this way enables the quantitative measurement of the field vector components near the center of an *individual* flux in terms of the distance

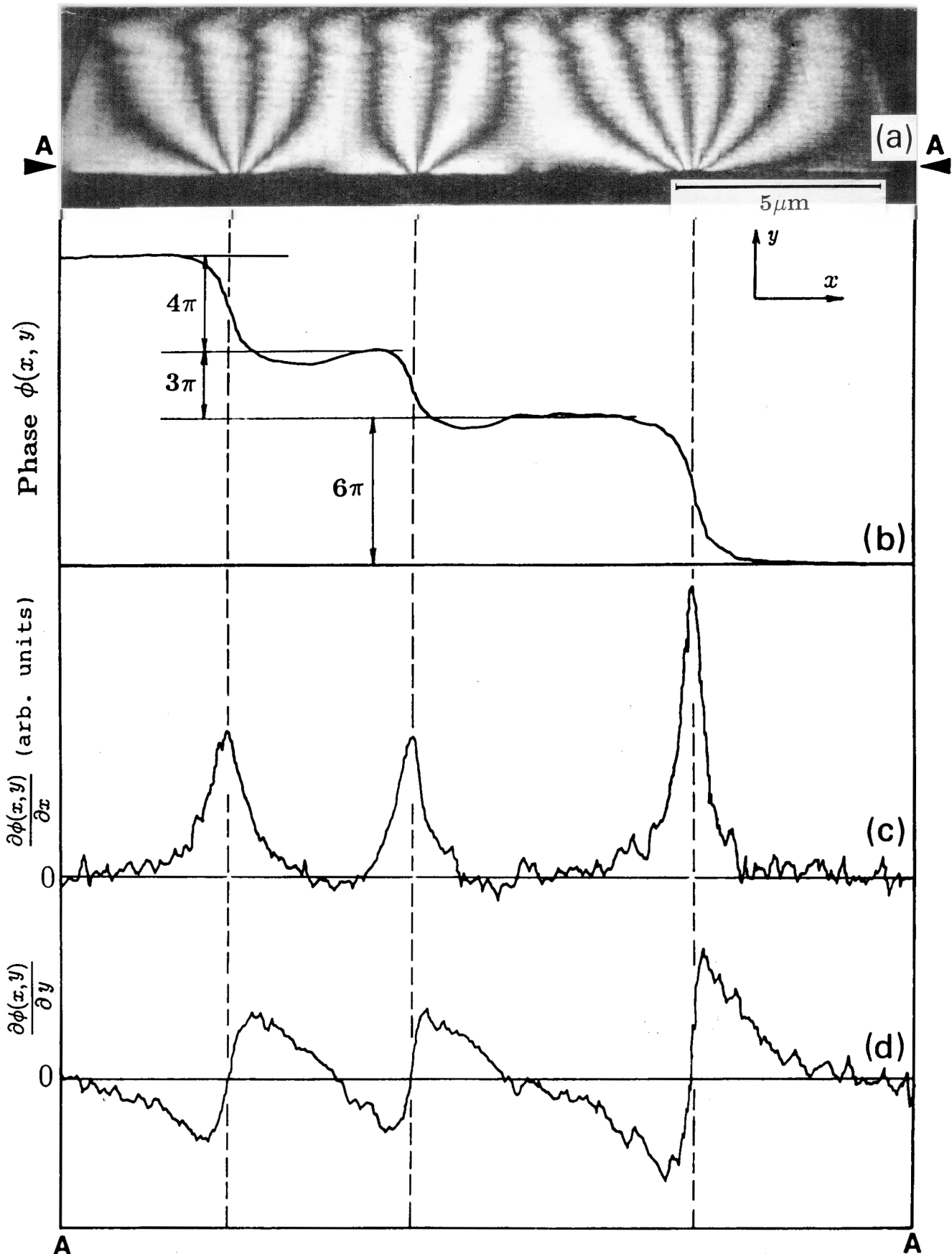


Fig. 6.16 Digital phase analysis for the fluxes appearing on the $1.0\mu\text{m}$ -thick film under the 5.00Oe -field. (a) Interference micrograph showing the MQF-A structure. (b) Line profile of the phase distribution along the line AA just above the superconductor surface in the micrograph (a). (c) Its derivative with x , $\frac{\partial\phi(x, y)}{\partial x}$. (d) Its derivative with y , $\frac{\partial\phi(x, y)}{\partial y}$.

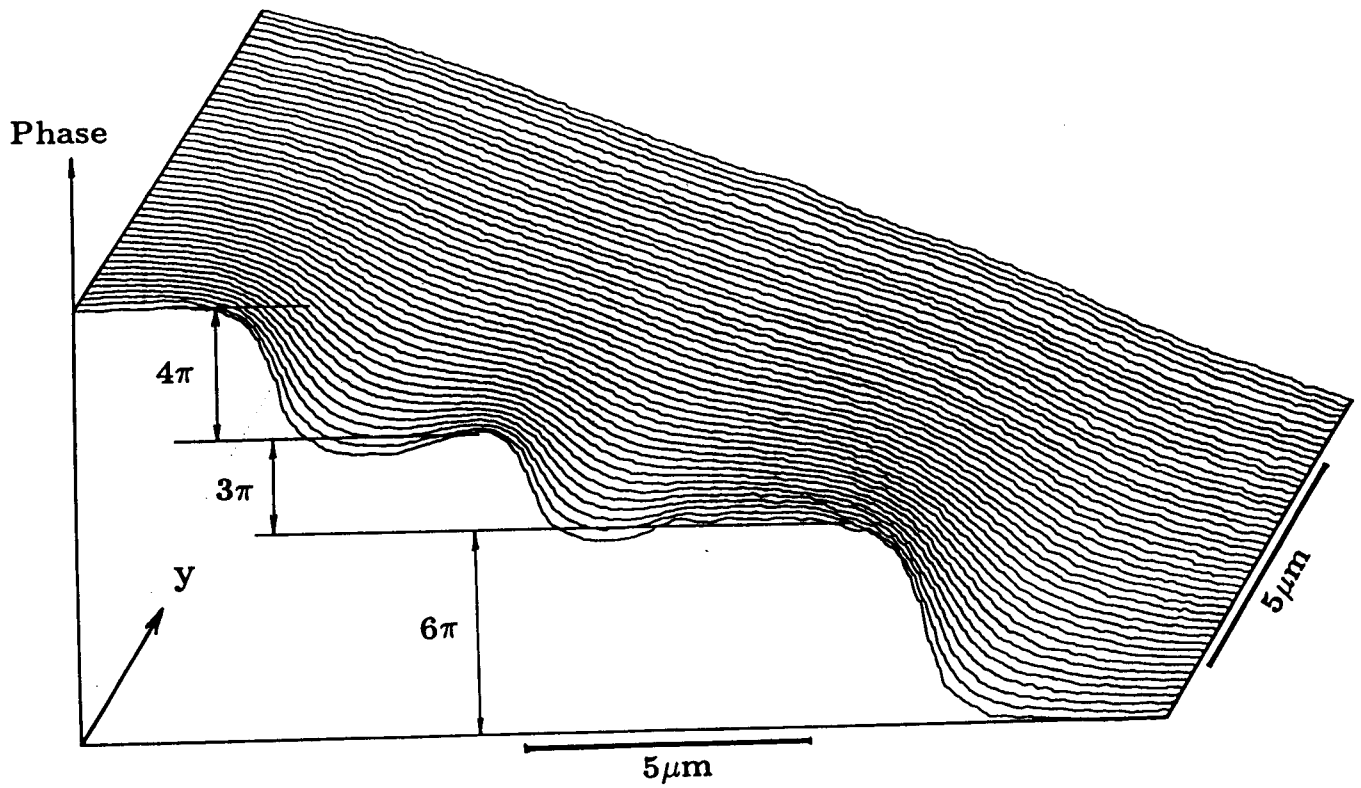


Fig. 6.17 Electron wavefront reconstructed by the fringe scanning interferometry. The hologram taken from the MQF-A structure shown in Fig. 6.16 was analyzed. The near side of the wavefront ($y = 0$) is adjacent to the lead film surface.

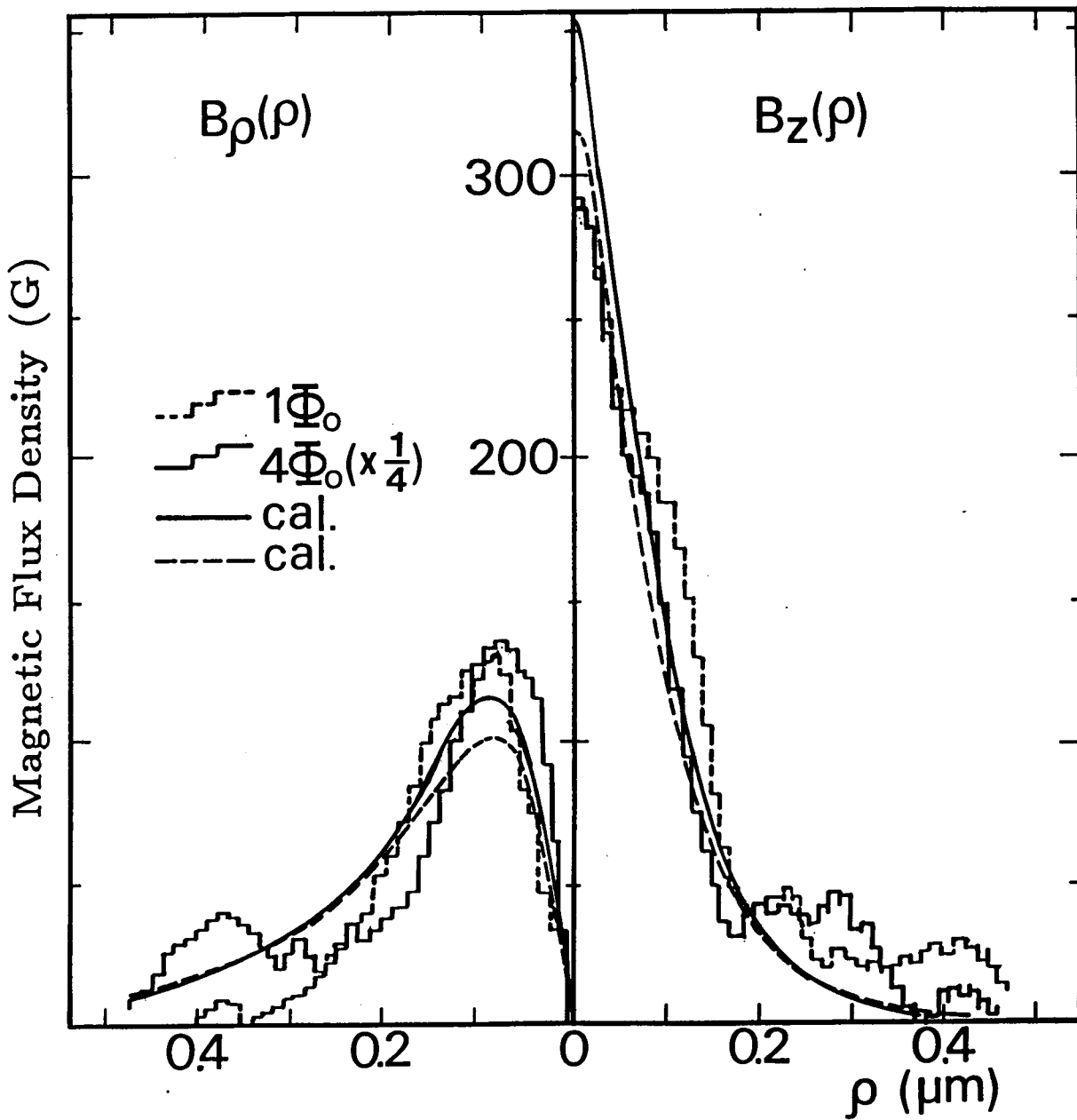


Fig. 6.18 Field vector components, $B_y(\rho)$, normal to the surface, and $B_x(\rho)$, parallel to the surface, around the flux center just above the superconducting lead film surfaces. The broken dash-lines are for the SQF line shown in Fig. 6.13. The broken solid lines are for the MQF-A line shown in Fig. 6.14. The curved solid lines are the distributions calculated from the GL equation with the Clem model using the parameters $\xi = 90\text{nm}$, $\lambda = 50\text{nm}$. The curved dash-lines are the calculated ones with the parameters $\xi = 76\text{nm}$, $\lambda = 63\text{nm}$.

from the core axis.

The same analysis for the SQF line shown in Fig. 6.13 was carried out, and its result is shown as the broken dash-lines in Fig. 6.18. The field distributions of the SQF and MQF-A almost coincide.

I next analyzed the flux of the MQF-B structure in the $1.7\mu\text{m}$ -thick film under the 12.2Oe field. Figure 6.19 (b) is the line profile of the phase distribution along the line AA just above the superconductor surface in the interference micrograph (a). Since, as in Fig. 6.16, the phase shifts at the flux exits are multiples of π , it is concluded that the fluxes are quantized in units of $\frac{h}{2e}$. But the phase changes are slower in broader areas compared with those in Fig. 6.16, which means the lower flux density in the MQF-B compared with that of the SQF and MQF-A lines. The derivatives $\frac{\partial\phi(x,y)}{\partial x}$ and $\frac{\partial\phi(x,y)}{\partial y}$ were calculated and shown in Fig. 6.19 (c) and (d). I analyzed the field components of the flux with four flux quanta appearing at the left end in this figure with use of Eqs. (120)~(123). The result shown in Fig. 6.20 is apparently different from the ones in Fig. 6.18. The B_y distribution shows, in particular, the nearly uniform flux penetration through a semi-macroscopic normal region.

By introducing the fringe scanning interferometry, in this way, we can not only determine the flux amounts with much higher accuracy compared with the interference micrograph observation, but also analyze the internal field distributions in three dimensions.

6.6 Discussions

6.6.1 Detection of a single fluxon

The contrast produced by a single fluxon in Lorentz microscopy have been calculated by the several authors [6.3][6.61]~[6.64] to find that the position detection of a single fluxon is near the observation limit from the uncertainty principle.

Using the phase difference $d\phi$ between the two paths 1 and 2 in Fig. 6.7, $d\phi = \frac{\partial\phi}{\partial x}dx$, the deflection angle of the incident electron beam β by the magnetic field of a single fluxon is given by $\beta = \frac{d\phi}{k_z dx}$, where k_z is the z -component of the wavenumber vector of

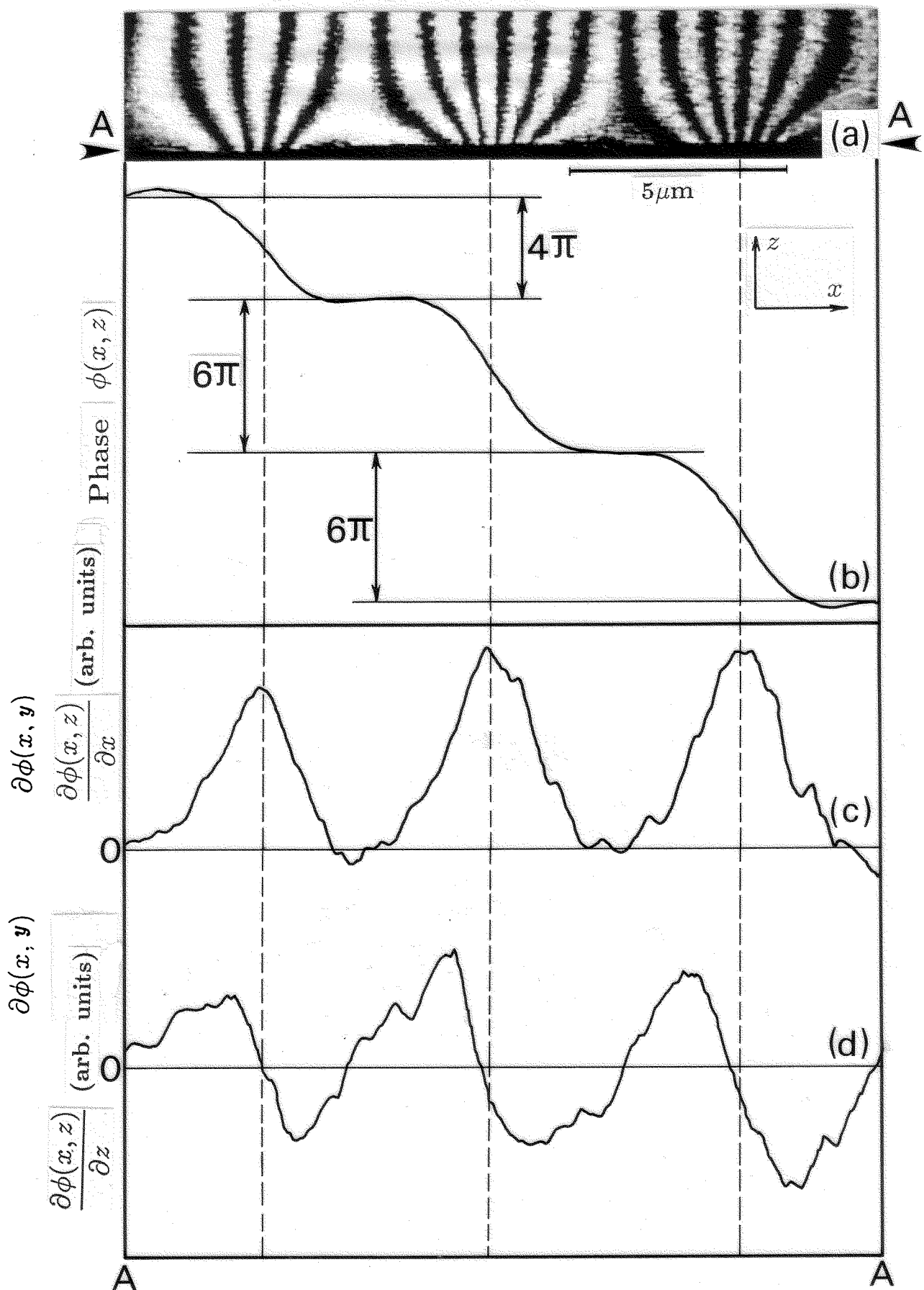


Fig. 6.19 Digital phase analysis for the fluxes appearing on the $1.7\mu\text{m}$ -thick film under the 12.2Oe -field. (a) Interference micrograph showing the MQF-B structure. (b) Line profile of the phase distribution along the line AA just above the superconductor surface in the micrograph (a). (c) Its derivative with x , $\frac{\partial\phi(x, y)}{\partial x}$. (d) Its derivative with y , $\frac{\partial\phi(x, y)}{\partial y}$.

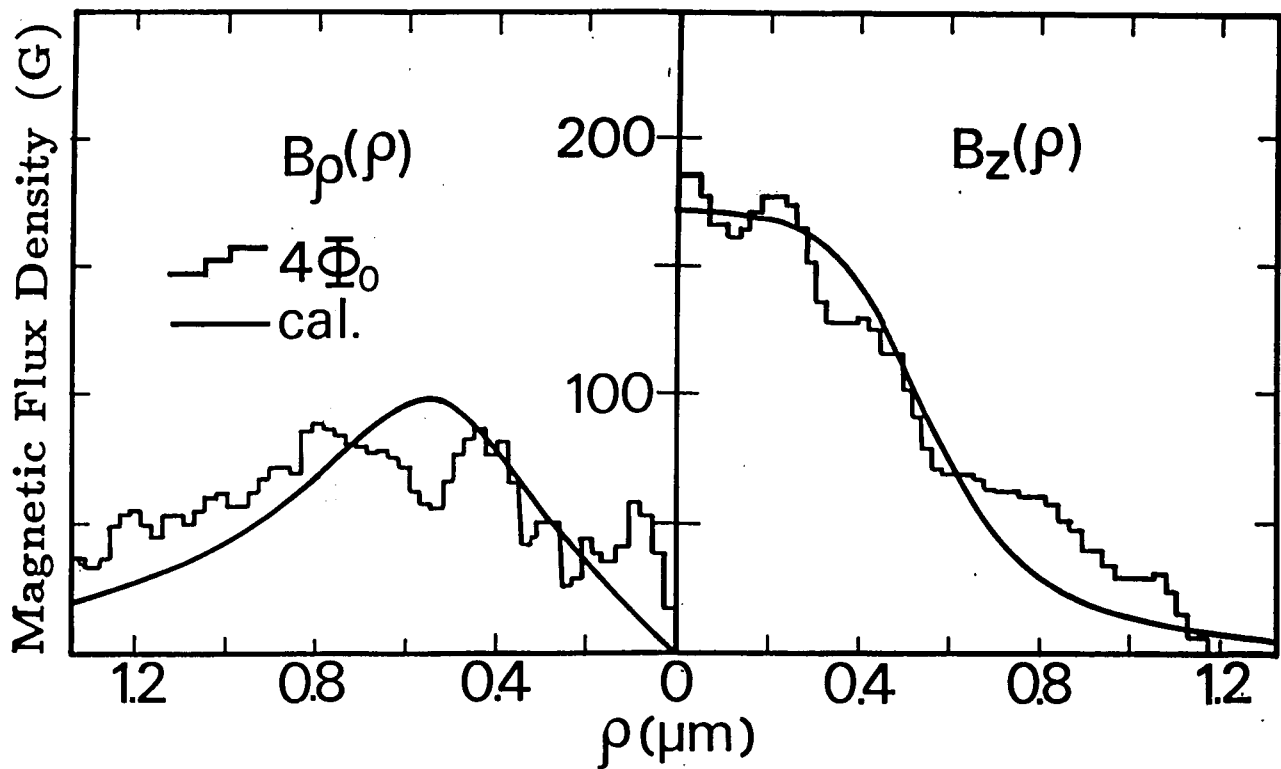


Fig. 6.20 Field vector components, $B_y(\rho)$, normal to the surface, and $B_x(\rho)$, parallel to the surface, around the flux center just above the superconducting lead film surfaces. The broken solid lines are the flux distribution in the MQF-B line shown in Fig. 6.15. The curved solid lines are the distribution calculated from the GL equation with a model Eq. (148) with $R = 0.4\mu\text{m}$, $\xi = 90\text{nm}$, $\lambda = 50\text{nm}$.

the incident electron. The phase difference $d\phi$ is expressed with the amount of the flux between the two paths $d\Phi$ as $d\phi = \pi \frac{d\Phi}{\Phi_0}$ (Eq. (63)), where $\Phi_0 = \frac{h}{2e}$. The momentum change of the incident electron beam in the x direction dp_x , on the other hand, is given by $dp_x = p_x \beta$, where p_x is the momentum component in the incident direction. Consequently we get

$$dp_x \cdot dx = \frac{h}{2} \frac{d\Phi}{\Phi_0} . \quad (145)$$

On the other hand, the spread Δx of the wavepacket in the x direction consisting of plane waves with the momentum uncertainty dp_x is related by

$$dp_x \cdot \Delta x \geq h , \quad (146)$$

from the uncertainty principle. Since the spatial resolution of real observations dx is always $dx \geq \Delta x$, therefore, we get from Eqs. (145) and (146)

$$\frac{d\Phi}{\Phi_0} \geq 2 . \quad (147)$$

This implies that the observation of magnetic fluxes with spatial resolution of dx needs the flux (change) of order of Φ_0 in the interval of dx . In other words, in the case of the observation of a single fluxon, its position can be determined only with the precision of order of its diameter.

The present report, however, shows the observation of a single fluxon with the flux resolution $d\Phi \sim \frac{\Phi_0}{100}$ and the spatial resolution dx of approximately one-hundredth of its diameter. This seems to contradict the uncertainty principle above mentioned.

A classical picture such as the above discussion on the connection between the spatial and flux resolutions is not applicable to the electron holography. The observation in image-electron holography is carried out essentially in quantum mechanical. The spatial resolution is not determined by the wavepacket spread in the direction perpendicular to the propagation. In our holography electron microscope, the electron wavepacket widely spread $\sim 50\mu m$ in the x -direction at the specimen plane. Utilizing a part of the wavepacket as an object wave, an in-focused image is formed with spatial resolution as high as conventional electron microscopes. The remaining part of the wavepacket is utilized as a reference wave. The high resolution for magnetic fluxes is achieved by

interfering the object wave with the reference one, irrespective of the spatial resolution of the image. Utilizing the reference wave in the electron holography, the high resolution for magnetic fluxes can be obtained without any reduction of the spatial resolution.

6.6.2 Magnetic flux structures of lead films

Now I compare the experimental and calculated results on the internal field distributions of quantized fluxes. The curved dash-lines in Fig. 6.13 (a) show the flux distribution calculated from the GL equation Eq. (129) with the Clem model Eq. (133) for the SQF line using the parameters $\xi = 90nm$, $\lambda = 50nm$. The observed and calculated distributions qualitatively agree, implying that I actually observed the flux exit just on the superconductor surface. More detailed comparison is possible in Fig. 6.13 (b) with the phase-difference-amplified interference micrograph. The calculated distribution (curved solid lines) considerably agrees, particularly at the flux root just above the surface.

In the case of the MQF-A line in Fig. 6.14, the agreement with the calculated distribution with the Clem model, which is the same as that of the SQF line in Fig. 6.13, is also considerable. Since, as shown in Fig. 6.10, the difference of the magnetic flux distribution between the Clem model Eq. (133) and the Lasher model Eq. (143) for the MQF lines ($n = 4$) is evident, I can conclude from my observation that the MQF-A structure is better described by the Clem's order parameter for the SQF line than that of Lasher's for n -quanta MQF line. Figures 6.13 and 6.14 show that the field distributions around the center of the SQF and MQF-A lines are in the same character with the exception of their flux amounts.

At the region far from the surface in the images of Figs. 6.13 and 6.14, the calculated lines slightly deviate from the observed ones. This is because of the boundary conditions for solving the GL equations. Equation (134) do not accurately reflect the real circumstances, which affects the distributions at the circumference in the images. Experimentally, moreover, the fringe distributions at the region far from the superconductor surface is apparently affected by slight inclination of the mirrors in the optical reconstruction interferometer (Fig. 3.1). Anyway, our main interest lies in the internal field distribution at the flux root just on the surface.

As mentioned in the previous section, the root of the MQF-B line shown in Fig. 6.15 seems much broader than those of the SQF and the MQF-A lines. This feature is qualitatively explained by the Lasher's order parameter Eq. (143) for the MQF line as shown in Fig. 6.10, which, however, does not give quantitative agreement satisfactorily with the observed MQF-B line. In order to better simulate the flux distribution of the MQF-B line shown in Fig. 6.15, I assume an order parameter;

$$\Psi(\rho, \varphi, y) = \begin{cases} \left\{1 - e^{-\frac{(\rho-R)^2}{\xi^2}}\right\}^{\frac{1}{2}} \cdot e^{-in\varphi} & (y < 0, \rho > R) \\ 0 & (y < 0, 0 \leq \rho \leq R) \\ 0 & (y \geq 0) \end{cases} \quad (148)$$

instead of Eq. (143). This model implies that a circular normal region of the radius R appears in the superconducting phase and the magnetic flux bundle of n -quanta penetrates therein. The curved dash-lines in Fig. 6.15 show the flux distribution calculated from the GL equation Eq. (129) using this model of $R = 0.4\mu m$, $n = 4$, $\xi = 90nm$, and $\lambda = 50nm$. The agreement of the observed pattern is fairly good, which shows distinct difference from the SQF and the MQF-A lines.

The field vector components are also compared. The curved solid lines and the curved dash-lines in Fig. 6.18 show the calculated distributions with the Clem's order parameter Eq. (133) using the parameters $\xi = 90nm$, $\lambda = 50nm$, and $\xi = 76nm$, $\lambda = 63nm$, respectively (compare with the curved lines in Fig. 6.8). The experimental results for the SQF (broken dash-lines) and the MQF-A (broken solid lines) are considerably traced by the calculated curves. The MQF-A line, in particular, penetrates in the form of a filament of as fine as the SQF line. I cannot here obtain a definite conclusion which pair of the GL parameters here adopted in the calculation is more appropriate.

Concerning the MQF-B line, the curved solid lines in Fig. 6.20 are calculated with a model Eq. (148), which fairly well trace the experimental results (broken solid lines). This field distribution can not be explained by any curves in Fig. 6.8, implying that the broadening of the flux root in the MQF-B line is intrinsic, not due to the shadowing of a finer root by the curved lead film edge.

It should be pointed out here that the flux density just above the normal region on the superconductor surface in the MQF-B structure is estimated approximately 180G

from Fig. 6.20, which is much lower than the thermodynamical critical field $\sim 500G$ of bulk superconducting lead at $T = 4.2K$. The internal field in the normal domain in a macroscopic intermediate state, on the other hand, is expected to be approximated by the thermodynamic critical field. This extraordinary reduction of the flux density in the normal region of the MQF-B structure is considered to come from the surface and size effects. As estimated in Section 6.4 and observed in Section 6.5, the flux lines rapidly disperse out from the superconductor surface, and its flux density fairly decreases even near the center of the normal region compared with that in the inner bulk region. Since the MQF-B lines, moreover, have much smaller size in geometry compared with a macroscopic intermediate state, its characteristics such as the flux density in the normal region can be different from that of the intermediate state in a bulk superconductor. For instance, certain reduction of the critical field in thin films has been observed [6.35][6.36].

Another remark remains to be made concerning the implication of the observed MQF-A and MQF-B lines. They do not directly correspond to the Lasher's MQF and the Goren's NS structures, respectively. They predicted their structures only at relatively high field regions, while our observations were carried out under very weak fields, just above the "lower critical field" $(1-D)H_c$ (see Fig. 6.1). Since the critical value of the GL parameter κ for the transition between the type-I and -II behaviors in superconducting characteristics is predicted to be $\kappa = \frac{1}{\sqrt{2}} = 0.707$ from the original GL theory, the estimated values $\kappa = 0.56 \sim 0.59$ for our lead films at $T = 4.2K$ seem to be considerably small for the transition. Detailed investigations, however, have revealed the attractive interaction among fluxons in a narrow κ -range near $\kappa = \frac{1}{\sqrt{2}}$, called the intermediate-mixed state [6.24][6.25][6.36]. Auer and Ullmaier [6.65] observed the transition from the type-I to -II state at κ values as small as 0.6 in the range of low temperature $\frac{T}{T_c} < 0.4$. The phase diagram in which the type-I and the type-II state including the intermediate-mixed state are classified in terms of κ and T , has been investigated by many researchers [6.1]. Our observed MQF-A and MQF-B structures, therefore, may be understood as some transition characteristics between the type-I and -II superconductors. Besides this effect, some additional features such as the pinning [6.9] and surface effects may raise the variety of magnetic flux structures like the MQF-A and MQF-B lines under low magnetic fields.

6.7 Conclusions

1. I have succeeded to directly image a singly quantized flux emerging on the surface of superconducting lead films in the form of magnetic flux line distributions using the electron holography technique. Combining the fringe scanning interferometry, furthermore, the flux quantum $\frac{h}{2e}$ have been determined for individual fluxes with precision of $\sim \frac{h}{100e}$. This method has also allowed one to analyze in detail the distributions of the field vector components around individual fluxon centers.
2. The fluxon pairs, consisting of two anti-parallel fluxons, have been observed only in the lead films of $0.2\mu m$ thickness, not in thicker films. These may be the ones predicted in the Kosterlitz-Thouless theory.
3. Under certain restricted observation conditions, i.e., under low fields and low temperatures, I have clearly observed the changes of the magnetic flux structures of superconducting lead films with increase of the film thickness. In addition to the singly quantized flux structure in the $0.2\mu m$ -thick films, two types of the multiply quantized flux structures have been newly observed in thicker films.
4. I have numerically solved the Ginzburg-Landau equations to calculate the field distributions around the fluxon center near the superconductor surface. Considerable agreement between the calculated and the experimental results was obtained. In particular, the internal field distribution of the MQF-A line appearing in the $1.0\mu m$ -thick lead film has been found to be the same as that of the SQF line in the $0.2\mu m$ -thick film.

Chapter 7

Concluding remarks

Although the original purpose of Gabor, the breakthrough of the resolution limit of electron microscopy with use of electron holography, has not yet been realized, the unique applications of electron holography have been developed as interference microscopy. The direct measurement of the phase of electron waves provides valuable information of a specimen under investigation. The present work has shown the experimental techniques to improve the measurement precision of electron phase, leading to the detailed analysis of electromagnetic fields and the thickness distribution of microscopic objects. The "sensitivity-enhanced electron holography" with the phase resolution of $\sim \frac{2\pi}{100}$ and the spatial resolution of $\sim 0.3 \text{ nm}$, in principle, now enables even the direct observation of the magnetic field from a single Bohr magneton and the three-dimensional structures of DNA's. These are the future subjects of electron holographic investigations.

The present study has also emphasized the numerical data acquisition of the electron phase distribution, which leads to the tomographic measurements of electromagnetic fields as well as the three-dimensional structure of microscopic objects. The defectoscopy at atomic resolution with electron holography, especially, will be powerful tool both in science and in technology.

Dynamical observations in electron holography is another important future subjects which has not yet been intensively investigated in spite of its great potentiality. By recording electron holograms with a video-tape recorder or so, and by analyzing the hologram with an image-processing computer using the subfringe interferometries described in Chapter 3, we will be able to make a real-time observation of the electron phase variation. Dynamical changes of magnetic structures in superconductors and magnetic fine particles

will be directly and individually imaged. In superconductors, for example, the detailed investigations of the flux flow, flux pinning, flux-line-lattice melting, and others, will provide both interesting physical insights on superconductors and some guiding principles for material development towards high superconducting critical currents [7.1].

The improvement of the phase sensitivity, spatial resolution, and time resolution has given rise to expectations that electron holography will become a unique and useful tool for investigating the microscopic world ranging from fundamental physics to practical technologies.

References

Chapter 1

- [1.1] L.de Brogile, Nature 112,540 (1923); Ann. d. Phys. ser. 10,2(1925).
- [1.2] C.J. Davisson and L. H. Germer, Phys. Rev. 30, 705 (1927); Proc. Nat. Acad. 14,317 (1928).
- [1.3] C. P. Thomson, Proc. Roy. Soc. A117, 600 (1928); ibid. A119, 651 (1928).
- [1.4] S. Kikuchi, Japan. J. Phys. 5, 83 (1928)
- [1.5] Rupp, Ann. d. Phys. 85, 981 (1928)
- [1.6] H. Busch, Ann. d. Phys. 81, 974 (1926)
- [1.7] M. Knoll and E. Ruska, Ann. d. Phys. 12, 607 (1932); ibid. 12, 641 (1932).
- [1.8] E. Ruska, Z. Phys. 87, 580 (1934).
- [1.9] D. Gabor, Proc. Roy. Soc. London, Ser. A197, 454 (1949); Proc. Phys. Soc. London, Ser. B64, 449 (1951).
- [1.10] M. E. Haine and Mulvery, J. Opt. Soc. Am. 42, 763 (1952).
- [1.11] T. Hibi, J. Electron Microsc. 4, 10 (1956).
- [1.12] A. Tonomura, A. Fukuhara, H. Watanabe, and T. Komoda, Japan. J. Appl. Phys. 7, 295 (1968).
- [1.13] J. Munch, Optik 43, 79 (1975).
- [1.14] M. Bonnet, M.Troyon, and P. Gallion, in *Proceedings of the 9th International Congress in Electron Microscopy*, Tronto, edited by J. M. Sturgess (Microscopical Society of Canada, Tronto), vol.1, p.222 (1978).
- [1.15] G. Möllenstdt and H.Dücker, Naturwissenschaften 42, 41 (1955).
- [1.16] K. Yada, K. Shibata, and T. Hibi, J. Electron Microsc. 22, 223 (1973).
- [1.17] A. Tonomura, Japan. J. Appl. Phys. 11, 493 (1972).
- [1.18] G. Pozzi and G. F. Missiroli, J. Microsc. 18, 103 (1973).
- [1.19] S. Martelli, G. Matteucci and M. Vittori Antisari, Phys. Status Solidi A 49, K103(1978).

- [1.20] P. G. Merli, G. F. Missiroli and G. Pozzi, *J. Microsc.* **21**, 11 (1974).
- [1.21] P. G. Merli, G. F. Missiroli and G. Pozzi, in *proceedings of 6th European Congr. on Electron Microsc.*, Jerusalem, p.478 (1976).
- [1.22] W. Rodewald, *Opt. Acta* **24**, 665 (1977).
- [1.23] B. Lischke, *Phys. Rev. Lett.* **22**,1366 (1969); H. Wahl, *Optik* **30**, 508 (1970).
- [1.24] R. G. Chambers, *Phys. Rev. Lett.* **5**, 3 (1960); H. Boersch, H. Hamisch, K. Grohman, and D. Wohlleben, *Z. Phys.* **165**, 79 (1961).
- [1.25] L. H. Fowler, L. Marton, J. A. Simpson, and J. A. Suddeth, *J. Appl. Phys.* **32**, 1153 (1961); G. Möllenstedt and W. Bayh, *Phys. B1* **18**, 299 (1962).
- [1.26] E. N. Leith and J. Upatnieks, *J. Opt. Soc. Am.* **52**, 1123 (1962).
- [1.27] G. Möllenstedt and H. Wahl, *Naturwissenschaften* **55**, 340 (1968).
- [1.28] I. Weingärtner, W. Mirande, and E. Menzel, *Optik* **30**, 318 (1969).
- [1.29] A. V. Crewe, D. N. Eggenberger, D. N. Wall, and L. N. Welter, *Rev. Sci. Instrum.* **39**, 576 (1968); A. V. Crewe, J. Wall, and J. Langmore, *Science* **168**, 1338 (1970).
- [1.30] A. Tonomura, T. Matsuda, and J. Endo, *Japan. J. Appl. Phys.* **18**, 9 (1979).
- [1.31] H. Lichte, *Optik* **70**, 176 (1985).
- [1.32] A. Tonomura, *Rev. Mod. Phys.* **59**, 639 (1989).
- [1.33] A. Tonomura, T. Matsuda, T. Kawasaki, J. Endo, and N. Osakabe, *Phys. Rev. Lett.* **54**, 60 (1985).
- [1.34] S. Frabboni, G. Matteucci, and G. Pozzi, *Phys. Rev. Lett.* **55**, 2196 (1985).
- [1.35] Y. Aharonov and D. Bohm, *Phys. Rev.* **115**, 485 (1959).
- [1.36] A. Tonomura, N. Osakabe, T. Matsuda, T. Kawasaki, J. Endo, S. Yano, and H. Yamada, *Phys. Rev. Lett.* **56**, 792 (1986); N. Osakabe, T. Matsuda, T. Kawasaki, J. Endo, A. Tonomura, S. Yano, and H. Yamada, *Phys. Rev.* **A34**, 815 (1986).
- [1.37] T. T. Wu and C. N. Yang, *Phys. Rev.* **D12**, 3845 (1975).
- [1.38] J. H. Brunning, C. R. Herriot, D. P. Rosenfeld, A. D. White, and D. J. Brangaccio, *Appl. Opt.* **13**, 2693 (1974).
- [1.39] T. Yatagai, K. Ohmura, S. Iwasaki, S. Hasegawa, J. Endo, and A. Tonomura, *Appl. Opt.* **26**, 377 (1987).
- [1.40] S. Hasegawa, T. Kawasaki, J. Endo, A. Tonomura, Y. Honda, M. Futamoto, K.

Yoshida, F. Kugiya, and M. Koizumi, *J. Appl. Phys.* **65**, 2000 (1989); S. Hasegawa, T. Kawasaki, J. Endo, M. Futamoto, and A. Tonomura, in *Proc. 46th Electron Microsc. Soc. Am.* p. 842 (1988).

[1.41] D. J. DeRosier and A. Klug, *Nature* **217**, 130 (1968).

[1.42] S. Hasegawa, T. Matsuda, J. Endo, N. Osakabe, M. Igarashi, T. Kobayashi, M. Naito, A. Tonomura, and R. Aoki, *Phys. Rev. B*, in print.

Chapter 2

[2.1] A. Tonomura, J. Endo, T. Matsuda, T. Kawasaki, and H. Ezawa, *Am. J. Phys.* **57**, 117 (1989).

[2.2] H. Boersch, *Z. Phys.* **139**, 115 (1954).

[2.3] T. Hibi, *J. Electron Microsc.* **4**, 10 (1956).

[2.4] E. W. Müller, *Z. Phys.* **106**, 541 (1937).

[2.5] G. Binnig, H. Rohrer, *Helv. Phys. Acta.* **55**, 726 (1982).

[2.6] A. V. Crewe, D. N. Eggenberger, D. N. Wall, and L. N. Welter, *Rev. Sci. Instrum.* **39**, 576 (1968); A. V. Crewe, J. Wall, and J. Langmore, *Science* **168**, 1338 (1970).

[2.7] G. Möllenstedt and H. Dücker, *Naturwissenschaften* **42**, 41 (1955).

[2.8] L. Marton, *Phys. Rev.* **85**, 1057 (1952).

[2.9] G. G. Matteucci, G. F. Missirole, and G. Pozzi, *Ultramicrosc.* **8**, 403 (1982).

[2.10] J. M. Cowley, *Diffraction Physics*, North-Holland Pub. Comp., 1981, chaps. 1~3.

[2.11] K. Matsumoto and T. Oze, *Seisan-kenkyu*, **19**, 18 (1967) (in Japanese).

[2.12] O. Bryngdahl, *J. Opt. Soc. Am.* **59**, 142 (1969).

[2.13] O. Bryngdahl and A. W. Lohmann, *J. Opt. Soc. Am.* **58**, 141 (1968).

[2.14] K. Matsumoto and M. Takashima, *J. Opt. Soc. Am.* **60**, 30 (1970).

[2.15] A. Tonomura, T. Matsuda, J. Endo, and N. Osakabe, *Phys. Rev. Lett.* **54**, 60 (1985).

[2.16] K. Matsuda, C. H. Freund, and P. Hariharan, *Appl. Opt.* **20**, 2763 (1969).

[2.17] J. Endo, T. Kawasaki, T. Matsuda, N. Osakabe, and A. Tonomura, in *Proceedings of the 13th International Commission for Optics*, ed. H. Ohzu (Organizing Committee of ICO-13, Sapporo, 1984) p. 480.

Chapter 3

- [3.1] M. Takeda, *Kougaku* **13**, 55 (1984) (in Japanese).
- [3.2] T. Yatagai, *O plus E* **70** (1983); *Seimitsu-kikai* **51**, 13 (1985) (in Japanese).
- [3.3] N. A. Massie, R. D. Nelson, and S. Holly, *Appl. Opt.* **18**, 1797 (1979).
- [3.4] J. H. Bruning, D. R. Herriott, J. E. Gallagher, D. P. Rosenfeld, A. D. White, and D. J. Brangaccio, *Appl. Opt.* **13**, 2693 (1974).
- [3.5] D. T. Moore, R. Murray and F. B. Neves, *Appl. Opt.* **17**, 3959 (1978); *Opt. Eng.* **18**, 46 (1979).
- [3.6] M. Takeda, H. Ina, and S. Kobayashi, *J. Opt. Soc. Am.* **72**, 156 (1982).
- [3.7] S. Yokozeki, K. Patorski, and K. Ohnishi, *Opt. Commun.* **14**, 401 (1975).
- [3.8] T. Aarii, S. Yatsuya, N. Wada, and K. Mihama, *Japan. J. Appl. Phys.* **17**, 259 (1978).
- [3.9] T. Hayashi, T. Ohno, S. Yatsuya, and R. Uyeda, *Japan. J. Appl. Phys.* **16**, 705 (1977).
- [3.10] A. Tonomura, T. Matsuda, and J. Endo, *Phys. Rev. Lett.* **44**, 1430 (1980).
- [3.11] A. Tonomura, T. Matsuda, R. Suzuki, A. Fukuhara, N. Osakabe, H. Umezaki, J. Endo, K. Shinagawa, Y. Sugita, and H. Fujiwara, *Phys. Rev. Lett.* **48**, 1443 (1982).
- [3.12] A. Tonomura, H. Umezaki, T. Matsuda, N. Osakabe, J. Endo, and Y. Sugita, *Phys. Rev. Lett.* **51**, 331 (1983).

Chapter 4

- [4.1] S. Iwasaki and T. Nakamura, *IEEE Trans. Magn.* **MAG-13**, 1272 (1977).
- [4.2] A. Iijima, K. Shiiki, and K. Shinagawa, *Jpn. J. Appl. Phys.* **24**, L11 (1985).
- [4.3] I. A. Beardsley, *J. Appl. Phys.* **53**, 2582 (1982).
- [4.4] K. Ouchi and S. Iwasaki, *IEEE Trans. Magn.* **MAG-18**, 1110 (1982).
- [4.5] N. Curland and D. E. Speliotis, *J. Appl. Phys.* **41**, 1099 (1970).
- [4.6] J. Daval and D. Randet, *IEEE Trans. Magn.* **MAG-6**, 768 (1970).
- [4.7] D. D. Dressler and J. H. Judy, *IEEE Trans. Magn.* **MAG-10**, 674 (1974).
- [4.8] T. Chen, *IEEE Trans. Magn.* **MAG-17**, 1181 (1980).

- [4.9] S. Iwasaki and K. Ouchi, *IEEE Trans. Magn.* **MAG-14**, 849 (1978).
- [4.10] K. Nishimoto, *Recent Magnetism for Electronics*, (Ohmsha and North-Holland, Tokyo, 1984), vol. 15, p. 29.
- [4.11] K. Goto, T. Sakurai, and O. Kitakami, *Jpn. J. Appl. Phys.* **25**, 1358 (1986).
- [4.12] N. Osakabe, K. Yoshida, Y. Horiuchi, T. Matsuda, H. Tanabe, T. Okuwaki, J. Endo, H. Fujiwara, and A. Tonomura, *Appl. Phys. Lett.* **42**, 746 (1983).
- [4.13] K. Yoshida, T. Okuwaki, N. Osakabe, H. Tanabe, Y. Horiuchi, T. Matsuda, K. Shinagawa, A. Tonomura, and H. Fujiwara, *IEEE Trans. Magn.* **MAG-19**, 1600 (1983).
- [4.14] Y. Honda, M. Futamoto, T. Kawasaki, K. Yoshida, M. Koizumi, F. Kugiya, and A. Tonomura, *Jpn. J. Appl. Phys.* **26**, L923 (1987).
- [4.15] M. Futamoto, Y. Honda, H. Kakibayashi, and K. Yoshida, *IEEE Trans. Magn.* **MAG-21**, 1426 (1985).
- [4.16] K. Yoshida, Y. Honda, T. Kawasaki, M. Koizumi, F. Kugiya, M. Futamoto, and A. Tonomura, *IEEE Trans. Magn.* **MAG-23**, 2073 (1987).
- [4.17] A. Fukuhara, K. Shinagawa, A. Tonomura, and H. Fujiwara, *Phys. Rev.* **B27**, 1839 (1983).
- [4.18] J. Schwinger, R. Burow, K. E. Elssner, J. Grzanna, R. Spdaczyk, and K. Merkel, *Appl. Opt.* **22**, 3421 (1983).
- [4.19] S. Iwasaki, Y. Nakamura, and H. Muraoka, *IEEE Trans. Magn.* **MAG-17**, 2535 (1981).

Chapter 5

- [5.1] *Image Reconstruction from Projections*, ed. G. T. Herman, Springer-Verlag, 1979.
- [5.2] *Computer Processing of Electron Microscope Images*, ed. P. W. Hawkes, Springer-Verlag, 1980 Chaps. 3, 4.
- [5.3] V. V. Pikalov and N. G. Preobrazhenskii, *Sov. Phys. Usp.* **26**, 974 (1983).
- [5.4] P. D. Rowly, *J. Opt. Soc. Am.* **60**, 705 (1979).
- [5.5] R. D. Matulka and D. J. Collins, *J. Appl. Phys.* **42**, 1109 (1971).
- [5.6] P. W. Schreiber, A. M. Hunter, II, and D. R. Smith, Jr., *Plasma Phys.* **15**, 635 (1973).

- [5.7] D. W. Sweeney and C. M. Vest, *Appl. Opt.* **12**, 2649 (1973).
- [5.8] R. N. Bracewell and A. C. Riddle, *Astrophys. J.* **150**, 427 (1967).
- [5.9] D. J. DeRosier and A. Klug, *Nature* **217**, 130 (1968).
- [5.10] R. A. Crowther, D. J. DeRosier, and A. Klug, *Proc. Roy. Soc. Lond.* **A317**, 319 (1970).
- [5.11] D. J. DeRosier, *Contemp. Phys.* **12**, 437 (1971) A. Klug, *Philos. Trans. Roy. Soc. London* **B261**, 173 (1971).
- [5.12] W. H. Oldendorf, *IRE Trans. BME-8*, 68 (1961).
- [5.13] D. E. Kuhl and R. Q. Edwards, *Radiology* **80**, 653 (1963).
- [5.14] A. M. Cormack, *J. Appl. Phys.* **34**, 2722 (1963); *ibid.* **35**, 2908 (1964).
- [5.15] R. Gordon, G. T. Herman, *Three-Dimensional Reconstruction from Projections: A Review of Algorithms*, in *International Review of Cytology* **38**, ed. G. A. Bourne and J. F. Danielli, Academic Press, NY, 1974, pp. 111-151.
- [5.16] T. F. Budinger and G. T. Gullborg, *IEEE Trans. NS-21*, 2 (1974).
- [5.17] R. M. Mersereau and A. V. Oppenheim, *Proc. IEEE* **62**, 1319 (1974).
- [5.18] R. N. Bracewell, *Aust. J. Phys.* **9**, 198 (1956).
- [5.19] S. F. Smerd and J. P. Wild, *Philos. Mag.* **8**, 119 (1957).
- [5.20] M. D. Altschuler, *Reconstruction of the Global-Scale Three-Dimensional Solar Corona*, in *Image Reconstruction from Projections*, ed. G. T. Herman, Springer-Verlag, 1979, pp. 105-145.

Chapter 6

- [6.1] R. P. Huebener, *Magnetic Flux Structures in Superconductors* (Springer-Verlag, New York, 1979).
- [6.2] For example, M. Tinkham, *Introduction to Superconductivity* (McGraw-Hill, Inc., New York, 1975).
- [6.3] T. Suzuki and A. Seeger, *Comments on Solid State Phys.* **3**, 128, 173 (1971).
- [6.4] H. Boersch, B. Lischke and H. Solling, *Phys. Stat. Solidi* **61**, 215 (1974)
- [6.5] T. Matsuda, S. Hasegawa, M. Igarashi, T. Kobayashi, M. Naito, H. Kajiyama, J. Endo, N. Osakabe, A. Tonomura, and R. Aoki, *Phys. Rev. Lett.* **62**, 2519 (1989).

- [6.6] T. Yatagai, K. Ohmura, S. Iwasaki, S. Hasegawa, J. Endo, and A. Tonomura, *Appl. Opt.* **26**, 377 (1987).
- [6.7] S. Hasegawa, T. Kawasaki, J. Endo, A. Tonomura, Y. Honda, M. Futamoto, K. Yoshida, F. Kugiya, and M. Koizumi, *J. Appl. Phys.* **65**, 2000 (1989).
- [6.8] J. R. Clem, *J. Low Temp. Phys.* **18**, 427 (1975).
- [6.9] T. Barbee, *Appl. Phys. Lett.* **14**, 156 (1969).
- [6.10] H. Boersch, U. Kunze, B. Lischke, and W. Rodewald, *Phys. Lett.* **44A**, 273 (1973).
- [6.11] B. Lischke and W. Rodewald, *Phys. Status Solidi (b)* **63**, 97 (1974); *ibid.* **62**, 377 (1974).
- [6.12] W. Rodewald, *Phys. Lett.* **55A**, 135 (1975); Thesis, Technischen Universität Berlin (1977).
- [6.13] G. J. Dolan and J. Silcox, *Phys. Rev. Lett.* **30**, 603 (1973).
- [6.14] G. J. Dolan, *J. Low Temp. Phys.* **15**, 111, 133 (1974).
- [6.15] Kosterlitz and D. Thouless, *J. Phys.* **C6**, 1181 (1973).
- [6.16] M. Tinkham, *Phys. Rev.* **129**, 2413 (1963); *Rev. Mod. Phys.* **36**, 268 (1964).
- [6.17] E. Guyon, C. Caroli, A. Martinet, *J. Phys. Radium* **25**, 683 (1964).
- [6.18] J. Pearl, *Appl. Phys. Lett.* **5**, 65 (1964); *J. Appl. Phys.* **37**, 4139 (1966).
- [6.19] K. Maki, *Ann. Phys.* **34**, 363 (1965).
- [6.20] G. Lasher, *Phys. Rev.* **154**, 345 (1967); *ibid.* **140**, A523 (1965).
- [6.21] A. L. Fetter and P. C. Hohenberg, *Phys. Rev.* **159**, 330 (1967).
- [6.22] R. N. Goren and M. Tinkham, *J. Low Temp. Phys.* **5**, 465 (1971).
- [6.23] U. Essman and H. Träuble, *Phys. Lett.* **24A**, 526 (1967).
- [6.24] H. Träuble and U. Essman, *J. Appl. Phys.* **39**, 4052 (1968); *J. Sci. Instr.* **43**, 344 (1966); *Phys. Status Solidi* **18**, 813 (1966); *ibid.* **20**, 95 (1967); *ibid.* **25**, 373, 395 (1968).
- [6.25] N. V. Sarma, *Phys. Lett.* **25A**, 315 (1967); *Phil. Mag.* **17**, 1233 (1968); *ibid.* **18**, 171 (1968).
- [6.26] A. L. Schawlow, *Phys. Rev.* **101**, 573 (1956).
- [6.27] U. Krögeloh, *Phys. Lett.* **28A**, 657 (1969).
- [6.28] B. Obst, *phys. stat. solid. (b)* **45**, 453, 467 (1971).
- [6.29] A. Bodmer, U. Essman, and H. Träuble, *phys. stat. solid. (a)* **13**, 471 (1972).

- [6.30] C. P. Herring, *Phys. Lett.* **47A**, 105 (1974).
- [6.31] P. L. Gammel *et al.*, *Phys. Rev. Lett.* **59**, 2592 (1987).
- [6.32] A. Ourmazd *et al.*, *Phys. Rev.* **B36**, 8914 (1987).
- [6.33] L. Ya Vinnikov *et al.*, *Solid State Commu.* **67**, 421 (1988).
- [6.34] G. J. Dolan *et al.*, *Phys. Rev. Lett.* **62**, 827 (1989).
- [6.35] G. D. Cody and R. E. Miller, *Phys. Rev.* **173**, 481 (1968); *ibid.* **5**, B1834 (1972).
- [6.36] R. E. Miller and G. D. Cody, *Phys. Rev.* **173**, 494 (1968). B1834 (1972).
- [6.37] B. L. Brandt, R. D. Parks and R. D. Chaudhari, *J. Low Temp. Phys.* **4**, 41 (1971).
- [6.38] M. D. Maloney, F de la Cruz, and M. Cordona, *Phys. Rev.* **B5**, 3558 (1972).
- [6.39] E. H. Brandt, *J. Low Temp. Phys.* **73**, 355 (1988).
- [6.40] D. Cribier, B. Jacrot, L. M. Rao, and B. Farnoux, *Phys. Lett.* **9**, 106 (1964); J. Schelten *et al.*, *Phys. Rev.* **B12**, 1772 (1975).
- [6.41] G. Pozzi and U. Valdre, *Phil. Mag.* **23**, 745 (1971).
- [6.42] E. H. Darlington and U. Valdre, *J. Phys. E: Sci. Instrum.* **8**, 321 (1975).
- [6.43] H. F. Hess, R. B. Robinson, R. C. Dynes, J. M. Valles, Jr., and J. V. Waszczak, *Phys. Rev. Lett.* **62**, 214 (1989); *ibid* **64**, 2711 (1990).
- [6.44] P. Pincus *et al.*, *Phys. Lett.* **13**, 21 (1964).
- [6.45] I. I. Gurevich *et al.*, *Phys. Lett.* **40A**, 143 (1972); D. R. Harschman *et al.*, *Phys. Rev.* **B36**, 2386 (1987).
- [6.46] P. B. Alers, *Phys. Rev.* **105**, 104 (1957); W. DeSorbo, *Phys. Rev. Lett.* **4**, 406 (1960).
- [6.47] A. Meshkovsky and A. Shalnikov, *Zh. Eksp. Teor. Fiz.* **11**, 1 (1947); *ibid.* **34**, 312 (1958).
- [6.48] A. Tonomura, *Rev. Mod. Phys.* **59**, 639 (1987).
- [6.49] B. Shinozaki, R. Aoki, T. Miyazaki, M. Katayama, and S. Yamashita, *J. Phys. Soc. Japan* **50**, 1868 (1981).
- [6.50] J. Schelten *et al.*, *Phys. Rev.* **B12**, 1772 (1975).
- [6.51] R. Koepke and G. Bergmann, *Z. Phys.* **242**, 31 (1971).
- [6.52] G. Brandli and J. L. Olsen, *Mater. Sci. Eng.* **4**, 61 (1969).
- [6.53] K. Fuchs, *Proc. Cambridge Phil. Soc.* **34**, 100 (1938); E. H. Sondheimer, *Advanc.*

Phys. 1, 1 (1952).

[6.54] F. London, *Superfluids*, vol. 1 (John Wiley & Sons, New York, 1950) p.143.

[6.55] G. Eilenberger, Z. Phys. 214, 195 (1968).

[6.56] C. Kon'no, M. Saji, N. Sagawa, and Y. Umetani, *Proc. Fall Joint Computer Conf.*, 1026, Dallas (1986).

[6.57] M. Tinkham, in *Low Temperature Physics*, edited by C. DeWitt, B. Dreyfus, and P. G. de Gennes, (Gordon and Breach, Science Publishers, Inc., New York, 1962), p. 166.

[6.58] G. E. Peabody and R. Meservey, Phys. Rev. B6, 2579 (1972).

[6.59] B. A. Huberman and S. Doniach, Phys. Rev. Lett. 43, 959 (1979).

[6.60] D. S. Fisher, Phys. Rev. B22, 1190 (1980).

[6.61] D. Wohlleben, J. Appl. Phys. 38, 3341 (1967).

[6.62] H. Yoshioka, J. Phys. Soc. Japan 21, 948 (1966); P. C. Colliex, B. Jouffrey, and M. Kleman, Acta. Cryst. A24, 692 (1968).

[6.63] M. J. Goring and J. P. Jakubovics, Phil. Mag. 15, 393 (1967).

[6.64] C. Capiluppi, G. Pozzi and U. Valdre, Phil. Mag. 26, 865 (1972).

[6.65] J. Auer and H. Ullmaier, Phys. Rev. B7, 136 (1973).

Chapter 7

[7.1] T. Matsuda, A. Fukuhara, T. Yoshida, S. Hasegawa, A. Tonomura, and Q. Ru, Phys. Rev. Lett. 66, 457 (1991).

List of the published papers

1. T. Yatagai, K. Ohmura, S. Iwasaki, S. Hasegawa, J. Endo, and A. Tonomura, "Quantitative phase analysis in electron holographic interferometry", *Applied Optics*, **26**, 377-383 (1987).
2. S. Hasegawa, T. Kawasaki, J. Endo, M. Futamoto, and A. Tonomura, "Digital phase analysis in interference electron microscopy", in *Proceedings of the 46th Annual Meeting of the Electron Microscopy Society of America*, ed. G. W. Bailey, Milwaukee, 1988, pp. 842-843 (San Francisco Press, Inc.).
3. Y. Honda, M. Futamoto, S. Hasegawa, T. Kawasaki, F. Kugiya, M. Koizumi, K. Yoshida, and A. Tonomura, "Recorded magnetization patterns of highly *c*-axis oriented Co-Cr film observed by electron holography", *Journal de Physique*, **C8**, 1969-1970 (1988).
4. S. Hasegawa, T. Kawasaki, J. Endo, A. Tonomura, Y. Honda, M. Futamoto, K. Yoshida, F. Kugiya, and M. Koizumi, "Sensitivity-enhanced electron holography and its application to magnetic recording investigations", *Journal of Applied Physics*, **65**, 2000-2004 (1989).
5. S. Hasegawa, T. Matsuda, J. Endo, A. Tonomura, and R. Aoki, "Direct observation of superconducting magnetic fluxons using electron holography", in *Proceedings of the 2nd International Symposium on Superconductivity (ISS '89)*, Tsukuba, 1989, pp. 635-638 (Springer-Verlag).
6. T. Matsuda, S. Hasegawa, M. Igarashi, T. Kobayashi, M. Naito, H. Kajiyama, J. Endo, N. Osakabe, A. Tonomura, and R. Aoki, "Magnetic field observation of a single

flux quantum by electron-holographic interferometry", *Physical Review Letters*, **62**, 2519-2522 (1989).

7. S. Hasegawa, T. Matsuda, J. Endo, N. Osakabe, M. Igarashi, T. Kobayashi, M. Naito, A. Tonomura, and R. Aoki, "Magnetic flux quanta in superconducting thin films observed by electron holography and digital phase analysis method", *Physical Review B*, **43**, 7631-7650 (1991).

8. T. Matsuda, A. Fukuhara, T. Yoshida, S. Hasegawa, A. Tonomura, and Q. Ru, "Computer reconstruction from electron holograms and observation of fluxon dynamics", *Phys. Rev. Lett.* **66**, 457-460 (1991).

9. S. Hasegawa, T. Matsuda, J. Endo, N. Osakabe, and A. Tonomura, "Phase tomography in electron holography", *Optik*, in preparation (1991).

10. S. Hasegawa, S. Ino, Y. Yamamoto, and H. Daimon, "Chemical analysis of surfaces by total-reflection-angle X-ray spectroscopy in RHEED-experiments (RHEED-TRAXS)", *Japan. J. Appl. Phys.* **24**, L387-L390 (1985).

11. S. Hasegawa, H. Daimon, and S. Ino, "A study of adsorption and desorption processes of Ag on Si(111) surface by means of RHEED-TRAXS", *Surf. Sci.* **186**, 138-162 (1987).

12. S. Ino, S. Hasegawa, H. Matsumoto, and H. Daimon, "High sensitivity detection of a few atomic layers of adsorbate by RHEED-TRAXS (total-reflection-angle X-ray spectroscopy)", in *Proc. 2nd Int. Conf. on the Structure of Surfaces (ICSOS II)*, Amsterdam, pp. 334-339 (1987).

Acknowledgments

I would like to express my great appreciation for the general guidance and continuous encouragement during the present study received from Dr. Akira Tonomura of Hitachi Advanced Research Laboratory (ARL). I also thank Dr. Junji Endo, Hiroto Kasai, Takeshi Kawasaki, Tsuyoshi Matsuda, Takao Matsumoto, and Nobuyuki Osakabe, my collaborators at ARL, who worked on development of the apparatus and experiments on electron holography. Thanks are also due to Professor Toyohiko Yatagai of University of Tsukuba for the guidance on the fringe scanning interferometry, and Professor Ryoza Aoki of Osaka University for his valuable discussions on superconductivity. Dr. Ushio Kawabe and Dr. Yoshinobu Tarutani of Hitachi Central Research Laboratory (CRL) gave valuable advice during the present study on superconductivity. Dr. Akira Fukuhara drew my attention to the theoretical aspects on the electron holographic observations. Dr. Masaaki Futamoto, Dr. Yukio Honda, Dr. Kazuetsu Yoshida, Dr. Fumio Kugiya, and Dr. Makoto Koizumi of CRL were my collaborators in the study on magnetic recording. The present investigation on superconductors was carried out with Dr. Toshio Kobayashi, Dr. Masayoshi Naito, Dr. Masukazu Igarashi, Dr. Hiroshi Kajimura, Seiichi Kondo, Hisashi Nagano. Katsuyuki Ohmura of University of Tsukuba, and Dr. Shigeo Iwasaki of National Research Laboratory for Metrology helped the experiments of the fringe scanning interferometry. Acknowledgments are finally due to Dr. Eiichi Maruyama, the Director of ARL, for his continuous encouragement during the present study, and Professor Shozo Ino of University of Tokyo for introducing me into the exciting world of experimental physics.

Quantitative phase analysis in electron holographic interferometry

Toyohiko Yatagai, Katsuyuki Ohmura, Shigeo Iwasaki, Shuji Hasegawa, Junji Endo, and Akira Tonomura

Holographic interferometry in an electron microscope and its phase analysis technique are described. The fringe scanning method is used to gain high sensitivity in phase detection. An example of measuring a magnetic field of a fine particle is presented. The measurement accuracy for median filtering is about 1/70 fringe corresponding to the magnetic flux sensitivity of 6×10^{-17} Wb. Noise reduction techniques are also discussed.

I. Introduction

Holography has been successfully used in an electron microscope since the field-emission electron microscope was developed.¹⁻³ This microscope differs from a conventional electron microscope in two respects: a field-emission electron gun provides a coherent electron beam and a Möllenstedt-type electron biprism is used as a wavefront beam splitter for recording holograms.

In an earlier stage of the electron holography technique, correction of spherical aberration in an electron optical system was a major objective to improve its spatial resolution.⁴⁻⁶ Then a 3-D imaging technique, a phase-contrast method, and an interferometric technique⁷ were discussed. Among applications of electron holography, electron holographic interferometry promises to make unique contributions. With its thickness variations and magnetic field distributions in a microscopic region can be detected.

To gain high sensitivity in interferometric phase measurement, the use of the optical phase amplification technique^{8,9} was discussed to obtain tenfold amplification of the reconstructed phase by using higher diffraction orders.^{7,10} Recently Takeda *et al.*, used the FFT method of subfringe analysis for electron

holographic fringes.¹¹ They described phase variations much smaller than 2π that could be detected without recourse to optical reconstruction or optical interferometric measurements.

In this paper, using the fringe scanning technique for fringe analysis of an electron interference hologram is discussed. It gives us high sensitivity and high spatial resolution in phase measurement. The quantitative phase measurement technique in electron holographic interferometry is useful for magnetic field measurements in the microscopic region as well as for small thickness variation evaluation. We first present a brief review of electron holographic interferometry and then discuss the use of the fringe scanning technique.

II. Electron Holographic Interferometry

A. Electron Holography

A schematic diagram of an electron holographic system is shown in Fig. 1. A specimen is positioned in one-half of a collimated beam; the other half is used as the reference beam. An image of the specimen is formed through an objective lens. A Möllenstedt-type electron biprism is situated between the objective lens and the image plane. The Möllenstedt biprism is composed of a central thin wire and two ground-potential electrodes on both sides. Application of a positive electric potential to the wire makes the image and the reference beam overlap giving interference fringes. The interference fringe pattern is magnified by a magnification lens and recorded on film as an electron hologram.

By using an optical system an image of an electron hologram can be reconstructed, as shown in Fig. 2. A hologram is illuminated by a collimated monochromatic light. An electron objective lens has a very large spherical aberration, which limits the resolution of the

Toyohiko Yatagai and K. Ohmura are with University of Tsukuba, Institute of Applied Physics, Tsukuba Science City, Ibaraki 305, Japan; S. Iwasaki is with National Research Laboratory for Metrology, Tsukuba Science City, Ibaraki 305, Japan; and the other authors are with Hitachi, Ltd., Advanced Research Laboratory, Kokubunji, Tokyo 185, Japan.

Received 23 June 1986.

0003-6935/87/020377-06\$02.00/0.

© 1987 Optical Society of America.

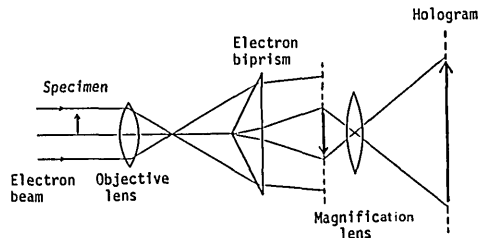


Fig. 1. Schematic diagram of an electron hologram recording.

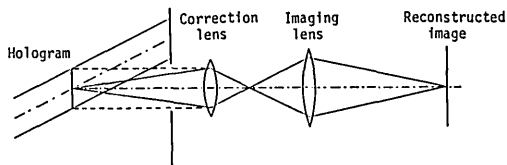


Fig. 2. Optical reconstruction system of an electron hologram. Phase difference amplification is done by using higher-order diffracted waves.

electron microscope. When this spherical aberration needs to be reduced, a correction lens is used in an optical reconstruction system to compensate the spherical aberration of the electron optics.

B. Phase in Reconstructed Image

In an optically reconstructed image, the phase of the transmitted electron beam is also reconstructed. Superimposing a plane reference wavefront on the reconstructed image gives an interference fringe pattern corresponding to the phase contours of the object. In an optical reconstruction system for the interference microscope based on the electron holography, two collimated laser beams coherent with each other illuminate a hologram, so that the plus K th order and the minus K th order reconstructed images make a phase-difference amplified interference pattern by a factor of $2K$. As described later, a combination of the first- and zero-order diffracted waves is used to obtain an interferogram without phase amplification.

The phase difference between an object beam and a reference beam is caused by two sources: thickness variation and magnetic flux. The effective refractive index n of a nonmagnetic specimen can be derived as

$$n = 1 + V_0/2\phi_0, \quad (1)$$

where V_0 is the mean potential of the specimen and ϕ_0 is the initial electron potential. Thus the phase change due to thickness variation d is given by

$$\Delta\phi = n \cdot d. \quad (2)$$

The phase difference resulting from the magnetic flux is described by

$$\Delta\phi = -2\pi \cdot e/h \cdot \int B_n dS, \quad (3)$$

where e is the electron charge and h is Planck's constant. According to Eq. (3), a 2π phase difference or one fringe in an interferogram corresponds to a closed magnetic flux of $h/e = 4 \times 10^{-15}$ Wb. This value

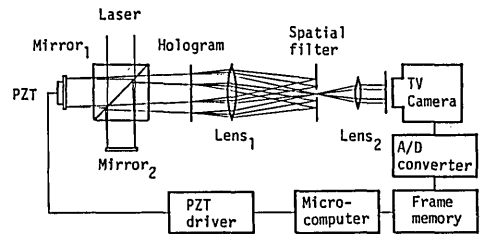


Fig. 3. Schematic diagram of hologram reconstruction and fringe analysis.

represents high sensitivity compared with that of any other conventional field-measurement techniques.

III. Phase Analysis

A. Procedure and Experimental Apparatus

Figure 3 is a schematic of the setup for reconstructing an electron hologram and making the fringe scanning phase detection of the reconstructed image. In the first experiment presented, the zero-order diffracted wave is used as the reference beam and so the plus first-order and the zero-order diffracted waves are superimposed to obtain an interference fringe pattern. One of the reconstructed beams is phase shifted with a PZT driven modulation mirror, so that the phase of the interference fringe pattern is adjusted to make phase-sensitive detection. When making phase-difference amplification of the reconstructed image, we superimpose the plus and the minus first orders of diffraction to obtain an interference fringe pattern with the twice-amplified phase distribution.

The interference fringe pattern is detected with a high-resolution low-distortion TV camera and is stored in a frame memory. Fringe data are transferred to a minicomputer. The PZT transducer is controlled by a minicomputer via a D-A converter.

B. Algorithm

Let us suppose that the interference fringe pattern with the modulated reference phase δ_n can be written as

$$f(x,y,\delta_n) = a(x,y) + b(x,y) \cos[\phi(x,y) + \delta_n], \quad (4)$$

where $\phi(x,y)$ is the phase to be evaluated and $a(x,y)$ and $b(x,y)$ are the average fringe intensity and the fringe contrast, respectively. In the fringe scanning method, one of the mirrors is stepwise moved through half of the wavelength so that the relative phase δ_n of the interferogram is changed:

$$\delta_n = 2\pi/N \quad (N = 1, 2, \dots, N-1), \quad (5)$$

where N denotes the number of mirror movements. The irradiance at each point in the interference pattern goes through one cycle of periodic variation. The computer determines a best-fit sinusoidal function for the irradiance vs the amount of phase shift at each point of the interference pattern. The phase of the best-fit function is a direct measure of the test wavefront.

According to the fringe scanning phase detection principle,¹² summations with sinusoidal weights

$$c(x,y) = \sum_{n=0}^{N-1} f(x,y,\delta_n) \cos 2\pi n/N, \quad (6)$$

$$s(x,y) = \sum_{n=0}^{N-1} f(x,y,\delta_n) \sin 2\pi n/N \quad (7)$$

are calculated to extract the sinusoidal parts of the intensity variation. The phase of the interferograms is given by

$$\phi(x,y) = \tan^{-1} \frac{s(x,y)}{c(x,y)}. \quad (8)$$

The calculated arctangent values are wrapped between $\pm\pi$ rad. The unwrapped phase value gives the correct shape corresponding to the phase profile.

C. Data Analysis Software System

To make automatic data acquisition and phase analysis, we developed a software system whose flow diagram is shown in Fig. 4. If necessary, prior to entering a main processing routine, preprocessing procedures are performed. The preprocessing step includes the piezoelectric translator calibration. The nonlinear characteristic of the piezoelectric translator is measured. The coefficients of the calibration quadratic curve of translation vs the input voltage are evaluated.¹³ By using these evaluated coefficients, a corrected voltage is available for the phase-shifting procedures.

In the first processing step, a series of interferograms with different reference phases and the first-order reconstructed image without the reference beam are stored in a computer memory. This first-order reconstructed image is used to reduce background noise in the interferograms in the next step. Noise reduction procedures are performed in the second step. TV frame averaging, unweighted local averaging, and median filtering are used to reduce statistical noise in interferograms. To obtain enhanced fringe contrast and to reduce the background noise, the first-order reconstructed image is subtracted from the interferogram data. The phase of the interferogram is calculated according to Eq. (8). The computation of phase by any inverse trigonometric function only provides phase principal values between $\pm\pi$ rad. In the third step, this phase unwrapping is performed. In the postprocessing step, the aberration of the optical interferometer and the tilt phase term are subtracted from the unwrapped phase data. Finally, calculated phase data are displayed in an arbitrary format.

D. Noise Reduction

The noise sources to be considered in electron holographic interferometry are (1) phase irregularity in a carbon film base which supports the specimen, (2) speckle noise caused by dust and such in the optical reconstruction system, (3) thickness irregularity and scattering of a hologram, and (4) electronic statistical noise: shot noise and thermal noise in a TV camera.

In spatial noise due to the first three sources, we use noise reduction techniques by digital image processing

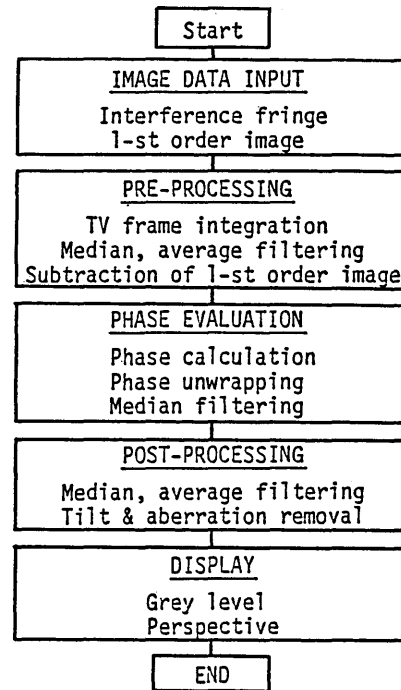


Fig. 4. Flow diagram of the software system for automatic data acquisition and phase analysis.

including local averaging, median windowing, and some spatial filtering. In particular, median window filtering is powerful in reducing salt-and-pepper spatial noise without reducing spatial resolution. Spatially independent noise such as salt-and-pepper noise in the analyzed phase distribution is serious enough to perform phase unwrapping, resulting in fatal errors near the phase discontinuity area. TV frame averaging in time provides for reduction of the statistical noise from the fourth statistical source above.

In addition to the technique mentioned above, speckle noise due to the reconstructed optical system could be reduced by using incoherent illumination to decrease the effects of diffraction patterns from dust and by using a liquid gate method to compensate phase irregularity in a hologram surface.

IV. Experimental

As shown in Fig. 3, the experimental system is divided into two parts: optical and electronic. The optical system used is a Twyman-Green interferometer with a reference phase-modulation function. The fringe analysis system consists of high-resolution TV camera (Hamamatsu C1000), frame memory, piezoelectric translator and its driver, and a DEC LSI-11/23 mini-computer system. The video signal is converted to an 8-bit digital signal and stored in the frame memory of a Hamamatsu C1901 with a 16-bit resolution. Because of the 16-bit resolution in the intensity range, 256 frames maximum can be accumulated in the frame memory to reduce statistical noise in the video signal. A piezoelectric translator (Burleigh PZ-91) makes the phase modulation. A programmable high voltage sup-

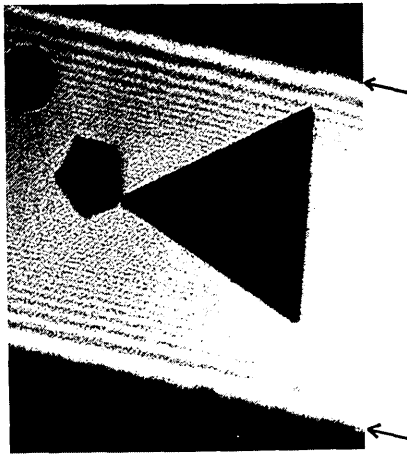


Fig. 5. Magnified version of an electron hologram. Holographic carrier fringes are observed between the arrows.

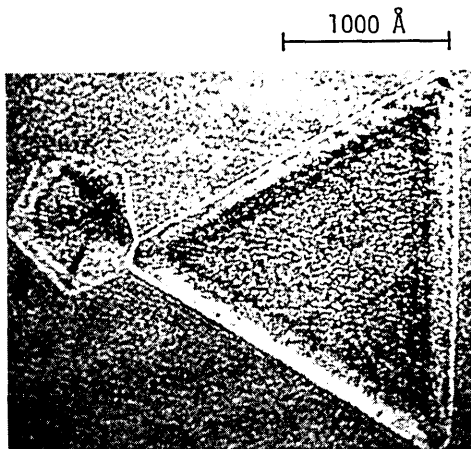


Fig. 6. Reconstructed image of a cobalt particle.

ply is developed in which a 12-bit Datal HK12BGC D-A converter generates the reference signal.

Electron holograms are recorded in a 125-kV field-emission electron microscope. The interference fringes are magnified 30,000 times in the electron microscope and recorded on Kodak 4489 electron microscope film as a hologram. The carrier frequency is 20 lines/mm. A magnified version of an electron hologram is shown in Fig. 5. The specimen is a magnetic cobalt particle mounted on a carbon thin film. Between the arrows indicated in the figure two electron beams are the overlapped and interferometric fringes obtained. The number of holographic carrier fringes in this area is ~ 250 .

Figure 6 shows a reconstructed image of a cobalt particle. The image is reconstructed without a reference beam in the optical system shown in Fig. 3. The size of the particle is ~ 2000 Å. The speckle noise is obvious in the reconstructed image.

The interferometric fringe pattern is shown in Fig. 7(a), which is obtained by superimposing the first-order diffracted wave and the zero order from the hologram of Fig. 5. An intensity profile along a central cross section is shown in Fig. 7(b). The interferogram

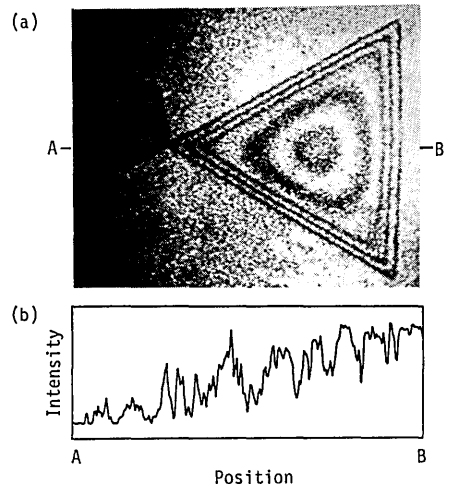


Fig. 7. Interference micrograph of (a) magnetic particle and (b) its fringe intensity profile along a central cross section.

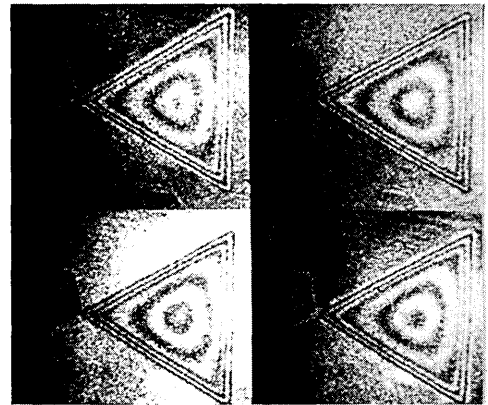


Fig. 8. Interferometric micrograms with different reference phases.

has a salt-and-peppery appearance due to the randomness of the speckle. Five interference fringes are observed in the reconstructed image. Since the particle is verified to be planar and triangular by another method, the outer three fringes are due to the thickness variation and the inner two fringes correspond to magnetic flux inside the particle.

Figure 8 shows interferograms with $\pi/2$ reference phase difference. The principal values of the phase are calculated according to Eq. (8). The calculated phase distribution is shown in Fig. 9(a). Phase irregularity from speckle noise is observed in the phase profile along a central cross section shown in Fig. 9(b). By using a 3×3 pixel median filtering window, this type of phase irregularity is reduced as shown in Fig. 10.

Figure 11 shows a grey level version of an unwrapped phase distribution and its profile along a central cross section. In the unwrapped phase distribution, a tilted phase term due to optical misalignment or a background phase is compensated by using a least-squares-estimation method. A 3-D plot of the unwrapped phase distribution is shown in Fig. 12.

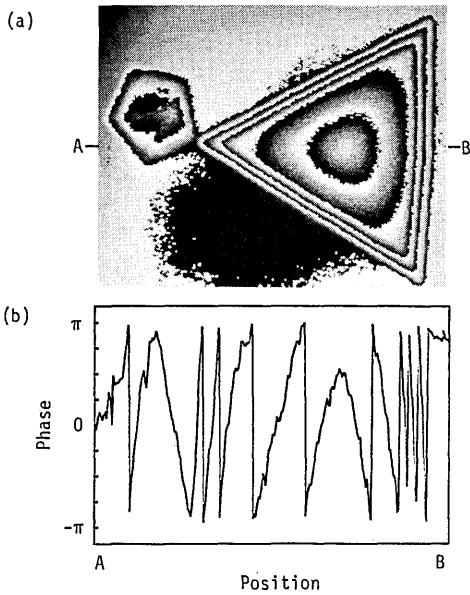


Fig. 9. Calculated phase distribution: (a) wrapped phase and (b) its profile along a central cross section.

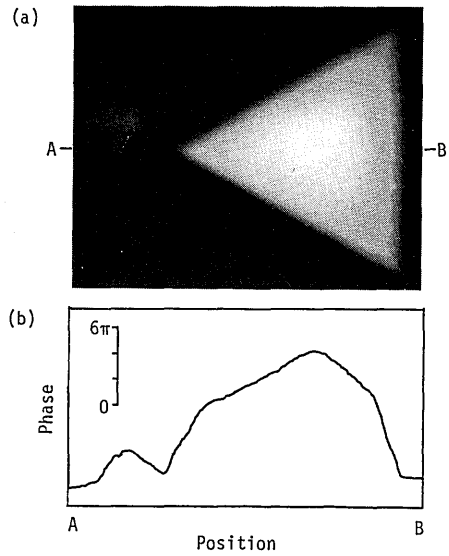


Fig. 11. (a) Unwrapped phase distribution and (b) its profile along a central cross section.

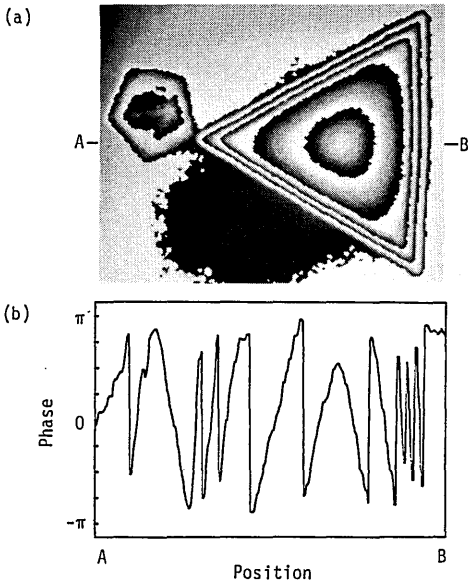


Fig. 10. Result of median window filtering of phase distribution shown in Fig. 9.

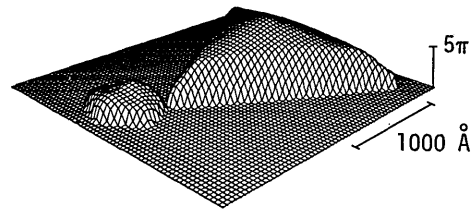


Fig. 12. Three-dimensional plot of the phase distribution shown in Fig. 11.

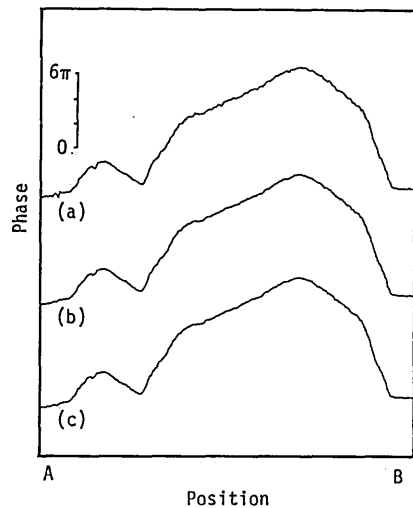


Fig. 13. Phase profiles in linear parts of Figs. 9(b) and 10(b). Evaluated phase variances are $1/50$ and $1/70$ fringes, respectively.

To evaluate the measurement noise or the accuracy limit of the measurement, variance of the calculated phase data is estimated. Figure 13 shows the phase profiles for evaluation of measurement noise. The phase profile (a) in Fig. 13 is an unfiltered phase obtained by unwrapping the profile shown in Fig. 9(b). Median filtering of the phase profile (a) gives the phase profile (b), which corresponds to Fig. 11(b). The phase profile (c) is the result of twice-applied median filtering of the phase profile (b). The noise levels or accuracy limits (a), (b), and (c) are estimated to be $1/50$, $1/60$, and $1/70$ fringe spacing, respectively.

In the phase amplification case, higher diffraction orders are used to make interference fringes. If the plus first order and the minus first order in reconstruction are used, the phase of the interferogram is magnified by a factor of 2.

V. Concluding Remarks

We have described the importance of the phase-sensitive detection method in the electron holographic microscope. The fringe scanning phase-detection technique is applied to a phase-amplified holographic fringe pattern recorded with magnetic field distribution. In the present experiment the measurement accuracy is from about 1/50 to 1/70 fringe, depending on filtering. This corresponds to a magnetic flux sensitivity of from 6×10^{-17} to 8×10^{-17} Wb. Using higher diffraction orders, a noise reduction technique, and a more stable interferometer, we expect to obtain much higher accuracy of the present situation. According to theoretical considerations 1/1000-fringe accuracy for the fringe scanning algorithm is expected in the ideal case.

This paper is based on one presented at the OSA Topical Meeting on Holography, 31 Mar.–2 Apr. 1986.

References

1. A. Tonomura, J. Endo, and T. Matsuda, "An Application of Electron Holography to Interference Microscopy," *Optik* **53**, 143 (1979).
2. A. Tonomura, *et al.*, "Electron Holography Technique for Investigating Thin Ferromagnetic Films," *Phys. Rev. B* **25**, 6799 (1981).
3. A. Tonomura, "Application of Electron Holography Using a Field-Emission Electron Microscope," *J. Electron Microsc. Jpn.* **33**, 101 (1984).
4. D. Gabor, "Microscopy by Reconstructed Wave Fronts," *Proc. Soc. London Ser. A* **197**, 454 (1949).
5. D. Gabor, "Microscopy by Reconstructed Wavefronts: II," *Proc. Phys. Soc. B* **64**, 449 (1951).
6. A. Tonomura, T. Matsuda, and J. Endo, *Jpn. J. Appl. Phys.* **18**, 1373 (1979).
7. J. Endo, T. Matsuda, and A. Tonomura, "Interference Electron Microscopy by Means of Holography," *Jpn. J. Appl. Phys.* **18**, 2291 (1979).
8. K. Matsumoto and M. Takashima, "Phase-Difference Amplification by Nonlinear Holograms," *J. Opt. Soc. Am.* **60**, 30 (1970).
9. K. Matsuda, C. H. Freund, and P. Hariharan, "Phase-Difference Amplification Using Longitudinally Reversed Shearing Interferometry: An Experimental Study," *Appl. Opt.* **20**, 2763 (1981).
10. J. Endo, T. Kawasaki, T. Matsuda, N. Osakabe, and A. Tonomura, "Sensitivity Improvement in Electron Holographic Interferometry," in *Conference Digest, Thirteenth Congress of the International Commission for Optics*, Sapporo (1984), p. 480.
11. M. Takeda and Q-S. Ru, "Computer-Based Highly Sensitive Electron-Wave Interferometry," *Appl. Opt.* **24**, 3068 (1985).
12. J. H. Bruning, D. R. Herriot, D. P. Rosenfeld, A. D. White, and D. J. Brangaccio, "Digital Wavefront Measuring Interferometer for Testing Optical Surfaces and Lenses," *Appl. Opt.* **13**, 2693 (1974).
13. T. Yatagai and T. Kanou, "Aspherical Surface Testing with Shearing Interferometer Using Fringe Scanning Detection Method," *Opt. Eng.* **23**, 357 (1984).

Books continued from page 376

Physics of New Laser Sources. Edited by N. ABRAHAM, F. ARECCHI, A. MOORADIAN, and A. SONA. Plenum Press, New York, 1986. 460 pp. \$75.00.

This book is a collection of articles based on the lectures and seminars presented at the NATO Advanced Study group of the Europhysics School of Quantum Electronics which was held at Centro I Cappuccini, San Miniato, Tuscany, 11–21 July 1984. The subject matter of the articles provides updated information for young researchers and advanced graduate students who are already engaged in the area of lasers or for those wishing to enter this area. The topics covered are also likely to be of interest to both scientists from industrial laboratories as well those in the academic community.

Abraham, Arecchi, Mooradian, and Sona assembled at the meeting some of the world's pioneers in the laser field to lecture on the developments of new laser sources currently available up to 1984. The topics reviewed in this book are excimer, alexandrite, dye, pulse compression, semiconductor, and C^3 lasers, free electron lasers, synchrotron radiation, and Er lasers to name a few. Articles on phase conjugation and stimulated Raman scattering are also present. Two important laser sources not covered in the text in any great depth are other tunable solid-state lasers based on Cr^+ , V^+ , and Ti^+ ions and the supercontinuum laser.

This book can help serve as a reference for the end laser user community who needs to be informed about the state of the art of the future laser generation and how to explore uses of these new laser sources in future applications.

R. R. ALFANO

Laser Processing and Diagnostics: Proceedings of an International Conference. Edited by D. BAUERLE. Springer-Verlag, New York, 1984. 551 pp. \$34.00.

Laser Processing and Diagnostics is the proceedings of an international conference held in Linz, Austria, 15–19 July 1984. This interdisciplinary conference was devoted to fundamental aspects and applications of laser processing. The invited and contributed papers contained in the proceedings volume are compiled into five separate complementary chapters on topics ranging from basic studies of photophysical and photochemical processes at surfaces to photo-assisted semiconductor processing and laser diagnostics of gas phase and surface processes. The primary emphasis of the book is in the area of laser processing of electronic materials. The papers are generally well written, and the editor has organized them into a coherent and logical format. Also, an extensive subject index has been compiled; this is a valuable addition that is often lacking in conference proceedings.

The first chapter is devoted to fundamental aspects of the interaction between laser radiation and solid surfaces and applications of transient heating methods for processing of electronic materials. The chapter contains fifteen papers which address issues relating to laser-induced phase transformations in Si, Ge, Te, GaAs, CdTe, InSb, Si-on-insulator structures and metals. Since such a wide variety of materials is treated, details concerning laser–solid interactions in any single system are necessarily limited. Nevertheless, the chapter provides a good introduction to laser annealing and transient processing and offers an informative survey of work in this field.

The emphasis of the second chapter is on the photophysics and photochemistry of gas–surface interactions. Although this is a rela-

continued on page 409

Shuji Hasegawa, Takeshi Kawasaki, Junji Endo, and Akira Tonomura
Advanced Research Laboratory, Hitachi, Ltd., Kokubunji, Tokyo 185, Japan

Yukio Honda, Masaaki Futamoto, Kazuetsu Yoshida, Fumio Kugiyu, and
Makoto Koizumi
Central Research Laboratory, Hitachi, Ltd., Kokubunji, Tokyo 185, Japan

(Received 7 June 1988; accepted for publication 31 October 1988)

The sensitivity for electron-phase measurement in electron holography has been improved to better than $2\pi/100$ by the application of digital interferometry at the optical reconstruction stage. This enables quantitative measurement of magnetic flux as small as $(1/100)(h/e)$ ($= 4.1 \times 10^{-17}$ Wb), hitherto undetectable, with high spatial resolution. With this technique, we have observed the distribution of leakage magnetic field from a thin cross section of a perpendicularly magnetized recording film (cobalt-chromium) with a recording density as high as 300 kFCI (85 nm bit length), the highest density ever directly observed.

I. INTRODUCTION

Electron holography¹ enables explicit measurement of the phase distribution of electron wave functions as well as their amplitude. This differentiates electron holography from conventional electron microscopy in which only the amplitude of the wave function is recorded. Since the phase of an electron wave is affected by electromagnetic, scalar, and vector potentials,² the electric and magnetic fields can be determined from the measured phase data. In this study we analyzed magnetic fields leaking from the surface of perpendicularly magnetized recording cobalt-chromium (CoCr) films developed for information storage media with high recording density in magnetic recording systems.

At the first stage of electron holography, the three-dimensional (3D) form of the wavefront, i.e., the equiphase surface of the electron wave transmitted through the investigated region, is recorded as an interference pattern called a hologram by overlapping a reference wave onto the transmitted wave in an electron microscope. Next, a similar wavefront is optically reconstructed by illuminating the hologram with a laser beam. Various laser interferometry techniques can then be applied at the reconstruction stage to analyze the wavefront with high accuracy and sensitivity. Longitudinally reversed shearing interferometry was adopted to remake a twice phase-difference-amplified hologram.³ Higher-order diffracted beams from a phase hologram were used to obtain a phase-difference amplified wavefront.⁴ By making conjugated higher-order diffracted beams interfere with each other using two coherent illuminating beams, the 3D form of the wavefront is visualized as a highly amplified contour map. The degree of phase-difference amplification hitherto obtained using these techniques ranged up to approximately 30.⁵ In other words, contour fringes can be drawn at every $2\pi/30$ phase interval in the interference micrograph. For magnetic fields, these contour fringes show magnetic flux lines in units of $(1/30)(h/e)$, because one contour fringe interval without phase-difference amplification corresponds to a magnetic flux flow of h/e ($= 4.1 \times 10^{-15}$ Wb, where h is Planck's constant and e is electron charge) according to Aharonov and Bohm.^{2,6} In

this way the magnetic field distribution can be quantitatively measured by counting the number of contour fringes.

This sensitivity, however, is insufficient for quantitative analysis of very small amounts of magnetic flux such as in high-density magnetic recordings. For this reason we have adopted "fringe scanning interferometry" using digital image processing techniques at the optical reconstruction stage.⁷ This allows us to more precisely obtain subfringe information recorded in the interference pattern.

CoCr thin films have been intensively investigated as suitable media for perpendicular magnetic recording (PMR)⁸ with high recording density. Theoretical studies on the recording mechanism have been carried out using computer simulations.^{9,10} Several reports have also been presented on attempts to experimentally observe recorded magnetization configurations using Lorentz microscopy,¹¹ the Bitter method,^{12,13} and the colloid scanning electron microscopy (SEM) method.¹⁴ Although these methods reveal the magnetization configuration in recorded media, they have insufficient sensitivity and spatial resolution for quantitative analysis of high recording density PMR. The intensity of the leakage magnetic field from the surface of the PMR film with recording densities up to 100 kFCI (kilo flux change per inch) was measured using electron holography.^{15,16} In this present paper the stray field from the 300-kFCI PMR film is analyzed more quantitatively. This is the highest recording density ever directly observed.

II. EXPERIMENTAL PROCEDURES

The Co-20 wt.% Cr alloy film (200 nm in thickness) was deposited on a Ge layer by electron beam heating in a vacuum of 10^{-4} Pa.¹⁵ As shown in Fig. 1, the magnetizations digitally recorded on the CoCr film in contact with a ring-type magnetic head are antiparallel bit by bit, the bit length being 85 nm (300 kFCI). The gap length and track width of the magnetic head were 0.25 and 70 μm , respectively. The saturation magnetization of the CoCr film was 250 kA/m. The recording was performed with all 1's non-return-zero (NRZ) signal. The Ge substrate layer promotes preferential c -axis orientation of the CoCr film.¹⁷ Magnetic fields leak

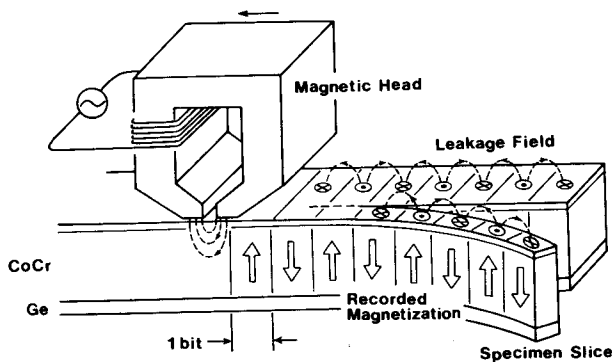


FIG. 1. Schematic illustration for sample preparation. Digital magnetic recording on a CoCr film is performed in a perpendicular magnetization mode in contact with a ring-type magnetic head. The bit length is 85 nm, which corresponds to a recording density of 300 kFCl. The medium is then sliced by a microtome for electron microscopic observation.

from the surface of the film covered with an inorganic protective layer (15 nm thickness). These stray fields are read out by a magnetic head in magnetic recording systems. The film was then sliced with a microtome to approximately 100 nm thick for microscopic observation. An electron wave illuminated the sample in an electron microscope from the direction indicated by the arrow in Fig. 2. Although the incident electron wave could not penetrate the film because of the insufficient acceleration voltage (100 kV) of the electron microscope used in this experiment, the wave passing through the leakage field in the empty space near the top edge of the sliced film was utilized to form holograms. The wavefront of the incident wave, which is plane, is deformed by the leakage field during passing through it, as shown schematically in the figure. Off-axis holograms are formed by making the transmitted electron wave interfere with a refer-

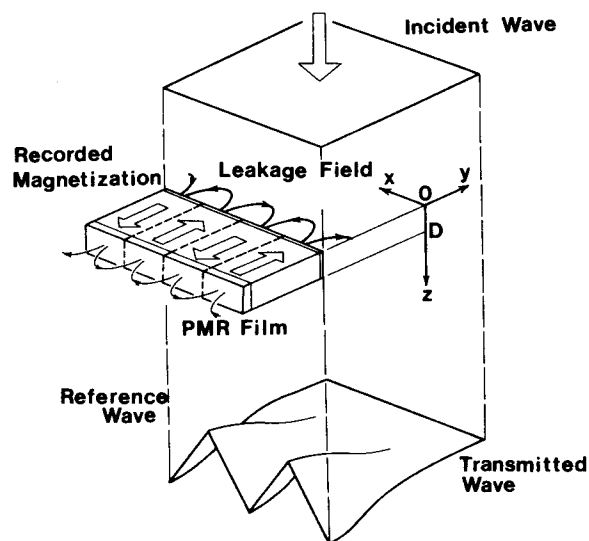


FIG. 2. The electron wavefront is deformed by the leakage magnetic field from the top edge of the recorded CoCr sliced film. The three-dimensional form of the transmitted wavefront is recorded on an electron microscope film as a hologram by overlapping a reference wave in an electron microscope.

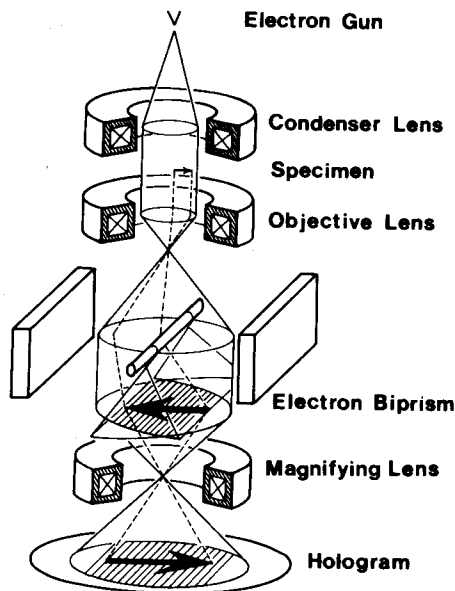


FIG. 3. Electron-optical system for electron holography. Using a coherent electron wave emitted from a cold field-emission electron gun, an off-axis hologram is made by a Möllenstedt-type electron biprism.

ence plane wave. The hologram thus obtained contains all information of the transmitted wave, its phase and amplitude.

The electron optics in the microscope is shown schematically in Fig. 3. The microscope employed was a HU-12A-type Hitachi transmission electron microscope devised for electron holography with a field-emission electron gun and a Möllenstedt-type electron biprism.¹⁸ The electron wave passing through the far left region, ~ 300 nm from the investigated field at the specimen plane, is utilized as a reference wave. The fringing field extends virtually, decaying exponentially from the PMR film edge, into the reference wave area at the specimen plane. But the reference wave is regarded as a plane wave because the phase change caused by the fringing field in the reference wave area is less than $2\pi/1000$, which is much smaller than the experimental precision. Moreover, since the divergence angle of the illuminating electron beam is 1×10^{-8} rad, the incident wave is also regarded as a plane wave with $2\pi/1000$ accuracy. An image hologram with magnification of 6000 is obtained by applying a positive voltage (~ 20 V) to the central thin wire of the electron biprism. The hologram was recorded on FG electron microscope films. The hologram width and its carrier fringe spacing were set to be 4 mm and $70\text{--}150$ μm on the film or 600 nm and $10\text{--}20$ nm at the specimen plane, respectively.

At the first half of the optical reconstruction stage, the techniques previously developed for phase-difference amplification as described in the previous section were adopted. A reversal hologram was made on a Sakura high-resolution plate from the original one by contact printing to enhance the contrast of the recorded fringes. He-Ne laser beams irradiated onto the reversal hologram on an optical bench are diffracted by its carrier fringes, and some diffracted waves emerge as well as the transmitted wave (see Fig. 2 in Ref. 3).

Only the \pm first-order diffracted waves are selected with a diffraction lens and an aperture, and interfered with each other to form a twice-phase-difference amplified hologram. This hologram was recorded on Kodak High-Speed Holographic Plate 131 and bleached to obtain a phase hologram. Next, in a Twyman–Green-type interferometer as shown in Fig. 4, the $\pm N$ th diffracted laser beams from the phase hologram interfere with each other to form a $4N$ times phase-difference-amplified interference image. The interference fringes in this image are contour lines of the wavefront, or equiphase lines of $2\pi/4N$ interval. In this experiment, interference images were made with 16-times phase-difference amplification using the \pm fourth-order diffracted light waves.

At the latter half of the optical reconstruction stage, fringe scanning interferometry was employed. Stepwise movement of the mirror *A* of the interferometer, driven by a piezoelectric transducer (PZT), causes a fringe shift in the $4N$ -times phase-difference-amplified interference image. Images at four different mirror positions, of which position interval is $\lambda/8$ (λ is the wavelength of the He-Ne laser), were synchronously stored through a TV camera (512×512 pixels) in a HIDIC-IP Hitachi image processing minicomputer. The phase value at each pixel on the image was calculated from the brightness values at the same pixel in the four images, and the original electron wavefront is numerically reconstructed.⁷ The pixel on the image in this experiment corresponded to a 0.9 nm square. From this phase data, magnetic flux lines in arbitrary units and field vector components were calculated.

II. RESULTS AND DISCUSSIONS

The numerically reconstructed wavefront of the electron wave passing near the top edge of the CoCr recording film slice is shown in Fig. 5. Since the sign of the phase shift, i.e., retardation or advance in wave propagation, is automatically determined in fringe scanning interferometry, the 3D form of the wavefront can be completely reconstructed. The deformation of the wavefront decreases with increased distance from the film edge. A phase shift smaller than $2\pi/10$

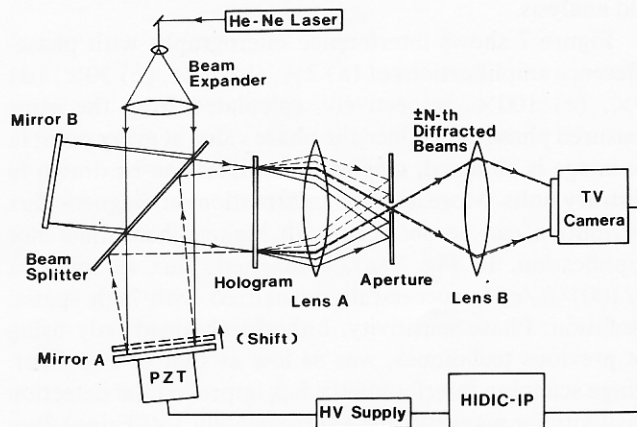


FIG. 4. Optical reconstruction setup with fringe scanning interferometry. A minicomputer HIDIC-IP controls the movable mirror *A* through a piezoelectric transducer (PZT) and processes reconstructed interference images taken in through a TV camera.

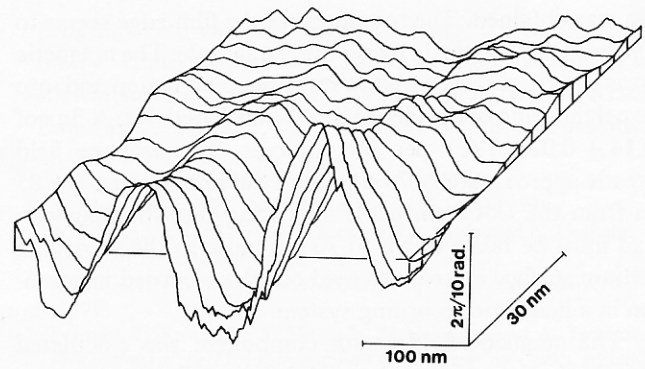


FIG. 5. A bird's-eye view of the numerically reconstructed wavefront of the electron wave passed through the leakage magnetic field from the CoCr film.

rads is successfully detected at a high signal-to-noise (S/N) ratio. If the magnetic field generated by the recording head reached the bottom of the CoCr layer at the digital recording process and the layer was wholly magnetized to the bottom, the straying field from the bottom edge as well as from the front edge of the sliced CoCr film had been expected to be detected. But wavefront deformation by the field straying from the bottom edge was not observed within the present experimental precision, implying that the recorded magnetization in the film does not penetrate to the bottom.

The contour lines of this wavefront was next calculated to obtain an interference micrograph. Figure 6(a) shows the result in a contour map of $2\pi/70$ -phase interval. The lines are also magnetic flux lines in units of $(1/70)(h/e)(=5.9 \times 10^{-17} \text{ Wb})$. In the figure, the recording film is shadowed because the electron wave could not pass through the film and no phase information from this

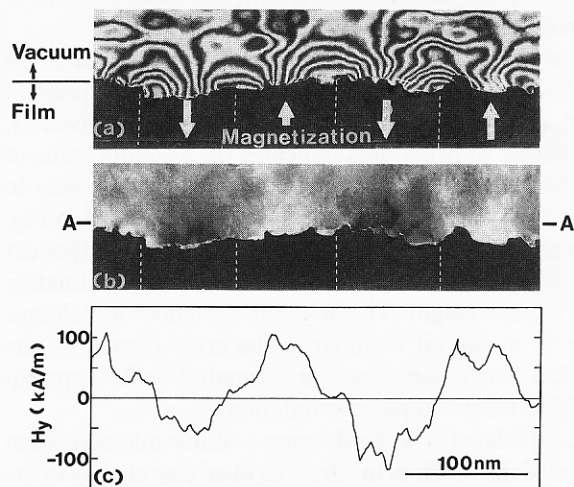


FIG. 6. Leakage magnetic field in the empty vacuum near the CoCr sliced film edge. (a) Interference micrograph with a 70-times phase-difference amplification, calculated from the measured phase data. The shadowed lower half of the figure is the recording medium and the upper, a vacuum. One fringe interval corresponds to a phase shift of $2\pi/70$ or magnetic flux of $(1/70)(h/e)$. (b) Perpendicular component of the leakage magnetic field vector is displayed in a grey scale image. White means positive (upward vector) and black means negative (downward). The degree of brightness indicates the absolute value of the component. (c) The line profile along *A-A* in (b).

area was obtained. The roughness of the film edge seems to have been caused partly by slicing the sample. The magnetic flux is clearly observed to flow out from a bit region and into the neighboring both sides of the 85-nm-length bit. A flux of $(0.14 \pm 0.02)(h/e)$ per bit emerges. The leakage field spreads approximately 70 nm from the film surface (or 85 nm from the CoCr surface), indicating that the magnetic head must be taken down to 70 nm close to the recording medium surface in order to read out the recorded information in a magnetic recording system.

The magnetic field vector component was calculated from the measured phase data. The phase difference between two arbitrary electron wave trajectories is described following Aharonov and Bohm² as

$$\Delta\phi = -\frac{e}{\hbar} \int \mathbf{B} \cdot d\mathbf{S}, \quad (1)$$

where \mathbf{B} is magnetic flux density. The integral is performed over the surface enclosed by the two trajectories: one is that of the reference wave and the other the wave transmitted through the investigated field. Since the electron wave propagates along the z axis (see Fig. 2) and the surface element vector $d\mathbf{S}$ is perpendicular to the z axis, Eq. (1) leads to

$$\frac{\partial(\Delta\phi)}{\partial x} = -\frac{e}{\hbar} \mu_0 \int H_y dz, \quad (2)$$

$$\frac{\partial(\Delta\phi)}{\partial y} = \frac{e}{\hbar} \mu_0 \int H_x dz, \quad (3)$$

where μ_0 is the permeability of vacuum. We obtain only the projection of the field vector onto the observation plane. Since the field is not uniform along the z direction, we must assume that H_x and H_y are constant at the PMR film edge ($0 < z < D$) and zero elsewhere in order to calculate the field vector component from the phase distribution. The validity of this assumption becomes worse with increased distance in the y direction from the PMR film edge.

Figure 6(b) shows the perpendicular component of the leakage field H_y in a grey scale image. White means positive (upward vector) and black means negative (downward), and the degree of brightness indicates the absolute value of the component. The leakage field vector is clearly seen to turn over bit by bit. Numerical values along line $A-A$ in Fig. 6(b) are shown in Fig. 6(c). The perpendicular component of the leakage field varies sinusoidally with approximately 100 kA/m peak height. The field direction does not change so abruptly at the bit boundary. The error caused by the assumption above mentioned is estimated to be approximately 15% from computer simulation.

The calculated stray field, using a simple magnetization model inside the medium in which an ideal step change in the recorded magnetization and no demagnetization effect were assumed, was qualitatively in accordance with this experimental result. This contrasts with perpendicular magnetic recording with lower recording density, in which the steplike change in magnetization direction with reduction of strength at the bit center due to demagnetization effect has been observed with a Hall probe.¹⁹ It can be concluded, therefore, that the demagnetization effect is negligibly small in the 300-kFCI PMR from the stray field analysis. A more

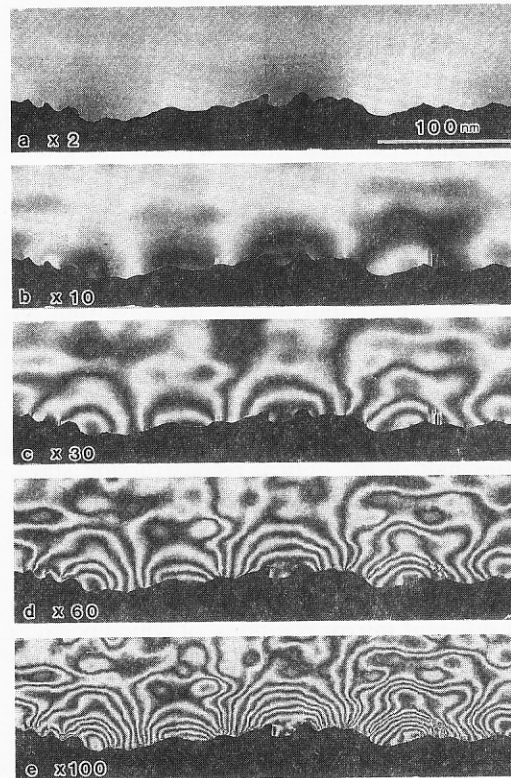


FIG. 7. Interference micrographs with phase-difference amplifications of (a) 2, (b) 10, (c) 30, (d) 60, and (e) 100 times, respectively, calculated from the same measured phase data. One fringe interval corresponds to a magnetic flux of (a) $1/2$, (b) $1/10$, (c) $1/30$, (d) $1/60$, and (e) $1/100$ of h/e , respectively.

realistic magnetization model which includes a finite transition width at the bit boundary and complex magnetic domain structures in the film will be necessary for quantitative discussion.

In this way, digital image processing techniques enabled the magnetic field to be displayed in a field vector component distribution, which should be contrasted with the previous method in which only the magnetic flux flow was displayed. This also made it possible to estimate the internal magnetization configuration in the medium from the stray field analysis.

Figure 7 shows interference micrographs with phase-difference amplifications of (a) $2\times$, (b) $10\times$, (c) $30\times$, (d) $60\times$, (e) $100\times$, respectively, calculated from the same measured phase data. Once the phase value at every point in the image is obtained, magnetic flux lines can be drawn in arbitrary units. More detailed information on magnetic flux distribution can be obtained with higher phase-difference amplification. In Fig. 7(e), a magnetic flux as small as $(1/100)(h/e)$ is successfully visualized with high spatial resolution. Phase sensitivity, hitherto obtained only using the previous techniques, was as low as that of Fig. 7(c). Fringe scanning interferometry has improved the detection sensitivity for magnetic flux approximately $3\times$. Fringe fluctuations in the micrographs seem to be due to granular noise in the hologram, speckle noise, and Fresnel diffraction effect from the central filament of the electron biprism. Phase measurement error in fringe scanning interferometry is caused

mainly from control error in PZT movement,²⁰ which was suppressed to less than $2\pi/400$ in this experiment.

Since the electron wave passing through the investigated region experiences the whole field along its trajectory, only the projection of the 3D field distribution onto the observation plane can be obtained as mentioned before. Therefore, electron holography in the present stage has no resolving power in the wave propagation direction. Deflection of the electron wave in the field was also neglected in the present analysis because of the extreme weakness of the magnetic field investigated. In general, however, decomposition to the (x,y,z) components of the field vector in the form of 3D distribution from the projected data using the computer tomographic technique, taking the deflection effect of the wave trajectory into account, is one of the future subjects.

IV. CONCLUSION

Phase sensitivity in electron holography has been improved to less than $2\pi/100$ by fringe scanning interferometry at the optical reconstruction stage, combined with phase-difference amplification techniques. This sensitivity allows detection of magnetic flux as small as $(1/100)(h/e)$ ($= 4.1 \times 10^{-17}$ Wb) with high spatial resolution. With this technique, recording in perpendicular magnetization mode with 300 kFCI recording density in a CoCr film has been confirmed for the first time by direct observation of the stray field.

ACKNOWLEDGMENTS

The authors would like to thank Professor Toyohiko Yatagai of the University of Tsukuba who offered computer

programs and valuable advice on fringe scanning interferometry. Thanks are also due to Dr. Akira Fukuhara, Tsuyoshi Matsuda, and Nobuyuki Osakabe of Advanced Research Laboratory, Hitachi, Ltd., for their helpful discussions.

- ¹A. Tonomura, *Rev. Mod. Phys.* **59**, 639 (1987).
- ²Y. Aharonov and D. Bohm, *Phys. Rev.* **115**, 485 (1959).
- ³A. Tonomura, T. Matsuda, T. Kawasaki, J. Endo, and N. Osakabe, *Phys. Rev. Lett.* **54**, 60 (1985).
- ⁴J. Endo, T. Matsuda, and A. Tonomura, *Jpn. J. Appl. Phys.* **18**, 2291 (1979).
- ⁵J. Endo, T. Kawasaki, T. Matsuda, N. Osakabe, and A. Tonomura, in *Proceedings of the 13th International Commission for Optics*, edited by H. Ohzu (Organizing Committee of ICO-13, Sapporo, 1984), p. 480.
- ⁶A. Tonomura, T. Matsuda, J. Endo, T. Arai, and K. Mihama, *Phys. Rev. Lett.* **44**, 1430 (1980).
- ⁷T. Yatagai, K. Ohmura, S. Iwasaki, S. Hasegawa, J. Endo, and A. Tonomura, *Appl. Opt.* **26**, 377 (1987).
- ⁸S. Iwasaki and T. Nakamura, *IEEE Trans. Magn.* **MAG-13**, 1272 (1977).
- ⁹A. Iijima, K. Shiiki, and K. Shinagawa, *Jpn. J. Appl. Phys.* **24**, L11 (1985).
- ¹⁰I. A. Beardsley, *J. Appl. Phys.* **53**, 2582 (1982).
- ¹¹K. Ouchi and S. Iwasaki, *IEEE Trans. Magn.* **MAG-18**, 1110 (1982).
- ¹²S. Iwasaki and K. Ouchi, *IEEE Trans. Magn.* **MAG-14**, 849 (1978).
- ¹³K. Nishimoto, *Recent Magnetism for Electronics* (Ohmsha and North-Holland, Tokyo, 1984), Vol. 15, p. 29.
- ¹⁴K. Goto, T. Sakurai, and O. Kitakami, *Jpn. J. Appl. Phys.* **25**, 1358 (1986).
- ¹⁵Y. Honda, M. Futamoto, T. Kawasaki, K. Yoshida, M. Koizumi, F. Kugiyama, and A. Tonomura, *Jpn. J. Appl. Phys.* **26**, L923 (1987).
- ¹⁶K. Yoshida, Y. Honda, T. Kawasaki, M. Koizumi, F. Kugiyama, M. Futamoto, and A. Tonomura, *IEEE Trans. Magn.* **MAG-23**, 2073 (1987).
- ¹⁷M. Futamoto, Y. Honda, H. Kakibayashi, and K. Yoshida, *IEEE Trans. Magn.* **MAG-21**, 1426 (1985).
- ¹⁸G. Möllenstedt and H. Dücker, *Naturwissen.* **42**, 41 (1955).
- ¹⁹S. Iwasaki, Y. Nakamura, and H. Muraoka, *IEEE Trans. Magn.* **MAG-17**, 2535 (1981).
- ²⁰J. Schwider, R. Burow, K. E. Elssner, J. Grzanna, R. Spdaczyk, and K. Merkel, *Appl. Opt.* **22**, 3421 (1983).

Magnetic-flux quanta in superconducting thin films observed by electron holography and digital phase analysis

Shuji Hasegawa,* Tsuyoshi Matsuda, Junji Endo, Nobuyuki Osakabe, Masukazu Igarashi, Toshio Kobayashi, Masayoshi Naito, and Akira Tonomura
Advanced Research Laboratory, Hitachi, Ltd., Hatoyama, Saitama 350-03, Japan

Ryozo Aoki

Department of Electrical Engineering, Faculty of Engineering, Osaka University, Yamadaoka, Suita 565, Japan

(Received 27 August 1990; revised manuscript received 17 December 1990)

Singly quantized magnetic fluxes in superconducting lead films have been directly observed in the form of magnetic-flux-line distributions by using an electron-holography technique. Combining this with the digital-phase-analysis method, we were able to determine the flux quantum $h/2e$ for individual fluxes with a precision of $\sim h/100e$, and analyze the distributions of field-vector components around the fluxon centers. The internal-field distributions obtained were compared with those calculated from the Ginzburg-Landau equations with use of some models, and an overall agreement was found between them. We also observed the changes of the magnetic-flux structures of lead thin films as a function of their thickness. Fluxon pairs were observed in $0.2\text{-}\mu\text{m}$ -thick films, which may correspond to those suggested by Kosterlitz-Thouless theory.

I. INTRODUCTION

An essential character of superconductivity which has manifested itself in macroscopic quantum state is magnetic-flux quantization in units of $\Phi_0 = h/2e$ (fluxon), a ratio between two universal constants. An exact measurement of the quantity Φ_0 and analysis of the internal structure of a fluxon, therefore are of great importance for basic research on superconductivity.^{1,2} Fluxons form a flux-line lattice in type-II superconductors under external magnetic fields, and they are forced to move by transport currents. When its electromagnetic driving force exceeds the fluxon pinning force, the fluxon starts to move in viscous flow with energy dissipation, resulting in Ohmic resistance and thus limiting the superconducting critical current. Investigation of the static and dynamic behaviors of the fluxons, therefore, play an important role for basic research as well as for industrial applications of superconductors.

As reviewed in Sec. II various kinds of experimental techniques have been employed for the observation of fluxons since the prediction of Abrikosov. Although, especially, the methods using electron waves such as Lorentz microscopy were considered powerful, they have not yet attained fully satisfactory results, because the observation had to be carried out near the measurement limitation from the uncertainty principle, as suggested by Suzuki and Seeger.³ Only some special techniques of electron wave interferometry by Boersch *et al.*⁴ have succeeded in detection of the fluxon existence in a superconducting hollow cylinder without microscopic site determination.

By introducing an electron-holographic technique, on the other hand, we have recently succeeded to overcome the measurement limitation for simultaneously obtaining

high spatial resolution and magnetic-flux sensitivity.⁵ Singly quantized fluxes emerging on the surface of superconducting lead film has been directly imaged in the form of magnetic-flux lines. The present paper reports the detailed analysis on the internal-field distributions around the fluxon center by combining the digital-phase-analysis method⁶ with electron holography. This method allows a numerical measurement of the phase distribution of electron waves by the techniques of digital data processing.⁷ A decomposition of the magnetic-field-vector components from the electron phase distribution has become possible by utilizing the axisymmetry of the fluxon-field distributions. Then a direct comparison between the experimental analysis and the results of theoretical calculation is available. We have numerically calculated the internal-field distribution around the fluxon center in terms of the Ginzburg-Landau (GL) equations, using some models such as the Clem model.⁸ In consequence, an overall agreement was found between the experimental and calculated results.

We also observed structure changes in the magnetic-flux distributions of thin lead films, as a function of their thickness. Our results on the structural transition from the type-I to the type-II-state behaviors of lead films were consistent with those of earlier works.⁹⁻¹⁴ Fluxon pairs consisting of two antiparallel fluxons were also observed in $0.2\text{-}\mu\text{m}$ -thick lead films, which may correspond to the ones suggested in Kosterlitz-Thouless theory.¹⁵

In Sec. II we briefly review the earlier works on the magnetic-flux structures of thin films of type-I superconducting materials, and the experimental techniques for their investigations. Section III is devoted to describing our experimental details and analysis methods supplemented with some mathematical expressions. In Sec. IV, we calculate the internal-field distributions of quantized

fluxes penetrating through a superconductor by numerically solving the GL equations using some models. In particular, the flux spread near the surface of the superconductor is evaluated for a comparison with experiment. Experimental results are shown in Sec. V, and compared with the calculated results in Sec. VI, and finally summarized in Sec. VII.

II. BACKGROUNDS

It is appropriate for the purpose of electron-holographic observation to select a superconducting material of the low value of the GL parameter κ , because the fluxons in such a material are so fine that the flux density is high enough to be detectable. From this point of view, we selected the material lead, of which pure thin films could be simply prepared. The type-I superconductor such as lead enters the intermediate state under the magnetic field between $(1-D)H_c$ and H_c (H_c is the critical field; D is the demagnetization factor). In this state, the macroscopic normal regions (N), through which magnetic fluxes penetrate, appear in the superconducting phase (S). When the thickness of the specimen along the external field becomes thinner, the N/S distribution structure changes in the way that the N region is divided into smaller dimension of normal spots. The variation is based on the change of the thermodynamical free energy which is composed of the N/S interface energy and the nonuniform-magnetic-field energy. Both are in counter-proportional relation with the N/S structure size, whence its equilibrium size is determined from the minimum energy condition for given thickness of the superconductor.

The N/S interface energy can be expressed in terms of the effective GL parameter κ . When the specimen thickness becomes as thin as a critical thickness, the κ value approaches $1/\sqrt{2}$ and the normal spot size is in microscopic scale of the penetration depth λ , containing the magnetic flux quantized in units of Φ_0 . This means that sufficiently thin films of any superconducting materials can go into type-II superconducting states with the mixed state. At the intermediate region of the thickness, the N/S structures and its corresponding magnetic-flux distributions show various kinds of patterns; normal spots (NS) containing macroscopic amounts of fluxes, multiply quantized fluxes (MQF), and singly quantized fluxes (SQF).

Tinkham¹⁶ has pointed out the possibility of the N/S structure changes even for type-I superconducting materials. After this prediction, the magnetic-flux structures in superconducting films have been theoretically studied within GL theory in more detail by Guyon *et al.*,¹⁷ Pearl,¹⁸ Maki,¹⁹ Lasher,²⁰ and Fetter and Hohenberg.²¹ They mainly discussed the stability of each magnetic-flux structure and the critical thickness of the film. According to Lasher,²⁰ as the film thickness increases, the MQF line structures are increasingly more energetically favorable than the SQF structures in the high-field region. In the MQF structure, individual flux bundle with several flux quanta can arrange in the lattice form like Abrikosov's. With further increase of the film thickness, normal-state spots with finite diameters appear

in the superconducting phase and semimacroscopic multiquanta fluxes penetrate therein. This is Goren's normal-spot (NS) model.²² And finally, the laminar structure is most favorable at the sufficiently thick superconductors.

These magnetic-flux structures in thin films of superconducting materials have been experimentally observed in various ways. Direct observations of the SQF static distributions on lead alloy films were performed by Essman and Träuble,^{23,24} and also by Sarma²⁵ with use of the modified Bitter method which had been applied for imaging the domain boundaries in ferromagnetic materials.²⁶ This powerful method has been intensively applied for the investigations of magnetic flux distributions in type-I and -II superconductors of various thicknesses by Barbee,⁹ Rodewald *et al.*,^{10,11,12} and Dolan and Silcox,^{13,14} and many other investigators.²⁷⁻³⁰ The transition from the type-I to type-II-state behavior was also detected by electrical and magnetic measurements.³¹⁻³⁴ Since reports on this particular subject are too numerous to cite comprehensively, the reader should consult Ref. 1 in which is cited additional literature on related work. Earlier results on the magnetic-flux structures in films of type-I superconductors, e.g., lead, may be summarized in a phase diagram at a relatively high temperature T ($T < T_c$), as sketched in Fig. 1. Although the figure is only qualitative and should not be taken strictly, it enables us to explain the conditions under which each investigation is performed, involving the present work. Although most of the earlier works, theoretically and experimentally, were carried out in relatively high-field regions, the present observation covers only very-low-field regions, just above the Meissner phase, due to the ap-

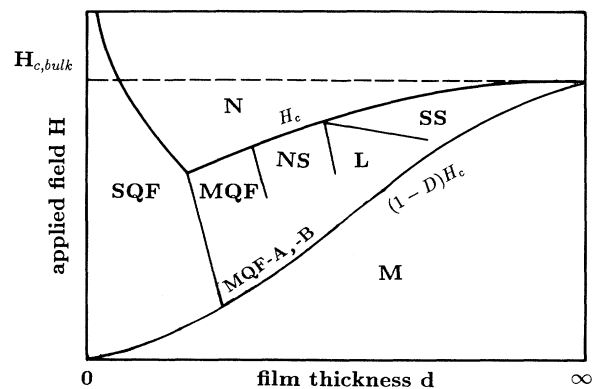


FIG. 1. Schematic phase diagram showing various magnetic-flux structures in a film of a type-I superconducting materials under the magnetic field perpendicular to the film surface. The structures depend on the film thickness and the applied magnetic field. M: Meissner state, N: normal state, SQF: singly quantized flux line structure, MQF: multiply quantized flux line structure, NS: normal spot structure, L: laminar structure, SS: superconducting spot structure. $H_{c,bulk}$ indicates the thermodynamical critical field of a bulk superconductor. D denotes the demagnetization factor. Two types of multiply quantized flux line structures, MQF-A and MQF-B, are found in the present study.

paratus limitation.

In addition to the Bitter method, various kinds of experimental techniques have been employed to observe the magnetic-flux structures in superconductors.^{1,35} They are summarized in Fig. 2 based on their spatial resolution and the sensitivity for magnetic flux. It shows rough estimations of availability of typical experimental methods. The shaded area covers the resolution and sensitivity necessary for observing the mixed state in type-II superconductors. The neutron diffraction method³⁶ allows very quantitative analysis on the flux structures, only when the flux is well periodically distributed. Electron microscopic observations such as shadow electron microscopy,³⁷ electron interferometry,⁴ and out-of-focus electron microscopy,³⁸ have not yet obtained enough spatial resolution and flux sensitivity at the same time. As suggested by Suzuki and Seeger,³ in particular, it is almost impossible to observe the internal field distribution of a single fluxon by out-of-focus electron microscopy because of the uncertainty principle. Recent observation using scanning tunneling microscopy³⁹ reveals a flux-line lattice, which, however, does not probe the magnetic flux itself, but rather the electronic-state changes near the fluxon center at the surface.

Electron holography,⁵ on the other hand, enables one to directly observe individual fluxons quantitatively with high spatial resolution and analyze the internal-field distribution of an individual fluxon, even though the fluxes are themselves not periodically distributed. This method has another advantage in dynamical observation of fluxons. Several investigators tried to observe the movement of the magnetic fluxes in, for instance, lead foils with transport current by means of the Bitter method²⁴ and the shadow electron microscopy.⁴⁰ They have not yet, however, attained satisfactory results, because the former technique is lacking in time resolution and the latter is poor in spatial resolution. In contrast to those tech-

niques, electron holography has sufficiently high temporal and spatial resolution to allow observation of SQF movements. In this paper, though, we focus our attention on static observations of fluxons.

Electron holography was invented by Gabor⁴¹ in order to improve the resolution of electron microscopes. In spite of unsuccessful advances in his original idea, however, an alternate form of the application of electron holography has been successfully developed.⁴² Direct observation of very weak magnetic fields with angstrom resolution has been realized. The principle underlying electron-holographic observation is the Aharonov-Bohm effect.⁴³ The phase of electron waves is affected by magnetic fields, or more strictly speaking, by the magnetic vector potential because the waves carry electric charge.⁴⁴ So we can directly observe the magnetic fields by electron holography which allows an explicit measurement of the phase distribution of the electron wave functions. This fact differentiates electron holography from laser holography in which no magnetic information can be deduced for charge-neutral photons. We have analyzed the detailed magnetic structures of thin films, fine particles, and magnetic recording materials.⁴² The magnetic field distributions are revealed in the form of magnetic flux lines in electron holography micrographs (interference micrographs). Since each line in the micrograph corresponds to a definite amount of magnetic flux h/ne (h is Planck's constant, e is the electric charge of an electron, and n is an integer up to about 100), we can quantitatively analyze the field just by counting the number of the lines. In this paper, furthermore, a more quantitative field analysis is shown by introducing the digital-phase-analysis method.

III. EXPERIMENTAL PROCEDURES AND ANALYSIS METHOD

A. Sample preparation

Superconducting lead film of thickness ranging from 0.1 μm to several μm were fabricated by vacuum deposition on one side of a tungsten wire of 30 μm diameter at room temperature. We have chosen the film thicknesses according to the earlier works which report that the transition of the magnetic-flux structures from the type-I- to the type-II-state takes place in this range of the thickness.^{14,31} The tungsten wire surface was made clean and smooth in advance by direct current heating up to 2300 K in vacuum. The sample is shown in Fig. 3. The lead film was made up of grains of single crystals, so that special attention was paid to preparation of films almost totally free from surface roughness, pinholes, and cracks at grain boundaries. The critical temperature of the lead films was measured to be 7.2 K, and the residual resistance ratio R_R , $\rho_{300\text{ K}}/\rho_{7.5\text{ K}}=50-80$ for 0.2- μm -thick films and better for thicker films. The quality of the prepared films were recognized in same grade with the specimens in other studies^{14,31} because of the similar R_R values.

The R_R value, a measure of the disorder in the film structure, always corresponds to the effective mean free path,⁴⁵

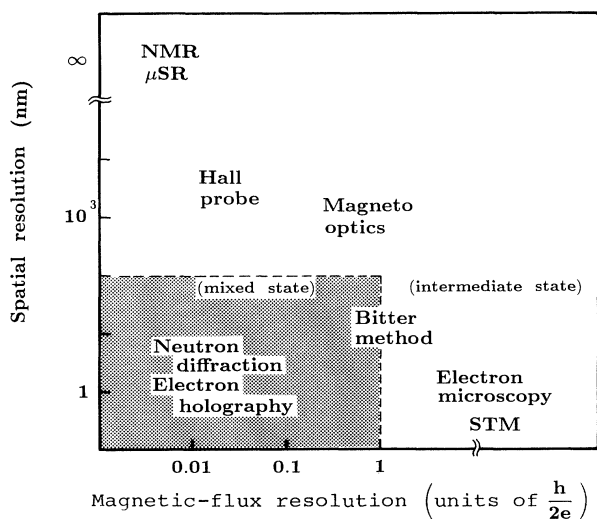


FIG. 2. Typical experimental methods to observe the flux structures in superconductors. They are roughly classified in terms of their spatial resolutions and magnetic-flux resolutions.

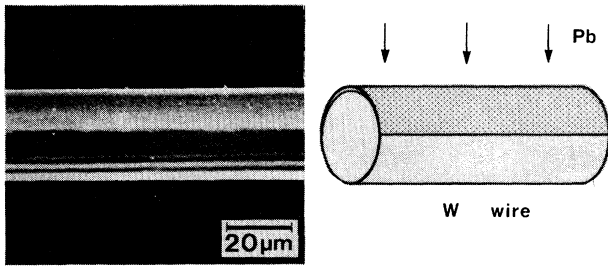


FIG. 3. Scanning electron micrograph of the observation sample. The lead film was deposited on one side of a tungsten wire of $30\ \mu\text{m}$ diameter.

$$l = (R_R - 1) \frac{\rho l}{\rho_{300\text{ K}}}, \quad (1)$$

where the values of ρl and $\rho_{300\text{ K}}$ are obtained from the literature;⁴⁶ $\rho l = 1.5 \times 10^{-11}\ \Omega\text{cm}^2$, $\rho_{300\text{ K}} = 21\ \mu\Omega\text{cm}$. From the values of R_R for our lead films; $R_R = 50\text{--}80$ for the $0.2\text{-}\mu\text{m}$ -thick films, we obtain $l = 360\text{--}560\text{ nm}$.

In the case of sufficiently thin films, on the other hand, the effective mean free path is limited primarily from diffuse reflection of the electrons at the sample surfaces. According to the Fuch's classical theory of the size effect,⁴⁷

$$\frac{1}{l} = \frac{1}{l_\infty} + \frac{3}{8d}, \quad \frac{l}{l_\infty} > 0.1, \quad (2)$$

where l_∞ is the mean free path of a bulk specimen of the same purity and defect content, and d is the film thickness. For the film of $d = 0.2\ \mu\text{m}$, using the value of l above obtained, l_∞ should be longer than $1.1\ \mu\text{m}$ estimated from Eq. (2). This implies that our lead films had enough high quality and purity so that the mean free path is not limited by the impurity and defect scatterings, but primarily by the film thickness.

The wire was fixed on a sample holder with indium-layer thermal contact. In our electron holography microscope (Fig. 4), the lead film was cooled down to be superconducting with fluxons under the magnetic field perpendicular to the film surface. Because the electron beam could not transmit through the film, we could only observe the fluxons spreading out into vacuum outside the film surface, not the fluxons in the film. So we had to catch the root of the fluxon just above the film surface in order to investigate the internal field distribution of the fluxon inside the film. For this reason the film was curved to ensure the fluxons exit at the extreme edge of the sample shadow.

But the observed fluxons were not necessarily located on the extreme edge of the sample shadow. In fact, fluxons with different root diameters were observed even on the same sample. Therefore, we cannot measure the intrinsic fluxon diameters with fluxons of broader roots which do not stand on the extreme edge and are probably shadowed by the edge. Since, however, it is considered that the fluxons with the finest roots among the large number of observed fluxons really exit at the extreme

edge of the sample shadow, they were used for the analysis of the inner field distribution around the fluxon center.

B. Electron-holography microscope

Our microscope was an H-800 type Hitachi transmission electron microscope devised for electron holography with a cold field-emission type electron gun and a Mollenstedt-type electron biprism.⁴⁸ Its operating voltage was 150 kV. It also had a sample cooling stage and electromagnet pairs to apply the magnetic field perpendicular to the lead film.

The sample-cooling stage depicted in Fig. 5 was set in the sample chamber of the microscope column and thermally connected to a liquid helium and nitrogen container which was set outside the column. The sample holder (SH) was introduced from the sample exchange chamber (EC) through the gate valve (GT) and rapidly cooled down from room temperature by thermal connection with the stage. The sample holder, which can be cooled down to 2.5 K by pumping out the liquid helium container, is surrounded with two shells for thermal radiation shielding. The intermediate shell (HJ1) was cooled down to 5 K with liquid helium and the outer (NJ) was 100 K with liquid nitrogen. The sample temperature could be reversibly set at any points between 2.5 and 20

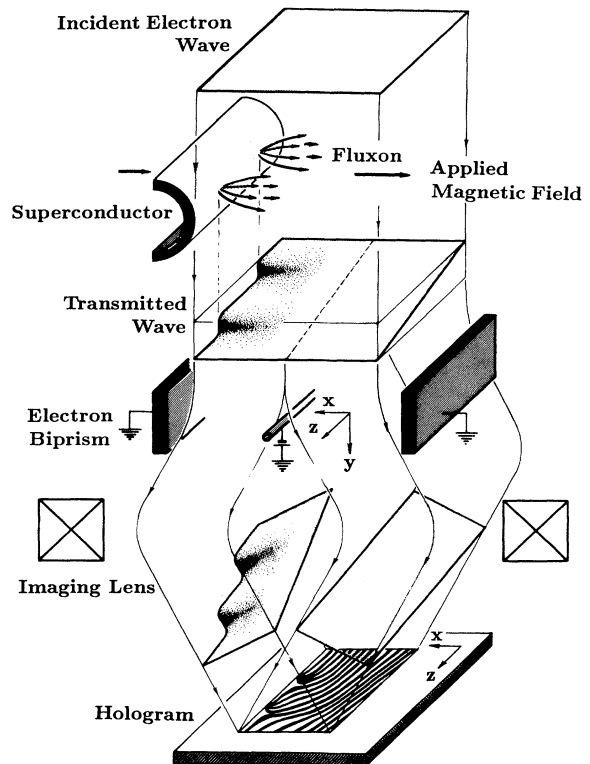


FIG. 4. The electron wave propagation in the electron holography microscope. The wavefront is deformed by the fluxons and divided into two parts, an object wave and a reference wave, by an electron biprism to form a hologram.

K with a heater attached to the stage. Annealed silver flexible foils of $30\ \mu\text{m}$ thickness (AF) were used for the thermal connection of the sample to the refrigerant container, and at the same time, for the absorption of the external mechanical vibrations.

The first electromagnet pair (EM1) produces the transverse magnetic field up to 35 Oe to create the fluxons in the lead film. Since the field, however, deflects the electron beam (EB), we need the second (EM2) and third electromagnet pairs (EM3) to correct the beam path for microscopic observation. The excitation of the latter two electromagnets are adjusted according to the first magnetic field strength. In this way it became possible to carry out the in-field cooling and the in-field observation, of which temperature and magnetic field ranges were 2.5–20 K and -35 –35 Oe, respectively.

The propagation of electron waves in the microscope is illustrated in Fig. 4. The illuminating electron wave, emitted from the field emission tip, is regarded as a plane wave $\psi_{\text{inc}} = \exp\{ik_0y\}$ (the wave propagates along the y axis and k_0 is the wave number of the electron). Transmitting through the sample region, the wave front is deformed by the magnetic field; the localized field of a fluxon causes steep phase change, although the wave front passing far from the lead film is only inclined smoothly because of a uniform field. By electron biprism action, the transmitted wave is divided into two parts, su-

perimposed, and interfere with each other. Interference fringes were recorded on a hologram. One of the divided waves, passed near the lead film surface, becomes an object wave which contains the information on the fluxons. It is expressed as

$$\psi_{\text{obj}} = \exp\{ik_1y + ik_2x + i\phi(x,z)\}, \quad (3)$$

where $\phi(x,z)$ is the phase shift caused by the fluxons, and the phase factor $\exp\{ik_2x\}$ denotes the beam deflection in the x direction by the electron biprism, and $k_0^2 = k_1^2 + k_2^2$. Another wave, passed through the far distant region, $\sim 6\ \mu\text{m}$ from the investigated lead film surface at the specimen plane, acts as a reference wave. It is expressed as a plane wave

$$\psi_{\text{ref}} = \exp\{ik_1y - ik_2x\}, \quad (4)$$

because the beam deflection by the biprism occurs in the symmetrically opposite ($-x$) direction with the object wave Eq. (3). The phase distribution of the object wave $\phi(x,z)$ is thus recorded in the form of interference fringe distributions, an off-axis hologram $I_{\text{hol}}(x,z)$;

$$I_{\text{hol}}(x,z) = |\psi_{\text{obj}} + \psi_{\text{ref}}|^2 \sim 1 + \cos \left[\frac{2k_2x}{M} + \phi \left(\frac{x}{M}, \frac{z}{M} \right) \right], \quad (5)$$

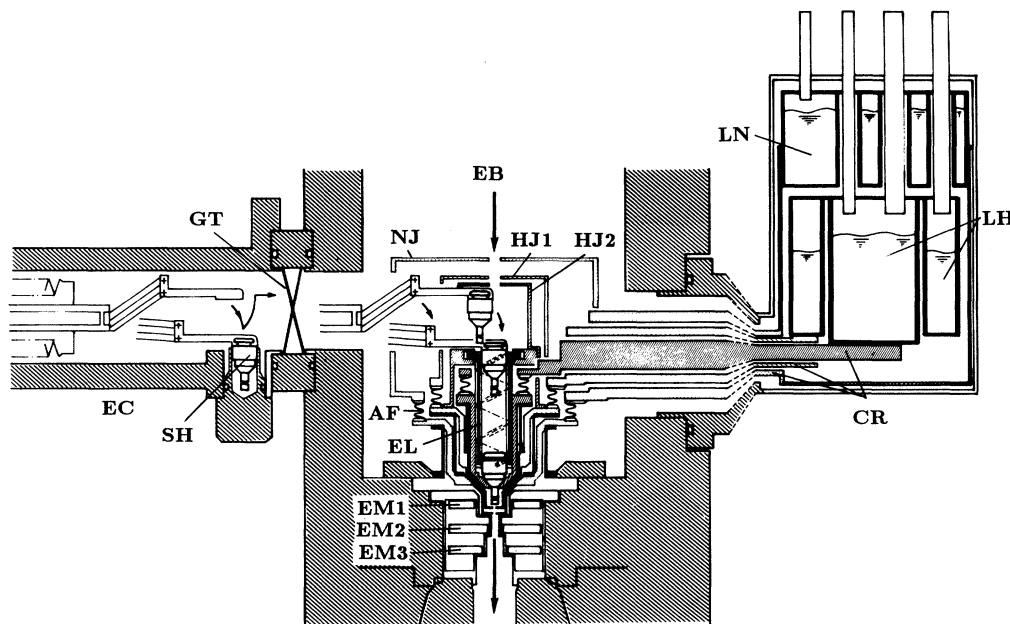


FIG. 5. The sample cooling stage and the electromagnet pairs equipped in the sample chamber of the electron microscope column. The sample holder (SH) is introduced from the exchange chamber (EC) through the gate valve (GT) into the column. The holder is set at the observation position by the elevator (EL) and thermally connected to the cooling stage. The stage is connected through a Cu rod (CR) to a liquid helium (LH) and nitrogen (LN) containers set outside the column. The stage and container are composed of three shells; the outer shell (NJ) is cooled down to 100 K by the liquid nitrogen, the intermediate shells (HJ1) is 5 K by the liquid helium, and the inner shell (HJ2), which contacts to the sample holder, is 2.5 K by pumping the inner liquid helium container. Thin flexible Ag foils (AF) thermally connect the sample and the refrigerant container, and at the same time, absorb mechanical vibrations. The first electromagnet pair (EM1) apply the magnetic field perpendicular to the sample lead film. The second (EM2) and the third (EM3) electromagnet pairs correct the electron beam (EB) path deflected by EM1 for microscopic observation.

where $\pi M/k_2$ is the carrier fringe spacing in the hologram and M is the magnification of the image. For simplicity we have neglected here the uniform phase shift by the uniform applied magnetic field.

Strictly speaking, the reference wave is not a plane wave because the magnetic field modulation by the fluxons virtually extends, decaying exponentially from the film surface, into the reference wave area at the specimen plane. Since, however, the phase change caused by the modulation in the reference wave area is estimated to be less than $\pi/200$ which is smaller than the experimental precision, the reference wave can be regarded as plane and the phase distribution recorded on the hologram is only the object wave's. Moreover the divergence angle of the illuminating electron beam is $\sim 1 \times 10^{-8}$ rad so that the incident wave is also regarded as a plane wave with $\pi/500$ accuracy.

The sample image was focused by the intermediate lens, because the objective lens was switched off to prevent the extra field applying the sample. An image hologram with magnification M of 1500–2000 was obtained by applying a negative voltage (~ -20 V) to the central thin wire of the electron biprism. The holograms were recorded on Kodak 4489 electron microscope films. The carrier fringes were set to be parallel to the lead film edge shadow, or perpendicular to the fluxons, in the hologram. The hologram width and its carrier fringe spacing were set to be 4–10 mm and 60–100 μm on the film, or 4–6 μm and 30–60 nm at the specimen plane, respectively.

C. Optical reconstruction with digital-phase-analysis method

Although the phase distribution $\phi(x, z)$ of the electron wave passed through the fluxons is recorded on the holo-

gram as Eq. (5), we cannot read out the phase information directly from it, because the interference fringes in the hologram are very fine and are not the contour phase lines. So we utilized a laser interferometer for the optical reconstruction to visualize the phase distribution as contour phase lines. After developing and fixing the hologram, it was set in a Twyman-Green-type laser interferometer as shown in Fig. 6. The He-Ne laser beam is divided into two beams by a beam splitter, and after reflected by the mirrors *A* and *B*, each beam irradiates the hologram. The illuminating laser beams are plane waves. In addition to the transmitted waves which are also plane waves, a set of the \pm first-order diffracted waves emerge from each illuminating beam, because the hologram with the carrier fringes acts as a grating. The diffracted waves have the phase information recorded on the hologram. Only the +first-order diffracted wave from the beam reflected by the mirror *A*

$$\psi_{+1} = \exp\{iK_1y + i2k_2x + i\phi(x, z)\} \quad (6)$$

and the –first-order one from another beam reflected by the mirror *B*

$$\psi_{-1} = \exp\{iK_1y - i2k_2x - i\phi(x, z)\} \quad (7)$$

were selected. Here $K_0 \equiv \{K_1^2 + (2k_2)^2\}^{1/2}$ corresponds to the wave number of the laser beam and the magnification M in Eq. (5) was omitted for simplicity. They were then adjusted to propagate in the *y* direction by inclining the mirrors,

$$\psi_{+1} = \exp\{iK_0y + i\phi(x, z)\}, \quad (8)$$

$$\psi_{-1} = \exp\{iK_0y - i\phi(x, z)\}, \quad (9)$$

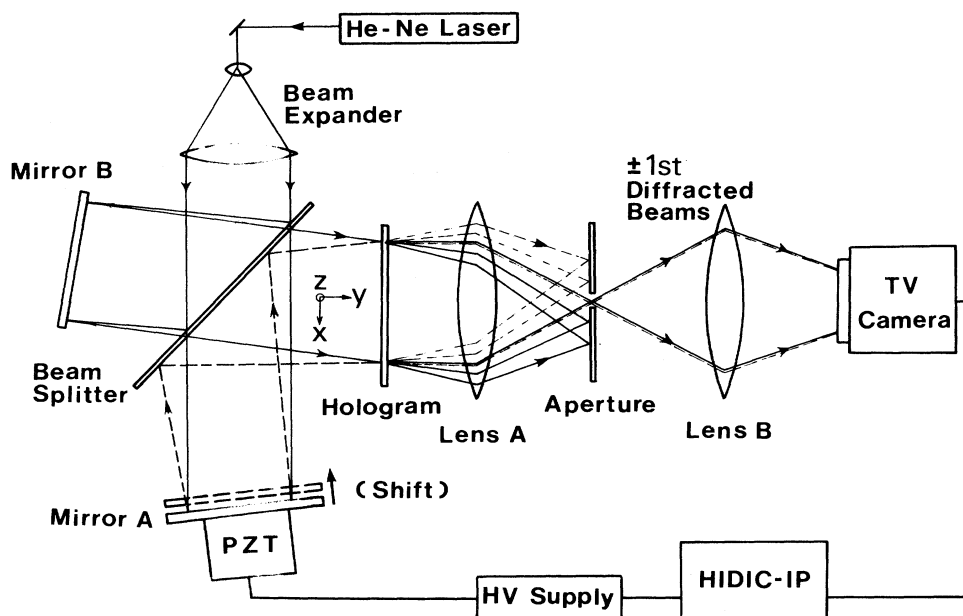


FIG. 6. Laser interferometer for the optical reconstruction with the fringe scanning interferometry. The interference micrographs are stored in a Hitachi image processing computer HIDIC-IP which also control a high voltage (HV) supply to derive a piezoelectric transducer (PZT).

and were made to interfere with each other to form an interference micrograph $I(x, z)$;

$$I(x, z) = |\psi_{+1} + \psi_{-1}|^2 \sim 1 + \cos\{2\phi(x, z)\}. \quad (10)$$

The carrier fringes are in this way removed, and the interference fringes in this image become contour phase lines of π interval. This is an interference micrograph.

The fringe intensity distribution in the real micrograph is, however, expressed as

$$I(x, z) = a(x, z) + b(x, z)\cos\{2\phi(x, z)\}, \quad (11)$$

instead of Eq. (10), because the average fringe intensity $a(x, z)$ and the fringe contrast $b(x, z)$ are not constant over the image due to the nonuniformity of the illuminating laser beams, nonlinearity of the photographic film, the speckle noise, and others. Although the interference micrograph Eq. (11) directly shows the phase distribution $\phi(x, z)$ in units of π , moreover, we cannot measure the phase distribution with the phase resolution higher than π . In other words, the phase information between the neighboring fringes in the interference micrograph cannot be displayed. To read out the subfringe information from the hologram with higher accuracy, then, we have adopted a digital phase analysis method called "fringe scanning interferometry"⁴⁹ which utilizes the digital image-processing technique with a computer. This method allows the numerical measurement of the phase distribution of the wave reconstructed from the hologram and improve the phase measurement precision up to $\sim \pi/50$.

Stepwise movement of the mirror A of the interferometer of Fig. 6, driven by a piezoelectric transducer (PZT), causes a fringe shift in the interference micrograph Eq. (11) because the relative phase difference between ψ_+ and ψ_- changes with the mirror movement. Images at four different mirror positions, of which position interval is $\lambda/8$ (λ is the wavelength of the He-Ne laser beam, 6328 Å),

$$I(x, z; n) = a(x, z) + b(x, z)\cos\left[2\phi(x, z) + \frac{2\pi n}{4}\right] \quad (12)$$

($n=0-3$) were synchronously stored through a TV camera (512×512 pixels) in a HIDIC-IP Hitachi image-processing minicomputer. A pixel corresponds to a ~ 8 -nm-square on the specimen plane. The irradiance at each pixel in the interference micrograph goes through one cycle of periodic variation with the mirror movement. The computer determines a best-fit sinusoidal function for the irradiance versus the amount of phase shift at each pixel in the micrograph. The phase of the best-fit function is a direct measure of the investigated wave front. According to the fringe-scanning phase-detection principle,⁴⁹ summations with sinusoidal weights

$$\begin{aligned} C(x, z) &= \sum_{n=0}^3 I(x, z; n) \cos\left[\frac{2\pi n}{4}\right] \\ &= I(x, z; 0) - I(x, z; 2), \end{aligned} \quad (13)$$

$$\begin{aligned} S(x, z) &= \sum_{n=0}^3 I(x, z; n) \sin\left[\frac{2\pi n}{4}\right] \\ &= I(x, z; 1) - I(x, z; 3), \end{aligned} \quad (14)$$

are calculated from the four images Eq. (12) to extract the sinusoidal parts of the intensity variation. This method enables one to separate the phase information $\phi(x, z)$ from the fringe average $a(x, z)$ and contrast $b(x, z)$ of the interference pattern. The phase of the pixel is then given by

$$\begin{aligned} \phi(x, z) &= \arctan \frac{S(x, z)}{C(x, z)} \\ &= \arctan \frac{I(x, z; 1) - I(x, z; 3)}{I(x, z; 0) - I(x, z; 2)}. \end{aligned} \quad (15)$$

The calculated arctangent values are wrapped between $\pm\pi$. The unwrapped phase value gives the correct shape corresponding to the phase profile. By performing the above calculation all over the pixels in the image, the electron wave front is numerically reconstructed.

D. Electron phase and magnetic field

We now review the relation between the phase of the electron wave and the magnetic field for preparing the analysis of the fluxon fields. The Aharonov-Bohm effect⁴³ predicts that the magnetic flux Φ causes the phase shift $\Delta\phi$ between the electron wave front elements passing through either side of the flux (Fig. 7):

$$\Delta\phi = 2\pi \frac{\Phi}{(h/e)}. \quad (16)$$

A single flux quantum $h/2e$ ($=2.07 \times 10^{-15}$ Wb), therefore, causes the phase shift of π . The contour phase lines

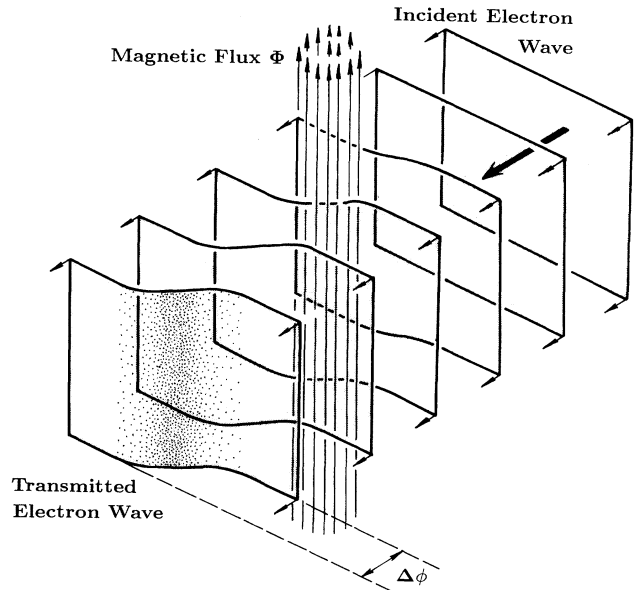


FIG. 7. The Aharonov-Bohm effect predicts that the phase shift $\Delta\phi$ of the electron wave transmitted through the magnetic flux Φ is related by $\Delta\phi = 2\pi\Phi/(h/e)$.

Transforming into the cylindrical coordinate, $B_z(x, y, z) = B_z(\rho, z)$ (B_z is independent of φ coordinate)

$$F(X, z) = -\frac{e}{\hbar} \int_0^{2\pi} d\varphi \int_0^\infty d\rho \rho B_z(\rho, z) e^{2\pi i \rho X \cos\varphi}. \quad (26)$$

Taking into account the definition of the n th order Bessel function

$$J_n(x) = \frac{1}{2\pi i^n} \int_0^{2\pi} d\varphi e^{i(x \cos\varphi + n\varphi)}, \quad (27)$$

Equation (26) is rewritten as

$$F(X, z) = -\frac{2\pi e}{\hbar} \int_0^\infty d\rho \rho B_z(\rho, z) J_0(2\pi\rho X). \quad (28)$$

After multiplying $X \cdot J_0(2\pi t X)$ to both sides of Eq. (28), and integrating with X we get

$$\int_0^\infty dX X F(X, z) J_0(2\pi t X) = -\frac{2\pi e}{\hbar} \int_0^\infty d\rho \int_0^\infty dX \rho X B_z(\rho, z) J_0(2\pi\rho X) J_0(2\pi t X). \quad (29)$$

By replacing $\eta = 2\pi X$, the right-hand side of Eq. (29) is

$$-\frac{e}{2\pi\hbar} \int_0^\infty d\rho \int_0^\infty d\eta \rho \eta B_z(\rho, z) J_0(\rho\eta) J_0(t\eta). \quad (30)$$

Using the identity for the Fourier-Bessel integral theorem for an arbitrary function $f(t)$,

$$f(t) = \int_0^\infty d\rho \int_0^\infty d\eta \rho \eta f(\rho) J_n(\rho\eta) J_n(t\eta), \quad (31)$$

Equation (30) is equivalent to $-(e/2\pi\hbar)B_z(t, z)$. Consequently Eq. (29) is reduced to

$$B_z(\rho, z) = -\frac{2\pi\hbar}{e} \int_0^\infty dX X F(X, z) J_0(2\pi\rho X). \quad (32)$$

In the same way, the ρ component is given as described in the Appendix by

$$B_\rho(\rho, z) = \frac{2\pi\hbar}{ie} \int_0^\infty dX X S(X, z) J_1(2\pi\rho X), \quad (33)$$

where

$$S(X, z) \equiv \int_{-\infty}^\infty dx \frac{\partial\phi(x, z)}{\partial z} e^{2\pi i x X}. \quad (34)$$

By differentiating the measured phase distribution of the electron wave and taking their Fourier transforms, each component of the field vector \mathbf{B} can be in this way calculated. In Sec. V we actually calculated the components from the phase data measured by the fringe scanning interferometry, and then the results are compared with the field distribution calculated from the Ginzburg-Landau equations.

IV. MODEL CALCULATIONS OF INTERNAL FIELD DISTRIBUTIONS

In this section we numerically calculate the internal field distributions of quantized magnetic fluxes near the surface of a superconductor. The magnetic-flux distribution around the fluxon center in the superconductor has been qualitatively described by the London model⁵¹ and semiquantitatively by the Clem model.⁸ For quantitative discussions for the field distribution, the GL equations, or more strictly speaking, the Eilenberger equations⁵² derived from the Gor'kov equation, should be solved. But it needs a huge numerical calculation with a high-speed

computer.

Since we could not observe the fluxons *in* the superconductor, but only the fluxons appearing *on* the superconductor surface as mentioned so far, the comparison with theories is not straightforward. For the flux begins to spread even below the superconductor surface so that the field distribution around the core axis differs from that in the inner bulk. Then we numerically solved the GL equations in the superconductor and the Maxwell equations in vacuum in order to correctly evaluate the flux spreading near the surface. Although our experiments were carried out in the range of low magnetic fields and low temperatures, in which the GL theory is not applicable, we start from the equations often used for phenomenological understanding. Since, however, the GL equations,

$$-\frac{\hbar^2}{2m} \left[\nabla - \frac{2ie}{\hbar} \mathbf{A} \right]^2 \Psi = \alpha \Psi - \beta |\Psi|^2 \Psi, \quad (35)$$

$$\frac{1}{\mu_0} \text{rot rot } \mathbf{A} = n_s \left[\frac{\hbar e}{2mi} (\Psi^* \nabla \Psi - \nabla \Psi^* \Psi) - \frac{2e^2}{m} |\Psi|^2 \mathbf{A} \right], \quad (36)$$

where $\Psi(\mathbf{r})$ is the order parameter, $\mathbf{A}(\mathbf{r})$ the vector potential, μ_0 the permeability of the vacuum, n_s the number density of the Cooper pairs, α and β are the coefficients calculated from the BCS theory, are nonlinear for the unknown functions $\Psi(\mathbf{r})$ and $\mathbf{A}(\mathbf{r})$, we cannot easily solve them. So we assumed some functions for $\Psi(\mathbf{r})$ and solved Eq. (36) only for $\mathbf{A}(\mathbf{r})$. Once the vector potential is obtained we can calculate the flux density $\mathbf{B}(\mathbf{r})$ and the persistent current density $\mathbf{j}(\mathbf{r})$ circulating around the flux:

$$\mathbf{B}(\mathbf{r}) = \text{rot } \mathbf{A}(\mathbf{r}), \quad (37)$$

$$\mathbf{j}(\mathbf{r}) = \frac{1}{\mu_0} \text{rot rot } \mathbf{A}(\mathbf{r}). \quad (38)$$

Using the coordinate system shown in Fig. 8, the fluxon near the surface is described by

$$\begin{aligned}
\Psi(\rho, \varphi, z) &= |\Psi(\rho, z)| e^{-i\varphi}, \\
\mathbf{A}(\rho, \varphi, z) &= A_\varphi(\rho, z) \hat{\varphi}, \\
\mathbf{B}(\rho, \varphi, z) &= B_\rho(\rho, z) \hat{\rho} + B_z(\rho, z) \hat{z}, \\
\mathbf{j}(\rho, \varphi, z) &= j_\varphi(\rho, z) \hat{\varphi},
\end{aligned} \tag{39}$$

where $\hat{\rho}$, $\hat{\varphi}$, and \hat{z} are the unit vectors for the respective directions. Equation (36) then has only the φ component:

$$\begin{aligned}
\frac{\partial^2 A_\varphi(\rho, z)}{\partial z^2} + \frac{\partial}{\partial \rho} \left[\frac{1}{\rho} \frac{\partial}{\partial \rho} [\rho A_\varphi(\rho, z)] \right] \\
- \frac{1}{\lambda^2} \left[A_\varphi(\rho, z) - \frac{\Phi_0}{2\pi\rho} \right] |\Psi(\rho, \varphi, z)|^2 = 0, \tag{40}
\end{aligned}$$

where the magnetic-flux penetration depth $\lambda = (m/2e^2\mu_0 n_s)^{1/2}$ and the magnetic-flux quantum $\Phi_0 = h/2e$. And then, from Eqs. (37) and (38),

$$B_\rho(\rho, z) = -\frac{\partial A_\varphi(\rho, z)}{\partial z}, \tag{41}$$

$$B_z(\rho, z) = \frac{1}{\rho} \frac{\partial}{\partial \rho} \{ \rho A_\varphi(\rho, z) \}, \tag{42}$$

$$\begin{aligned}
j_\varphi(\rho, z) &= \frac{1}{\mu_0} \left[\frac{\partial B_\rho(\rho, z)}{\partial z} - \frac{\partial B_z(\rho, z)}{\partial \rho} \right] \\
&= -\frac{1}{\lambda^2} \left[A_\varphi(\rho, z) - \frac{\Phi_0}{2\pi\rho} \right] |\Psi(\rho, \varphi, z)|^2. \tag{43}
\end{aligned}$$

For the SQF line we adopt the Clem model⁸ for the order parameter:

$$\Psi_1(\rho, \varphi, z) = \begin{cases} \frac{\rho}{(\rho^2 + \xi^2)^{1/2}} e^{-i\varphi} & (z \leq 0), \\ 0 & (z > 0), \end{cases} \tag{44}$$

where ξ is the coherence length which approximately corresponds to the radius of the fluxon. We assume the z independence of the order parameter near the superconductor surface. Equation (40) then becomes the Maxwell equation in vacuum $z > 0$. Equation (40) with Eq. (44) was numerically solved by the finite difference method using the DEQSOL (differential equation solver) program⁵³ with a Hitachi computer HITAC M680H. The area for solving the equation was a square of $\rho = 0-1 \mu\text{m}$, $z = -0.5-0.5 \mu\text{m}$ with 200×200 square meshes (Fig. 9), and the boundary conditions were

$A_\varphi = 0$, because of the symmetry on $\rho = 0$;

$$A_\varphi = \frac{\Phi_0}{2\pi\rho}, \text{ implying } B_\rho = 0, \text{ on } \rho = 1 \mu\text{m}; \tag{45}$$

$$A_\varphi = \frac{\Phi_0}{2\pi\lambda^2} \frac{\rho}{400},$$

implying $B_z = \text{const}$, on $z = 0.5 \mu\text{m}$;

$$\frac{\partial A_\varphi}{\partial z} = 0, \text{ implying } B_\rho = 0, \text{ on } z = -0.5 \mu\text{m}.$$

The boundary conditions Eq. (45) should be different between an isolated fluxon and a fluxon in a flux line lattice, but the calculated internal field distribution around the fluxon center near the superconductor surface was almost independent of the boundary conditions and the calculation area size. Our main interest in the analysis of the experimental results lies in the internal field distribution at the flux root just above the superconductor surface.

For numerically solving the GL equation Eq. (40) with the Clem model Eq. (44), we must estimate the characteristic parameters of our lead films, λ and ξ . In the case of superconductors characterized by the local field theory, the weak-field penetration depth $\lambda(T, d)$, which depends on the temperature T and possibly on the film thickness d , is given by⁵⁴

$$\lambda(T, d) = \lambda_L(T) \left[1 + \frac{\xi_0}{l} \right]^{1/2}. \tag{46}$$

Here, $\lambda_L(T)$ is the London penetration depth, ξ_0 is the Pippard coherence distance, and l is an effective mean free path arising from either scattering by impurities or

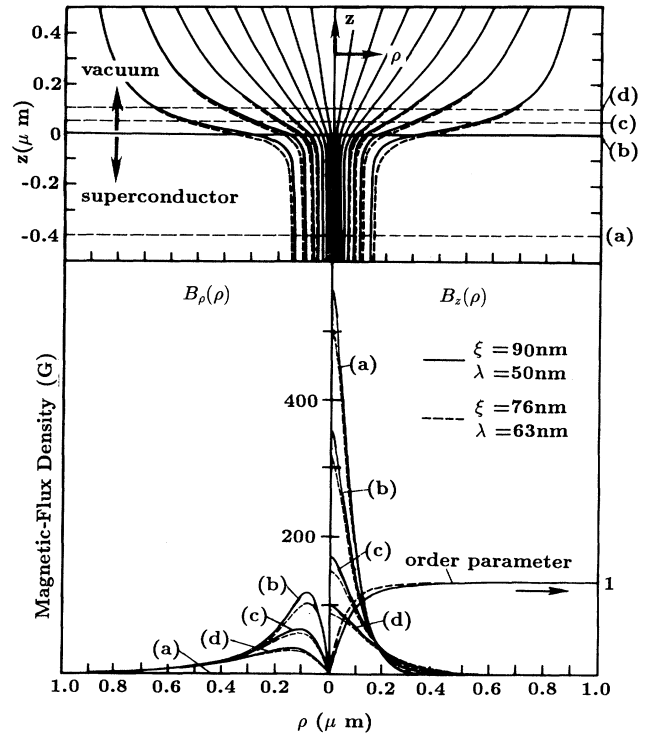


FIG. 9. The magnetic-flux distributions of a fluxon near the superconductor surface, calculated with the DEQSOL program using the Ginzburg-Landau equation Eq. (40) combined with the Clem model equation (44). The curved solid lines are calculated with the parameters, $\xi = 90 \text{ nm}$, $\lambda = 50 \text{ nm}$, and the curved dash lines are with $\xi = 76 \text{ nm}$, $\lambda = 63 \text{ nm}$. The upper figure shows the flux-line distributions. The lower figure shows the profiles of the field distribution along the lines indicated in the upper figure. The field-vector components are separately shown.

the surfaces of the film. Since a real sample, lead, is not, however, recognized to be quite local, Tinkham³¹ has suggested the following modification of Eq. (46) as a suitable extrapolation form for $\lambda(T, d)$;

$$\lambda(T, d) = \lambda(T, \infty) \left[1 + \frac{[\lambda_L(T)]^2 \xi_0}{[\lambda(T, \infty)]^2 l} \right]^{1/2}, \quad (47)$$

where $\lambda(T, \infty)$ is the bulk weak-field penetration depth. We assume the temperature dependence of λ 's by the usual Gorter-Casimir ones, namely, $\lambda(t) = \lambda(0) / (1 - t^4)^{1/2}$, where $t = T/T_c$. Then, Eq. (47) becomes

$$\lambda(T, d) = \frac{\lambda(0, \infty)}{(1 - t^4)^{1/2}} \left[1 + \frac{[\lambda_L(T)]^2 \xi_0}{[\lambda(T, \infty)]^2 l} \right]^{1/2}. \quad (48)$$

Using the values of the effective mean free path l obtained in Sec. III and $[\lambda_L(T)^2 / \lambda(T, \infty)^2] \xi_0 = 69$ nm at $T = 4.2$ K, $\lambda(0, \infty) = 44$ nm,³¹ we get $\lambda(4.2$ K, 200 nm) = 50–52 nm.

In the same way, the GL parameter $\kappa(T, d)$ is given by³¹

$$\kappa(T, d) = \kappa(T, \infty) \left[1 + \frac{[\lambda_L(T)]^2 \xi_0}{[\lambda(T, \infty)]^2 l} \right], \quad (49)$$

where

$$\begin{aligned} \kappa(T, \infty) &= \frac{2\sqrt{2} \pi H_c(T) [\lambda(T, \infty)]^2}{h/2e} \\ &= \frac{2\sqrt{2} \pi H_c(0) [\lambda(0, \infty)]^2}{(1 + t^2) h/2e}. \end{aligned} \quad (50)$$

Here, H_c is the thermodynamical critical field, $H_c(0) = 803$ G, and $h/2e = 2.07 \times 10^{-15}$ Wb, the flux quantum. We obtain, therefore, $\kappa(4.2$ K, 200 nm) = 0.56–0.59, and consequently, from the relation $\xi(T, d) = \lambda(T, d) / \kappa(T, d)$, we get $\xi(4.2$ K, 200 nm) = 88–90 nm. These values of the parameters, λ and ξ , for our lead films are not dissimilar to other reports,^{12,14} in spite of our unusual substrate for the lead deposition. We adopt these values hereafter.

The curved solid lines in Fig. 9 show the magnetic-flux distributions around the fluxon center, calculated from Eqs. (40) and (44) using the parameters $\xi = 90$ nm, $\lambda = 50$ nm. It shows that the flux begins to spread even below the superconductor surface. The field distribution in the inner bulk region of the superconductor coincides with the original Clem model:

$$B_z(\rho) = \frac{\Phi_0}{2\pi\lambda\xi} \frac{K_0[(\rho^2 + \xi^2)^{1/2} / \lambda]}{K_1(\xi/\lambda)}, \quad (51)$$

where K_0 and K_1 are the modified Bessel functions. The result with a wider calculation area ($\rho = 0 - 2.5$ μm , $z = -0.5 - 2$ μm) is utilized for the comparisons with experimental results in Sec. VI.

The same calculation was performed for comparison using the literature values for the parameters of a polycrystalline thin film of lead,⁵⁵ $\xi = 76$ nm, $\lambda = 63$ nm. The calculated results are shown with curved dash-lines in Fig. 9. Although the difference between the curved solid

lines ($\xi = 90$ nm, $\lambda = 50$ nm) and the curved dash-lines are distinguished in the superconductor, it is vanishing in vacuum with the distance from the superconductor surface. As a matter of course, the flux distribution in vacuum reflects less the internal field distribution in the superconductor. Since our experiments could catch the flux distribution only above the superconductor surface, it is difficult to quantitatively determine the values of the GL parameters. The calculated results with the both pairs of parameters are utilized for the comparison with the experimental results.

For comparison, moreover, the magnetic-flux distribution is also calculated with an order parameter:

$$\Psi_1(\rho, \varphi, z) = \begin{cases} \left[1 - \exp\left[-\frac{\rho^2}{\xi^2}\right] \right] e^{-i\varphi} & (z \leq 0), \\ 0 & (z > 0), \end{cases} \quad (52)$$

instead of the Clem's one Eq. (44), using $\xi = 90$ nm, $\lambda = 50$ nm. The calculated results are shown with the curved dash lines in Fig. 10, indicating that the difference of the flux distribution between the Clem model and the model equation (52) is clear only near the fluxon center, and is vanishing in vacuum.

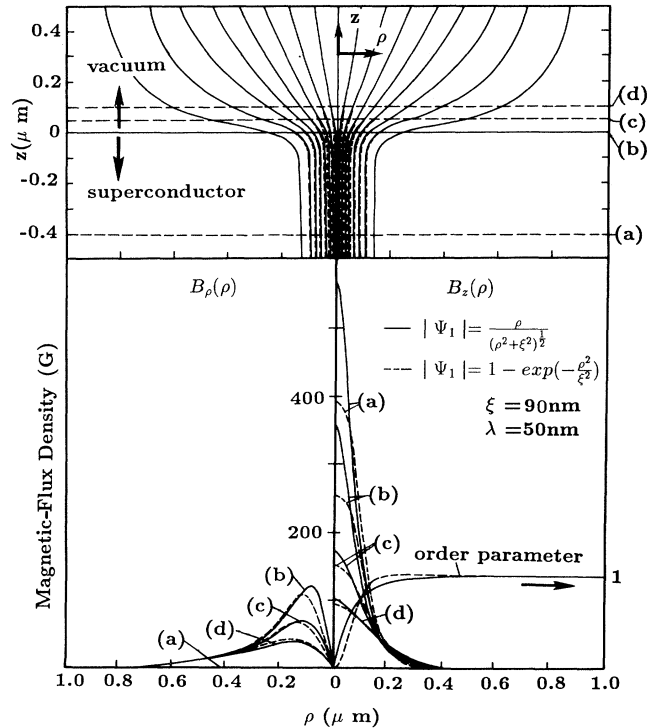


FIG. 10. The magnetic-flux distributions of a fluxon near the superconductor surface, calculated with the DEQSOL program using the GL equation Eq. (40). The curved solid lines are calculated with the Clem model Eq. (44), and the curved dash lines are with a model Eq. (52). Both are calculated with the parameters $\xi = 90$ nm, $\lambda = 50$ nm. The upper figure shows the flux-line distributions. The lower figure shows the profiles of the field distribution along the lines indicated in the upper figure. The field-vector components are separately shown.

According to Lasher,²⁰ the order parameter $\Psi_n(\rho)$ of a state consisting of MQF (n -flux quanta) is given in terms of that of the state of SQF $\Psi_1(\rho)$ as

$$\Psi_n(\rho) = \left[\Psi_1 \left(\frac{\rho}{\sqrt{n}} \right) \right]^n. \quad (53)$$

Then, using the Clem model Eq. (44), the order parameter of the MQF structure is given by

$$\Psi_n(\rho, \varphi, z) = \begin{cases} \left[\frac{\frac{\rho}{\sqrt{n}}}{\left[\frac{\rho^2}{n} + \xi^2 \right]^{1/2}} \right]^n e^{-in\varphi} & (z \leq 0), \\ 0 & (z > 0). \end{cases} \quad (54)$$

Figure 11 shows the calculated results from Eqs. (40) and (54) for $n = 1$ and 4 using $\xi = 90$ nm and $\lambda = 50$ nm. The ordinate, flux density, in the lower figure is normalized for the flux density of a SQF. The difference of the flux distributions between the two models can be dis-

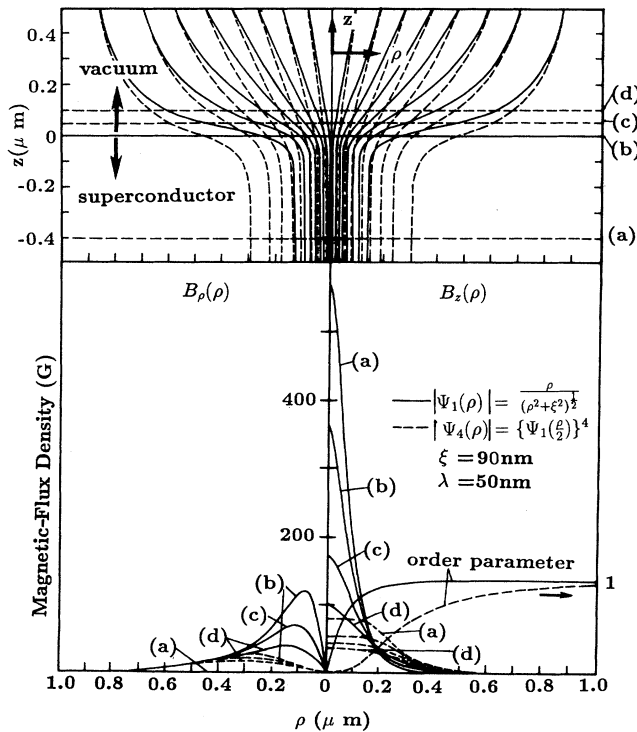


FIG. 11. The magnetic-flux distributions of a fluxon near the superconductor surface, calculated with the DEQSOL program using the GL equation Eq. (40). The curved solid lines are calculated with the Clem model Eq. (44), and the curved dash lines are with the Lasher model Eq. (54). Both are calculated with the parameters $\xi = 90$ nm, $\lambda = 50$ nm. The upper figure shows the flux-line distributions. The lower figure shows the profiles of the field distribution along the lines indicated in the upper figure. The field-vector components are separately shown.

tinguished even in the vacuum above the superconductor surface.

For the SQF line in a film of thickness d , the flux distribution was calculated by utilizing Clem's order parameter;

$$\Psi_1(\rho, \varphi, z) = \begin{cases} 0 & (z > 0), \\ \frac{\rho}{(\rho^2 + \xi^2)^{1/2}} e^{-i\varphi} & (-d < z \leq 0), \\ 0 & (z \leq -d). \end{cases} \quad (55)$$

The calculated result using $\xi = 90$ nm, $\lambda = 50$ nm, from Eq. (40) with Eq. (55) for $d = 4\lambda$ is shown in Fig. 12(b). It shows that the flux distribution just above the surface of the film is almost the same as that of the semi-infinite superconductor Fig. 12(a). We therefore utilize the results calculated for the semi-infinite superconductor for the comparison with the experimental results in Sec. VI.

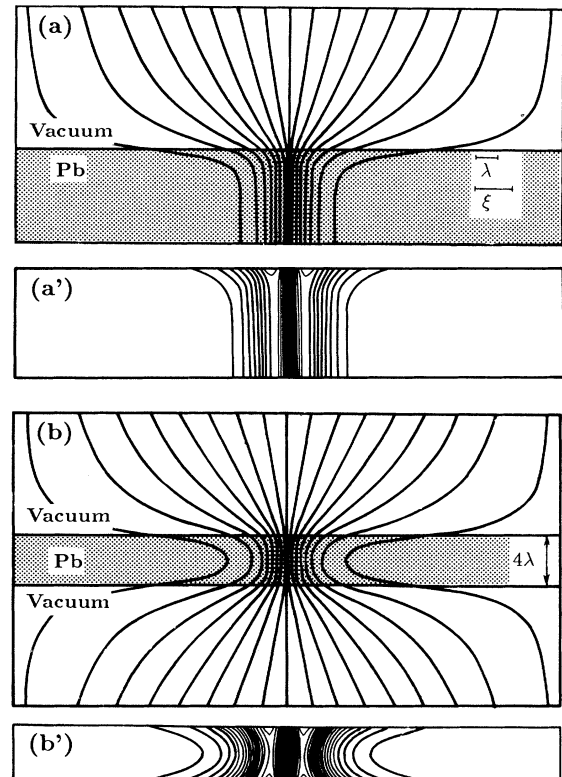


FIG. 12. The flux (upper figures) and circulating current (lower figures) distributions of a fluxon penetrating through (a) a semi-infinite and (b) a thin film of thickness $d = 4\lambda$ of superconductors are calculated with the DEQSOL program using the GL equation Eq. (40) combined with the Clem models, Eqs. (44) and (55), respectively.

V. EXPERIMENTAL RESULTS

A. Observations of magnetic-flux structures

After the in-field cooling in which the film was cooled down from 15 to 4.2 K under the magnetic field of the fixed strengths, the holograms were taken during applying the field (in-field observation). We observed three kinds of magnetic-flux structures in superconducting lead films, depending on the film thickness and the applied magnetic field. Figure 13 shows the interference micrographs with π -phase interval, in which a single interference fringe exactly corresponds to a magnetic-flux line of a single flux quantum $h/2e$. The shadowed areas are the curved lead films and we can only observe the flux spreading out into vacuum after penetrating through the films. The observation areas for a lead film are not necessarily the same under the different applied magnetic fields.

Although the fluxons were observed in the 0.2- μm -thick film under the 1.0-Oe field, the fluxons did not appear under the fields below 2.0 Oe for the 1.0- μm -thick film, and below 5.0 Oe for the 1.7- μm -thick film. This fact indicates that the Meissner phase is extended into the higher field region with increase of the film thickness (see Fig. 1).

In the case of films of 0.2 μm thickness [Figs. 13(a)–13(c)], the fluxes penetrate in the form of the SQF lines, independent of the applied fields. They are the SQF structures of Tinkham.¹⁶ With an increase of the film thickness to 1.0 μm [Figs. 13(d)–13(f)], flux bundles with several flux quanta penetrate in the form of thin filaments, and their exits on the surface are pointlike. This is a MQF structure, which we call “MQF-*A* type” hereafter. In this structure, with the applied magnetic field, the amount of the flux contained in a single MQF line increases and the number of the MQF lines also increases. In the case of 1.7 μm [Figs. 13(g)–13(i)], moreover, the flux penetrate in the form of flux bundles, as in the case of the 1.0- μm -thick film. But the diameters of the flux bundles are much larger than those of the MQF-*A* lines. We call this structure “MQF-*B* type” from now on. In this case, with increase of the field strength, the diameters of the flux exits on the film surface seem to increase, although the diameters seems to remain unaltered in the MQF-*A* structure in the 1.0- μm -thick film. Figure 13 clearly shows three kinds of structures, SQF, MQF-*A*, and MQF-*B*, in the form of the distribution of magnetic flux lines. The differences between these structures will be more clearly shown in the detailed analysis of the internal field distributions around the fluxon center in the next subsection.

Although the SQF lines tend to arrange in the lattice form according to Tinkham,¹⁶ the observed SQF lines in the film of 0.2 μm seem to arrange at random. This is thought to be originated from the strong pinning force caused by the inhomogeneity of the film, the most prominent of which are grain boundaries.¹⁴ The arrangement can also be made random by the creation and annihilation of the vortex-antivortex pairs in the Kosterlitz-Thouless (KT) region¹⁵ just below the superconducting

transition temperature. KT theory has been extensively discussed concerning the melting of the flux line lattices in two-dimensional superconductors.^{56,57} The fluxon pairs observed in Figs. 13(a) and 13(b) may correspond to the ones predicted in KT theory. The pairs may have been created when the film was cooled down through the KT regime, and “frozen” by pinning so that the opposite fluxons would have not met to annihilate each other. The polarity of each fluxon is easily distinguished in the interference micrograph. Unless the polarities of the two fluxons are opposite, the fluxons individually stand up and fan out, not make a pair. This is one of the unique features to the electron holographic observation compared with other experimental methods. The pairs were not observed in the films of 1.0- μm and 1.7- μm thicknesses. This is naturally understood because KT theory is applicable only for the two-dimensional system, and on the contrary, for this reason, it is suggested that the observed flux pairs are the ones predicted by KT theory.

Figure 14(a) shows the interference micrograph of the SQF line appearing in the 0.2- μm -thick film under the 3.7-Oe field, in which a single fringe exactly corresponds to a single flux quantum. Figure 14(b) is a phase-difference-amplified interference micrograph⁴² analyzed from the same hologram as Fig. 14(a). This micrograph was obtained by setting the contour phase lines at $\pi/4$ phase intervals, instead of π interval in Fig. 14(a), from the phase data numerically measured by the fringe scanning interferometry. This is called “eight-times amplified” so that a single fringe corresponds to a magnetic flux line of $h/8e$. The total amount of flux and the detailed flux distribution can be estimated with higher accuracy.

The MQF-*A* lines with four flux quanta emerging in the 1.0- μm -thick film under the 5.0-Oe field are shown in Figs. 15(a), and 15(b) is its eight-times phase-difference-amplified interference micrograph in which a single fringe corresponds to a magnetic flux line of $h/8e$. The flux penetrating through the superconductor looks as fine as that of the SQF in Fig. 14.

Figure 16 shows the MQF-*B* lines with four flux quanta appearing on the 1.7- μm -thick film under the field of 12.2 Oe. The root of the flux is much broader than that of the MQF-*A* line in Fig. 15, while the amounts of the flux are the same.

In this way, the structural changes from the SQF to the MQF-*A* and the MQF-*B* structures are clearly and directly shown in the form of magnetic-flux distributions in interference micrographs. The changes seem to originate only from the increase of the film thickness, because, from the R_R measurement, the quality of the films is estimated to remain unaltered with the thickness change.

B. Internal field distributions of quantized magnetic fluxes

The phase distributions of the electron waves transmitted through the fluxons were numerically measured and then the field vector components around the fluxon centers were decomposed using the digital phase analysis

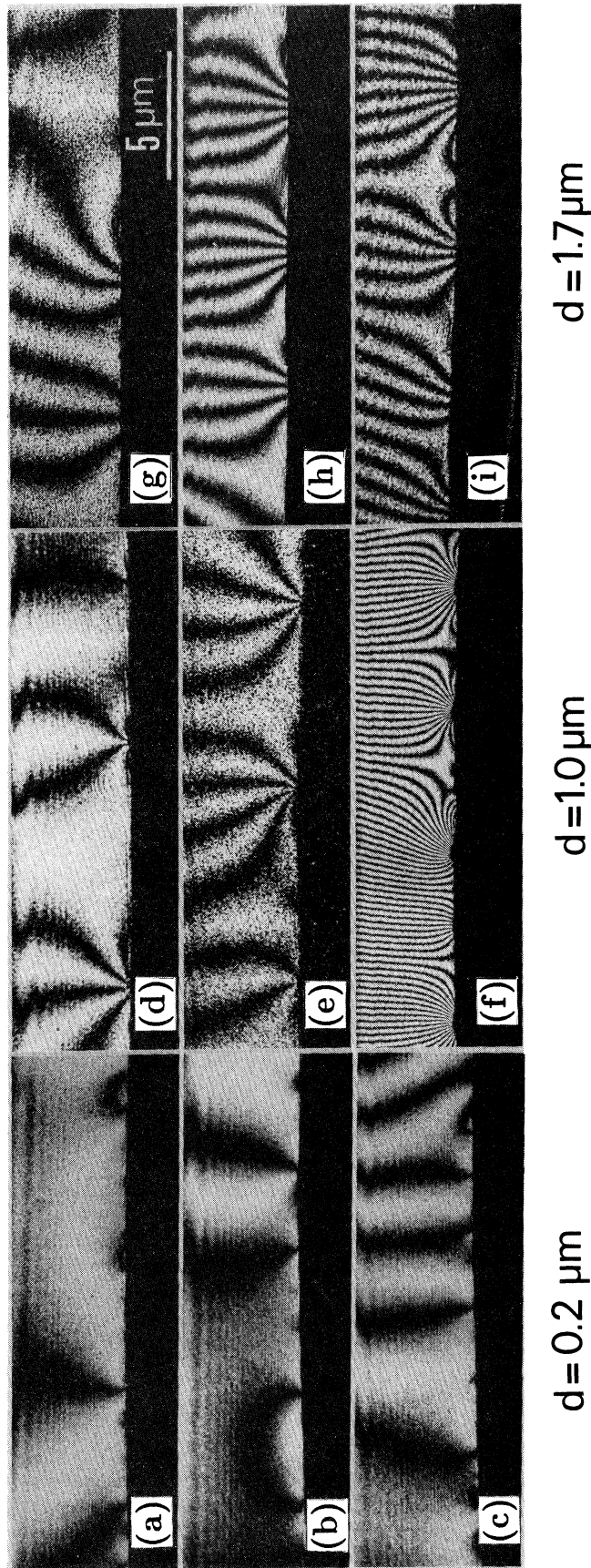


FIG. 13. Interference micrographs with phase interval of π showing the quantized magnetic fluxes appearing on the surfaces of the superconducting lead films. A single interference fringe exactly corresponds to a single flux quantum, $h/2e$. The magnetic-flux structures vary depending on the film thickness d and the applied field H . (a) $H = 1.6$ Oe, (b) $H = 3.7$ Oe, (c) $H = 5.0$ Oe for $d = 0.2 \mu\text{m}$. (d) $H = 3.7$ Oe, (e) $H = 5.0$ Oe, (f) $H = 18.3$ Oe for $d = 1.0 \mu\text{m}$. (g) $H = 7.5$ Oe, (h) $H = 12.2$ Oe, (i) $H = 18.3$ Oe for $d = 1.7 \mu\text{m}$.

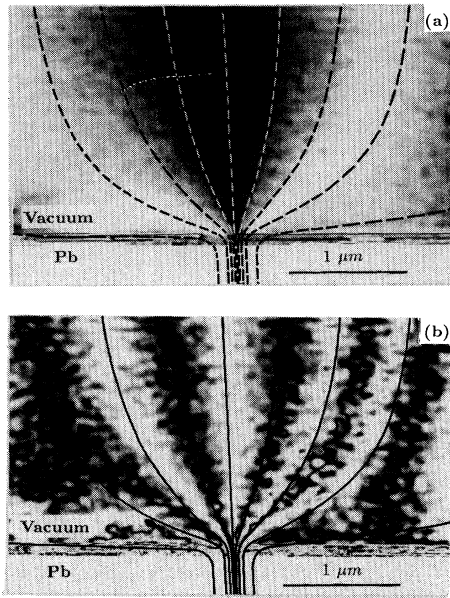


FIG. 14. A singly quantized flux (SQF) line appearing in the 0.2- μm -thick lead film under the 3.7-Oe field. (a) Interference micrograph showing the flux lines in units of $h/2e$, and (b) in units of $h/8e$ (an eight-times phase-difference amplified interference micrograph). The curved dash lines in (a) and the curved solid lines in (b) are the flux distribution calculated from the GL equation Eq. (40) with the Clem model equation (44) using the parameters $\xi=90$ nm, $\lambda=50$ nm.

method as described in Sec. III.

At first, we analyzed the hologram taken from the 1.0- μm -thick lead film under the 5.0-Oe field (MQF-*A*). Figure 17(b) shows the line profile of the phase distribution along the line *AA* just above the superconductor surface in the interference micrograph Fig. 17(a). It shows that the phase steeply shifts at the flux exits and does not shift between them. This shows the Aharonov-Bohm effect.

The wave front numerically reconstructed in this way is three dimensionally displayed in Fig. 18. The near side of the wave front ($z=0$) is adjacent to the lead film surface. This wave front is an expected one shown in Fig. 4. The sudden phase shifts at the flux exits are multiples of π , and their multiples are the number of fringes in Fig. 17(a). This fact precisely means the flux quantization in units of $h/2e$. The phase measurement precision in the fringe scanning interferometry⁷ corresponds to the flux resolution of $\sim h/100e$.

On the next step, the field-vector components were derived from the numerically measured phase distributions by the data processing method mentioned in Sec. III. The derivative $\partial\phi(x,z)/\partial x$ is calculated from the phase profile Fig. 17(b) and presented in Fig. 17(c). It has peaks at the flux exits because it is the line integral of the field-vector component B_z normal to the surface along the electron path as expressed by Eq. (23). In the same way Fig. 17(d) is the derivative $\partial\phi(x,z)/\partial z$ which corresponds to Eq. (24). Using these data, then, the field-vector com-

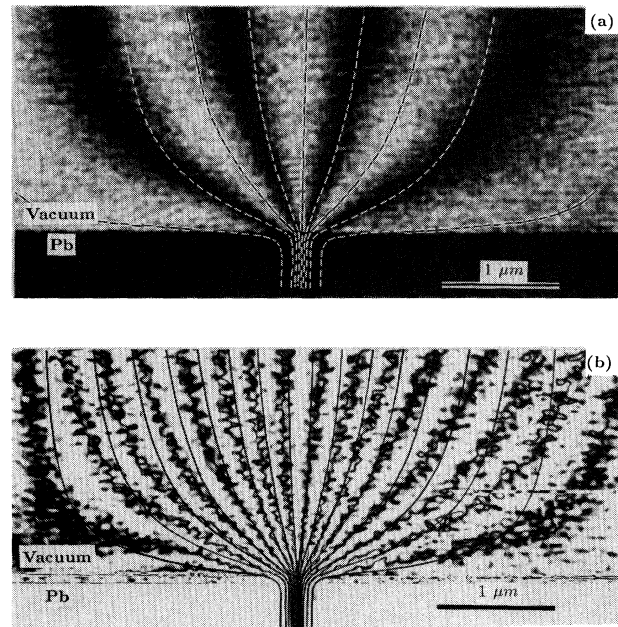


FIG. 15. A multiply quantized flux (MQF-*A*) line appearing on the 1.0- μm -thick lead film under the 5.0-Oe field. (a) Interference micrograph showing the flux lines in units of $h/2e$ and (b) in units of $h/8e$ (an eight-times phase-difference amplified interference micrograph). The curved dash-lines in (a) and the curved solid lines in (b) are the flux distribution calculated from the GL equation Eq. (40) with the Clem model equation (44) using the parameters $\xi=90$ nm, $\lambda=50$ nm.

ponents were calculated according to Eqs. (25), (32), (33), and (34). The solid broken lines in Fig. 19 show the result obtained from the flux bundle with four-flux quanta appearing at the left end of Fig. 17(a) or Fig. 15. The ordinate is normalized for the flux density of a SQF. Electron holography combined with the digital phase analysis method in this way enables the quantitative measurement of the field-vector components near the center of an *individual* flux in terms of the distance from the core axis.

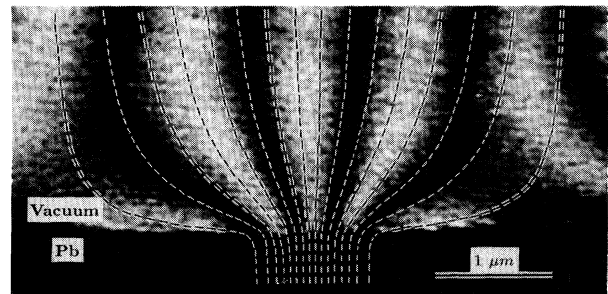


FIG. 16. A multiply quantized flux (MQF-*B*) line appearing on the 1.7- μm -thick lead film under the 12.2-Oe field. An interference fringe corresponds to the flux quantum $h/2e$. The curved dash lines shows the flux distribution calculated from the GL equation Eq. (40) with a model Eq. (59) with $R=0.4$ μm , $\xi=90$ nm, $\lambda=50$ nm.

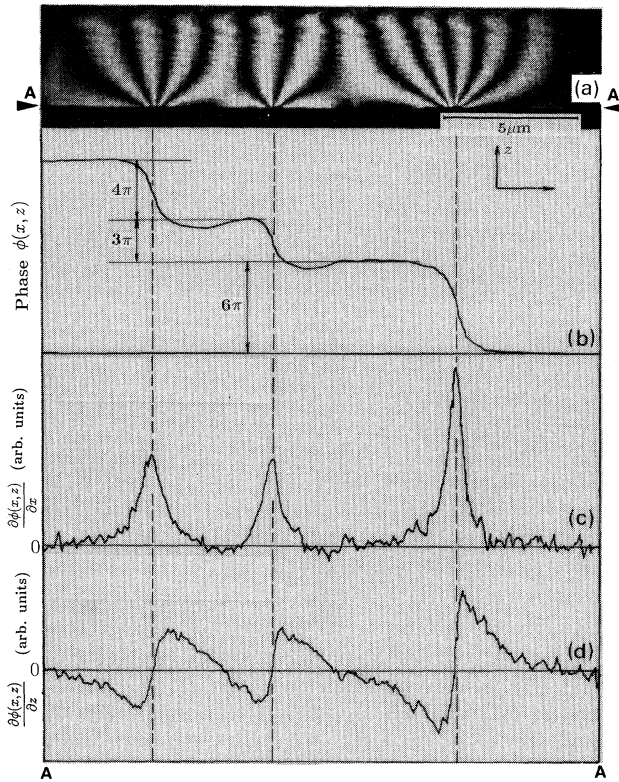


FIG. 17. Digital phase analysis for the fluxes appearing on the 1.0- μm -thick film under the 5.0-Oe field. (a) Interference micrograph showing the MQF-*A* structure. (b) Line profile of the phase distribution along the line *AA* just above the superconductor surface in the micrograph (a). (c) Its derivative with x , $\partial\phi(x, z)/\partial x$. (d) Its derivative with z , $\partial\phi(x, z)/\partial z$.

The same analysis for the SQF line shown in Fig. 14 was carried out, and its result is shown as the broken dash lines in Fig. 19. The field distributions of the SQF and MQF-*A* almost coincide.

We next analyzed the flux of the MQF-*B* structure in the 1.7- μm -thick film under the 12.2-Oe field. Figure 20(b) is the line profile of the phase distribution along the

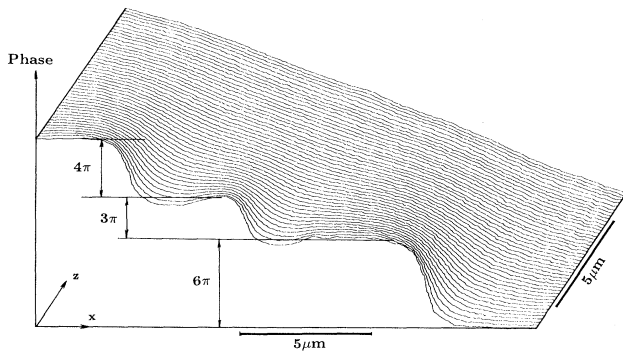


FIG. 18. Electron wave front reconstructed by the digital phase analysis method. The hologram taken from the MQF-*A* structure shown in Fig. 17 was analyzed. The near side of the wave front ($z=0$) is adjacent to the lead film surface.

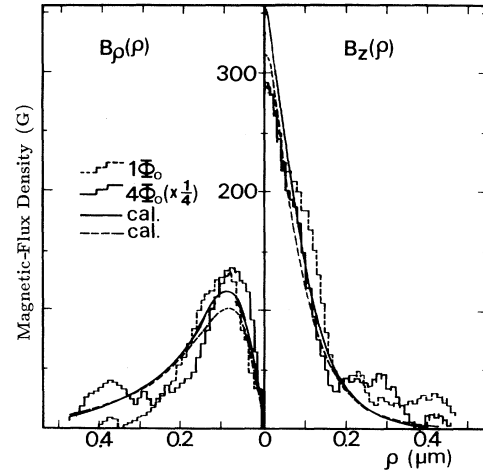


FIG. 19. Field-vector components, $B_z(\rho)$, normal to the surface, and $B_\rho(\rho)$, parallel to the surface, around the flux center just above the superconducting lead film surfaces. The broken dash lines are for the SQF line shown in Fig. 14. The broken solid lines are for the MQF-*A* line shown in Fig. 15. The curved solid lines are the distributions calculated from the GL equation Eq. (40) with the Clem model equation (44) using the parameters $\xi=90$ nm, $\lambda=50$ nm. The curved dash lines are the calculated ones with the parameters $\xi=76$ nm, $\lambda=63$ nm.

line *AA* just above the superconductor surface in the interference micrograph (a). Since, as in Fig. 17, the phase shifts at the flux exist are multiples of π , it is included that the fluxes are quantized in units of $h/2e$. But the phase changes are slower in broader areas compared with those in Fig. 17, which means the lower flux density in the MQF-*B* compared with that of the SQF and MQF-*A* lines. The derivatives $\partial\phi(x, z)/\partial x$ and $\partial\phi(x, z)/\partial z$ were calculated and shown in Figs. 20(c) and 20(d). We analyzed the field components of the flux with four-flux quanta appearing at the left end in this figure. The result shown in Fig. 21 is apparently different from the ones in Fig. 19. The B_z distribution shows, in particular, the nearly uniform flux penetration through a semimacroscopic normal region.

By introducing the digital phase analysis method, in this way, we cannot only determine the flux amounts with much higher accuracy compared with the interference micrograph observation, but also analyze the internal-field distributions in three dimensions.

VI. DISCUSSIONS

A. Detection of a single fluxon

The contrast produced by a single fluxon in Lorentz microscopy have been calculated by several authors^{3,58-61} to find that the position detection of a single fluxon is near the observation limit from the uncertainty principle.

Using the phase difference $d\phi$ between the two paths 1

and 2 in Fig. 8, $d\phi = (\partial\phi/\partial x)dx$, the deflection angle of the incident electron beam β by the magnetic field of a single fluxon is given by $\beta = d\phi/k_y dx$, where k_y is the y component of the wave number vector of the incident electron. The phase difference $d\phi$ is expressed with the amount of the flux between the two paths $d\Phi$ as $d\phi = \pi d\Phi/\Phi_0$ [Eq. (16)], where $\Phi_0 = h/2e$. The momentum change of the incident electron beam in the x direction dp_x , on the other hand, is given by $dp_x = p_y \beta$, where p_y is the momentum component in the incident direction. Consequently we get

$$dp_x dx = \frac{h}{2} \frac{d\Phi}{\Phi_0}. \quad (56)$$

On the other hand, the spread Δx of the wave packet in the x direction consisting of plane waves with the momentum uncertainty dp_x is related by

$$dp_x \Delta x \geq h, \quad (57)$$

from the uncertainty principle. Since the spatial resolution of real observations dx is always $dx \geq \Delta x$, we get

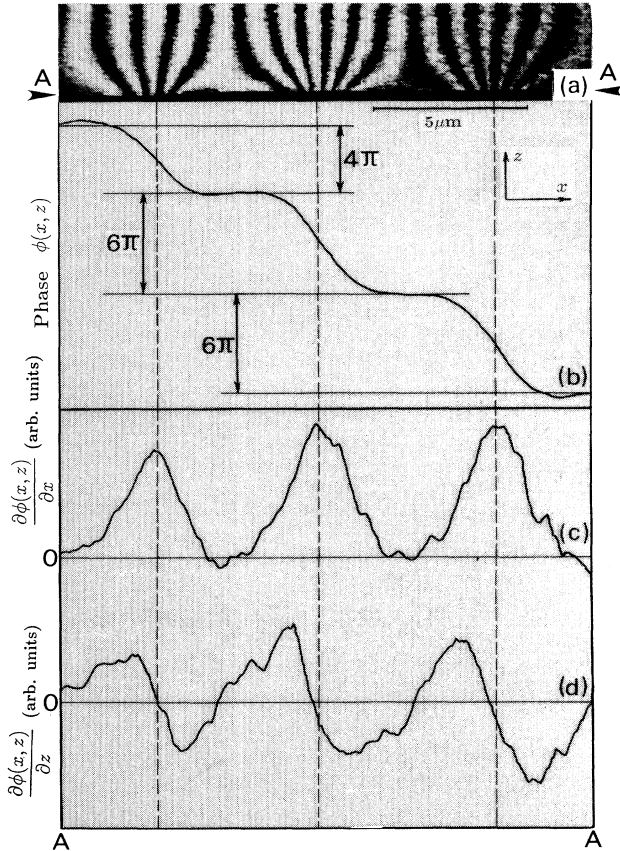


FIG. 20. Digital phase analysis for the fluxes appearing on the 1.7- μm -thick film under the 12.2-Oe field. (a) Interference micrograph showing the MQF-B structure. (b) Line profile of the phase distribution along the line AA just above the superconductor surface in the micrograph (a). (c) Its derivative with x , $\partial\phi(x, z)/\partial x$. (d) Its derivative with z , $\partial\phi(x, z)/\partial z$.

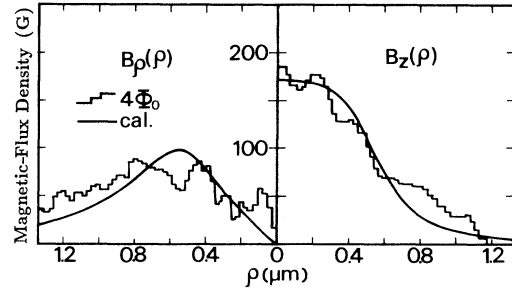


FIG. 21. Field-vector components, $B_z(\rho)$, normal to the surface, and $B_\rho(\rho)$, parallel to the surface, around the flux center just above the superconducting lead film surfaces. The broken solid lines are the flux distribution in the MQF-B line shown in Fig. 16. The curved solid lines are the distribution calculated from the GL equation Eq. (40) with a model Eq. (59) with $R = 0.4 \mu\text{m}$, $\xi = 90 \text{ nm}$, $\lambda = 50 \text{ nm}$.

therefore, from Eqs. (56) and (57),

$$\frac{d\Phi}{\Phi_0} \geq 2. \quad (58)$$

This implies that the observation of magnetic fluxes with spatial resolution of dx needs the flux (change) of order of Φ_0 in the interval of dx . In other words, in the case of the observation of a single fluxon, its position can be determined only with the precision of order of its diameter.

The present report, however, shows the observation of a single fluxon with the flux resolution $d\Phi \sim \Phi_0/100$ and the spatial resolution dx of approximately one-hundredth of its diameter. This seems to contradict the uncertainty principle mentioned above.

A classical picture such as the above discussion on the connection between the spatial and flux resolutions is not applicable to the electron holography. The observation in image-electron holography is carried out essentially in quantum mechanics. The spatial resolution is not determined by the wave packet spread in the direction perpendicular to the propagation. In our holography electron microscope, the electron wave packet widely spread $\sim 50 \mu\text{m}$ in the x direction at the specimen plane. Utilizing a part of the wave packet as an object wave, an in-focused image is formed with spatial resolution as high as conventional electron microscopes. The remaining part of the wave packet is utilized as a reference wave. The high resolution for magnetic fluxes is achieved by interfering the object wave with the reference one, irrespective of the spatial resolution of the image. Utilizing the reference wave in the electron holography, the high resolution for magnetic fluxes can be obtained without any reduction of the spatial resolution.

B. Magnetic flux structures of lead films

Now we compare the experimental and calculated results on the internal field distributions of quantized fluxes. The curved dash lines in Fig. 14(a) show the flux distribution calculated from the GL equation Eq. (40)

with the Clem model Eq. (44) for the SQF line using the parameters $\xi=90$ nm, $\lambda=50$ nm. The observed and calculated distributions qualitatively agree, implying that we actually observed the flux exit just on the superconductor surface. More detailed comparison is possible in Fig. 14(b) with a phase-difference-amplified interference micrograph.⁴² The calculated distribution (curved solid lines) considerably agrees, particularly at the flux root just above the surface.

In the case of the MQF-*A* line in Fig. 15, the agreement with the calculated distribution with the Clem model, which is the same as that of the SQF line in Fig. 14, is also considerable. Since, as shown in Fig. 11, the difference of the magnetic-flux distribution between the Clem model Eq. (44) and the Lasher model Eq. (54) for the MQF lines ($n=4$) is evident, we can conclude from our observation that the MQF-*A* structure is better described by Clem's order parameter for the SQF line than that of Lasher's for n -quanta MQF line. Figures 14 and 15 show that the field distributions around the center of the SQF and MQF-*A* lines are in the same character with the exception of their flux amounts.

At the region far from the surface in the images of Figs. 14 and 15, the calculated lines slightly deviate from the observed ones because of the boundary conditions for solving the GL equations. Equation (45) does not accurately reflect the real circumstances, which affect the distributions at the circumference in the images. Experimentally, moreover, the fringe distributions at the region far from the superconductor surface are apparently affected by the slight inclination of the mirrors in the optical reconstruction interferometer (Fig. 6). Anyway, our main interest lies in the internal field distribution at the flux root just on the surface.

As mentioned in the previous section, the root of the MQF-*B* line shown in Fig. 16 seems much broader than those of the SQF and the MQF-*A* lines. This feature is qualitatively explained by the Lasher's order parameter Eq. (54) for the MQF line as shown in Fig. 11, which, however, does not give quantitative agreement satisfactorily with the observed MQF-*B* line. In order to better simulate the flux distribution of the MQF-*B* line shown in Fig. 16, we assume an order parameter

$$\Psi(\rho, \varphi, z) = \begin{cases} \{1 - e^{-(\rho-R)^2/\xi^2}\}^{1/2} e^{-in\varphi} & (z < 0, \rho > R), \\ 0 & (z < 0, 0 \leq \rho \leq R), \\ 0 & (z \geq 0), \end{cases} \quad (59)$$

instead of Eq. (54). This model implies that a circular normal region of the radius R appears in the superconducting phase and the magnetic-flux bundle of n quanta penetrates therein. The curved dash lines in Fig. 16 show the flux distribution calculated from the GL equation Eq. (40) using this model of $R=0.4$ μm , $n=4$, $\xi=90$ nm, and $\lambda=50$ nm. The agreement of the observed pattern is fairly good, which shows distinct difference from the SQF and the MQF-*A* lines.

The field-vector components are also compared. The

curved solid lines and the curved dash lines in Fig. 19 show the calculated distributions with Clem's order parameter Eq. (44) using the parameters $\xi=90$ nm, $\lambda=50$ nm, and $\xi=76$ nm, $\lambda=63$ nm, respectively (compare with the curved lines in Fig. 9). The experimental results for the SQF (broken dash lines) and the MQF-*A* (broken solid lines) are considerably traced by the calculated curves. The MQF-*A* line, in particular, penetrates in the form of a filament as fine as the SQF line. We cannot obtain here a definite conclusion which pair of the GL parameters here adopted in the calculation is more appropriate.

Concerning the MQF-*B* line, the curved solid lines in Fig. 21 are calculated with a model Eq. (59), which fairly well traces the experimental results (broken solid lines). This field distribution cannot be explained by any curves in Fig. 9, implying that the broadening of the flux root in the MQF-*B* line is intrinsic, not due to the shadowing of a finer root by the curved lead film edge.

It should be pointed out here that the flux density just above the normal region on the superconductor surface in the MQF-*B* structure is estimated approximately 180 G from Fig. 21, which is much lower than the thermodynamical critical field ~ 500 G of bulk superconducting lead at $T=4.2$ K. The internal field in the normal domain in a macroscopic intermediate state, on the other hand, is expected to be approximated by the thermodynamic critical field. This extraordinary reduction of the flux density in the normal region of the MQF-*B* structure is considered to come from the surface and size effects. As estimated in Sec. IV and observed in Sec. V, the flux lines rapidly disperse out from the superconductor surface, and its flux density fairly decreases even near the center of the normal region compared with that in the inner bulk region. Since the MQF-*B* lines, moreover, have much smaller size in geometry compared with a macroscopic intermediate state, its characteristics such as the flux density in the normal region can be different from that of the intermediate state in a bulk superconductor. For instance, certain reduction of the critical field in thin films has been observed.^{31,32}

Another remark remains to be made concerning the implication of the observed MQF-*A* and MQF-*B* lines. They do not directly correspond to the Lasher's MQF and the Goren's NS structures, respectively. They predicted their structures only applicable at relatively high field regions, while our observations were carried out under very weak fields, just above the "lower critical field" $(1-D)H_c$ (see Fig. 1). Since the critical value of the GL parameter κ for the transition between type-I and -II behaviors in superconducting characteristics is predicted to be $\kappa=1/\sqrt{2}=0.707$ from the original GL theory, the estimated values $\kappa=0.56-0.59$ for our lead films at $T=4.2$ K seem to be considerably small for the transition. Detailed investigations, however, have revealed the attractive interaction among fluxons in a narrow κ range near $\kappa=1/\sqrt{2}$, called the intermediate-mixed state.^{24,25,32} Auer and Ullmaier⁶² observed the transition from type-I to -II states at κ values as small as 0.6 in the range of low temperature $T/T_c < 0.4$. The phase diagram in which type-I and type-II states including the intermediate-

mixed state are classified in terms of κ and T , has been investigated by many researchers.¹ Our observed MQF-*A* and MQF-*B* structures, therefore, may be understood as some transition characteristics between type-I and -II superconductors. Besides this effect, some additional features such as the pinning⁹ and surface effects may raise the variety of magnetic-flux structures like the MQF-*A* and MQF-*B* lines under low magnetic fields.

VII. SUMMARY

1. We have succeeded to directly image a singly quantized flux emerging on the surface of superconducting lead films in the form of magnetic-flux line distributions using the electron holography technique. Combining the digital phase analysis method, furthermore, the flux quantum $h/2e$ have been determined for individual fluxes with prediction of $\sim h/100e$. This method has also allowed one to analyze in detail the distributions of the field-vector components around individual fluxon centers.

2. The fluxon pairs, consisting of two antiparallel fluxons, have been observed only in the lead films of 0.2 μm thickness, not in thicker films. These may be the ones predicted by Kosterlitz-Thouless theory.

3. Under certain restricted observation conditions, i.e., under low fields and low temperatures, we have clearly observed the changes of the magnetic-flux structures of superconducting lead films with increase of the film thickness. In addition to the singly quantized flux structure in the 0.2- μm -thick films, two types of the multiply quantized flux structures have been newly observed in thicker films.

4. We have numerically solved the Ginzburg-Landau equations to calculate the field distributions around the fluxon center near the superconductor surface. Considerable agreement between the calculated and the experimental results was obtained. In particular, the internal field distribution of the MQF-*A* line appearing in the 1.0- μm -thick lead film has been found to be the same as that of the SQF line in the 0.2- μm -thick film.

ACKNOWLEDGMENTS

We would like to express our appreciation for the guidance and encouragement on fringe scanning interferometry received from Professor Toyohiko Yatagai of

Tsukuba University. We also gratefully acknowledge helpful discussions with Dr. Ushio Kawabe, Dr. Yoshinobu Tarutani of Hitachi Central Research Laboratory (CRL). Dr. Seiji Saito and Dr. Toshiyuki Onogi of Hitachi Advance Research Laboratory (ARL) drew our attention to the theoretical aspects on the fluxon core structure. Dr. Masaaki Futamoto and Dr. Yukio Honda of CRL made encouraging suggestions on the sample preparation. Miyuki Saji of CRL assisted the numerical calculation with the DEQSOL program. Our colleagues at ARL, Takeshi Tawasaki, Takao Matsumoto, Hiroto Kasai, Dr. Hiroshi Kajiyama, Hisashi Nagano, and Seichi Kondo helped with the experiments.

APPENDIX: CALCULATING THE B_ρ COMPONENT FROM THE PHASE DISTRIBUTION

We derive Eq. (33) from Eq. (24) by the similar method with the case of the B_z -component derivation. Transforming into the cylindrical coordinate, Eq. (24) is rewritten as

$$\frac{\partial\phi(x,z)}{\partial z} = \frac{e}{\hbar} \int_{-\infty}^{\infty} dy B_\rho(\rho,z) \cos\varphi. \quad (\text{A1})$$

Taking the Fourier transform with respect to x ,

$$\begin{aligned} S(X,z) &= \int_{-\infty}^{\infty} dx \frac{\partial\phi(x,z)}{\partial z} e^{2\pi i x X} \\ &= \frac{e}{\hbar} \int_{-\infty}^{\infty} dx \int_{-\infty}^{\infty} dy B_\rho(\rho,z) \cos\varphi e^{2\pi i x X} \\ &= \frac{e}{\hbar} \int_0^{2\pi} d\varphi \int_0^{\infty} d\rho \rho B_\rho(\rho,z) \cos\varphi e^{2\pi i \rho X \cos\varphi}. \quad (\text{A2}) \end{aligned}$$

The φ integral can be performed by taking into account the definition of the Bessel function Eq. (27):

$$S(X,z) = \frac{2\pi i e}{\hbar} \int_0^{\infty} d\rho \rho B_\rho(\rho,z) J_1(2\pi\rho X). \quad (\text{A3})$$

After multiplying $XJ_1(2\pi tX)$ to both sides of Eq. (A3), and integrating with X , we get

$$\int_0^{\infty} dX X S(X,z) J_1(2\pi tX) = \frac{2\pi i e}{\hbar} \int_0^{\infty} d\rho \int_0^{\infty} dX \rho X B_\rho(\rho,z) J_1(2\pi\rho X) J_1(2\pi tX). \quad (\text{A4})$$

By replacing $\eta = 2\pi X$, the right-hand side of Eq. (A4) is

$$\frac{ie}{2\pi\hbar} \int_0^{\infty} d\rho \int_0^{\infty} d\eta \rho \eta B_\rho(\rho,z) J_1(\rho\eta) J_1(t\eta). \quad (\text{A5})$$

Using the identity Eq. (31), Eq. (A5) is equivalent to

$(ie/2\pi\hbar)B_\rho(t,z)$. Consequently Eq. (A4) is reduced to Eq. (33):

$$B_\rho(\rho,z) = \frac{2\pi\hbar}{ie} \int_0^{\infty} dX X S(X,z) J_1(2\pi\rho X). \quad (\text{A6})$$

*Present address: Department of Physics, Faculty of Science, University of Tokyo, Hongo, Bunkyo-ku, Tokyo 113, Japan.

¹R. P. Huebener, *Magnetic Flux Structures in Superconductors* (Springer-Verlag, New York, 1979).

²For example, M. Tinkham, *Introduction to Superconductivity* (McGraw-Hill, New York, 1975).

³T. Suzuki and A. Seeger, *Comments Solid State Phys.* **3**, 128, 173 (1971).

- ⁴H. Boersch, B. Lischke, and H. Solling, *Phys. Status Solidi* **61**, 215 (1974).
- ⁵T. Matsuda, S. Hasegawa, M. Igarashi, T. Kobayashi, M. Naito, H. Kajiyama, J. Endo, N. Osakabe, A. Tonomura, and R. Aoki, *Phys. Rev. Lett.* **62**, 2519 (1989).
- ⁶T. Yatagai, K. Ohmura, S. Iwasaki, S. Hasegawa, J. Endo, and A. Tonomura, *Appl. Opt.* **26**, 377 (1987).
- ⁷S. Hasegawa, T. Kawasaki, J. Endo, A. Tonomura, Y. Honda, M. Futamoto, K. Yoshida, F. Kugiyu, and M. Koizumi, *J. Appl. Phys.* **65**, 2000 (1989).
- ⁸J. R. Clem, *J. Low Temp. Phys.* **18**, 427 (1975).
- ⁹T. Barbee, *Appl. Phys. Lett.* **14**, 156 (1969).
- ¹⁰H. Hoersch, U. Kunze, B. Lischke, and W. Rodewald, *Phys. Lett.* **44A**, 273 (1973).
- ¹¹B. Lischke and W. Rodewald, *Phys. Status Solidi B* **63**, 97 (1974); **62**, 377 (1974).
- ¹²W. Rodewald, *Phys. Lett.* **55A**, 135 (1975); thesis, Technischen Universität Berlin (1977).
- ¹³G. J. Dolan and J. Silcox, *Phys. Rev. Lett.* **30**, 603 (1973).
- ¹⁴G. J. Dolan, *J. Low Temp. Phys.* **15**, 111 (1974); **15**, 133 (1974).
- ¹⁵J. M. Kosterlitz and D. Thouless, *J. Phys. C* **6**, 1181 (1973).
- ¹⁶M. Tinkham, *Phys. Rev.* **129**, 2413 (1963); *Rev. Mod. Phys.* **36**, 268 (1964).
- ¹⁷E. Guyon, C. Caroli, A. Martinet, *J. Phys. Radium* **25**, 683 (1964).
- ¹⁸J. Pearl, *Appl. Lett.* **5**, 65 (1964); *J. Appl. Phys.* **37**, 4139 (1966).
- ¹⁹K. Maki, *Ann. Phys. (N.Y.)* **34**, 363 (1965).
- ²⁰G. Lasher, *Phys. Rev.* **154**, 345 (1967); **140**, A523 (1965).
- ²¹A. L. Fetter and P. C. Hohenberg, *Phys. Rev.* **159**, 330 (1967).
- ²²R. N. Goren and M. Tinkham, *J. Low Temp. Phys.* **5**, 465 (1971).
- ²³U. Essman and H. Träuble, *Phys. Lett.* **24A**, 526 (1967).
- ²⁴H. Träuble and U. Essman, *J. Appl. Phys.* **39**, 4052 (1968); *J. Sci. Instrum.* **43**, 344 (1966); *Phys. Status Solidi* **18**, 813 (1966); **20**, 95 (1967); **25**, 373 (1968); **25**, 395 (1968).
- ²⁵N. V. Sarma, *Phys. Lett.* **25A**, 315 (1967); *Philos. Mag.* **17**, 1233 (1968); **18**, 171 (1968).
- ²⁶A. L. Schawlow, *Phys. Rev.* **101**, 573 (1956).
- ²⁷U. Krögeloh, *Phys. Lett.* **28A**, 657 (1969).
- ²⁸B. Obst, *Phys. Status Solidi B* **45**, 453 (1971); **45**, 467 (1971).
- ²⁹A. Bodmer, U. Essman, and H. Träuble, *Phys. Status Solidi A* **13**, 471 (1972).
- ³⁰C. P. Herring, *Phys. Lett.* **47A**, 105 (1974).
- ³¹G. D. Cody and R. E. Miller, *Phys. Rev.* **173**, 481 (1968); **5**, B1834 (1972).
- ³²R. E. Miller and G. D. Cody, *Phys. Rev.* **173**, 494 (1968); **173**, B1834 (1972).
- ³³B. L. Brandt, R. D. Parks, and R. D. Chaudhari, *J. Low Temp. Phys.* **4**, 41 (1971).
- ³⁴M. D. Maloney, F. de la Cruz, and M. Cordona, *Phys. Rev. B* **5**, 3558 (1972).
- ³⁵E. H. Brandt, *J. Low Temp. Phys.* **73**, 355 (1988).
- ³⁶D. Cribier, B. Jacrot, L. M. Rao, and B. Farnoux, *Phys. Lett.* **9**, 106 (1964).
- ³⁷G. Pozzi and U. Valdre, *Philos. Mag.* **23**, 745 (1971).
- ³⁸E. H. Darlington and U. Valdre, *J. Phys. E* **8**, 321 (1975).
- ³⁹H. F. Hess, R. B. Robinson, R. C. Dynes, J. M. Valles, Jr., and J. V. Waszczak, *Phys. Rev. Lett.* **62**, 214 (1989); **64**, 2711 (1990).
- ⁴⁰B. Shinozaki, R. Aoki, T. Miyazaki, M. Katayama, and S. Yamashita, *J. Phys. Soc. Jpn.* **50**, 1868 (1981).
- ⁴¹D. Gabor, *Proc. R. Soc. London* **A197**, 454 (1949); **B64**, 449 (1951).
- ⁴²A. Tonomura, *Rev. Mod. Phys.* **59**, 639 (1987).
- ⁴³Y. Aharonov and D. Bohm, *Phys. Rev.* **115**, 485 (1959).
- ⁴⁴A. Tonomura, N. Osakabe, T. Matsuda, T. Kawasaki, J. Endo, S. Yano, and H. Yamada, *Phys. Rev. Lett.* **56**, 792 (1986).
- ⁴⁵R. Koepke and G. Bergmann, *Z. Phys.* **242**, 31 (1971).
- ⁴⁶G. Brandli and J. L. Olsen, *Mater. Sci. Eng.* **4**, 61 (1969).
- ⁴⁷K. Fuchs, *Proc. Cambridge Philos. Soc.* **34**, 100 (1938); E. H. Sondheimer, *Adv. Phys.* **1**, 1 (1952).
- ⁴⁸G. Möllenstedt and H. Dücker, *Naturwissenschaften* **42**, 41 (1955).
- ⁴⁹J. H. Bruning, D. R. Herriot, D. P. Rosenfeld, A. D. White, and D. J. Brangaccio, *Appl. Opt.* **13**, 2693 (1974).
- ⁵⁰D. J. DeRosier and A. Klug, *Nature (London)* **217**, 130 (1968).
- ⁵¹F. London, *Superfluids* (Wiley, New York, 1950), Vol. 1, p. 143.
- ⁵²G. Eilenberger, *Z. Phys.* **214**, 195 (1968).
- ⁵³C. Kon'no, M. Saji, N. Sagawa, and Y. Umetani, in *Proceedings of the Fall Joint Computer Conference*, 1026, Dallas (IEEE Computer Society Press, Washington, DC, 1986).
- ⁵⁴M. Tinkham, in *Low Temperature Physics*, edited by C. DeWitt, B. Dreyfus, and P. G. de Gennes (Gordon and Breach, New York, 1962), p. 166.
- ⁵⁵G. E. Peabody and R. Meservey, *Phys. Rev. B* **6**, 2579 (1972).
- ⁵⁶B. A. Huberman and S. Doniach, *Phys. Rev. Lett.* **43**, 959 (1979).
- ⁵⁷D. S. Fisher, *Phys. Rev. B* **22**, 1190 (1980).
- ⁵⁸D. Wohlleben, *J. Appl. Phys.* **38**, 3341 (1967).
- ⁵⁹H. Yoshioka, *J. Phys. Soc. Jpn.* **21**, 948 (1966).
- ⁶⁰M. J. Goring and J. P. Jakubovics, *Philos. Mag.* **15**, 393 (1967).
- ⁶¹C. Capiluppi, G. Pozzi, and U. Valdre, *Philos. Mag.* **26**, 865 (1972).
- ⁶²J. Auer and H. Ullmaier, *Phys. Rev. B* **7**, 136 (1973).

Magnetic Field Observation of a Single Flux Quantum by Electron-Holographic Interferometry

Tsuyoshi Matsuda, Shuji Hasegawa, Masukazu Igarashi, Toshio Kobayashi, Masayoshi Naito, Hiroshi Kajiyama, Junji Endo, Nobuyuki Osakabe, and Akira Tonomura
Advanced Research Laboratory, Hitachi, Ltd., Kokubunji, Tokyo 185, Japan

Ryozo Aoki^(a)

Department of Physics, Faculty of Science, Kyusyu University, Hakozaki, Higashi-ku, Fukuoka 812, Japan

(Received 1 March 1989)

The magnetic lines of force of a single flux quantum (fluxon) penetrating a superconducting film (Pb) were observed directly and individually by the electron holography technique using the Aharonov-Bohm effect. The phase contours of the electron wave not only confirm the quantized flux value $h/2e$ but also reveal, by phase amplification, internal structure of a single fluxon. With the film thickness $\lesssim 0.5 \mu\text{m}$, each fluxon, after penetrating the film, fans out or makes a U shape returning to another point on the film surface. With thicker films, fluxons form a bundle with a flux amounting to several times $h/2e$.

PACS numbers: 74.60.Ge, 61.16.Di, 74.70.Be

Many of the fruitful studies of superconductivity dealt with magnetic effects, such as the Meissner effect, the magnetic flux quantization,¹ and the lattice formation of fluxons in type-II superconductors.² One is naturally led to attempt observing the structure as well as the dynamical behavior of a single fluxon.

The first observation of fluxons was achieved by Essman and Träuble;³ they developed a high-resolution Bitter technique to observe a replica of the distribution of fine cobalt particles deposited on a type-II superconductor surface with an electron microscope, verifying Abrikosov's prediction² that the fluxons would form a triangular lattice.

The fluxons were observed also by electron interferometry utilizing the Aharonov-Bohm effect,⁴ in which two electron waves get a relative phase shift of π when their paths enclose a magnetic flux of $h/2e$, which is equal to the fluxon value. Lischke⁵ and Wahl⁶ detected the leakage of the fluxons trapped in a superconducting tube. Boersch *et al.*⁷ took a step forward to observe thermally activated jumps of pinned fluxons from one pinning center to another. Indeed, it is the merit of this

technique that it enables one to see the magnetic field pattern directly without recourse to its still replica, such as in the Bitter technique,³ thereby providing a new way to trace the dynamical behavior of fluxons. So far, however, the fluxon has been detected merely as a line of dislocations of parallel interference fringes by half of their spacing, the line not being sharp enough to permit a clean determination of the motion, not to mention the internal structure, of the fluxon. Another type of observation of a single fluxon has recently been achieved with scanning tunneling microscopy;⁸ this technique probes the electronic structure surrounding the fluxon at the superconductor surface, while the Aharonov-Bohm effect in the above experiments and ours senses the magnetic field structure.

The present Letter is the first report of our electron-holographic studies of the fluxons. We have succeeded in observing the magnetic field structure of a single fluxon penetrating a superconducting thin film. Recalling that the electron-holographic interferometry⁹ with n -times phase amplification (see below) produces one spacing displacement of fringes for a pair of electron

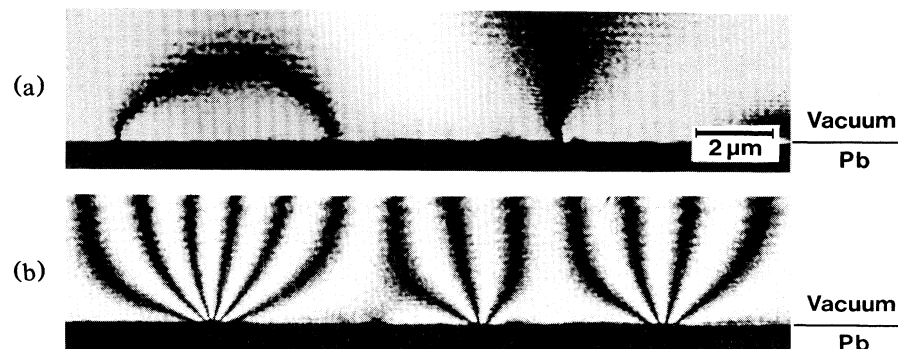


FIG. 1. Interference micrographs of magnetic fluxes penetrating superconducting Pb films (phase amplification, $\times 2$). Film thickness (a) $0.2 \mu\text{m}$ and (b) $1.0 \mu\text{m}$.

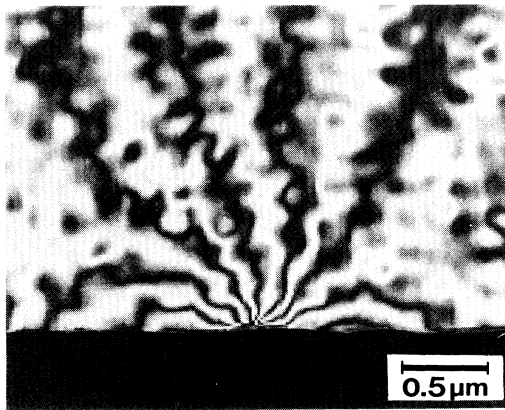


FIG. 2. 16-times phase-amplified interference micrograph of a single fluxon (film thickness $=0.2 \mu\text{m}$ and sample temperature $=4.5 \text{ K}$).

paths enclosing a magnetic flux of h/ne , we see in Fig. 1 ($n=2$) (a) isolated single fluxons that have penetrated a Pb film as thin as $0.2 \mu\text{m}$, and (b) a bundle of fluxons in the case of a Pb film of thickness $1 \mu\text{m}$. A closer look can be taken of a single fluxon by increasing the magnitude n of the phase amplification (Fig. 2, $n=16$). Further discussions will be given below after a brief description of our experimental procedure.

Our superconducting films were fabricated by evaporating Pb on one side of a tungsten wire (diameter of $30 \mu\text{m}$) at room temperature, whose surface was made clean and smooth in advance by flash heating to 2000 K with an electric current. A sample is shown in Fig. 3. The films were made up with grains of single crystals, so that special attention was paid to preparing films almost free from surface roughness, pinholes, and cracks on grain boundaries. The characteristics of the prepared samples were critical temperature $T_c = 7.2 \text{ K}$, and residual resistance ratio $\rho_{300 \text{ K}}/\rho_{7.5 \text{ K}} = 50-80$.

We note that, although Pb is a type-I superconductor, an applied magnetic field produces penetrating fluxons such that they are well separated from each other when the thickness of the Pb film is less than $0.5 \mu\text{m}$ (Ref. 10) as is the case for Fig. 1(a).

Our experiment consisted of two steps: electron-hologram formation and optical image reconstruction. The setup for the first step is shown schematically in Fig. 4. The electron microscope differs from a conventional one in four respects. First, a 150-kV field-emission gun is used so that the electron beam may be highly coherent and well collimated (illumination angle $=5 \times 10^{-8} \text{ rad}$). Second, it is equipped with a newly developed low-temperature stage, which can keep a sample at low temperatures down to 2 K . Third, it has a controllable electromagnet to apply a magnetic field of $0-100 \text{ G}$ on the sample in a horizontal direction. And fourth, an electron biprism¹¹ is installed to form an interference pattern between object and reference beams.

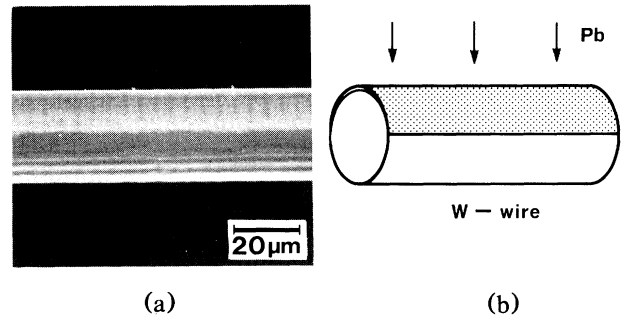


FIG. 3. Superconducting sample. (a) Scanning electron micrograph; (b) sketch.

In this experiment, we apply a weak magnetic field of $0.2-1.0 \text{ G}$ perpendicularly to the sample, and then cool the sample down to 4.5 K on the low-temperature stage. One-half of the collimated electron beam illuminates the sample for the observation of the magnetic fields penetrating the sample, and the other half acts as the reference beam. They are led to form an interference pattern on the image plane by the electron biprism. The image is formed through the intermediate lens and not through the usual objective lens, since the latter has to be turned off so that its magnetic field will not affect the sample. The image is enlarged $1000-2000$ times by electron lenses and is recorded on film to make a hologram, of which the spacing and the total number of interference fringes are $75 \mu\text{m}$ and 200 , respectively.

Optical reconstruction from the hologram using a He-Ne laser makes interference micrographs. The process is

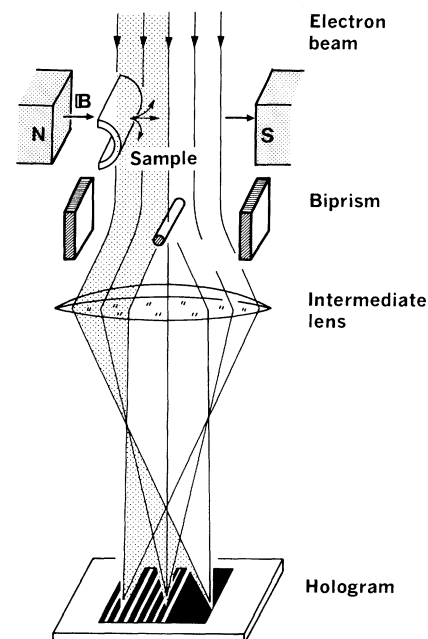


FIG. 4. Electron-optical system for hologram formation.

rather simple; a collimated laser beam illuminates the electron hologram to produce two diffracted beams, one carrying a reconstructed image and the other carrying its conjugate. A Mach-Zehnder-type interferometer makes these two images overlap to form a twice phase-amplified interference micrograph, taking advantage of the fact that two image amplitudes are complex conjugate to each other. This micrograph, prepared in the form of an interferogram, can be used as a twice phase-amplified hologram to repeat the above process to attain the higher phase amplification. Experimental details of the process are described in Ref. 12. An amplified interference micrograph can also be obtained using a digital image analysis technique.¹³

Let us now discuss the interference micrographs thus obtained for the magnetic fields penetrating the superconducting film. Figure 1 shows the twice phase-amplified contour fringes, which can be directly interpreted as projected magnetic lines of force, each representing a flux of $h/2e$.¹⁴ We note that, although a uniform external field is applied to the sample, only the magnetic fields generated by the current induced in the superconductor are observed here, because the uniform field affects equally the object electron beam passing by the sample and the reference beam passing far away. The magnetic lines of force are quite different in the two micrographs, Figs. 1(a) and 1(b), where film thicknesses are 0.2 and 1.0 μm , respectively. In the right half of Fig. 1(a), a magnetic line of force penetrates the film in an extremely localized region, and then fans out into free space. Its flux is $h/2e$ and therefore it is identified as a single fluxon. This identification is confirmed by further experiments as will be described below.

In addition to such an isolated fluxon, we observed an antiparallel pair of fluxons connected by a U-shaped line of force, as shown in the left half of Fig. 1(a). The antiparallel pair of fluxons may have been created when the film was cooled through the Kosterlitz-Thouless regime¹⁵ just below T_c , the presence of which is expected from the two-dimensional character of the thin film. The fluxon oriented against the applied magnetic field may survive to be observed as long as the field is not too strong and the pair is pinned by some mechanism so that the two would not meet to annihilate each other.

We emphasize that the antiparallel pair of fluxons has never been observed by any method, say, Bitter's, so far available, since none of them can tell the polarity of the magnetic field.

In the micrograph 1(b), magnetic flux penetrates the film in a bundle of several fluxons. This is a case of a thicker film, of thickness $\sim 1 \mu\text{m}$; it is known that the intermediate state occurs in a film thicker than 0.5 μm , causing the film to split into normal and superconducting domains.¹⁰

Internal structure of a fluxon line can be observed in highly phase-amplified interference micrographs. An ex-

ample is shown in Fig. 2; the amplification ratio n is 16, and consequently each line of force represents a flux of $h/16e$. We note that the number of lines here is 8, and hence the total flux amounts to $h/2e$ in agreement with the fluxon value. The diameter (half-width) of the fluxon at the superconductor surface is determined¹⁶ from this micrograph to be approximately 1500 \AA , which value is not inconsistent with the penetration depth $\sim 500 \text{\AA}$ (Ref. 17) of Pb. In order to extrapolate the fluxon profile into the superconductor, theoretical calculations are now in progress. Direct observations of the fluxons inside are also being planned with a higher-energy electron beam that can traverse the superconducting film.

In order to make sure that the magnetic fluxes we observed in the above experiments are due to supercurrents, we confirmed by the same electron-holographic interferometry (i) that the fluxes remain frozen even after the applied magnetic field is removed, and (ii) that the trapped fluxes disappear completely when the sample temperature is raised above T_c .

Thus, we have developed a method and observed the detailed structure of the magnetic field of a single fluxon. Our expectations are that this method will enable us to investigate various kinds of previously inaccessible fundamental features of superconductors. For example, it should help in determining the mechanism of anisotropic superconductivity in high- T_c materials, in clarifying the flux pinning mechanism limiting critical currents, and in searching for a possible flux quantum different from $h/2e$.^{18,19}

The authors would like to express special appreciation to Professor Chen Ning Yang of the State University of New York, Dr. Murray Peshkin of Argonne National Laboratory, Professor Hiroshi Ezawa of Gakushuin University, and Dr. Eizabro Yamada of Hitachi Central Research Laboratory for their valuable and stimulating discussions. Gratitude is extended to Dr. Ushio Kawabe, Dr. Yoshinobu Tarutani, and Dr. Masaaki Futamoto of Hitachi Central Research Laboratory for their helpful discussions and advice. Yukio Honda of Hitachi Central Research Laboratory and Hisashi Nagano, Takao Matsumoto, and Seiichi Kondo of Hitachi Advanced Research Laboratory also deserve thanks for their assistance during the experiments.

^(a)Present address: Department of Electrical Engineering, Faculty of Engineering, Osaka University, Yamadaoka, Suita 565, Japan.

¹B. S. Deaver and W. M. Fairbank, Phys. Rev. Lett. 7, 43 (1961); R. Doll and M. N abauer, Phys. Rev. Lett. 7, 51 (1961); N. Byers and C. N. Yang, Phys. Rev. Lett. 7, 46 (1961).

²A. A. Abrikosov, Zh. Eksp. Teor. Fiz. 32, 1442 (1957) [Sov. Phys. JETP 5, 1174 (1957)].

- ³U. Essman and H. Träuble, *Phys. Lett.* **24A**, 526 (1967).
See also P. L. Gammel *et al.*, *Phys. Rev. Lett.* **59**, 2592 (1987).
- ⁴Y. Aharonov and D. Bohm, *Phys. Rev.* **115**, 485 (1959).
See also A. Tonomura *et al.*, *Phys. Rev. Lett.* **56**, 792 (1986).
- ⁵B. Lischke, *Phys. Rev. Lett.* **22**, 1366 (1969).
- ⁶H. Wahl, *Optik (Stuttgart)* **28**, 417 (1968).
- ⁷H. Boersch *et al.*, *Phys. Status Solidi (b)* **61**, 215 (1974).
- ⁸H. F. Hess *et al.*, *Phys. Rev. Lett.* **62**, 214 (1989).
- ⁹A. Tonomura, *Rev. Mod. Phys.* **59**, 639 (1987).
- ¹⁰M. Tinkham, *Phys. Rev.* **129**, 2413 (1963); R. N. Goren and M. Tinkham, *J. Low Temp. Phys.* **5**, 465 (1971); G. J. Dolan, *J. Low Temp. Phys.* **15**, 111 (1974).
- ¹¹G. Möllenstedt and H. Dücker, *Naturwissenschaften* **42**, 41 (1954).
- ¹²A. Tonomura *et al.*, *Phys. Rev. Lett.* **54**, 60 (1985).
- ¹³S. Hasegawa *et al.*, *J. Appl. Phys.* **65**, 2000 (1989).
- ¹⁴A. Tonomura *et al.*, *Phys. Rev. Lett.* **44**, 1430 (1980).
- ¹⁵J. M. Kosterlitz and D. Thouless, *J. Phys. C* **6**, 1181 (1973).
- ¹⁶The fluxon diameter could not be estimated for all of the observed fluxon patterns, since some of the fluxons penetrated the superconductor sample at regions which were not at the extreme edge of the sample shadow. Their magnetic fields just at the superconductor surface were hidden in the shadow and consequently could not be measured.
- ¹⁷For example, H. R. Kerchner and D. M. Ginsberg, *Phys. Rev. B* **10**, 1916 (1974).
- ¹⁸V. B. Geshkenbein and A. L. Larkin, *Phys. Rev. B* **36**, 235 (1987).
- ¹⁹P. W. Anderson *et al.*, *Phys. Rev. Lett.* **58**, 2790 (1987).

Computer Reconstruction from Electron Holograms and Observation of Fluxon Dynamics

T. Matsuda, A. Fukuhara, T. Yoshida, S. Hasegawa,^(a) and A. Tonomura
Advanced Research Laboratory, Hitachi, Ltd., Hatoyama, Saitama 350-03, Japan

Q. Ru

*Tonomura Electron Wavefront Project, Research Development Corporation of Japan,
 c/o Advanced Research Laboratory, Hitachi, Ltd., Hatoyama, Saitama 350-03, Japan*

(Received 5 October 1990)

The customary optical reconstruction can be replaced with digital computations to dynamically and quantitatively observe microscopic magnetic fields. Electron holograms of time-varying fields are first recorded on videotape. Next, each hologram is reconstructed and phase amplified by computation. Interference micrographs are then reedited on the videotape. Using this method, the movement of fluxons trapped in a thin superconductive film of lead are observed for the first time near the critical temperature. The fluxon diameters on the surface look thicker when the sample temperature is raised from 5 K. Fluxons then begin to move near 7 K and finally disappear at the critical temperature 7.2 K.

PACS numbers: 61.16.Di, 74.60.Ge, 74.70.Be

Quantized magnetic flux (fluxon)¹ plays an important role in both the fundamental and the practical aspects of superconductivity. For example, the critical current of a superconductor depends on fluxon dynamics, i.e., how fluxons can be fixed at some pinning centers around the current level. A fluxon is shaped like an extremely thin thread unobservable even by optical microscopy. In addition, it has a very small magnetic flux, $h/2e$ ($=2 \times 10^{-15}$ Wb). For static observation, the Bitter method² has often been used. Here, magnetic powders sprinkled on superconductor surfaces and accumulated at fluxons are observed by electron microscopy. However, up to now no methods have been available to dynamically observe fluxons.

Recently, new methods³ have been developed for fluxon observation. From these, we used electron holography to directly and quantitatively observe magnetic lines of force of a single fluxon⁴ based on the Aharonov-Bohm effect,⁵ without recourse to its static replica. Thus, this provides us with a new possibility to observe the dynamical behavior of fluxons.⁶

Electron holography⁷ is a two-step imaging process. An electron interference pattern (hologram) between an object wave and a reference wave is first recorded in an electron microscope, and then the object image is reconstructed by laser-beam illumination onto the hologram. The exposure time for the recording is determined from the electron-beam brightness and the sensitivity of the photographic film. Note that it is at least a few seconds.

In the present experiment, we have attempted to use dynamic electron holography with video instead of a photographic system. The experimental arrangement is shown in Fig. 1. An electron interferogram (hologram) was formed in a 150-kV field-emission electron microscope⁸ in which a Möllenstedt-type electron biprism⁹ was installed. The interferogram was dynamically observed with a TV camera (Gatan) and recorded on videotape. The object magnification ranged from 10000

to 30000 times on a 20-cm monitor display. The video signal from the tape was digitized and stored in a memory device with 512 frames (max), and then transported frame by frame to the Appollo DN 10000 computer.

The electron phase distribution was numerically computed by the computer from the hologram recorded in each frame by the Fourier transform method,¹⁰ and was displayed as a phase-amplified ($2 \times$) contour map¹¹ in units of half an electron wavelength. Since a magnetic flux of h/e produces a phase shift of 2π between two electron waves enclosing the flux, one contour corresponds to the magnetic line of force from a single fluxon, $h/2e$.¹²

The quality of the resultant contour map was poor compared with that of conventional maps reconstructed from holograms recorded on film. This was inevitable for dynamic observation because the exposure time for taking an electron hologram was as short as $\frac{1}{30}$ s, and also because the number of carrier fringes in the hologram was as small as 10–50.

Therefore, to eliminate some deterioration, such as that due to Fresnel fringes produced from the biprism wire edges, we made use of the fact that the objects here

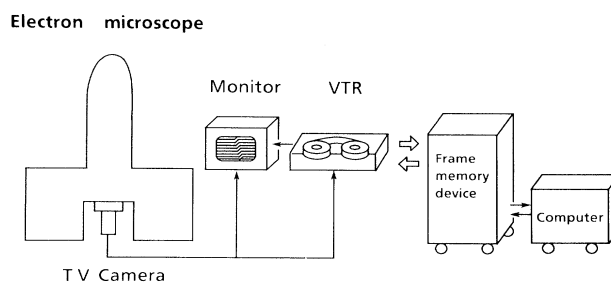


FIG. 1. Experimental arrangement for dynamic electron holography.

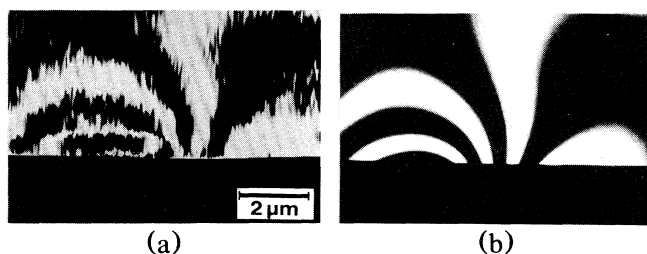


FIG. 2. Interference micrographs of trapped fluxons (phase amplification, $2\times$). (a) Original micrograph. (b) Processed micrograph.

were magnetic fields; magnetic fields in a vacuum cause phase distributions with harmonic-function shapes. Details of the numerical reconstruction and the image processing will be reported elsewhere.¹³

An example of a reconstructed contour map is shown in Fig. 2(a) and a computational improvement of it in Fig. 2(b). Evidently, the processing removes only noise and does not introduce any artifacts. Contour fringes here can be interpreted as magnetic lines of force in $h/2e$ flux units,¹² since the map is phase amplified 2 times. The direction of the flux can be determined from the corresponding interferogram. One can observe at a glance how magnetic flux trapped inside a superconducting Pb film leaks into the vacuum.

An arrangement for fluxon observation is schematically shown in Fig. 3.⁴ A thin tungsten wire $30\ \mu\text{m}$ in diameter was cleaned and smoothed by resistive heating, and lead, approximately $0.7\ \mu\text{m}$ in thickness, was evaporated onto one side of it. This sample was first cooled down to 5 K at the liquid-He low-temperature stage in the electron microscope. It was confirmed by observing an electron interferogram on the TV monitor that there were neither magnetic fields nor other disturbances such as electrostatic fields due to the charging effects. The sample temperature T was raised to around 8 K, just above the critical temperature $T_c = 7.2\ \text{K}$ for lead, and then a magnetic field of 0.5–5 G was applied perpendicular to the lead film. Since the intermediate lens was em-

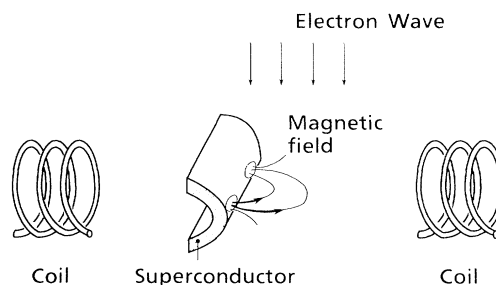


FIG. 3. Experimental arrangement for observation of fluxon bundles trapped in a superconductor.

ployed for image focusing and the magnetic objective lens was not used in this experiment, there was no magnetic field component parallel to the film. When the sample temperature was recooled to 5 K, the magnetic fluxons were trapped in separately squeezed units, fluxon bundles,¹⁴ by the superconducting lead film. The applied magnetic field was turned off to avoid even the slightest movement of the electron interference pattern during the observation due to the possible drift of the field-coil current.

The trapped fluxons remained stationary at 5 K as in our previous static observation.⁴ When the sample temperature was again raised, the diameters of the fluxons gradually increased. After the fluxons began to move at $T \sim T_c$, the produced hologram was recorded on videotape for 10–20 min without a break. Since the fluxons kept still for a period and then suddenly moved, only a short scene of a few seconds including the flux change was selected and reconstructed numerically for observation as magnetic lines of force. The manner of flux changes was rather spontaneous and various: Fluxons appeared to move abruptly from one pinning center to another, to go and return between two pinning centers, and finally vanish when an antiparallel pair of fluxons attracted each other. When T exceeded T_c , all trapped fluxons disappeared.

Figure 4 shows the time variation of the flux shown in Fig. 2. One may notice two differences from our previ-

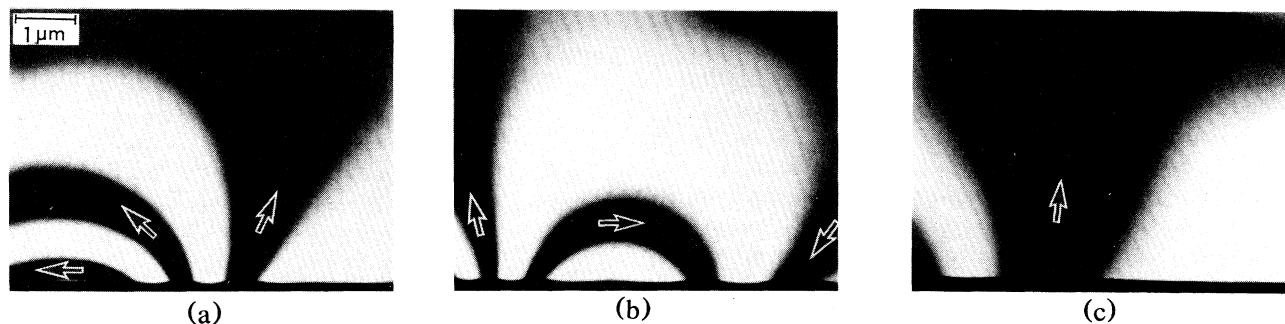


FIG. 4. Interference micrographs of fluxons trapped in superconducting lead film (phase amplification, $2\times$). (a) $t = 0\ \text{s}$. (b) $t = 0.13\ \text{s}$. (c) $t = 1.33\ \text{s}$.

ous static results⁴ observed at 4.5 K with the magnetic field on, where the fluxons were in the same direction as the applied field and had thin necks on the sample surface. In the present case, however, most trapped fluxons were antiparallel pairs, and did not have thin necks. Thick necks result from the increase in penetration depth at $T \sim T_c$. Thicker necks may be due to the fact that the fluxons move into the shadow of the wire, and that the electron beam cannot pass through their true necks. Antiparallel pairs of fluxons may have been produced when a strongly pinned fluxon attracted an oppositely directed fluxon from the film edge so as to make the total magnetic energy smaller, since fluxons can move at $T \sim T_c$.

Photographs (a)–(c) in Fig. 4 show how the thermally excited flux behaves: Three fluxons in the upward direction (shown by arrows in the figure) are trapped in the center of Fig. 4(a), and three magnetic lines of force leak into the vacuum. At $t = 0.13$ s, the fluxons shift to the left corner of Fig. 4(b). It can be seen in the frame that two upward fluxons and two downward fluxons are connected by magnetic lines of force. At $t = 1.33$ s, only a single upward fluxon remains, thereby producing a broad magnetic line. Strictly speaking, since the flux change is completed after a lapse of 0.03 s, a single frame interval, the behavior of a specific flux cannot be followed. It can be followed, however, if the time resolution becomes high enough to catch transient states between the two frames before and after the change. Or, one can follow the flux movement in a wider field of view even if the resolution is insufficient.

An example of a lower-magnification observation is shown in Fig. 5. One can see the whole aspect of mag-

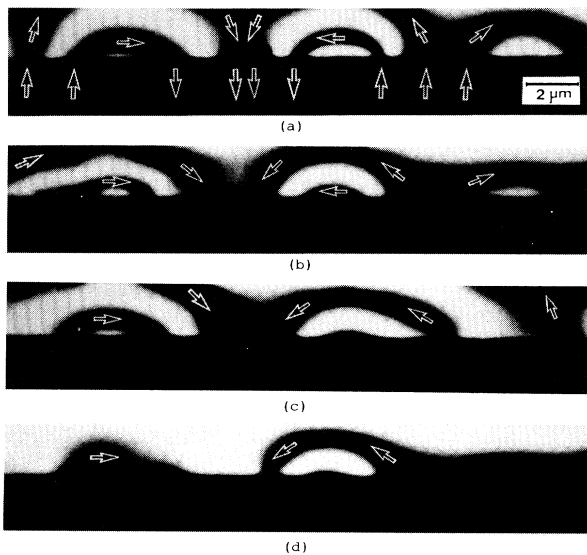


FIG. 5. Dynamic observation of fluxons trapped in superconducting lead film (phase amplification, $2\times$). (a) $t = 0$ s. (b) $t = 3.43$ s. (c) $t = 3.47$ s. (d) $t = 3.50$ s.

netic lines produced from up and down fluxons trapped at various locations of the superconductor. The flux dynamics can be explained here as follows.

Fluxons remained almost stationary for 3 s in Fig. 5(a) and then suddenly moved within only 0.03-s intervals as seen in the three successive frames (b), (c), and (d). The U-shaped double magnetic lines in the central part in Fig. 5(a) hardly change. Here, only the inner magnetic line shrinks from frame (a) to (b). The U-shaped magnetic line in the right part changes slightly as shown in the figure, while the double magnetic lines in the left part almost disappear within only 0.03 s between frames (c) and (d), presumably by approaching and overlapping two antiparallel fluxons. Thermal energy must have excited the flux and allowed it to move over the pinning barriers.

In other cases, however, the flux change was faster and two interferograms (holograms) before and after the change were doubly exposed in a single frame. The resultant contour map appears to consist of two regions having two different flux distributions as shown in Fig. 6. This map results from the production of a Moiré pattern of the two interferograms. Planning is now under way for a new system to resolve such quick fluxon dynamics.

In conclusion, the present technique, electron holography combined with video recording and computer reconstruction, could open the way to dynamic observation of microscopic magnetic fields. For the first time, fluxon dynamics were actually observed with a time resolution as fast as $\frac{1}{30}$ s. In the near future, we will try to observe fluxon movements through electric-current injection in the hope that such direct observations will elucidate the flux-pinning mechanism, especially for high-temperature superconductors.

We are very grateful to Professor C. N. Yang of the State University of New York for his helpful discussions. The authors would like to thank M. Takizawa and K. Shibata of the Central Research Laboratory, Hitachi, Ltd. for their kind cooperation in operating the frame

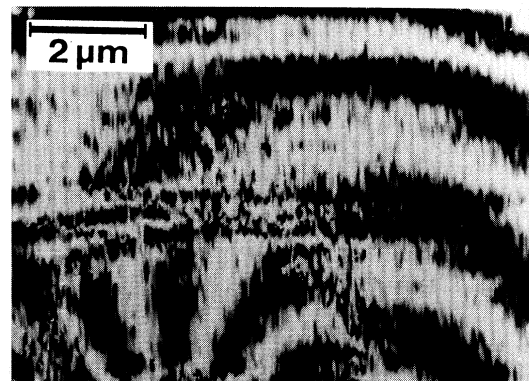


FIG. 6. Interference micrograph of fluxons in transit.

memory device and the Appollo DN 10000 computer.

^(a)Present address: Department of Physics, Faculty of Science, Tokyo University, Hongo, Tokyo 113, Japan.

¹B. S. Deaver and W. M. Fairbank, *Phys. Rev. Lett.* **7**, 43 (1961); R. Doll and M. Näbauer, *Phys. Rev. Lett.* **7**, 51 (1961); N. Byers and C. N. Yang, *Phys. Rev. Lett.* **7**, 46 (1961).

²U. Essman and H. Träuble, *Phys. Lett.* **24A**, 526 (1967).

³For example, H. F. Hess *et al.*, *Phys. Rev. Lett.* **62**, 214 (1989); J. Mannhart *et al.*, *Phys. Rev. B* **35**, 5267 (1987).

⁴T. Matsuda *et al.*, *Phys. Rev. Lett.* **62**, 2519 (1989).

⁵Y. Aharonov and D. Bohm, *Phys. Rev.* **115**, 485 (1959); see also M. Peshkin and A. Tonomura, *The Aharonov-Bohm Effect*, Lecture Notes in Physics Vol. 340 (Springer-Verlag,

Berlin, 1989).

⁶H. Boersch *et al.*, *Phys. Status Solidi (b)* **61**, 215 (1974).

⁷D. Gabor, *Proc. Roy. Soc. London A* **197**, 454 (1949); *B* **64**, 449 (1951). See for recent developments, A. Tonomura, *Phys. Today* **43**, No. 4, 22 (1990).

⁸A. V. Crewe *et al.*, *Rev. Sci. Instrum.* **37**, 576 (1968); see also A. Tonomura *et al.*, *J. Electron Microsc.* **28**, 1 (1979).

⁹G. Möllenstedt and H. Düker, *Naturwissenschaften* **42**, 41 (1955).

¹⁰M. Takeda and Q. Ru, *Appl. Opt.* **24**, 3068 (1985).

¹¹J. Endo, T. Matsuda, and A. Tonomura, *Jpn. J. Appl. Phys.* **18**, 2291 (1979); S. Hasegawa *et al.*, *J. Appl. Phys.* **65**, 2000 (1989).

¹²A. Tonomura *et al.*, *Phys. Rev. Lett.* **44**, 1430 (1980); see also A. Tonomura, *Rev. Mod. Phys.* **59**, 637 (1987).

¹³Q. Ru *et al.* (to be published).

¹⁴M. Tinkham, *Phys. Rev.* **129**, 2413 (1963); R. N. Goren and M. Tinkham, *J. Low Temp. Phys.* **5**, 465 (1971); G. J. Dolan, *J. Low Temp. Phys.* **15**, 111 (1974).

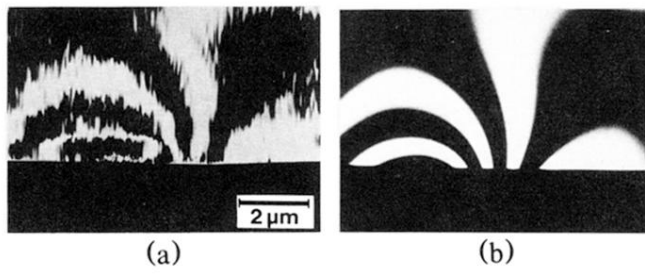


FIG. 2. Interference micrographs of trapped fluxons (phase amplification, $2\times$). (a) Original micrograph. (b) Processed micrograph.

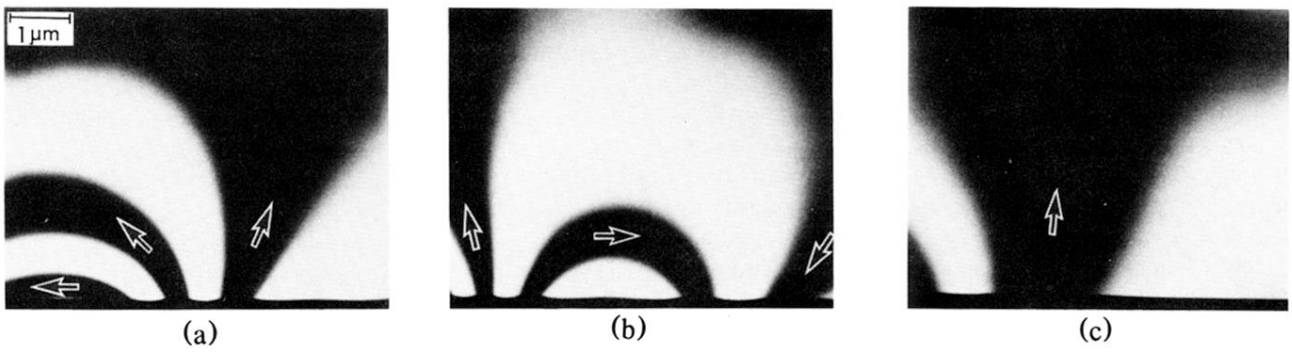


FIG. 4. Interference micrographs of fluxons trapped in superconducting lead film (phase amplification, $2\times$). (a) $t = 0$ s. (b) $t = 0.13$ s. (c) $t = 1.33$ s.

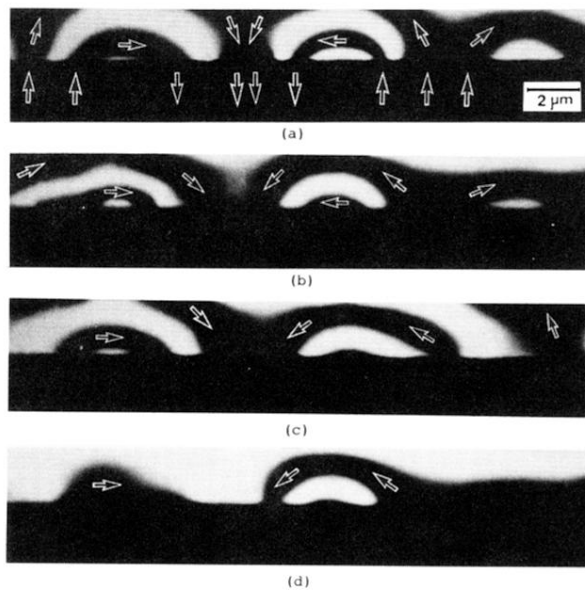


FIG. 5. Dynamic observation of fluxons trapped in superconducting lead film (phase amplification, $2\times$). (a) $t=0$ s. (b) $t=3.43$ s. (c) $t=3.47$ s. (d) $t=3.50$ s.

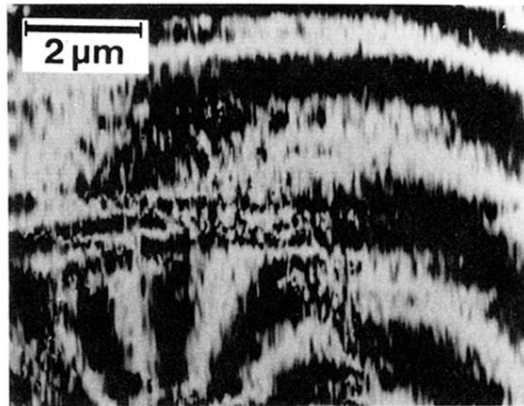


FIG. 6. Interference micrograph of fluxons in transit.

Chemical Analysis of Surfaces by Total-Reflection-Angle X-Ray Spectroscopy in RHEED Experiments (RHEED-TRAXS)

Shuji HASEGAWA,* Shozo INO, Youiti YAMAMOTO** and Hiroshi DAIMON

*Department of Physics, Faculty of Science,
 University of Tokyo, Hongo, Bunkyo-ku, Tokyo 113*

(Received May 7, 1985; accepted for publication May 25, 1985)

A new method for chemical analysis of surfaces by total-reflection-angle X-ray spectroscopy in RHEED experiments (RHEED-TRAXS) has been developed. When the X-ray take-off angle is set to be the critical angle for total reflection of the characteristic X-ray emitted from the deposited atoms on surfaces, the detection efficiency for the deposit becomes drastically higher owing to the refraction effect of the X-ray. This enhancement of surface sensitivity is demonstrated with Ag on Si(111). The smallest detectable amount of Ag is about 0.01 monolayer or less. This sensitivity is comparable to or higher than that of AES.

For chemical analysis of solids by an electron beam, two competing processes are of special interest: the generation of characteristic X-rays, used in X-ray microanalysis (XMA), and the generation of Auger electrons, used in Auger electron spectroscopy (AES). Because the escape depth of Auger electrons from the surface generally ranges from 5 to 30 Å,¹⁾ AES is effective for the chemical analysis of the several atomic layers of a surface. On the other hand, since the escape depth of X-rays is of the order of 1 μm, for XMA it has long been considered impossible to analyze the chemical composition of the last several atomic layers.

Recently Sewell *et al.*²⁻⁶⁾ and Ino *et al.*⁷⁾ showed that it is possible to detect an adsorbate of less than one monolayer by measuring the characteristic X-rays excited by the primary electron beam of RHEED (reflection high energy electron diffraction) during RHEED observations. This technique is far more sensitive to surfaces than usual XMA because the glancing angle of the primary electron beam with respect to the surface is so small (<5°) that the beam does not penetrate into the crystal so deeply. Therefore, the region of X-ray emission is restricted to within several hundred angstroms below the surface.

The information obtained by this X-ray spectroscopy is quite affected by the experimental conditions, such as the energy E_0 , the glancing angle θ_g and azimuthal angle ϕ of the incident electron beam with respect to the crystal orientation of the substrate, and the take-off angle θ_t of the emitted X-rays with respect to the surface (Fig. 1). In this paper we report some experimental results on the θ_t -dependence of the X-ray spectra because they were most drastically affected by the change of θ_t . It has been learned that the surface sensitivity of this X-ray spectroscopy becomes more than several score times as high as that of the one by Ino *et al.*⁷⁾ when the X-ray take-off angle θ_t is set very small and closely corresponding to the critical angle for total reflection of the marked characteristic X-

ray. Then the surface sensitivity of this X-ray spectroscopy, called "total-reflection-angle X-ray spectroscopy in RHEED experiments (RHEED-TRAXS)", becomes comparable to that of AES in general, and superior to it for the detection of heavier elements on surfaces. This enhancement of surface sensitivity around the total reflection angle in the RHEED-TRAXS can be largely explained by the refraction effect of the emitted X-rays at the surface.

Figure 1 is a schematic illustration of the usual RHEED apparatus combined with a Si (Li) solid-state X-ray detector. The X-rays excited by the primary electron beam of RHEED pass successively through two beryllium windows and reach the Si (Li) detector. The first beryllium window with a 10 mm diameter and 25 μm thick is used to seal the ultrahigh vacuum of the chamber and the second, 5 mm in diameter and 14 μm thick, to seal the vacuum of the detector tube in which the Si (Li) crystal is placed. A narrow slit is put in front of the second beryllium window to obtain the resolution of 0.08° on θ_t . The angle between the direction of the incident electron beam and that of the Si (Li) detector is fixed at 90° in this experiment. The X-ray take-off angle θ_t is varied

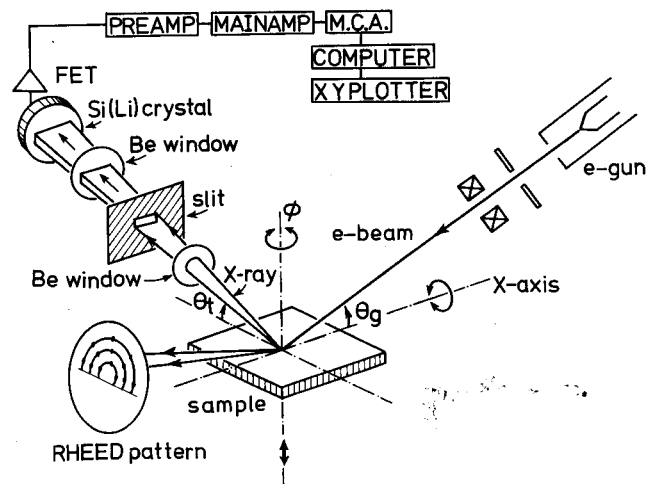


Fig. 1. Schematic illustration of the apparatus used for total-reflection-angle X-ray spectroscopy in RHEED experiments (RHEED-TRAXS).

*Present address: Advanced Research Laboratory, Hitachi Ltd., Kokubunji, Tokyo 185

**Present address: Electron Optics Technical and Engineering Division, JEOL, Ltd., Akishima, Tokyo 196

by rotating the sample around the X-axis (see Fig. 1).

A mirror polished Si(111) wafer was used as a substrate and was carefully cleaned by electron bombardment annealing to obtain a distortion-free surface. When a silicon wafer is heated to 1200°C in a vacuum of the order of 10^{-10} Torr, a clean and flat surface is usually obtained and a clear RHEED pattern of the 7×7 structure appears at room temperature.^{8,9} Ag was deposited onto this surface from W-filaments. The deposited film thickness was monitored by a quartz oscillator.

Figure 2 shows the θ_t -dependence of the X-ray spectra taken from a Si(111) surface onto which a 1.0 monolayer of Ag was deposited at room temperature. The energy of the primary electron beam was 15 keV and the glancing angle, 3.7° . The counting time was 120 sec for each measurement. When θ_t is set to be 2.6° , the intensity of the SiK_α line (1.74 keV), which comes from the Si substrate, is very strong compared with that of AgL_α (2.99 keV) and AgL_β (3.15 keV) lines which are emitted from the deposited Ag atoms. At $\theta_t = 0.6^\circ$, however, the

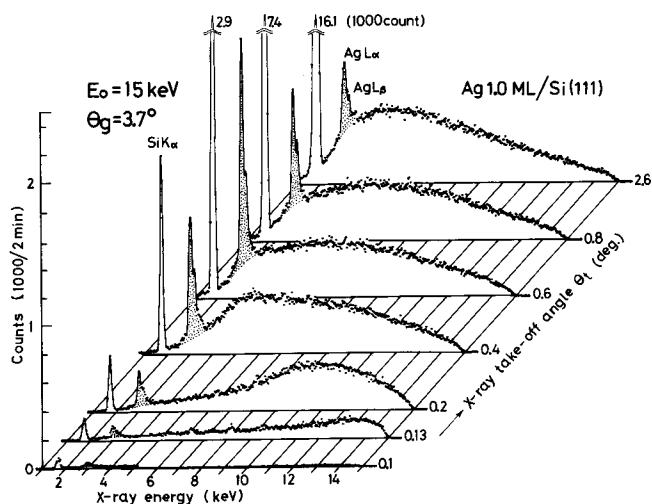


Fig. 2. X-ray spectra of RHEED-TRAXS taken at different take-off angles of the emitted X-ray from the Si(111) surface after Ag deposition of 1.0 monolayer. The energy E_0 and the glancing angle θ_g of the primary electron beam were 15 keV and 3.7° , respectively.

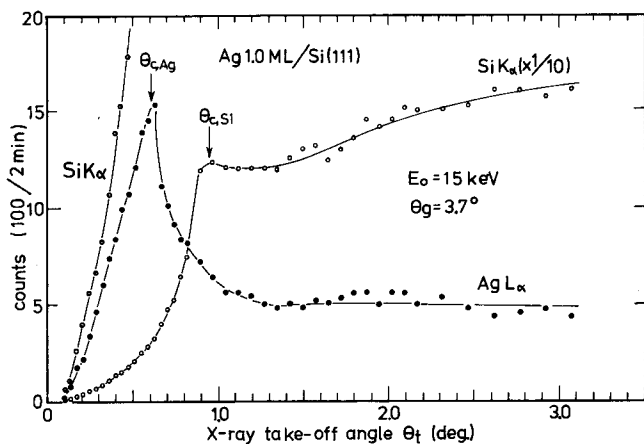


Fig. 3. Dependences of the absolute intensities (peak heights) of the characteristic X-rays on the X-ray take-off angle θ_t . The spectra were taken from the clean Si(111) surface after Ag deposition of 1.0 monolayer. Arrows show the critical angles for total reflection of each characteristic X-ray by silicon.

AgL_α line stands out from the fluctuation of the background continuous X-ray so clearly that the peak to background ratio increases about seven times more than that at $\theta_t = 2.6^\circ$. Hence, one can detect an extremely small quantity of Ag on the surface with much higher sensitivity at this take-off angle than at $\theta_t = 2.6^\circ$. When θ_t is less than 0.6° , the intensity of AgL_α line is comparable to that of SiK_α line and the shape of the continuous X-ray spectra varies markedly with θ_t .

In Fig. 3 the θ_t -dependences of the absolute intensities (peak heights) of AgL_α and SiK_α lines are shown. With the increase of θ_t , the intensity of the AgL_α line increases rapidly and takes a maximum value at $\theta_t = 0.6^\circ$, and then decreases to a smaller constant value. In contrast, the intensity curve of the SiK_α line bends sharply at $\theta_t = 1.0^\circ$ and then gradually increases as θ_t becomes larger than 1.0° . The critical angles for total reflection of AgL_α ($\theta_{c,Ag}$) and SiK_α ($\theta_{c,Si}$) lines by silicon are calculated on the basis of a free electron model and are indicated by arrows in Fig. 3. The AgL_α line intensity shows a strong peak, but the SiK_α line intensity a shoulder at each critical angle for total reflection.

The θ_t -dependence of the relative intensity (peak height ratio) of AgL_α line to SiK_α line is shown in Fig. 4. The relative intensity $\text{AgL}_\alpha/\text{SiK}_\alpha$ takes a maximum value around $\theta_t = 0.3^\circ$ and decreases rapidly when θ_t becomes larger than 0.6° . The value of $\text{AgL}_\alpha/\text{SiK}_\alpha$ at $\theta_t = 0.3^\circ$ is approximately 25 times as large as that at $\theta_t = 3.0^\circ$, which nearly corresponds to the experimental condition of the previous report by Ino *et al.*⁷ The relative intensity of the AgL_α line to the SiK_α line, which indicates the intensity ratio of the signal from the topmost layer of the surface to that from the substrate Si crystal below the Ag film, is an index of the surface sensitivity of this detection method. So it can be said that the surface sensitivity varies with θ_t as shown in Fig. 4 and is highest around $\theta_t = 0.3^\circ$.

The reason the intensities of the characteristic X-rays emitted from the deposited film and the substrate vary with the X-ray take-off angle θ_t in this way can be explained as follows. Since the refractive index of materials for X-rays is slightly less than unity, the X-ray emitted from the inner bulk refracts at the surface as shown in Fig. 5

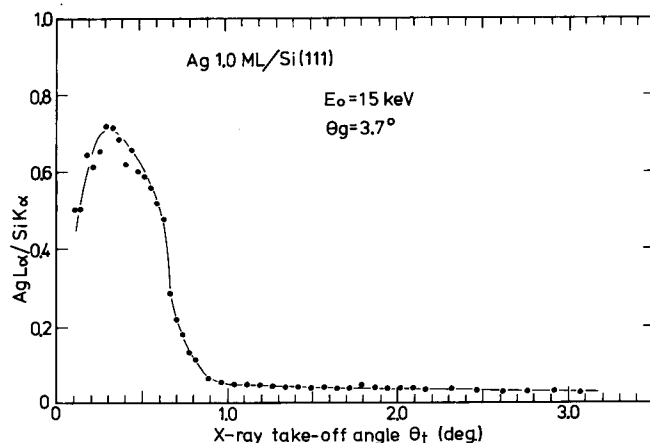


Fig. 4. Relative intensities of the characteristic X-ray (AgL_α line) from the deposit with respect to that (SiK_α line) from the substrate versus the X-ray take-off angle θ_t .

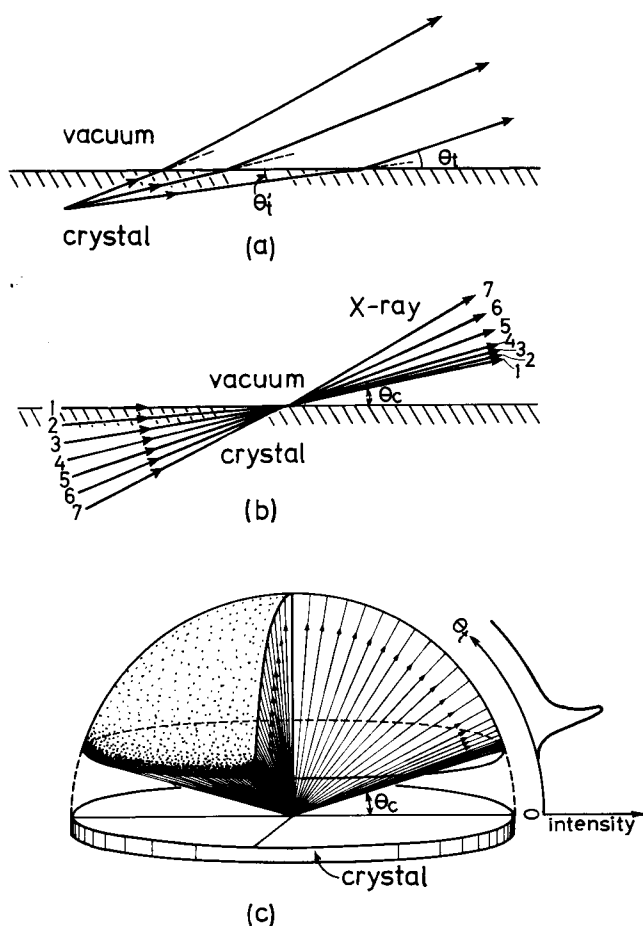


Fig. 5. Refraction effect of the emitted X-rays from the atom in the surface region. (a) Refraction of X-rays at the surface emitted from a point in the crystal. (b) The propagative directions of X-rays in the vacuum side change with the glancing angle θ_i' in the crystal. Although the X-ray emitted with a large θ_i' does not greatly change the propagative direction, the X-ray propagating with a small θ_i' changes its course remarkably. θ_c is the critical angle for total reflection. (c) The flux and the intensity distribution of X-rays emitted from an atom in the topmost layer.

(a). The take-off angle θ_t is slightly larger than the glancing angle θ_i' in the crystal. As θ_i' approaches zero, θ_t approaches a finite value θ_c , the critical angle for total reflection as shown in (b); hence, in the region of θ_t from 0 to θ_c , no x-rays would be emitted into the vacuum side. Therefore, if we ignore the self-absorption effect of X-rays, the intensity of the detectable X-rays emitted isotropically from an atom of the inner crystal is (1) zero for $0 < \theta_t < \theta_c$, (2) maximum at $\theta_t = \theta_c$ because the X-ray flux converges around $\theta_t = \theta_c$, and (3) a smaller constant for $\theta_t > \theta_c$. This intensity distribution along θ_t is similar to that of the AgL_α line shown in Fig. 3, except that the intensity of AgL_α remains for $0 < \theta_t < \theta_{c,\text{Ag}}$ (0.6°). This explanation of the intensity modulation by the refraction effect can thus also be applied qualitatively to the X-rays from the atoms in the topmost layer. The X-ray flux diverges into the vacuum from an emitting atom in the topmost layer as shown in (c). The discrepancy between theory and experiment in the intensity of AgL_α line for $0 < \theta_t < \theta_c$ may be attributed to the surface roughness, the absorption effect of X-rays, or the wave mechanical phenomenon including the distribution of refractive index at the surface. The features of the intensity curve of

the AgL_α line versus θ_t shown in Fig. 3 can be understood in this way by the refraction effect of the X-ray. Since the SiK_α line is emitted from the region ranging from the surface to the inner bulk crystal, the features of the intensity curves of SiK_α line versus θ_t shown in Fig. 3 can be understood by integrating the X-ray intensity emitted at each depth layer, taking into account the absorption effect of both the primary electron beam and the emitted X-ray in the material, and the refraction at the surface.

The reason for the enhancement of the surface sensitivity shown in Fig. 4 is considered to be as follows. The X-rays, which are emitted from the atoms in the topmost layer in the direction parallel to the surface, are considered to propagate through a pass line "1" as shown in Fig. 5(b). Then, if the X-ray detector is set along the pass line "1" in Fig. (b), at the critical angle θ_c for total reflection, we can detect the X-rays emitted only from the atoms near the surface. This preferential detection of only the surface atoms may be furthered when θ_t is set between 0 and θ_c because of the absorption effect of X-rays. In this condition, furthermore, when the θ_c of the characteristic X-ray from the substrate is larger than that of the deposit X-ray as in the case of SiK_α and AgL_α , the substrate X-ray scarcely reaches the detector. And, since θ_c is usually very small, the continuous background X-rays of the same energy as the marked characteristic line from the deposit, which come from the deeper bulk, are weak because of the absorption effect in the sample. Under these conditions, the S/N ratio (or peak to background ratio) of the detection of the surface composition increases about ten times as high as that of the previous experiment by Ino *et al.*⁷⁾ where θ_t was about 3° , far larger than the critical angle for total reflection (0.6°). Consequently, the detection sensitivity of Ag atoms on the Si (111) surface becomes comparable to or higher than that of AES.

The θ_t -dependences of the X-ray spectra can be summarized from two viewpoints, variation of the absolute intensity of the X-ray from the surface, and variation of the surface sensitivity (the detection efficiency of the surface composition) as follows. When the X-ray take-off angle θ_t is set to be the critical angle θ_c , for total reflection of AgL_α line from the deposited Ag atoms, its absolute intensity becomes two or three times as strong as that at $\theta_t > \theta_c$, and the detection efficiency for Ag atoms of 1.0 monolayer becomes 25 times as high as that at $\theta_t > \theta_c$. This phenomenon was observed also in the case of the Au/Si(111) system and hence these results can be generalized.

This X-ray spectroscopy is effective not only for chemical analysis of the topmost atoms, but also for chemical analysis of the deeper region from the surface. That is, if θ_t is set to be larger than θ_c , the X-ray from the inner bulk becomes detectable and the deeper region of the sample comes into view by means of X-ray. Thus, by changing θ_t , the depth profile of the element distribution can be determined non-destructively.

Moreover, in this RHEED-TRAXS the chemical composition and the periodicity of the atomic arrangement of the same surface area can be simultaneously examined. The X-ray spectra can be easily measured during the

deposition onto the surface or during the desorption from the surface without interrupting RHEED observation. These features remarkably contrast this method with LEED-AES (Low Energy Electron Diffraction-Auger Electron Spectroscopy). RHEED-TRAXS will thus be an effective tool for the chemical analysis of solid surfaces, and especially favorable for MBE (molecular beam epitaxy) and the analytical electron microscope.

Acknowledgement

The authors would like to thank Dr. T. Kawamura of Yamanashi University for his valuable suggestions. This work was partially supported by Toray Science Foun-

dation.

References

- 1) P. W. Palmberg: *Anal. Chem.* **45** (1973) 549A.
- 2) P. B. Sewell and M. Cohen: *Appl. Phys. Lett.* **11** (1967) 298.
- 3) P. B. Sewell and D. F. Mitchell: *J. Appl. Phys.* **42** (1971) 5879.
- 4) P. B. Sewell and D. F. Mitchell: *Surf. Sci.* **55** (1976) 367.
- 5) D. F. Mitchell, P. B. Sewell and M. Cohen: *Surf. Sci.* **61** (1976) 355.
- 6) D. F. Mitchell, P. B. Sewell and M. Cohen: *Surf. Sci.* **69** (1977) 310.
- 7) S. Ino, T. Ichikawa and S. Okada: *Jpn. J. Appl. Phys.* **19** (1980) 1451.
- 8) S. Ino: *Jpn. J. Appl. Phys.* **16** (1977) 891.
- 9) S. Ino: *Jpn. J. Appl. Phys.* **19** (1980) 1277.

A STUDY OF ADSORPTION AND DESORPTION PROCESSES OF Ag ON Si(111) SURFACE BY MEANS OF RHEED-TRAXS

Shuji HASEGAWA *, Hiroshi DAIMON and Shozo INO

*Department of Physics, Faculty of Science, University of Tokyo, Hongo, Bunkyo-ku,
Tokyo 113, Japan*

Received 12 November 1986; accepted for publication 9 March 1987

The Si(111)-Ag system was investigated by a new experimental technique for chemical analysis of solid surfaces, called total reflection angle X-ray spectroscopy in RHEED experiments (RHEED-TRAXS). By applying this method to the isothermal condensation and desorption experiments of Ag atoms, saturation coverages of surface structures and desorption energies of Ag atoms could be measured. The sticking probability and the desorption rate of Ag atoms can be directly measured in principle by the RHEED-TRAXS experiment, which is generally difficult by AES. By comparing the experimental results with those of AES, the features of the X-ray spectroscopy are discussed

1. Introduction

In a previous paper [1] it was shown that a spectrum analysis of X-rays excited by a primary electron beam of RHEED (reflection high energy electron diffraction) is useful for chemical analysis of solid surfaces. When the X-ray take-off angle with respect to the surface is set to be around the critical angle for total reflection of the characteristic X-rays of the surface species, the detection sensitivity of this method becomes as high as that of Auger electron spectroscopy (AES), because of the refraction effect of emitted X-rays at the surface. This technique was termed total reflection angle X-ray spectroscopy in RHEED experiments or RHEED-TRAXS for short.

A method of chemical analysis of solids by detecting characteristic X-rays excited with electron beams has been well known as X-ray microanalysis (XMA). Under the usual XMA condition, the X-rays from several atomic layers below the surface are swamped by the intense X-rays from the inner bulk region. But, when the X-rays are measured in the TRAXS condition, the X-rays from the bulk region cannot reach the detector and only the X-rays from the surface region can be detected. Moreover, in the RHEED-TRAXS,

* Present address: Advanced Research Laboratory, Hitachi Ltd., Kokubunji, Tokyo 185, Japan.

since the primary electron beam irradiates the sample at a grazing angle, the excitation efficiency of X-rays in surface region becomes much higher than the usual XMA.

The RHEED-TRAXS and AES are thought to differ from each other in the nature of the obtained information, which is mainly originated in the differing sampling region near the surface. Because the escape depth of Auger electrons is usually about 5 to 30 Å from the surface [2], AES is useful for the chemical analysis of a few surface layers. But the three-dimensional (3D) microcrystals on the surface are scarcely detected directly by AES experiments. So we can differentiate the growth modes of the deposited films from the shapes of the condensation curves. The condensation curve is measured as the change of the AES signal intensity versus the amount of the deposited atoms. For example, if the deposited film grows in the Stranski–Krastanov (SK) mode, the condensation curve bends sharply at the coverage where the two-dimensional (2D) phase completes and the 3D phase begins to grow. The gradient of the curve becomes nearly zero from this point. This can be explained as follows: Auger electrons that are emitted from the inner atoms of the 3D islands, which are thicker than the mean free path, cannot be detected. In this way the intensity of the AES signal is not simply proportional to the amount of the deposited atoms, and it strongly depends on the growth mode.

On the contrary, since the penetration lengths of the X-rays in matters, of which the energies are higher than 1 keV, are longer than 1 μm, X-rays from the inner atoms in the microcrystals on the surface can reach the detector without considerable attenuation. So when we study the initial stages of the deposited films, we can estimate that the intensity of the characteristic X-rays from the deposit is proportional to the number of atoms, independent of the growth mode. Therefore only by measuring the intensity variation of the characteristic line in this X-ray spectroscopy, the actual adsorption or desorption rate of the atoms, which constitute the 3D islands on surfaces, can be directly measured as well as the atoms in the 2D phases, which is impossible for AES experiments.

Taking advantage of the features of this X-ray spectroscopy which contrasts with the LEED (low energy electron diffraction)–AES method, isothermal condensation and desorption curves have been measured at the Si(111)–Ag system. The results have been compared with those of AES experiments. The preliminary experiments in this report show the usefulness of the X-ray spectroscopy for surface and thin film studies.

The system of metal films on semiconductors is of great technological interest as well as of scientific interest. In particular the Si(111)–Ag system is one of the most extensively studied subjects by various experimental methods from the viewpoint of epitaxy and surface structure analysis, because this system is a good example of an abrupt interface, with very limited interdiffusion of the two elements so that its structure analysis may be relatively easy.

Although the Ag film deposited on the clean Si(111) surface at room temperature grows in the Frank–van der Merwe mode developing the texture structure [3], it grows at an elevated substrate temperature in the SK mode [4]. That is, after the completion of the 3×1 and the $\sqrt{3} \times \sqrt{3}$ ($R30^\circ$) surface structures as 2D phases, the Ag islands grow epitaxially as a 3D phase on the $\sqrt{3} \times \sqrt{3}$ structure. The structural models for these 2D phases have been proposed by several investigators. Especially for the $\sqrt{3} \times \sqrt{3}$ structure, the proposed structural models can be classified into three groups on the basis of the saturation coverage θ_s of Ag in this phase: $\theta_s = 1/3$ [5,6], $2/3$ [7–13] and 1.0 [14–18] monolayer (ML). At present the possibility of $\theta_s = 1/3$ ML seems to be contradicted.

From the isothermal condensation and desorption experiments using the RHEED-TRAXS, the saturation coverages of the Ag in the Si(111)- 3×1 and $-\sqrt{3} \times \sqrt{3}$ structures have been estimated to be $1/3$ and 1.0 ML, respectively. The desorption energies of the Ag atoms in the Si(111)- 3×1 , $-\sqrt{3} \times \sqrt{3}$ structures and 3D crystals of SK mode have been also measured at 69 ± 1 , 64 ± 2 and 34 ± 2 kcal/mol, respectively, by directly measuring the desorption rate of Ag atoms from each phase. The possibility of a direct measurement of the sticking coefficient of Ag atoms on the Si(111) surface using the RHEED-TRAXS is suggested.

Section 2 gives a brief description of the experimental set-up and the sample preparation. Experimental results are reported in section 3, and discussed and compared with the AES results by LeLay et al. [7] in section 4.

2. Experimental procedure

Fig. 1 is a schematic illustration of the RHEED apparatus combined with a Si(Li) solid-state X-ray detector system. The RHEED apparatus was described in detail by Ino [19], and the combined RHEED-TRAXS system in previous papers [1,20]. The primary electron beam, of which the acceleration voltage is continuously variable from 5 to 30 keV, is converged by means of a magnetic lens, resulting in a beam divergence of about 1×10^{-4} rad and a beam diameter of about 0.1 mm at the sample surface. Since the glancing angle θ_g of the primary beam can be varied from 1° to 5° , the length of the irradiated surface area of the sample along the primary beam direction is from 1 to 6 mm. The distance from the sample to the Si(Li) crystal of the detector is variable in the range from 80 to 130 mm. The angle between the direction of the primary electron beam and that of the emitted X-rays detected by the Si(Li) detector was fixed at 90° in this experiment. This arrangement of the apparatus is the best for the RHEED-TRAXS experiment, because the X-ray take-off angle θ_i can be maintained constant against the inclination of the sample, that is, the rotation of the sample around an axis which is perpendicu-

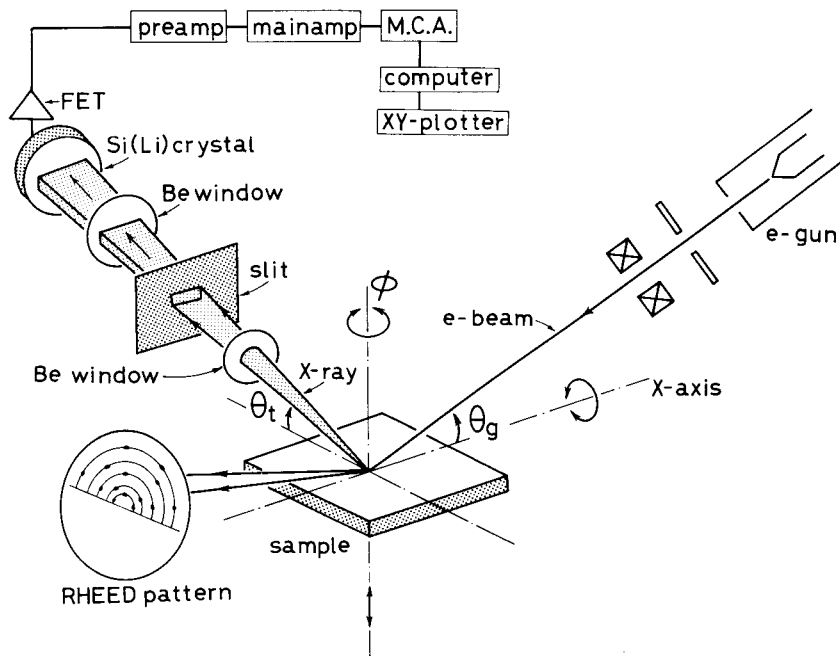


Fig. 1. Schematic illustration of the apparatus used for the total reflection angle X-ray spectroscopy in RHEED experiments (RHEED-TRAXS), which enables us to measure the X-rays and to observe the RHEED patterns simultaneously and continuously.

lar to the electron beam and parallel with the sample surface. θ_t is the most important parameter in this method. So the glancing angle θ_g of the primary electron beam and the take-off angle θ_t of the detected X-rays can be varied independently. Before the emitted X-rays reach the Si(Li) crystal, they pass successively through the beryllium window (10 mm in diameter and 20 μm thick) for the vacuum seal and through an air layer of about 10 mm thick, and finally through the second beryllium window (5 mm in diameter and 14 μm thick) of the detector. Therefore due to the absorption by the two beryllium windows and the air layer, the detection efficiency of the system for the X-rays, for energies smaller than about 3 keV, decreases as the photon energy decreases. In this report we have not corrected the spectra for these absorption effects, but the results are not seriously influenced by this omission.

The residual gas pressure in the chamber was less than 2×10^{-9} mmHg during the operation although the base pressure was less than 5×10^{-10} mmHg. A mirror-polished Si(111) surface of a silicon wafer cut from a single crystal with a resistivity of 18–25 Ω cm was used as a substrate for Ag deposition. Cleaning of the Si(111) substrate surface was performed by heating above 1200 $^\circ\text{C}$ in the chamber by directly passing current through the sample

strip to obtain a clear RHEED pattern of 7×7 structure at room temperature [19]. A surface temperature higher than 800°C was determined by an optical pyrometer. A temperature lower than 800°C was estimated by extrapolation on the basis of the relation between the surface temperature and the passing current, which was confirmed by measurement with a thermocouple and an infrared thermometer by Ichikawa and Ino [21].

Ag was evaporated from a tungsten filament and the amount deposited was monitored in-situ by a quartz oscillator during the deposition. The coverage of Ag is represented in this paper by the ratio θ of the number of deposited atoms to the number of lattice sites ($7.83 \times 10^{14} \text{ cm}^{-2}$) in the (111) atomic plane of the bulk silicon.

3. Experimental results

3.1. RHEED observation

We could observe the following variations of the RHEED pattern simultaneously with the X-ray measurement during isothermal condensation spectroscopy (ITCS) experiments. As Ag atoms were, at first, slowly deposited onto the Si(111) surface showing the 7×7 structure at room temperature (fig. 2), the background increased and the 7×7 reflections became weaker in intensity. At a deposition thickness of about 1 ML, faint broad streaks due to Ag layers appeared. Fig. 2b shows the RHEED pattern from such surface covered with 1.5 ML Ag. In this case it is known that the Ag layers are very thin crystals grown in the Frank-van der Merwe mode. Fig. 2c shows the RHEED pattern from the surface with 3.0 ML coverage, which indicates the texture of Ag layers [3,22,23]. We confirmed that patterns such as in fig. 2c persisted up to at least about 70 ML coverage.

Next, when Ag atoms were slowly deposited onto the Si(111)- 7×7 surface at an elevated temperature ($\sim 440^\circ\text{C}$), the RHEED patterns varied quite differently from that at room temperature deposition. With increasing Ag coverage, the $\sqrt{3} \times \sqrt{3}$ superstructure emerged at first in addition to the 7×7 structure and gained in intensity as shown in fig. 3a. Around 1 ML of Ag coverage, the 7×7 structure disappeared from the RHEED pattern and only the $\sqrt{3} \times \sqrt{3}$ structure was observed (fig. 3b). The pattern remained unchanged up to about 4 ML coverage. When the substrate temperature during the deposition of Ag atoms was lower than 290°C , faint spots and streaks due to Ag crystals appeared in the $\sqrt{3} \times \sqrt{3}$ pattern after the disappearance of the 7×7 superlattice spots (figs. 3c and 3d). At temperatures higher than 290°C , the spots and streaks of Ag crystals could not be observed. But it is concluded from the RHEED-TRAXS experiments that Ag crystals actually grow on the

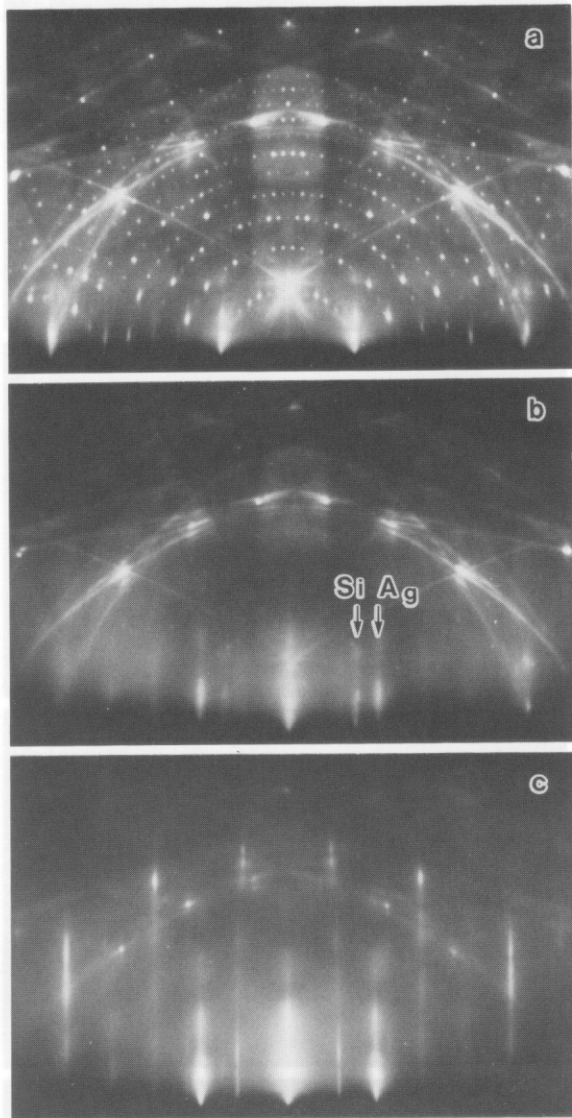
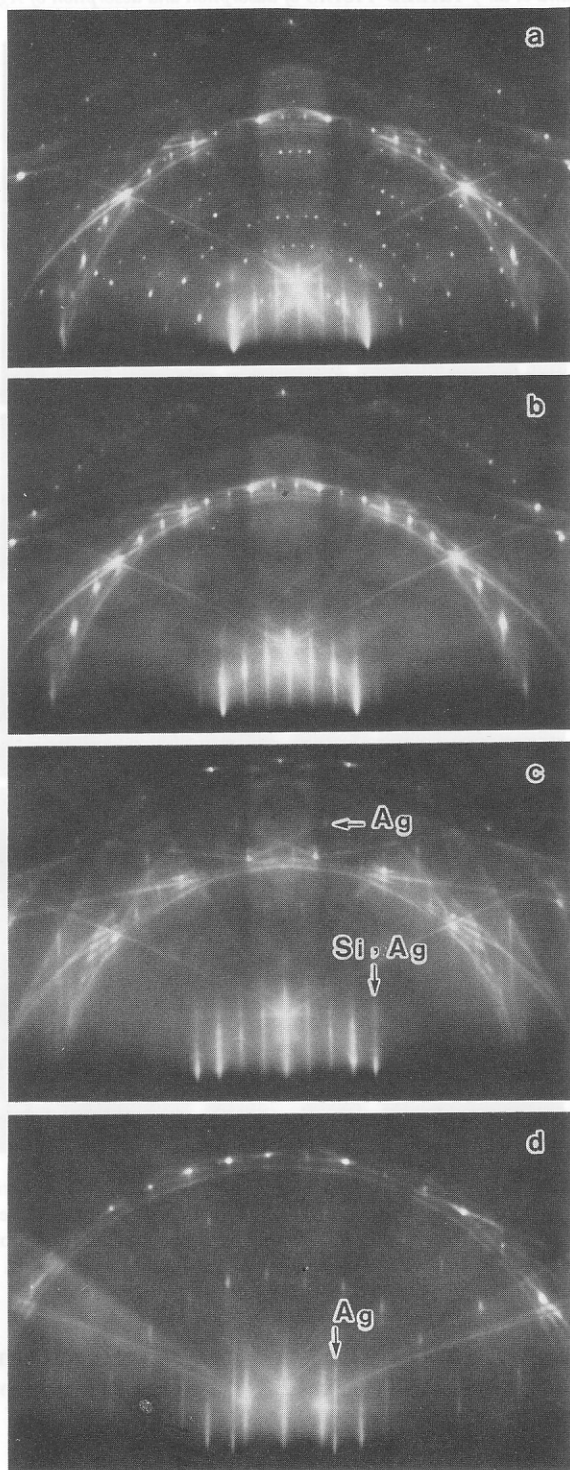


Fig. 2. Series of RHEED patterns ($E_0=15$ keV, $[112]$ incidence) taken during the isothermal condensation of Ag atoms onto Si(111) surface at room temperature. (a) Clean Si(111) surface showing the 7×7 structure. (b) $\theta = 1.5$ ML. Streaks due to Ag layers are seen on the blurred 7×7 structure. (c) $\theta = 3.0$ ML. The texture structure due to Ag layer develops in place of the 7×7 structure.

surface even at 440°C . Since Ag crystals formed at higher temperatures have large sizes, about $2\ \mu\text{m}$ in diameter [23], they may scarcely contribute to the RHEED pattern.



ing the bottom
 an Si(111) surface
 in the figure 1.7
 place of the 1.7
 patterns have
 structure to the

Fig. 1. Series of
 condensation of
 showing the 1.7
 structure (c) &
 surface even
 large sizes, a
 RHEED pat

Similarly, the RHEED observation could be carried out during isothermal desorption spectroscopy (ITDS) experiments of Ag atoms from the Si(111) surface. At first, 3 ML of Ag atoms were deposited onto the Si(111)- 7×7 surface at room temperature. Then the RHEED pattern of the texture of the Ag layer was observed as mentioned above (fig. 2c). As soon as the substrate temperature reached 560°C by passing the current directly through the sample, the RHEED pattern changed into the $\sqrt{3} \times \sqrt{3}$ structure (fig. 4a). By maintaining the substrate temperature at 560°C , Ag atoms thermally desorbed slowly from the surface and the RHEED pattern changed as follows. At first, the 3×1 structure began to emerge in addition to the $\sqrt{3} \times \sqrt{3}$ pattern (fig. 4b). This indicates that since the Ag saturation coverage of the 3×1 phase is smaller than that of the $\sqrt{3} \times \sqrt{3}$ phase, the $\sqrt{3} \times \sqrt{3}$ phase transforms partially into the 3×1 phase during the Ag desorption. Soon after that, the $\sqrt{3} \times \sqrt{3}$ pattern disappeared and only the 3×1 pattern remained. Fig. 4c was taken at this instance. In figs. 4b and 4c, the 6×1 structure is seen. This structure is formed when the surface showing the 3×1 structure is cooled down to lower than 220°C [22]. Directly after that, in place of the $\sqrt{3} \times \sqrt{3}$, the 7×7 pattern emerged and gradually increased in intensity (fig. 4d). The intensities of the 3×1 spots, on the contrary, decreased. This shows that the domain of the adsorbed layer, the 3×1 phase, is converted into the clean surface of the Si(111)- 7×7 phase by the desorption. Finally all Ag atoms desorbed from the surface and the whole surface was covered with the 7×7 phase. The same change of the RHEED pattern during the desorption of Ag atoms could be observed at substrate temperatures from 550 to 640°C . Hence the two different structures, the $\sqrt{3} \times \sqrt{3}$ and the 3×1 , are formed by differences in Ag coverages, not by differences in substrate temperatures.

3.2. RHEED-TRAXS

During the ITDS of Ag atoms from the Si(111) surface (figs. 4a–4d), the X-rays excited by the primary electron beam of RHEED were continuously detected. The variation of their energy spectra with the duration time of desorption at the substrate temperature $T_s = 560^\circ\text{C}$ is shown in fig. 5. The characteristic X-ray peaks of the Si $K\alpha$ line (1.74 keV) emitted from the Si

Fig. 3. Series of RHEED patterns ($E_0 = 15$ keV) taken during the isothermal condensation of Ag atoms onto Si(111) surface at $T_s = 440^\circ\text{C}$. The RHEED patterns at 440°C and at room temperature were the same. So photos were taken after cooling the sample down to room temperature in order to take clear diffraction patterns. (a)–(c) $[\bar{1}\bar{1}2]$ incidence. (a) $\theta = 0.5$ ML. The 7×7 and $\sqrt{3} \times \sqrt{3}$ structures coexist. (b) $\theta = 1.0$ ML. Only the $\sqrt{3} \times \sqrt{3}$ structure is observed. (c) $\theta = 3.0$ ML. (d) Same sample as (c), but $[110]$ incidence. Especially, the surface of (c) and (d) was prepared at $T_s = 290^\circ\text{C}$, in order to show the clear spots from Ag crystals which coexist with the $\sqrt{3} \times \sqrt{3}$ structure.

substrate and the Ag $L\alpha$ line (2.99 keV) emitted from the deposited Ag are clearly seen on the continuous X-ray background. The energy of the primary electron beam and its glancing angle θ_g with respect to the surface were 15 keV and 3.7° , respectively. The counting time was 90 s for each spectrum. The take-off angle θ_t of the detected X-rays with respect to the surface was 0.5° , which is smaller than the critical angle (0.6°) for total reflection of the Ag $L\alpha$ line by silicon. Around this small θ_t region, the intensity of the Ag $L\alpha$ line is enhanced due to the refraction effect of the Ag $L\alpha$ line and the detection efficiency for the Ag film becomes very high as reported in the previous paper [1].

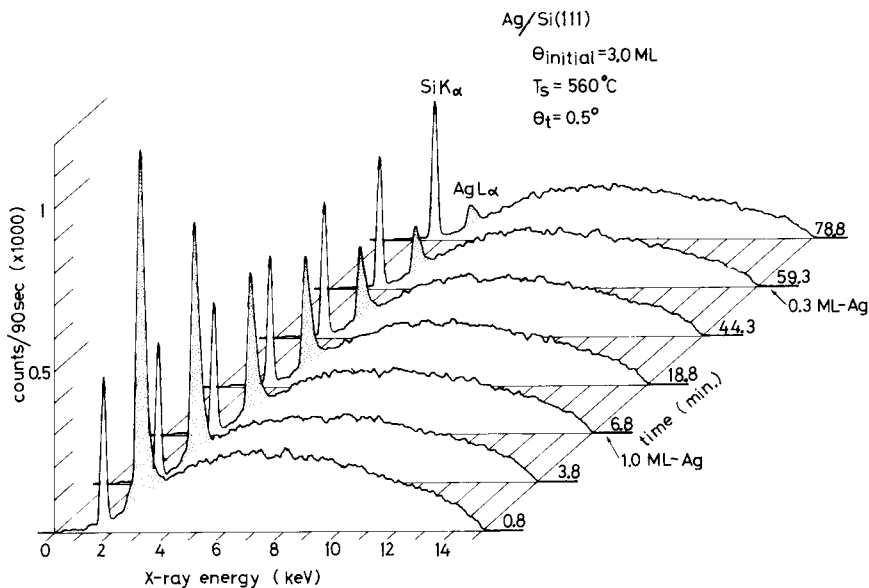


Fig. 5. X-ray spectra of RHEED-TRAXS taken from the Ag-adsorbed-Si(111) surface during the isothermal desorption spectroscopy. 3.0 ML Ag was initially deposited onto the clean Si(111) surface. The intensities of the characteristic lines vary during the following isothermal desorption at $T_s = 560^\circ \text{C}$.

Fig. 4. Series of RHEED patterns taken during the isothermal desorption of Ag atoms from Si(111) surface at $T_s = 560^\circ \text{C}$. The photos were taken after cooling the sample down to room temperature in order to show the diffraction patterns clearly. After the preparation of the same surface as shown in fig. 2c at room temperature, the substrate temperature is abruptly raised up to 560°C and maintained. The texture changes instantly into the $\sqrt{3} \times \sqrt{3}$ structure as shown in (a). The spots from Ag crystals were scarcely seen. With the desorption of Ag atoms, the RHEED patterns change from (a) to (b) $\sqrt{3} \times \sqrt{3}$ and 3×1 structures, and to (c) 3×1 structure, and to (d) 3×1 and 7×7 structures, and finally to the 7×7 structure of the clean surface. The 6×1 structure in (b) and (c) is not seen at $T_s = 560^\circ \text{C}$.

Fig. 5 shows that the intensity of the Ag $L\alpha$ line decayed as the Ag atoms thermally desorbed, although that of the Si $K\alpha$ line remained constant. The amount of Ag atoms left on the Si(111) surface after 6.8 and 59.3 min of thermal desorption, the spectra of which are shown in fig. 5, can be estimated to be about 1.0 and 0.3 ML, respectively, by means of ITCS and ITDS experiments as mentioned below. Here one must pay attention to the fact that the Ag $L\alpha$ peak from the 1.0 ML Ag film is more intense than the Si $K\alpha$ peak from the substrate, which indicates that the detection depth in the Si substrate is extremely restricted, unlike the usual X-ray microanalysis (XMA). The Ag $L\alpha$ peak from the ultra-thin Ag film (0.3 ML or less) stands out clearly from the continuous background fluctuation and its intensity can be determined with high accuracy in spite of the extremely small coverage. In this way, by means of the RHEED-TRAXS experiment, an amount of Ag atoms less than one monolayer on the Si(111) surface can be detected accurately. Its accuracy is comparable to that of AES or higher in some cases. This indicates that the X-ray spectroscopy has a high enough sensitivity for surface studies.

3.3. Isothermal condensation spectroscopy (ITCS) by RHEED-TRAXS

The ITCS curves were measured by RHEED-TRAXS, which show the intensity variations of the Ag $L\alpha$ versus the thickness of the deposited Ag film at different fixed substrate temperatures T_s . In RHEED-TRAXS, during Ag deposition, monitoring the coverage by X-ray measurement in addition to a quartz oscillator and observing by RHEED the structure change can be done simultaneously and continuously without changing the geometrical arrangement of the experimental components, which is difficult in the LEED-AES method. The deposition rate of Ag was about 0.15 ML/min.

Fig. 6 shows the results of the ITCS experiments. Its abscissa indicates the nominal Ag coverage measured by a quartz oscillator. The variations of the RHEED patterns observed simultaneously are indicated. In the case of room-temperature deposition, the Ag $L\alpha$ line intensity increases almost linearly with the Ag coverage as shown in fig. 6c. In this case, as mentioned above, the Frank-van der Merwe type growth of Ag film progresses as schematically illustrated in fig. 7c. That is, Ag atoms condense on the surface in layer-by-layer form. The gradient of the ITCS curve of fig. 6c becomes slightly smaller as the Ag coverage exceeds about 2 ML. This is attributed to the self-absorption effect of the X-rays.

The ITCS curves at elevated substrate temperatures, however, bend at definite coverages as seen in figs. 6a and 6b. In these cases the Ag film grows in the SK mode. The coverages of the bending points are 0.9 ± 0.1 ML at $T_s = 440^\circ\text{C}$ and 0.8 ± 0.1 ML at $T_s = 480^\circ\text{C}$, respectively. The gradient after the bending point becomes smaller as the substrate temperature is higher. The 7×7 superstructure spots, which coexisted with the $\sqrt{3} \times \sqrt{3}$ spots, could be

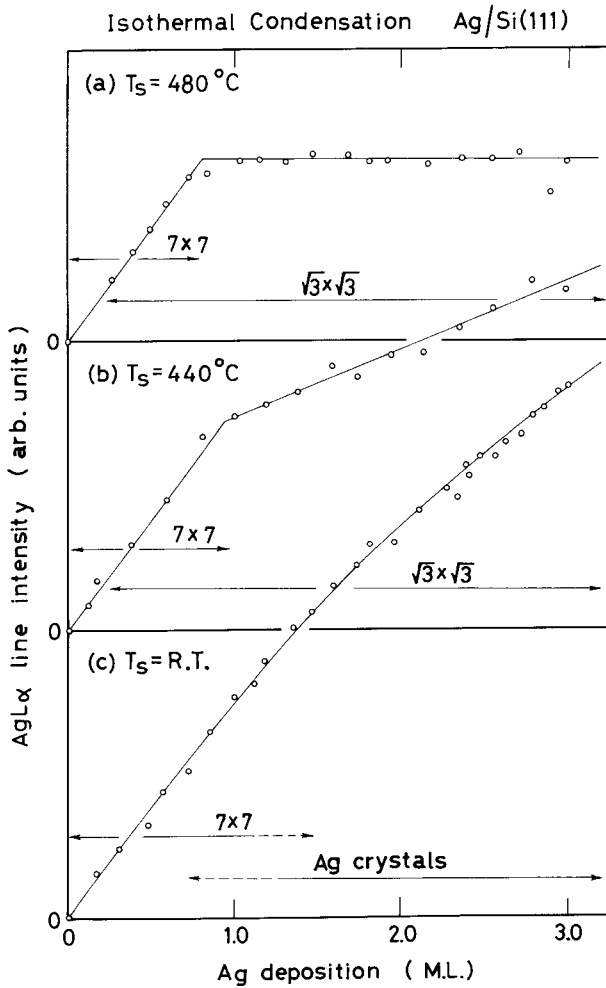


Fig. 6. Variations of the intensity of the Ag $L\alpha$ line during the isothermal condensation spectroscopy at different fixed substrate temperatures. The RHEED patterns observed simultaneously are also shown. The abscissa indicates the nominal Ag coverage measured by a quartz oscillator.

seen until the coverage of the bending points (fig. 3a). When the coverage exceeded that at the bending points, only the $\sqrt{3} \times \sqrt{3}$ structure could be observed in the RHEED pattern (fig. 3b). Taking into account this RHEED observation and the ITCS curves at high substrate temperatures, it is suggested that the $\sqrt{3} \times \sqrt{3}$ structure completes at the coverages of the bending points in the ITCS curves. As mentioned in subsection 3.5, the arriving Ag atoms

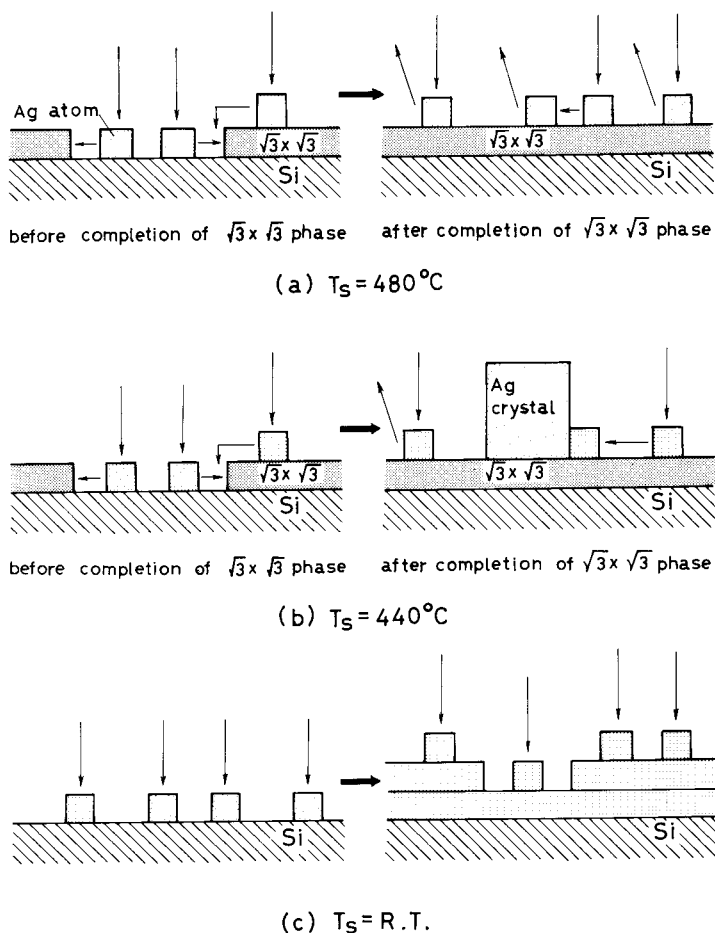


Fig. 7. Schematic illustration of the condensation of Ag atoms on Si(111) surface. (a) Condensation at $T_s = 480^\circ\text{C}$. Before the completion of the $\sqrt{3} \times \sqrt{3}$ phase, Ag atoms adsorb with unit probability and are captured in the $\sqrt{3} \times \sqrt{3}$ phase. After the completion, the arriving Ag atoms scarcely adsorb onto the $\sqrt{3} \times \sqrt{3}$ phase. (b) Condensation at $T_s = 440^\circ\text{C}$. Even after the completion of the $\sqrt{3} \times \sqrt{3}$ phase, Ag atoms adsorb with a small probability and are involved in the 3D Ag crystals on the $\sqrt{3} \times \sqrt{3}$ phase (Stranski-Krastanov mode). (c) Condensation at $T_s = \text{R.T.}$ Ag atoms adsorb with unit probability, resulting in the Frank-van der Merwe growth.

adsorb with a sticking probability of 100% and are involved in the $\sqrt{3} \times \sqrt{3}$ phase before the completion of the $\sqrt{3} \times \sqrt{3}$ phase, although they scarcely adsorb after the completion at $T_s = 480^\circ\text{C}$ (fig. 7a). On the other hand, at $T_s = 440^\circ\text{C}$, as shown in fig. 7b, after the completion of the $\sqrt{3} \times \sqrt{3}$ phase, the arriving Ag atoms adsorb onto the $\sqrt{3} \times \sqrt{3}$ phase with small probability and are involved in 3D Ag crystals. In the belief that the sticking probability

of Ag atoms on the Si(111) surface before the completion of the $\sqrt{3} \times \sqrt{3}$ phase is 100% at these substrate temperatures, we conclude that the $\sqrt{3} \times \sqrt{3}$ structure completes at a Ag coverage of 0.8 ± 0.1 ML at $T_s = 480^\circ\text{C}$ and 0.9 ± 0.1 ML at $T_s = 440^\circ\text{C}$, respectively.

When we consider the atomic arrangement of Ag atoms in the $\sqrt{3} \times \sqrt{3}$ unit mesh, however, the saturation coverage θ_c of the $\sqrt{3} \times \sqrt{3}$ structure is confined within three coverages, 1/3, 2/3 or 1 ML. So θ_c may be estimated to be 1.0 ML from these results. This conclusion will be reinforced by the isothermal condensation and desorption spectroscopy (ITCDS) mentioned below. But there might be room for discussion of this result. The above conviction of a sticking probability of 100% is corroborated experimentally by some researchers [17]. The reason why the gradients of the ITCS curves at elevated substrate temperatures become smaller after the completion of the $\sqrt{3} \times \sqrt{3}$ structure will be discussed later.

3.4. Isothermal desorption spectroscopy (ITDS) by RHEED-TRAXS

During the ITDS experiment described in figs. 4 and 5, the intensities of the characteristic X-rays (Ag $L\alpha$ and Si $K\alpha$) changed as summarized in fig. 8. The abscissa of fig. 8 indicates the duration time of the desorption, and its ordinate, the normalized intensities of the Ag $L\alpha$ and Si $K\alpha$ lines. The ITDS curves 1, 2 and 3 are measured at $T_s = 560, 575$ and 585°C , respectively. The intensity of the Ag $L\alpha$ line decays more rapidly with increasing substrate temperature. On the contrary, the intensity of the Si $K\alpha$ line (curve 4) measured at $T_s = 560^\circ\text{C}$ remains nearly constant, regardless of the decrease of the Ag film thickness. It means that the absorption effect of the Si $K\alpha$ line by the Ag layer is negligible in this case.

The three ITDS curves of the Ag $L\alpha$ line show the following common features. (1) These curves consist of some straight line segments which bend at the points B, C and D. Since the intensity of the Ag $L\alpha$ line at the point B is one-third of that at the point A which corresponds to the initial coverage of Ag (3.0 ML), we can estimate that the amount of Ag left on the surface at the point B is 1.0 ML, assuming proportionality of the Ag $L\alpha$ line intensity with the amount of Ag atoms. Similarly, the refraction points C and D may correspond to coverages of 2/3 and 1/3 ML, respectively. These estimations will be also supported by the ITCDS experiments in the next subsection. (2) If we regard the segments of the curves in the period from 3.0 ML (point A) to 1.0 ML (point B), from 1.0 ML (point B) to around 2/3 ML (point C) and from 1/3 ML (point D) to 0 ML (point E) as straight, the desorption rate of Ag atoms during the period AB is the highest and that during the period DE is the lowest, because the gradients of the ITDS curves directly indicate the desorption rates of Ag atoms as mentioned in the next subsection. (3) Between the points B and C, the 3×1 structure began to appear in the RHEED

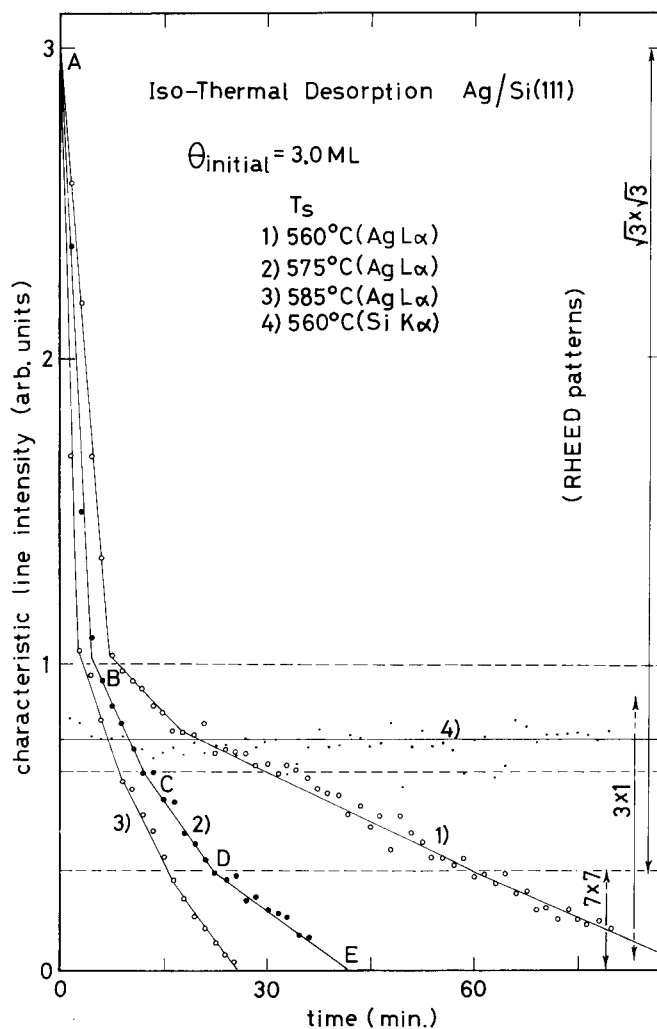


Fig. 8. Variations of the intensities of the characteristic X-ray lines during the isothermal desorption spectroscopy at various substrate temperatures.

pattern. Around point D, the $\sqrt{3} \times \sqrt{3}$ structure disappeared and, in place of it, the 7×7 structure emerged.

Taking these results of the ITDS experiments and those of the ITCS experiments in the previous subsection as well as the RHEED observations into consideration, the ITDS curve of the Ag L α line can be interpreted as follows. Since the $\sqrt{3} \times \sqrt{3}$ structure has been observed always during the period corresponding to the segment AB of fig 8, the Ag atoms desorb

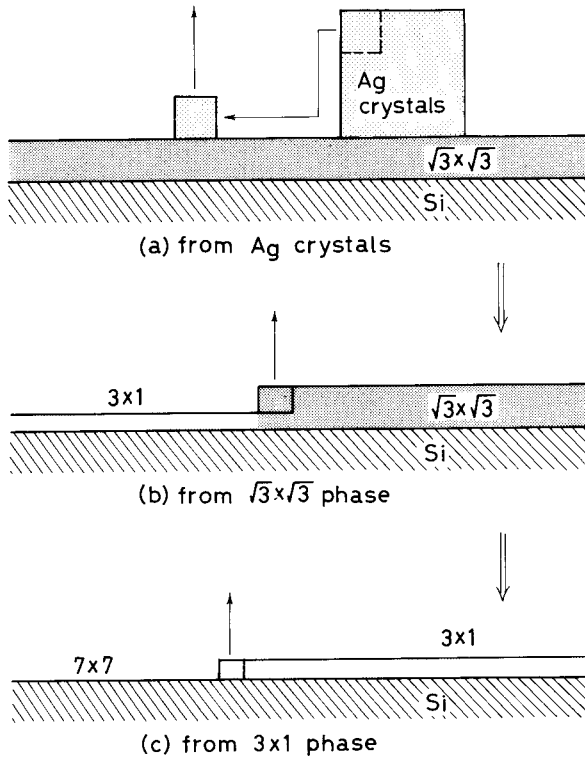


Fig. 9. Schematic illustration of the thermal desorption mechanism of Ag atoms deposited onto the Si(111) surface. (a) Desorption from 3D Ag crystals on the $\sqrt{3} \times \sqrt{3}$ phase. (b) Desorption from the $\sqrt{3} \times \sqrt{3}$ phase, resulting in the conversion from the $\sqrt{3} \times \sqrt{3}$ phase to the 3×1 phase. (c) Desorption from the 3×1 phase, resulting in the conversion from the 3×1 phase to the 7×7 phase.

preferentially from the 3D islands formed on the $\sqrt{3} \times \sqrt{3}$ structure and these islands become small as illustrated in fig. 9a. Although the Ag atoms constituting the $\sqrt{3} \times \sqrt{3}$ structure may also desorb, the desorption rate may be so small that it is negligible compared with that of the 3D islands. Moreover, since the amount of Ag atoms desorbing from the $\sqrt{3} \times \sqrt{3}$ phase is considered to be supplied by diffusing from the 3D islands, only the 3D islands become small. This expectation is based on the property of the SK-type growth that the adhesion energy of the Ag atoms in the completed 2D phase ($\sqrt{3} \times \sqrt{3}$ structure) is larger than that of the Ag atoms constituting the 3D crystal. At point B in fig. 8, all 3D islands disappear and the whole surface is covered by the $\sqrt{3} \times \sqrt{3}$ phase. The coverage of Ag at point B corresponds to the saturation coverage of the $\sqrt{3} \times \sqrt{3}$ structure. From point B, the desorption of the Ag atoms from the $\sqrt{3} \times \sqrt{3}$ phase begins to dominate and the

transformation from the $\sqrt{3} \times \sqrt{3}$ to the 3×1 phase begins as shown in fig. 9b. So during the period from B to D, these two surface structures coexist. With the lapse of time, the domain of the $\sqrt{3} \times \sqrt{3}$ phase decreases while that of the 3×1 phase increases. At point D when the 7×7 structure appears in place of the $\sqrt{3} \times \sqrt{3}$ structure, the whole surface of the Si(111) is covered with the 3×1 phase. The amount of Ag atoms left on the surface at this point D corresponds to the saturation coverage of the 3×1 structure. During the period of the segment DE, the Ag atoms desorb from only the 3×1 phase to change into the 7×7 phase of the clean Si(111) surface (fig. 9c). The ITDS curves of the Ag $L\alpha$ line (fig. 8) show that the three phases of the deposited Ag (3×1 , $\sqrt{3} \times \sqrt{3}$, and 3D islands) can be distinguished from the desorption rate, assisted by the simultaneous RHEED observation, which enables us to characterize these adsorbed structures quantitatively.

3.5. Isothermal condensation and desorption spectroscopy (ITCDS) by RHEED-TRAXS

In order to ascertain the absolute coverage of Ag atoms on the Si(111) surface at each bending point B, C, D in fig. 8, the ITCS and ITDS experiments were successively carried out in this order. Such experiments also confirm that the intensity of the Ag $L\alpha$ line is proportional to the amount of Ag atoms on the surface, independent of the growth mode.

Curve (a) in fig. 10 shows the ITCS curve up to 3.0 ML Ag deposition at a substrate temperature of 440°C which is the same as in fig. 6b, and the following ITDS curve at a substrate temperature of 550°C . At point A, the Ag deposition was turned off and the substrate temperature was abruptly raised from 440 to 550°C . By this temperature change, the ITCS experiment is switched to the ITDS experiment. During the condensation corresponding to the segment GA in fig. 10a, the arriving Ag atoms are captured in the 3D phase on the $\sqrt{3} \times \sqrt{3}$ -2D phase, and an SK-type film is built up. Hence the segment AB of the ITDS part in fig. 10a corresponds to the segment AB in fig. 8, during which the Ag atoms in the 3D phase predominantly desorb. So the points B in figs. 8 and 10 correspond with one another. Moreover the Ag $L\alpha$ line intensity at point B in fig. 10a is equal to that at point G. At point G the Ag coverage is about 1.0 ML. Therefore, the coverage at the point B in figs. 10 and 8 are estimated to be about 1.0 ML.

It can be said that the intensity of the Ag $L\alpha$ line in the period AB of fig. 8 is directly proportional to the amount of Ag atoms, although they constitute a 3D phase, because the Ag $L\alpha$ intensity at B is one-third of that at A. This property of the X-ray spectroscopy markedly contrasts with AES in which 3D islands hardly contribute to the signal. Of course, the proportionality of the X-ray intensity with the amount of Ag atoms in the 2D phases is also

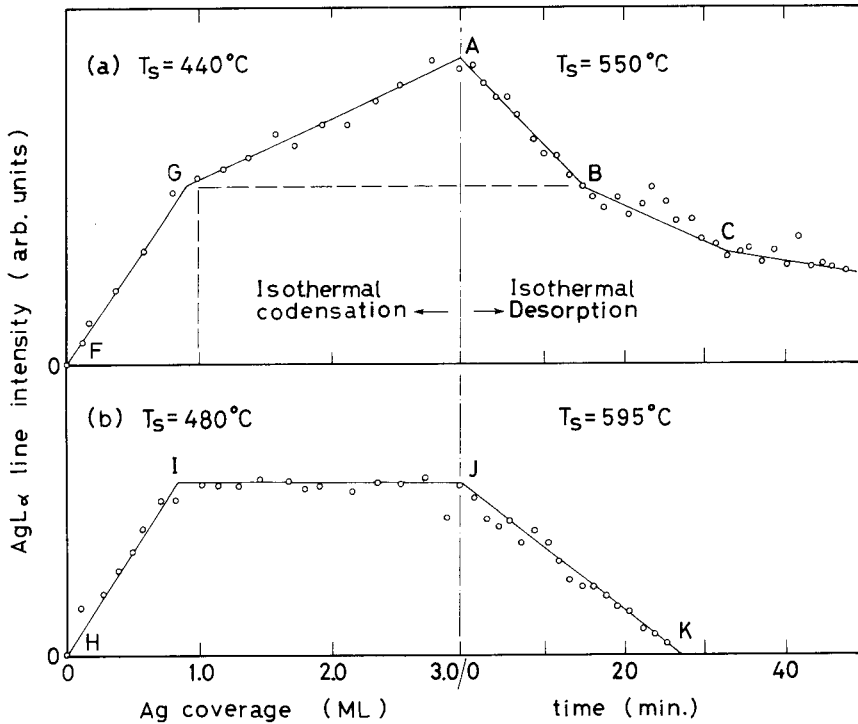


Fig. 10. Variations of the intensity of the Ag $L\alpha$ line during the ITCS and the successive ITDS on the Si(111) surface at various fixed substrate temperatures (isothermal condensation and desorption spectroscopy, ITCDS).

concluded. Hence the coverages at C and D of fig. 8 are determined to be $2/3$ and $1/3$ ML, respectively. As a result, the saturation coverages of the $\sqrt{3} \times \sqrt{3}$ and the 3×1 structures are estimated to be 1.0 and $1/3$ ML, respectively.

From the above result about the proportionality of the Ag $L\alpha$ line intensity to the amount of Ag atoms, the physical origin of the ITCS curves (a) and (b) in fig. 6 is understood as follows. In the ITCS curve (a) in fig. 6, the intensity of the Ag $L\alpha$ line increases linearly up to around 1.0 ML, but it stops to increase despite the higher amount of deposition. That is, the intensity of the Ag $L\alpha$ line maintains a constant value after the completion of the $\sqrt{3} \times \sqrt{3}$ structure in spite of the continuation of the Ag deposition. This directly indicates that the Ag atoms scarcely adsorb onto the Si(111)- $\sqrt{3} \times \sqrt{3}$ surface at 480°C , although they adsorb with unit probability before the completion of the $\sqrt{3} \times \sqrt{3}$ structure. In other words, the sticking coefficient of Ag atoms abruptly changes from 1 to 0 at the point where the $\sqrt{3} \times \sqrt{3}$ structure is completed, as illustrated schematically in fig. 7a. In the case of curve (b) in fig. 6, the sticking coefficient changes from 1 to ~ 0.3 at ~ 1.0 ML. After the

completion of the $\sqrt{3} \times \sqrt{3}$ phase, as shown in fig. 7b, adsorbed Ag atoms are captured in 3D Ag crystals. So the intensity of the Ag $L\alpha$ line increases even after the completion of the $\sqrt{3} \times \sqrt{3}$ phase.

A similar ITCS curve measured with the substrate temperature of 480 °C during adsorption and the successive ITDS curve measured at 595 °C during desorption is shown as curve (b) in fig. 10. Contrasting with the desorption part of curve (a) in fig. 10, the intensity of the Ag $L\alpha$ line begins to decrease linearly down to zero. This indicates that no 3D islands grew on the surface and only the $\sqrt{3} \times \sqrt{3}$ -2D phase existed at point J, which is consistent with the above conclusion about the non-adsorption of Ag atoms on the $\sqrt{3} \times \sqrt{3}$

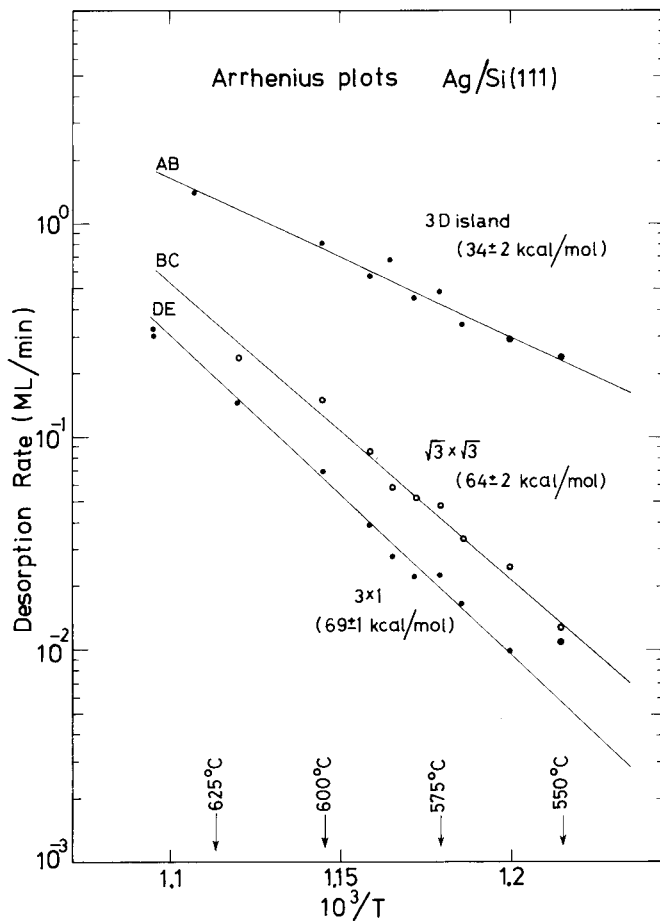


Fig. 11. Desorption rates of Ag atoms from each phase versus the substrate temperature (Arrhenius plots). The desorption rates are obtained from the gradients of each segment in the ITDS curves.

Table 1

Saturation coverages of Ag-adsorbed surface structures and desorption energy of Ag atoms from each phase; the results by LeLay et al. [7] using AES are also shown for comparison

	Saturation coverage (ML)		Desorption energy (kcal/mol)	
	AES ^{a)}	RHEED-TRAXS ^{b)}	AES ^{a)}	RHEED-TRAXS ^{b)}
3D crystals	–	–	67	34 ± 2
$\sqrt{3} \times \sqrt{3}$ structure	2/3	1.0	65	64 ± 2
3 × 1 structure	1/3	1/3	68	69 ± 1

^{a)} From Lelay et al. [7].

^{b)} Present work.

phase at $T_s = 480^\circ\text{C}$. The desorption part JK corresponds to the segments BCDE in fig. 8, but the segment JK seems to be a straight line with only one gradient, which is different from the ITDS curve in fig. 8 although the RHEED pattern changes in the same way. That is, the Ag atoms seem to desorb from both the $\sqrt{3} \times \sqrt{3}$ and 3×1 phases with the same desorption energy. The reason of this discrepancy between figs. 8 and 10b will be discussed in the next section.

3.6. Desorption energies of Ag atoms

Since the scale of the ordinate of fig. 8 corresponds to the absolute coverage of Ag from the reason mentioned above, the desorption rates of the Ag atoms from the 3D islands, the $\sqrt{3} \times \sqrt{3}$ phase and the 3×1 phase are derived directly from the gradients of the segments in the ITDS curves corresponding to the segments AB, BC, and DE in fig. 8, respectively. Their temperature dependences, Arrhenius plots, are summarized in fig. 11. From this figure the desorption energy of Ag atoms from each phase is determined as shown in table 1 where the results of the AES experiment by LeLay et al. [7] are also shown for reference.

4. Discussions

4.1. Comparison between RHEED-TRAXS and AES

The ITCS curve similar to fig. 6a involves different physical phenomena between RHEED-TRAXS and AES, although their shapes are apparently the same. When the gradient of the ITCS curves by AES measurement becomes almost zero after the completion of the 2D phase in the SK mode, there exist two possibilities for this phenomenon. The first one is, of course, that the sticking probability becomes actually zero, and the second one corresponds to the growth of the 3D phase. These two cannot be distinguished only by AES

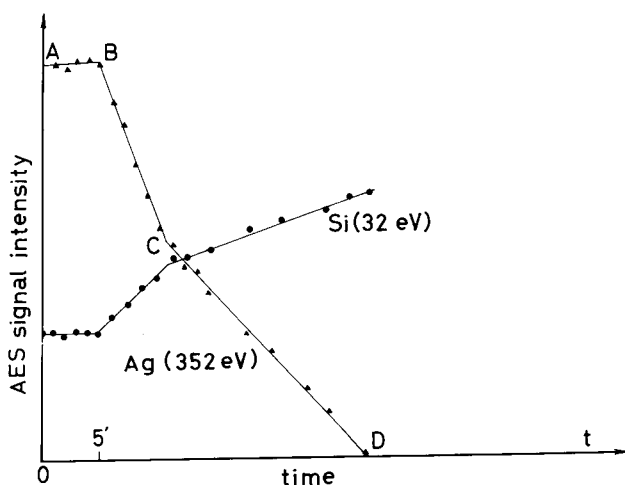


Fig. 12. ITDS curves taken from the Si(111)–Ag surface using AES by LeLay et al. [7]. The substrate temperature is 587 °C. The initial coverage of Ag is 3.38 ML.

experiment. In TRAXS, however, such confusion would hardly occur because the intensity of the Ag $L\alpha$ line is almost proportional to the amount of Ag atoms on the surface even though they constitute the 3D phase. That is, curve (a) in fig. 6 indicates that the amount of Ag atoms does not actually increase after the completion of the $\sqrt{3} \times \sqrt{3}$ phase. In this way the changes of the gradients of the ITCS curves by TRAXS correspond directly to the changes of the sticking probability. The gradient of the ITCS curve by AES at $T_s = 400$ °C after the completion of the $\sqrt{3} \times \sqrt{3}$ phase is almost zero [7,15], but that by TRAXS at $T_s = 440$ °C is not zero as shown in fig. 6b. This fact supports our conclusion mentioned above.

This difference is shown more clearly in the ITDS curves. Fig. 12 shows the ITDS curve of AES at a substrate temperature of 587 °C by LeLay et al. [7]. The segment AB in this figure corresponds to the period of the desorption of the 3D Ag islands. But the intensity of the AES signals from the Ag atoms scarcely changes. The intensity of the Ag $L\alpha$ line in fig. 8, however, decreases with the desorption of the 3D Ag islands. In this way the variation of the amount of the 3D Ag islands as well as of the 2D Ag phases is directly measured by RHEED-TRAXS.

4.2. Saturation coverages and desorption energies

LeLay et al. [7] have examined the Si(111)–Ag system by similar ITDS and ITCS experiments using AES. Their results and ours are summarized in table 1, and compared as follows: (1) Saturation coverages: The saturation coverages of the 3×1 phase coincide, but those of the $\sqrt{3} \times \sqrt{3}$ phase are different.

This discrepancy is a decisive factor for the atomic arrangement model of this superstructure. (2) Desorption energy: The desorption energies of the 2D phases (the $\sqrt{3} \times \sqrt{3}$ and the 3×1) coincide, but those of the 3D phase differ by a factor of ~ 2 . This discrepancy may be due to the difference of experimental methods. In RHEED-TRAXS, the desorption rate can be directly measured from the gradients of the segment AB in the ITDS curves as shown in fig. 8. But LeLay et al. obtained it from the initially deposited amount of Ag and measuring the duration of the segment AB in the ITDS curve (fig. 12), so it may contain an accidental error. From their result, furthermore, the desorption energy of the 3D phase is larger than that of the $\sqrt{3} \times \sqrt{3}$ phase. It seems inconsistent with the thermodynamical feature of the SK film. Our result for the 3D phase (34 kcal/mol) seems reasonable from this viewpoint. But it seems too small compared with the evaporation heat of the pure bulk Ag (60 kcal/mol). This may perhaps be attributed to a special desorption mechanism or a size effect of the Ag microcrystals on the surface. For example, as shown in fig. 9a, when Ag atoms desorb from the 3D phase, they do not desorb directly from 3D crystals, but dissociate first from 3D crystals and diffuse on the 2D phase and then desorb from the surface. If this mechanism actually occurs, the desorption energy of Ag atoms from the 3D phase must apparently be small compared with the evaporation heat of pure Ag, because the binding energy of Ag atoms adsorbed on the $\sqrt{3} \times \sqrt{3}$ phase is smaller than that of Ag atoms constituting the 3D islands.

In the ITDS curves of Ag (fig. 8) the segment CD can be understood as the period during which Ag atoms desorb from the 3×1 phase as well as from the $\sqrt{3} \times \sqrt{3}$ phase. That is, it is a transitional period from the period BC (the $\sqrt{3} \times \sqrt{3}$ phase is dominant) to the period DE (the 3×1 phase is dominant). But the segment CD seems straight in some cases. So there might be another explanation for the segment CD. For example, there might be a zero-order thermal desorption of Ag atoms from a 2D phase in the duration CD which is different from the $\sqrt{3} \times \sqrt{3}$ phase corresponding to the segment BC or the 3×1 phase corresponding to the segment DE. It may suggest the possible existence of another type of $\sqrt{3} \times \sqrt{3}$ phase of which the saturation coverage is $2/3$ ML because the Ag coverage of the point C is $2/3$ ML. In fact, LeLay et al. [24] have inferred the existence of two kinds of $\sqrt{3} \times \sqrt{3}$ phases, of which the saturation coverages are $2/3$ and $0.8\text{--}1.0$ ML, respectively, from a LEED-AES experiment. On the other hand, an experimental result of micro-probe AES has been reported [4], which insists that the saturation coverage of microregions in the $\sqrt{3} \times \sqrt{3}$ phase is $2/3$ ML. As yet there is no model which explains these reports and our results consistently.

4.3. ITDS and ITCs

The ITDS part JK of the ITCDS curve (b) in fig. 10, which was measured after the Ag deposition at a high substrate temperature, seems straight with

only one gradient, although it corresponds to the segments BCDE in fig. 8. This shows a zero-order desorption with only one desorption energy. During this measurement, RHEED patterns, of course, changed from the $\sqrt{3} \times \sqrt{3}$ to the 3×1 and finally to the 7×7 superstructures. In the case of fig. 8, 3.0 ML of Ag were initially deposited on the clean surface at room temperature, and changed into the SK-type film by rapid heating and subsequent annealing of the ITDS experiment. The resulting $\sqrt{3} \times \sqrt{3}$ structure showed similar RHEED patterns as that at the high temperature deposition in the case of fig. 10b. But there is a possibility that the 2D phases formed by these two different methods are different from each other in spite of the same periodicity of atomic arrangements. The difference in the ITDS curves between figs. 10b and 8 may be originated from this effect.

We have concluded that the sticking coefficient of Ag atoms onto the $\sqrt{3} \times \sqrt{3}$ layer at $T_s = 480^\circ\text{C}$ is nearly zero, although it is almost unity before the completion of the $\sqrt{3} \times \sqrt{3}$ structure at the same surface temperature. This result indicates that the surface energy of the $\sqrt{3} \times \sqrt{3}$ surface is so small compared with that of the clean Si(111)- 7×7 surface that the Ag atoms on the $\sqrt{3} \times \sqrt{3}$ phase are much more loosely bound than that on the 7×7 surface. This consideration is consistent with the experimental results that the desorption energy of the 3D islands on the $\sqrt{3} \times \sqrt{3}$ phase is much smaller than that of the $\sqrt{3} \times \sqrt{3}$ phase. The evaporated Ag atoms which arrive on the $\sqrt{3} \times \sqrt{3}$ surface, therefore, scarcely adsorb at $T_s = 480^\circ\text{C}$, in contrast with the complete condensation onto the Si(111)- 7×7 surface at the same T_s (fig. 7a). This comparison of surface energies between the $\sqrt{3} \times \sqrt{3}$ and 7×7 phases is reasonable from the thermodynamical viewpoint of the SK system that the 2D phase would be formed to decrease the dangling bonds of the substrate surface and the surface energy of the resulting adsorbed 2D phase becomes smaller than that of the substrate surface and that of the deposited material.

4.4. Availability of RHEED-TRAXS

A comparison between RHEED-TRAXS and AES concerning the detection of 3D islands on surfaces was discussed in subsection 4.1. We enumerate other properties of RHEED-TRAXS which in general contrast with AES as follows: (1) Unlike the LEED-AES method, since it is the primary electron beam of RHEED that excites the X-rays which are detected, this method enables us to carry out an "in-situ" observation of atomic arrangement and chemical analysis of the same surface area. (2) This X-ray spectroscopy may be more favorable for quantitative chemical analysis than AES. The secondary electrons and the inelastically scattered electrons constitute a higher background in AES measurements compared with the X-ray spectroscopy. Moreover, because of the extremely small escape depth of Auger electrons, the intensity attenuation of emitted Auger electrons in the sample is highly affected by

various factors such as multiple scattering, surface roughness and aggregation states of atoms, etc. Although these factors make a quantitative analysis difficult in the case of AES, the X-ray measurement in RHEED-TRAXS may be scarcely affected by these phenomena because of their high energies and extremely small interaction with matters. (3) This X-ray spectroscopy is available not only for the chemical analysis of the topmost atomic layer on the surface but also for a deeper region below the surface. That is, by making the X-ray take-off angle larger and keeping away from the angle region of total reflection, the X-rays from the deeper region also reach the detector. The detection depth below the surface becomes several hundred ångströms, which has been experimentally confirmed by setting the X-ray take-off angle at $\sim 3^\circ$ in the previous experiment [20]. Under such large take-off angle condition the detection depth becomes restricted by the diffusion depth of the primary electron beam, not by the effective escape depth of the emitted X-rays. In this way the depth profile of the element distribution may be studied non-destructively by changing the take-off angle of the X-rays in RHEED-TRAXS. (4) The X-ray emission is a competing relaxation process of ionized atoms with the emission of Auger electrons, and its ratio grows larger as the atomic number increases. So RHEED-TRAXS is more favorable for the detection of heavier atoms.

RHEED-TRAXS has, on the other hand, the following shortcomings: (1) Because the critical angles of total reflection of X-rays are in general small, in order to obtain a sharp enhancement of the intensity of the marked characteristic X-rays by the refraction effect, one must control the take-off angle very accurately and prepare a very flat surface on a nearly atomic scale. But it is rather difficult, because the take-off angle easily changes by a slight distortion of the surface. We observed that a slight distortion and slip bands of Si wafers caused by a heat-treatment of the samples affected the X-ray intensities. (2) The data acquisition in the present apparatus is less prompt than in the case of the usual AES system. In order to reduce the statistical error, it takes about one minute or more to accumulate the data for one spectrum.

Acknowledgements

The authors would like to express their sincere thanks to Dr. Yoshihiko Gotoh of The Research Institute for Iron, Steel and Other Metals, Tohoku University for his valuable discussions. They also wish to acknowledge Mr. Hiroatsu Matsumoto and Mr. Katsuyuki Fukutani for their assistance in the experiments.

References

- [1] S. Hasegawa, S. Ino, Y. Yamamoto and H. Daimon, *Japan. J. Appl. Phys.* 24 (1985) L387.
- [2] P.W. Palmberg, *Anal. Chem.* 45 (1973) 549A.
- [3] Y. Gotoh and S. Ino, *Thin Solid Films* 109 (1983) 255.
- [4] M. Hanbücken, M. Futamoto and J.A. Venables, *Surface Sci.* 147 (1984) 433, and references therein.
- [5] K. Spiegel, *Surface Sci.* 7 (1967) 125.
- [6] F. Bauer and H. Poppa, *Thin Solid Films* 12 (1972) 167.
- [7] G. LeLay, M. Manneville and R. Kern, *Surface Sci.* 72 (1978) 405.
- [8] M. Saitoh, F. Shoji, K. Oura and T. Hanawa, *Japan. J. Appl. Phys.* 19 (1980) 421.
- [9] M. Saitoh, F. Shoji, K. Oura and T. Hanawa, *Surface Sci.* 112 (1982) 306.
- [10] Y. Terada, T. Yoshizawa, K. Oura and T. Hanawa, *Japan. J. Appl. Phys.* 20 (1981) L333.
- [11] Y. Terada, T. Yoshizawa, K. Oura and T. Hanawa, *Surface Sci.* 114 (1982) 65.
- [12] S. Kono, H. Sakurai, K. Higashiyama and T. Sagawa, *Surface Sci.* 130 (1983) L299.
- [13] J. Stöhr and R. Jaeger, *J. Vacuum Sci. Technol.* 21 (1982) 619.
- [14] Y. Horio and A. Ichimiya, *Surface Sci.* 133 (1983) 393.
- [15] Y. Gotoh, A. Chauvet, M. Manneville and R. Kern, *Japan. J. Appl. Phys.* 20 (1982) L853.
- [16] G.V. Hansson, R.Z. Bachrach, S. Bauer and P. Chiaradia, *Phys. Rev. Letters* 46 (1981) 1033.
- [17] F. Wehking, H. Beckermann and R. Niedermayer, *Surface Sci.* 71 (1978) 364.
- [18] A. Julg and A. Allouche, *Intern. J. Quantum Chem.* 22 (1982) 739.
- [19] S. Ino, *Japan. J. Appl. Phys.* 16 (1977) 891.
- [20] S. Ino, T. Ichikawa and S. Okada, *Japan. J. Appl. Phys.* 19 (1980) 1451.
- [21] Y. Ichikawa and S. Ino, *Surface Sci.* 105 (1981) 395.
- [22] Y. Gotoh and S. Ino, *Japan. J. Appl. Phys.* 17 (1978) 2097.
- [23] Y. Gotoh, S. Ino and H. Komatsu, *J. Crystal Growth* 56 (1982) 498.
- [24] G. LeLay, A. Chauvet, M. Manneville and R. Kern, *Appl. Surface Sci.* 9 (1981) 190.